Tesis doctoral

Departament d'Enginyeria Electrònica

# Evaluation of die attach materials for high temperature power electronics appictions and analysis of the Ag particles sintering solution

Luis Alberto Navarro Melchor

Xavier Jorda Sanuy
Xavier Perpiña

Directores

Gabriel Abadal Berini

Tutor

# Contents

**Abstract** **i**

**Resumen** **iii**

**Resum** **v**

**CHAPTER 1 Introduction and Motivation** **1**

1.1. Introduction 1

1.2. Motivation 1

1.3. Objectives 3

1.4. Organization and Brief Description of this Thesis 3

1.5. Conclusions 5

1.6. References 5

**CHAPTER 2 Power Electronics Packaging Review** **7**

2.1. Introduction 7

2.2. Power Electronics 7

*2.2.1. Semiconductor Devices and Power Electronics Applications* 9

2.3. Power Electronics Packaging 13

*2.3.1 Typical Power Electronics Package Structure* 14

*2.3.2. Advanced Power Packaging Solutions* 18

*2.3.2.1. Pressure Contact Assembly Structure (Press-Pack)* 18

*2.3.2.2. Spring Pressure Contacts* 19

*2.3.2.3. Deposited Metallization Technologies* 20

*2.3.2.4. Thinpack Technology* 22

*2.3.2.5. Area Array or Bumping Interconnection Technologies* 22

*2.3.3 High Temperature Power Electronics Packaging* 23

2.4 Conclusions 25

2.5. References 27

**CHAPTER 3 Ag Nano-Particles Sintering as Die-Attach Solution** **31**

3.1. Introduction 31

3.2. The Die-Attach Layer in Power Electronics Assemblies 31

3.3. Methods for the Assessment of Die-Attach Layers 35
3.4. Ag Nano-Particles Sintering for Die-Attach Applications 46
*3.4.1. Sintering Physical Basis* 47
*3.4.1.1 Geometric Stages of Sintering* 48
*3.4.1.2. Sintering Mechanisms* 50
*3.4.1.3. Sintering Types* 52
*3.4.1.4. Particle Influence on Sintering for Die-Attach Applications* 54
*3.4.2. Ag Nano-Particles Sintering Pastes for Die-Attach Applications* 59
3.5. Conclusions 62
3.6. References 62

**CHAPTER 4 Development of Ag Nano-Particles Sintering Process 69**
4.1. Introduction 69
4.2. Ag Nano-Particles Paste Characterization 69
4.3. Test Vehicle Development for Die-Attach Assessment 77
*4.3.1. Devices used for Die-Attach Assessment* 78
*4.3.2. Substrates used for Die-Attach Assessment* 80

*4.4. Sintering Process and Experimental set-up for Manufacturing Sintered Die-Attach Layers based on Ag Particles* 83
*4.4.1. Screen Printing Methodology* 85
*4.4.2. Drying Process* 86
*4.4.3. Sintering Press Development* 87
4.5. Conclusions 90
4.6. References 90

**CHAPTER 5 Analysis of the Ag Sintering Process Parameters 97**
5.1. Introduction 97
5.2 Influence of the Sintering Pressure 97
*5.2.1. Microstructure of the Die-Attach Layer* 97
*5.2.2. Die-Shear Results for Sintering Pressure Influence* 103
5.3. Influence of the Sintering Temperature 106
*5.3.1. Microstructure of the Die-Attach Layer* 107
*5.3.2. Influence of the Sintering Temperature on the Die-Shear Results* 114

5.4. Influence of the Initial Ag Paste Thickness and Drying Method 120
5.5. Influence of the Sintering Time 127
5.6. Influence of the Substrate Condition 131
*5.6.1. Influence of the Substrate Surface Roughness* 132
*5.6.1.1. Substrate Surface Roughness influence at 0 MPa Sintering Pressure* 132
*5.6.1.2. Substrate Surface Roughness influence at 7 MPa Sintering Pressure* 133
*5.6.2. Influence of the Substrate Surface Treatment* 134
*5.6.3. Influence of the Substrate Surface Material* 136
*5.6.3.1. Influence of the Substrate Surface Material at 0MPa* 136
*5.6.3.2. Influence of the Substrate Surface Material at 7 MPa* 136
5.7. Conclusions 142
5.8. References 145

**CHAPTER 6 Analysis of High Temperature Die Attach Materials under Thermal Cycling** **149**
6.1. Introduction 149
6.2. Initial Evaluation of High Temperature Die-Attach Materials 150
6.3. Thermal Cycling Tests 154
*6.3.1. Experimental Set-Up* 156
6.4. Thermo-Mechanical Stress Analysis in the Test Vehicles 159
*6.4.1. Thermal Stress Module in COMSOL Multiphysics* 160
*6.4.2. Boundary Conditions and Mesh Definition for the Thermo-Mechanical Simulations* 163
*6.4.3. Analysis of Basic Thermo-Mechanical Phenomena on Single Die Structure* 167
*6.4.4. Simulated Stress Distributions for AuGe and PbSnAg Die-Attaches* 174
*6.4.5 Warping Measurements* 175
6.5. Experimental Thermal-Cycling Results 179
6.6. Conclusions 187
6.7. References 189

**CHAPTER 7 General Conclusions and Discussion** **193**

# CHAPTER 1 Introduction and Motivation

## 1.1. Introduction

This chapter will describe the motivation and the main objectives of this research work, which is related to the development of manufacturing die-attach layers based on sintered Ag particles, its comparison with solder alloys and their thermo-mechanical assessment. Besides, a brief description of the organization of this thesis is provided.

## 1.2. Motivation

At the dawn of the second decade of 21$^{st}$ century, global environment and energy generation are some of the most significant issues of our society. According to the Kyoto protocol, the main countermeasures to face them are greenhouse gas emission reduction, energy saving, and rational use of energy. In this scenario, power electronics is the key technology to carry out these actions, since it efficiently manages, distributes and generates electrical energy respecting the environment.

Currently, power electronic systems are present in many market segments; such as: Domestic and office appliances, heating, ventilation and air conditioning, digital consumer, communication, factory automation and drives, traction, automotive and renewable energies. Besides, new challenges in this research field are devoted to the design of even more efficient power electronic systems (rational use of energy), as well as their expansion in the automotive arena with the electric car or in the aeronautic field with the development of more electric aircrafts (greenhouse gas emission reduction).

One bottleneck to meet these targets and challenges is related to the robust and reliable design, fabrication, packaging and integration of commercially available semiconductor power devices. In this sense, the implantation of power electronic systems can be highly improved by increasing their levels of integration and miniaturisation. One of the possible solutions consists in increasing the switching frequency of the power devices as this allows reducing the volume and weight of

magnetic passive components, although in many cases this results also in a junction temperature increase. In line with this integration strategy, there is another approach consisting in allowing the increase of the maximum operation junction temperature of the power devices. The effect of this approach is a drastic reduction of the thermal management requirements, avoiding bulky and heavy heat-sinks, fans, heat-exchangers, etc.

As it has been discussed, increasing the levels of integration (and consequently the power densities) of power converters, is practically correlated with higher operation junction temperatures. In parallel, there is also a big interest in power electronics systems suitable for operating in harsh environments and, in particular, at extreme temperatures, as these are the conditions of several critical fields: space, aeronautical, well logging, etc. This fact increases the interest in new technological solutions allowing the implementation of high temperature power converters, as their application range is extremely wide and strategic. Consequently, the framework of this thesis can be placed in the field of the "high temperature electronics" ("*electronics operating at temperatures in excess of those normally encountered by conventional silicon based or their auxiliary components*" [1]).

In the particular case of the design of power electronics packaging technologies, the implementation of die-attach layers is one of the most critical steps of the manufacturing process. In order to assure suitable operation and resistance to wear-out, this connection must fulfil some requirements, such as sufficient adhesion between die and substrate (so that the die does not detach from the substrate), high electrical and thermal conductivities, suitable mechanical properties to avoid and support the thermo-mechanical stresses and high melting point to guarantee the reliability in harsh environments. Currently, the most common die-attach material used is the family of the PbSnAg alloys [2, 3], although its melting point is not suitable for very high temperature applications (> 300 ºC). Furthermore, lead-based alloys are not environmentally friend and therefore several legislations around the world are gradually limiting the use of lead in electronics [4, 5]. To address this concern several Pb-free alloys and materials have been introduced, including sintered Ag particles, although many aspects of these new technologies still require additional research. This work will

try to contribute to improve the knowhow in this field, and in particular, in using sintered Ag particles as a high temperature die-attach solution.

## 1.3. Objectives

This research work aims at the development of the process technology for manufacturing die-attach layers based on sintered Ag particles. This work will provide useful information about the influence of the most relevant sintering parameters on the quality of the die-attach and the physical understanding of the basic mechanisms explaining such influences. Another relevant objective of the work is to compare the sintered Ag solution with other solder joint materials for power electronic packaging for high temperature applications. For this purpose, experimental tests based on thermal cycling will be performed in order to identify the best solution.

## 1.4. Organization and Brief Description of this Thesis

This thesis is composed by 7 chapters, including the present one, and their content is briefly presented below:

Chapter 2 will describe the importance of power electronics in our society, its main applications, the most used semiconductor devices and the most relevant packaging structures. Main emphasis will be provided to the description of power electronics packaging technology, comparing current technologies, new trends and solutions mainly oriented to high temperature power electronics. This comparison will be performed detailing the materials, benefits and drawbacks among them. On the other hand, some comments are performed on their ageing and long-term reliability, pointing out that the thermo-mechanical stresses experienced under working conditions are among the main ageing agents.

Chapter 3 will define the die-attach technology based on sintering of Ag particles. First, it will be described the main categories of die-attach materials and their thermo-mechanical properties. Then a brief review of the most used methods for failure analysis (FA) will be provided, as well as the description of the methods used in this study to

analyse the quality and the degradation of the die-attach layers. Finally, the sintering theory and its adaptation to allow sintering as a die-attach technique will be described.

Chapter 4 will present the two pastes based on Ag particles used in this work and their main initial properties using different characterization tools (thermo-gravimetric analysis, SEM, etc.). Then, the test vehicle used for characterizing the die-attach layers and their process conditions will be described, providing also the most relevant physical thermo-mechanical parameters of each material involved in their development. Finally, the sintering process and the experimental set-up developed for manufacturing sintered die-attach layers, and their assessment methodology, will be explained. The discussions will address in particular the developed screen printing tools, the drying and temperature profile implementation method and the specific sintering press designed and fabricated for this research work.

Chapter 5 will describe and analyse the influence of the main Ag sintering process parameters, which determine the properties of the final sintered layer. The parameters that will be analysed are pressure, temperature and sintering time. Additionally, the drying step of the Ag paste, which is critical in the manufacturing process, will be also evaluated. Finally, the parameters and characteristics correlated to the substrate condition (surface plating material, roughness and treatment), will be also analysed. This chapter will not only explain the reasons for some of the observed parameter influences, but will also provide useful information for implementing power assemblies using sintered Ag die-attach layers.

Chapter 6 will present a comparative analysis of the thermo-mechanical performance of established high-temperature die-attach materials as a solder alloys (AuGe and PbSnAg) and sintered layers (based on sintering of Ag particles) under harsh thermal cycling tests. The study will focus on test vehicles using bare Cu substrates, due to the practical interest of this solution that avoids plating with Au or Ag, reducing the final cost of the package. Thermally cycled test vehicles will be evaluated using the methods described in chapter 3 (die-shear tests, optical and acoustic microscopy inspections), the test vehicles described in chapter 4 and the sintering processes of chapter 5. As the focus of this work is on high temperature electronics, a specific thermal cycling test set-up was required and its design details are also provided.

Besides, to support the interpretation of the thermal cycling results, auxiliary thermo-mechanical simulations and warpage measurements have been carried out.

Finally, chapter 7 will provide the conclusions of this technological research work.

## 1.5. Conclusions

This chapter provided the framework and the motivation of this research work. Besides, the main objectives and general description of the chapters that constitutes this study have been summarized.

## 1.6. References

[1] F.P. McCluskey, R. Grzybowski, and T. Podlesak. “High Temperature Electronics”. CRC press 1997.

[2] J. Felix, “Impact of material and process parameters in soft solder die bonding,” in *Proc. Semicon,* 2006, pp. 1 - 3.

[3] R. Khazaka, L. Mendizabal, D. Henry, R. Hanna, “Survey of High Temperature Reliability of Power Electronics Packaging Components,” *IEEE Transactions on Power Electronics,* vol. 30 , no. 5, pp. 2456 - 2464, September 2014.

[4] F. P. McCluskey, M. Dash, Z. Wang, and D. Huff, “Reliability of High Temperature solder Alternatives,” *Microelectronics Reliability*, vol. 46, no. 9 - 11, pp. 1910 - 1914, 2006.

[5] Y. Li and C. P. Wong, “Recent advances of conductive adhesives as a lead-free alternative in electronic packaging: Materials, processing, reliability and applications,” *A Review Journal* of *Materials Science and Engineering,* vol. 51, no. 1 - 3, pp. 1 - 35, January 2006.

# CHAPTER 2 Power Electronics Packaging Review

## 2.1. Introduction

This chapter aims at explaining the importance of power electronics in our society, its main applications, the used semiconductor devices and the most relevant packaging structures. Main emphasis will be provided to the description of power electronics packaging technology, comparing current technology, new trends and solutions mainly oriented to high temperature power electronics. This comparison will be performed detailing the materials, benefits and drawbacks among them. On the other hand, some comments are performed on their ageing and long-term reliability, pointing out that the thermo-mechanical stresses experienced under working conditions are among the main ageing agents.

## 2.2. Power Electronics

Over the last years, power electronics has acquired major relevance in our lives. It constitutes the key technology to efficiently manage, distribute and generate electrical energy respecting the environment. Currently, power electronic systems are present in many market segments such as: domestic and office appliances, heating, ventilation and air conditioning, digital consumer, communication, factory automation and drives, traction, automotive and renewable energies. The design of such systems involves the fields shown in Figure 2.1, since power electronics is a multidisciplinary and complex technology [1, 2, 3]. The most significant are:

1) *Microelectronic design and solid state physics.* They are important for developing the semiconductor power devices used in every power electronic system.
2) *Component thermal management, electromagnetic compatibility and circuit theory.* They are necessary for a safe and optimum system design and operation.

3) *Control theory and signal processing.* They ensure an efficient control chain of the power system.
4) *Electrical Engineering concepts.* They are essential for optimizing the interaction between power electronics and electromechanical drives, for correct design of passive elements, etc.
5) *Simulation Tools for Virtual Prototyping.* Multi-physics simulation packages are required for performing virtual prototyping and ensuring the proper operation of the power electronic system, saving cost and time.

The success and fast evolution of power electronics can be mainly attributed to the development of the semiconductor power devices, which allowed in fact the development of energy efficient systems and a more rational use of energy. This is clearly observed in the case of "smart grids" for the management of electrical energy generation and distribution [4]. Their aim is to make an intelligent use of power electronics to distribute electrical energy in a more efficient and cost saving manner, which would not be possible without the current power semiconductor devices. Figure 2.2 plots predictions of US energy consumption versus year [5]. This figure compares such predictions in three different situations: a "frozen" efficiency case, where no additional efficiency improvement measures are taken beyond 2009, a "reference case" based on an analysis from the US Energy Information Association (EIA), and finally a "semiconductor enabled efficiency scenario" (SEES) where a more aggressive usage of semiconductor devices is assumed. The main conclusion that can be extracted from Figure 2.2 is that the power consumption in the frozen efficiency and reference cases does not show the same improvement in terms of consumed power than that achieved when semiconductor devices are employed. They allow also reaching such interesting results in other power electronics applications, therefore being of paramount importance in the whole energy scenario providing a solution to the energy market demands according to Kyoto's protocol. In order to provide an in-depth overview of the role of power semiconductor devices in the most important power electronics applications, their status, trends, and contributions made to the overall application scenario are detailed in the next section.

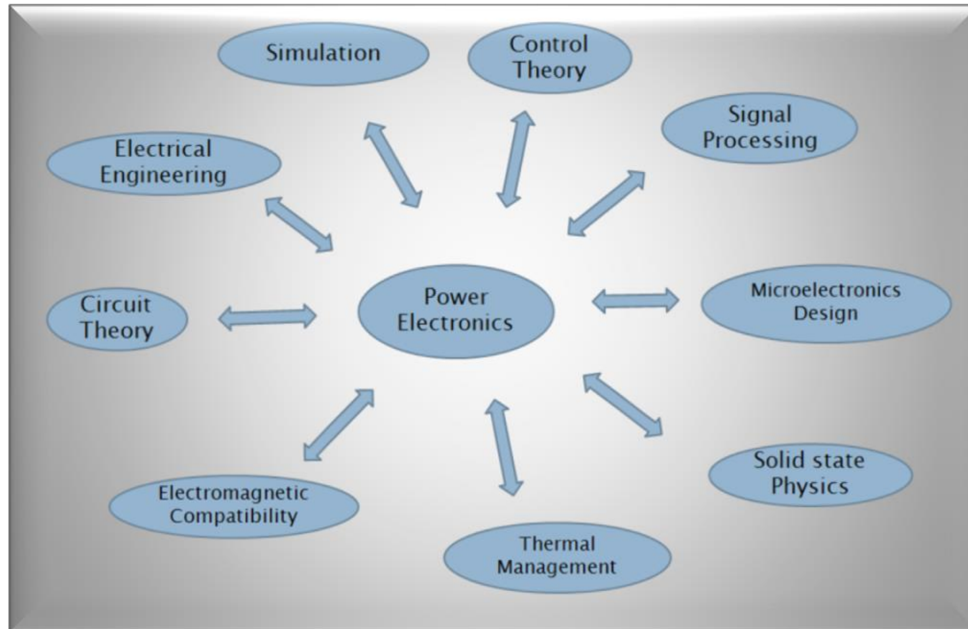


**Figure 2.1. Fields related with power electronic systems [3].**

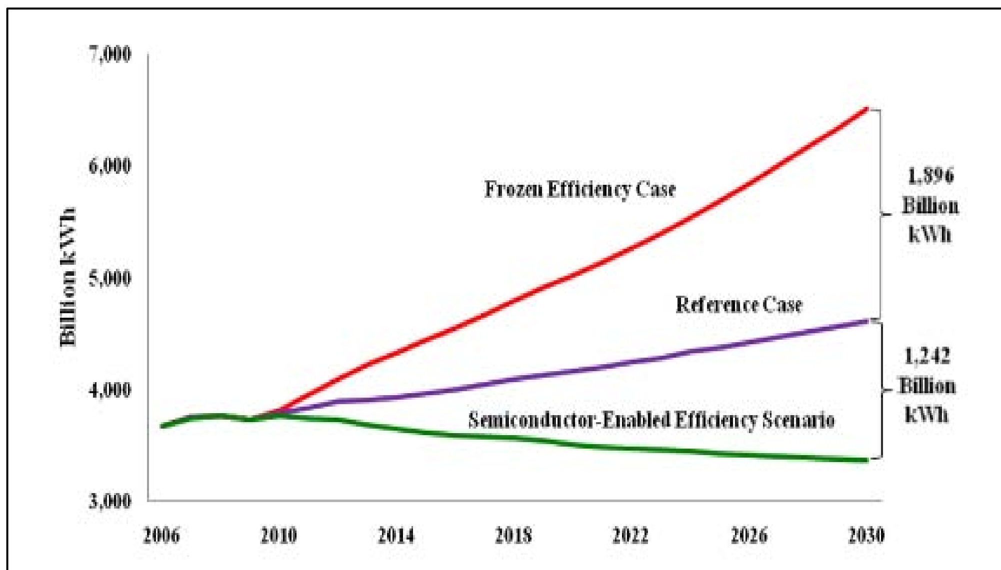


**Figure 2.2. Future electricity use scenarios for the US considering power electronics contribution [5].**

### 2.2.1. Semiconductor Devices and Power Electronics Applications

The role of power semiconductor devices in power systems is to control the current flow within the power converter (forward state) and sustain the voltage when the current is diverted to another component (blocking state), e.g. another converter leg [3]. The most commonly used power semiconductor devices are diodes, SCRs (Switched Controlled Rectifier), GTOs (Gate Turn-off Thyristor), MCTs (Mosfet Controlled

Thyristors), BJTs (Bipolar Junction Transistor), MOSFETs (Metal Oxide Semiconductor Field Effect Transistor), and IGBTs (Insulated Gate Bipolar Transistor). They can be divided in two main families: controlled switches (or simply switches) (GTOs, MCTs, MOSFETs, and IGBTs) and rectifiers (Fast Recovery Diodes or FREDs and low-frequency rectifying diodes) [6]. The main difference between them is that the former are switched-off and –on with an external control signal (current or voltage), whereas the latter depends on circuit variables. Other classification criterion for power semiconductor devices considers the current distribution within the device (topology) [2]. According to this, devices can be categorized into lateral and vertical topologies. In the case of vertical devices, the current flows across the bulk of the chip active area, which is injected from its upper to its back side or vice versa. In high current rating applications, such devices are interconnected in parallel using multi-chip packaging technologies to ensure the required current levels, as will be explained further on. In the case of lateral devices, the current mainly flows close to the chip surface, thus being injected and collected close to the upper face of the device. To have an idea, the current conduction across the chip bulk corresponds to no more than a 5 % area of the entire chip (e.g., Laterally Diffused MOSFETs or LDMOS). Such devices are used in power integrated circuits (power ICs, also known as smart power circuits), which monolithically integrate these lateral devices with logic control circuitry [7, 8, 9].

Another classification criterion for power switches is based on their voltage blocking capability: low voltage and high voltage switches. Currently, a single power switch suitable for any application does not exist, since the requirements in terms of current, breakdown voltage and switching speed cannot be satisfied simultaneously. Thus, for applications such as compact power supplies and disk drivers that require relatively low blocking voltages (< 100V) and high switching speeds (>100 kHz operation), it is common to use power MOSFETs [3]. In the cases that blocking voltages exceed 600 V (up to 6kV) and medium switching speeds are needed (1-20 kHz), IGBTs are the best choice [6, 10]. This operation range corresponds to medium- and high-power applications, the most important being railway traction, motor control and industrial drives. Probably, the IGBT is the most versatile device among the power switch families. It covers the widest application area in terms of current ratings, blocking voltage and switching speed. The IGBT versatility relies on its internal structure (hybrid structure) proposed in 1982 by Baliga [10]: it consists in a wide base

p-n-p transistor driven by an integrated short channel MOSFET. This combination produces a very high power gain (typically $>10^6$) because of the high input impedance resulting from the MOS gate structure (voltage control, MOS-gated device), and the low on-state voltage drop resulting from the internal physics of bipolar devices [6]. Therefore, for high voltage power electronics applications, the IGBT has replaced silicon bipolar power transistor and the gate turnoff thyristors (GTO). Finally, high voltage (>5 kV), high current ratings (>5 kA), and low switching frequencies (<500 Hz) are controlled by SCRs (thyristors) and GTOs.

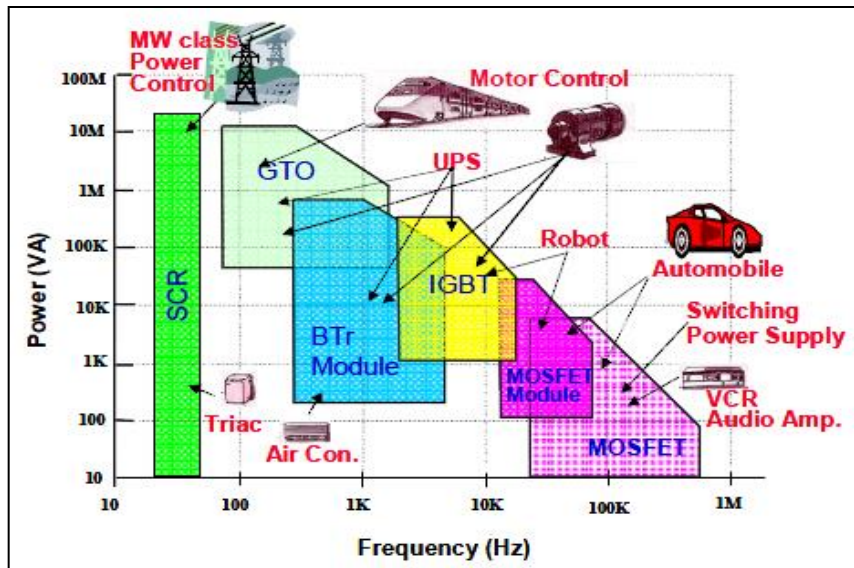


**Figure 2.3. Power versus switching frequency and applications fields of power devices in 1997 [11].**

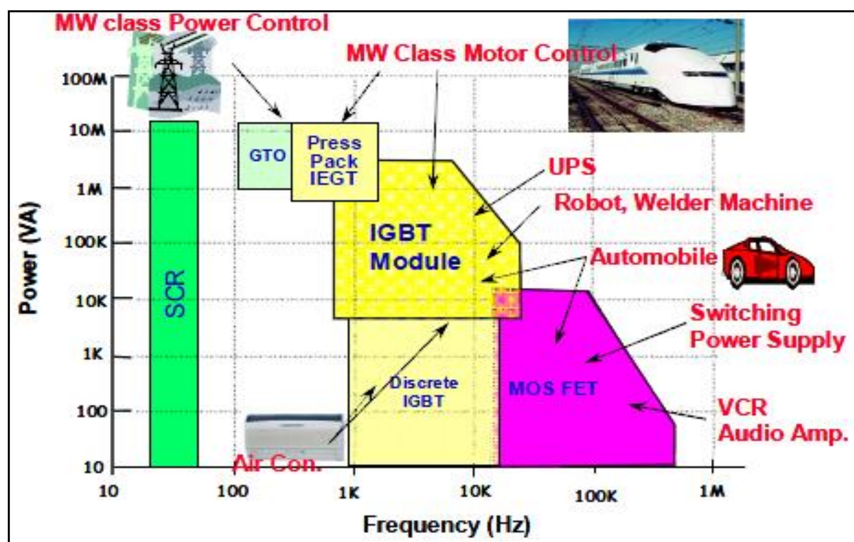


**Figure 2.4. Power versus switching frequency and applications fields of power devices in 2005 [11].**

In this scenario, some power electronics applications are typically powered by certain power semiconductor devices, as it is the case for [4, 12]:

1) SCRs and GTOs are mainly employed in HVDC transmission lines
2) IGBTs have enabled AC motor drives for locomotives or hybrid cars (traction), industrial applications, and developing more efficient home air conditioners.
3) MOSFETs have enabled switching power supplies for industrial and consumer applications.

To have an idea about the power electronics evolution and the usage of power vertical switches in the last 15 years, some of its application fields in 1997 and 2005 are shown in Figures 2.3 and 2.4, respectively [11]. Such figures plot the power managed by the power system versus the commutation frequency of the power switch. The difference between them is that most of the applications of GTOs and BJTs have been occupied by IGBTs. MOS-gated devices are predominantly used in almost all application fields, including LDMOS in power ICs, MOSFETs for low voltage and medium voltage applications and IGBTs for high power applications.

A particular case not included in Figures 2.3 and 2.4 concerns Power ICs. Although they represent a small fraction of the power device market, they cover a wide range of applications, such as switch-mode power supplies, point-of-load supplies, servo-motor drives, etc. Perhaps the most important application using Power ICs concerns switching power supplies. Power switches with low on resistance and fast switching speed are required to improve their efficiency, reliability, and cost. Over the years, power ICs have evolved from bipolar technologies to highly integrated power BCD style technologies incorporating CMOS and LDMOS transistors and many types of passives along with thick power metal levels. Today, advanced power technologies are at a 0.13μm integration level, but for many power management designs an optimum node can be around 0.25 – 0.35 μm. This is a good compromise for cost, complexity and competitive switching efficiency. Figure 2.5 reflects the economic impact of what is depicted in Figures 2.3 and 2.4. It shows the classification of various segments within the power device market, custom design, rectifiers and power diodes, thyristors, MOSFETs, IGBTs, bipolar, linear regulators, etc. This chart includes both discrete and power ICs. However, this figure does not show the solid state lighting market, which is

mostly made up of light emitting diodes (LED). The LED industry has become increasingly important and is beginning to contribute to the overall efficiency improvement shown in Figure 2.2. Therefore, Power ICs are providing the control function for these new and highly efficient illumination sources [4].

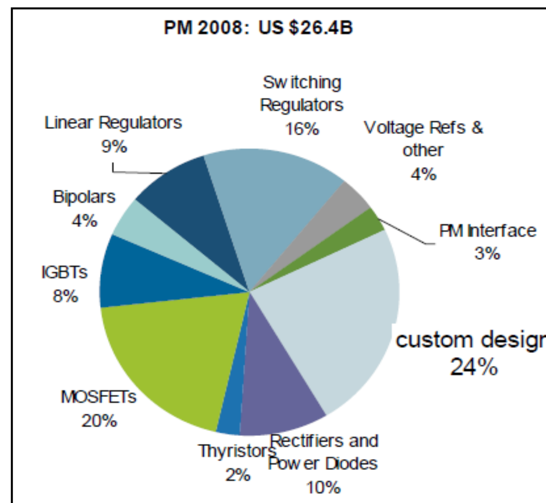


**Figure 2.5. The power semiconductor market in 2008 [4].**

## 2.3. Power Electronics Packaging

Under the name "power electronics packaging" we include all the technologies and solutions providing:

1) Electrically interconnection for one or several power semiconductor devices.
2) Extraction of the dissipated heat through a thermal path separated (or not) from the electric path.
3) Isolation of the high voltages from other critical parts of the system
4) Mechanical support to the devices.

In this context, power electronics packaging plays an important technical and economical role because it constitutes the interface between the raw semiconductor device and the circuit application. One of the most critical issues related with power devices packaging concerns the reliability and robustness limits of the final component, as it is based on the combination of heterogeneous sub-assemblies and materials, including their interfaces and joints which are potential sources of defects and faults.

### 2.3.1. Typical Power Electronics Package Structure

Two main packaging scenarios can be found in power electronics, concerning the packaging field: *discrete power devices* and *multi-chip power modules*. As both scenarios share similar problems and solutions, Figure 2.6 shows the generic structure of a typical power electronics package for discrete or module components. Its main parts are [13]:

1) *Power semiconductor chips or dice* (IGBT, FRED, MOSFET, Thyristor, Rectifier, etc.). They provide the electrical switching function.
2) *Die-attach*. It provides mechanical assembly of the device, as well as electrical and thermal contact on its backside.
3) *Top-side chip interconnections*. They provide electrical contact on the device top-side. Figure 2.6 shows as an example the wire-bonding technology. In some cases, the top-side interconnections can also provide top heat extraction.
4) *Electrically insulating and thermally conductive substrate*. It provides mechanical support for the devices, tracks and terminals, as well as electrical insulation between some of them. It also provides an efficient heat extraction path.
5) *Encapsulant material.* Typically it consists on a conformal coating or casting for environmental and mechanical protection.
6) *Base plate*. It provides mechanical support as well as heat spreading and heat conduction to the external heat dissipation system.
7) *Terminals and pins*. They allow the connection of the packaged device with the application circuit.
8) *Case or cover*. The housing structure that protects the overall component.

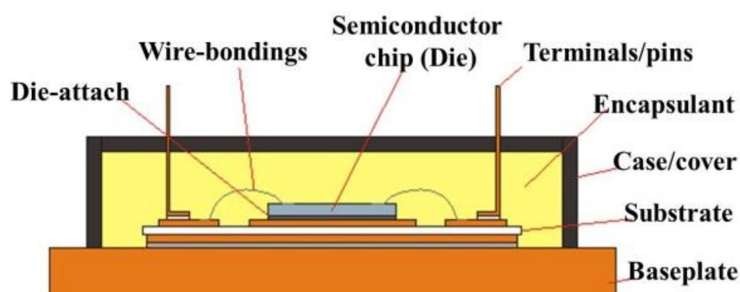


**Figure 2.6. Typical power electronics package structure.**

Each one of these parts involves different materials. The optimum set of materials is defined for each kind of application and environmental conditions. Depending on its functionality and its position in the package structure, each material requires particular characteristics described by the physical parameters (electrical resistivity, thermal conductivity, etc.). Typical materials used in power packaging are:

1) *Power semiconductor devices*. Although other semiconductors have been also introduced (SiC JFETs and rectifiers, AlGaN/GaN HEMTs, AsGa diodes, etc.), Si-based devices are the most commonly used.
2) *Die-attach*. The most common die-attach material used up to date is the PbSnAg alloy but now other Pb-free alloys and materials have been introduced, including sintered Ag nano-particles. This solution will be studied in depth in the next chapters.
3) *Top-side interconnections*. The most used technique is large Al wire-bonding. Other solutions include pressure-type contact and metal bumps.
4) *Electrically insulating/thermally conductive substrate*. For high power applications, the most common solution is based in ceramic substrates with Cu layers on top and backside. The typical technology is the DCB (Direct Copper Bonded) based on different ceramic materials: $Al_2O_3$, AlN, $Si_3N_4$, BeO. For low and medium power ratings, metal (typically Al) substrates with a ceramic-filled polymer (typically epoxy) insulating layer are used instead of the ceramic ones. This is the IMS technology (Insulated Metal Substrate).
5) *Encapsulant*. Thermoset and thermoplastic materials including silicones and epoxies are employed. The increasing voltage ranges provided by SiC devices, represent a challenge for the development of new reliable encapsulant materials.
6) *Base plate*. Typically, it is based on Ni plated Cu slabs. Other used materials are metal matrix composites, such as Cu matrix composites reinforced with diamond, Al matrix reinforced with SiC or carbon-reinforced composites. These composites allow matching the coefficient of thermal expansion (CTE) of the base plate with that of the substrates and semiconductors.
7) *Terminals and pins*. Cu leads and pins are the most common solutions, but some specific packages are based on Mo plates (press pack solutions), spring-loaded pins, etc.

In order of importance, the package begins at the interface of the chip itself, which is considered the first-level packaging, to higher levels of packaging such as substrate-level and system-level packaging. First-level packaging consists in the attachment of one or more bare chips to a substrate, the interconnection from these chips to the package leads and their protection with an encapsulant. The first-level interconnection has a major role, because it directly interfaces with the chips, not only electrically, but also thermally and mechanically. For reducing the temperature rises and consequently thermal stresses for the chips handling more power, it is necessary a thermal-friendly interconnection design. And lastly, reliability of the first-level interconnection is vital in ensuring that the electronic assemblies have an extended lifetime. At this point, a good thermo-mechanical matching (CTE matching) between neighbouring materials is crucial, as will be further explained in Chapter 3.

As it has been shown, power electronics packages are heterogeneous components, involving several engineering fields. Some of them are interrelated due to coupling mechanisms between different physical phenomena. We have already mentioned the thermo-mechanical effects which will be one of the focus of this work, but there are other aspects that are taken into account during the design phase such as the optimization of the electrical circuit of the package (parasitic inductance and resistance reduction), its electromagnetic compatibility (low parasitic radiation and conduction), its mechanical roughness, or thermal management guidelines. Perhaps, package thermal management concerns the most critical part, in which more engineering efforts are addressed. The goal in thermal management design is removing the heat dissipated by the power devices, constraining the maximum device temperature below specified values, and minimizing thermal gradients between components. The heat must ultimately be transferred from the package to a heat sink. In this framework, the thermal analysis techniques are used during the design phase to predict the temperatures and heat fluxes that will occur in an electronics package during its real operation. Thermal analysis involves the understanding of the fundamental heat transfer mechanisms, design tools such as thermal simulators and the thermal parameters of the materials involved in the design [14].

In order to give a more precise overview of the power packaging scenario, we will describe two examples of the most commonly used solutions for discrete and multi-chip

power module components. In the simple discrete TO-247 package, power semiconductor devices are soldered to a copper flange (acting as substrate, collector terminal and baseplate), and source and gate terminals are connected from the aluminium chip bonding pad to nickel-plated copper leads. The top of the chip and wire-bondings are encapsulated with a molding compound (usually based on a ceramic-filled epoxy) to provide insulation, mechanical support and protection [1, 15, 16]. Figure 2.7 (a) shows an external view of such a TO-247 package and Figure 2.7 (b) depicts its internal view.

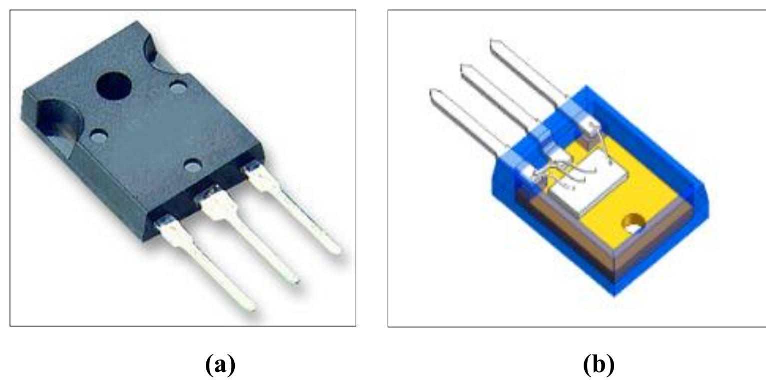

**(a) (b)**

**Figure 2.7. (a) External aspect of a TO-247 discrete package. (b) Internal view of this package [16].**

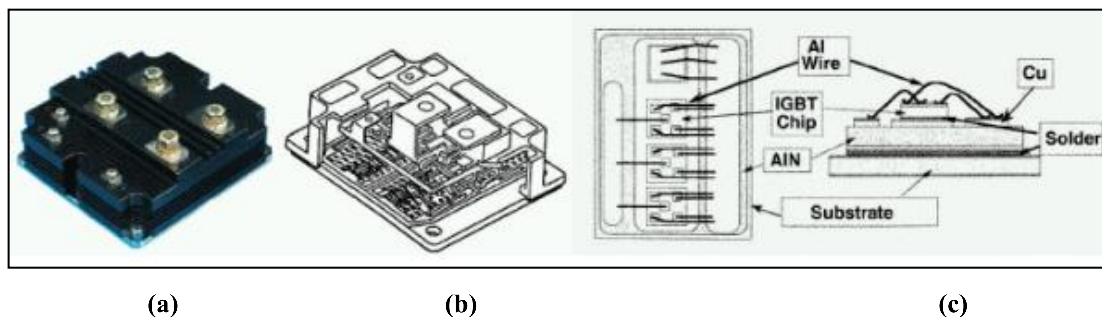


**(a) (b) (c)**

**Figure 2.8. IGBT power modules and schematic of interconnect hierarchy: (a) 6.5 kV IGBT module package; (b) inside of a similar power module; and (c) power module components [17].**

In the case of a multi-chip power module, chips are typically connected by wire-bonding technology. In such modules a DCB substrate is commonly used as a base for the power device (switching device and freewheeling diodes). DCB provides an excellent electrical insulation as well as good thermal conduction due to the direct bonding of copper on ceramic materials; such as alumina and aluminium nitride. Joining materials for device attachment and DCB to base plate attachment are usually solder alloys. Figure 2.8 (a) shows a 6.5kV IGBT module [17], figure 2.8 (b) shows the inside

of a similar module, and figure 2.8 (c) shows the devices interconnection within a multi-chip power module.

### 2.3.2. Advanced Power Packaging Solutions

In the framework of power packaging, advanced solutions have been proposed as an alternative to the classical structures presented above. For example, wire-bonding free technologies have been developed with the aim of improving the package reliability. Currently, wire-bonding is the most common chip-level top-side interconnection technology in power electronics packaging. This is due to the fact that this technology can easily adapt changes in the package design at a lower cost. This flexibility in the design and low cost, combined with continue efforts in process improvement, indicate that wire-bonding will continue to be the predominant method for chip level interconnection in the near future. Nevertheless, wire-bonding constitutes the weakest point concerning reliability in many high power or harsh environment applications. Consequently, innovative wire-bonding free interconnect techniques received a significant research effort in recent years, bringing, in addition, other benefits: lower interconnection resistance, lower noise levels and parasitic oscillations, better thermal management, higher level of system integration between power devices as well as driver circuitry, controls, sensors and communication connections, and last, reduced cost.

We present below, the most significant advanced power packaging contributions described in the recent literature, many of them characterized by different top-side interconnection approaches. Table 2.1 summarizes the advantages and disadvantages of the different advanced power packaging technologies described below [16].

#### 2.3.2.1. Pressure Contact Assembly Structure (*press-pack*)

One of the proposed wire-bonding free technologies is the pressure contact technology, also known as “press-pack”. The pressure contact concept, experienced through several stages, has now evolved to a sandwiched structure which includes anode-side Cu plate, anode-side Mo CTE compensating metal disc, silicon device, cathode-side CTE compensating Mo disc and cathode-side grooved Cu post, as

represented in Figure 2.9. Due to the soldering absence, this method eliminates the residual stress on each material, but also raises the concern of mechanical damage caused by pressure force. This solution is applied mainly in high power semiconductor devices (e.g, diodes, thyristors, or GTOs) for high-power applications [1, 18 ]. Nevertheless, research interest in the study of a pressure contact technology applied to IGBTs also raised due to the extensive use of this device and examples have been presented from several manufacturers, as for example the one shown in Figure 2.9(b) (press-pack IGBTs from ABB Semiconductors). Another noticeable example is the one presented in [19], showing a press-pack solution developed for SiC-based diodes.

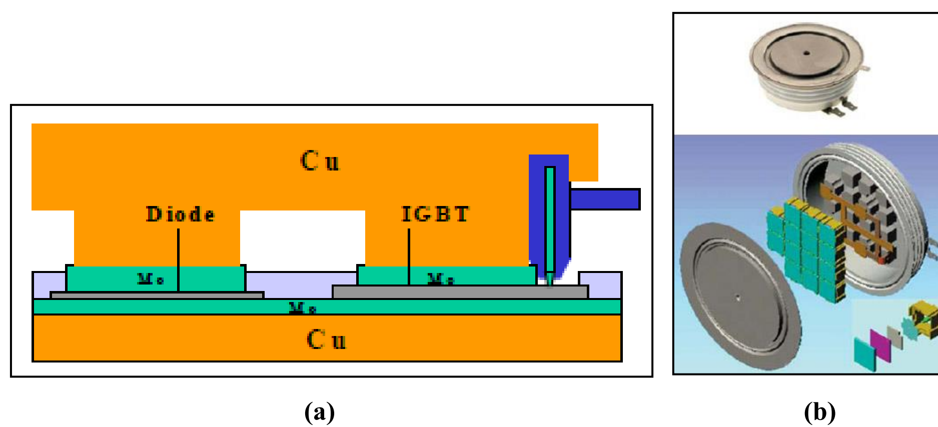


**Figure 2.9. Pressure contact assembly structure a) Schematic cross section [1, 18]. b) Parts of a real IGBT press-pack.**

### 2.3.2.2. Spring Pressure Contacts

Another alternative interconnection technology for replacing wire-bondings is spring pressure contacts [20]. Figure 2.10 shows an IGBT package with spring pressure contact technology. The IGBT and diode dies are soldered on a DBC substrate using a die-attach material.

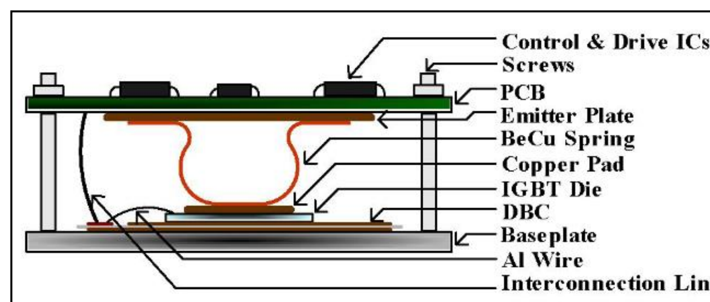


**Figure 2.10. Cross section of a spring contact structure [20].**

Another copper pad is placed on the emitter area of the die fixed with silicone adhesive in flank. In this case, the spring contact, made of beryllium-copper (BeCu) alloy, is soldered on the top plate electrode and pressed on the copper pad. Therefore, the emitter area is connected by a spring. In the upper face of the PCB, control and driver ICs are assembled. Furthermore, the spring made of BeCu offers properties that help reducing thermal stresses, also offering an additional thermal path. One problem of this structure is the introduced contact resistance that depends on the spring compression and affects the electrical performances.

#### 2.3.2.3. Multilayer Technologies

Another wire-bonding free technology described for power packaging is based on metallization layers directly deposited on the device electrodes [16]. Metal layers and signal planes connect power devices to the rest of the circuit, and are implemented using chemical or physical deposition. Deposited metallization package technology includes General Electric's "Power Overlay" (POL) technology and embedded power technology.

Concerning the thin-film "Power Overlay" developed at General Electric, it aims at reducing the cost of mass production and improving the reliability and efficiency of power electronics packages [21]. This technology has eliminated wire-bonding through the usage of metalized Cu vias/polyimide to achieve power and control interconnection. Figure 2.11 shows a cross-section of the POL design, where power electronics devices are soldered to a DCB substrate from the backside. Differences in device thickness are compensated by copper shims.

This technology has the following advantages [1, 16]:

1. Elimination of wire-bonding with metallurgical interconnections.
2. Lower interconnection parasitic inductance, allowing higher operation frequency.
3. Improved thermal performance by minimizing the number of interfaces and allowing two-sided heat removal.

4. Reduced profile and more flexible packaging options allowing innovative stacking approaches for circuit packaging, including components assembled on top.
5. Low cost.

Besides, the inherent multilayer nature of POL technology will facilitate the integration of gate drivers and other circuits into the three-dimensional package stack of Power Electronics Building Blocks (PEBB) modules.

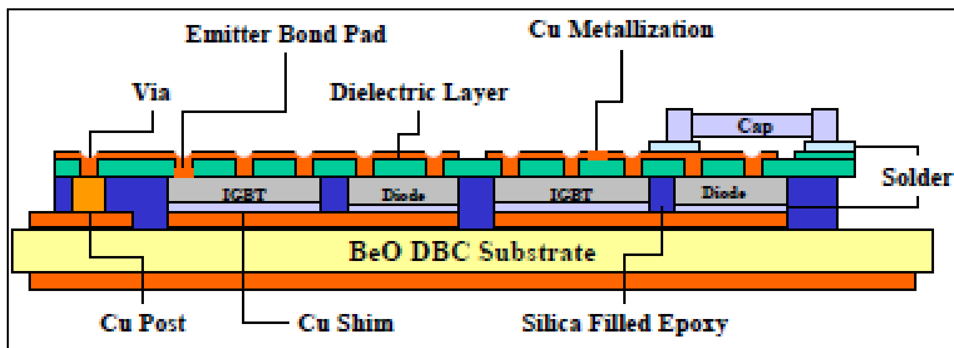


**Figure 2.11. GE's Power Overlay Technology.**

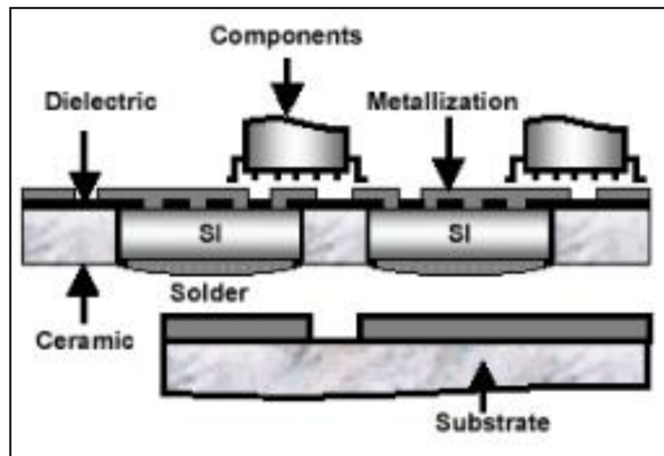


**Figure 2.12. Cross section schematic of the Embedded Power technology.**

Another example of a multilayer technology, is the "Embedded Power" concept developed at Virginia Tech that uses ceramic substrates, deposited metal layers, screen printable dielectric materials and solders to enclose power devices [22]. There are three major parts in the structure: the embedded power stage; electronic circuitry and base substrate, forming a monolithic power module. Figure 2.12 shows a schematic cross section of the embedded power module. Components on top of the structure are gate

drivers, control and protection circuits. The substrate provides electrical interconnection and a thermal path for the heat extraction, while the deposited metal layer provides only electrical interconnection. Another important aspect is that this is an all-low temperature (< 250 ºC) hybrid processing technology.

### 2.3.2.4. Thinpack Technology

Another advanced solution is the Thinpack technology. In this technology, a ceramic lid, with holes drilled in it and filled with solder, is attached to the chip by solder reflow (Figure 2.13). Specific routing can be made in the ceramic interposer to connect electrodes on the chip to circuits. This technique was claimed to increase power module yields to nearly 100%. The thin ceramic lid shrinks package volume, decreases thermal resistance and it also serves as the base for integration of other circuit components [23].

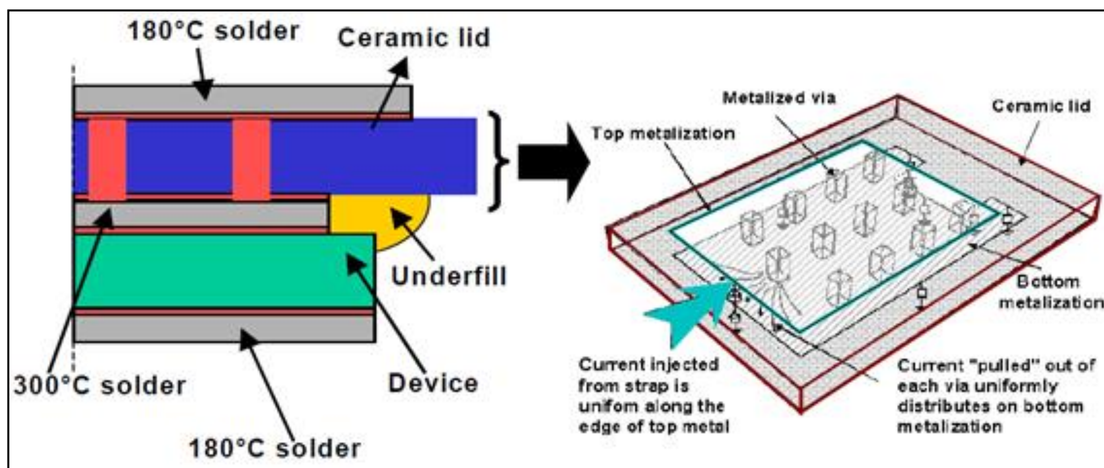


**Figure 2.13. Schematics of ThinPack cross - section and three - dimensional view [23].**

### 2.3.2.5. Area Array or Bumping Interconnection Technologies

Area array interconnect is another wire-bonding free technology. For interconnections between device electrodes and the defined substrate metallization, solder area array bumping uses area-populated metallurgical bumps or conductive polymer bumps. Besides, bumps provide a heat dissipation path from the chip to the substrate and act as a mounting support for the chip as well as a buffer to relieve strain due to the CTE mismatch between chip and substrate.. Sometimes, the silicon chips are

placed facedown when joining them to the substrate and this type of packaging is also named "flip chip". Figure 2.14 shows an example of an IGBT transistor where the top emitter connections have been performed using solder bumps, following a technology developed at IMB-CNM [24].

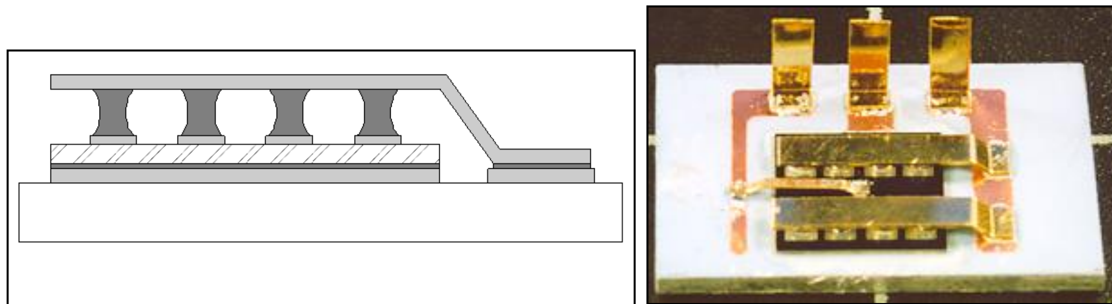

**Figure 2.14. Schematic cross-section and picture of an IGBT with solder bumps on the top emitter pads.**

### 2.3.3 High Temperature Power Electronics Packaging

High temperature packaging is defined as the one required for "electronics operating at temperatures in excess of those normally encountered by conventional silicon based or their auxiliary components'' [25]. It is essential for severe and extremely harsh environments, in which the usage of conventional packages is impractical (e.g., commercial and military aircrafts, automobiles with longer lifetimes and greater fuel economy, chemical processes with ultra-precise control and minimal waste, or spacecraft and satellites). Currently, standard packaging techniques in the market developed for Si based devices, offer maximum temperatures up to about 175 ºC. This insufficient maximum working temperature severely constrains the levels of power density and environment that SiC and GaN devices can operate (350 ºC and higher) [26, 27, 28].

The capability to use power electronics devices at elevated temperatures will not only make new products and applications possible (such as those mentioned above), but it will also decrease the cooling requirements of more standard applications, avoiding large, heavy, and complex cooling systems. For example, if a power transistor is dissipating 10W to the ambient air at 25 ºC through a heat-sink with a thermal resistance of 10 K/W, the semiconductor temperature reaches 125 ºC, a relatively safe

| Technologies | | Advantages | Disadvantages/concerns |
|---|---|---|---|
| Wire-bonding<br>(IGBT, MOSFET) | | ✓ High flexibility to adapt to various devices;<br>✓ No special requirement on wafer processing;<br>✓ Lowest cost per connection;<br>✓ Improved reliability. | × Low throughput due to sequential bonding process;<br>× Large parasitic noises due to long interconnect path;<br>× Poor thermal management;<br>× Inapplicable to 3D integration. |
| Press-pack<br>(GTO,IGCT,IGBT) | | ✓ Best reliability due to fatigue-free structure;<br>✓ Explosion-free;<br>✓ Low thermal impedance, double-sided cooling. | × Special cooling scheme;<br>× Special insulation approach;<br>× Hermetic sealing;<br>× High cost packaging. |
| Multilayer Technologies (IGBT, MOSFET) | GE POL | ✓ Much better electrical performance than wire-bonding due to short interconnect path;<br>✓ 3D, multilayer integration applicable. | × High parasitic capacitance;<br>× Lack of stress reliever between silicon and copper interconnect (high demand for structure cohesion);<br>× Processing complexity;<br>× High cost due to laser drilling, sputtering. |
| | Embedded power | ✓ Compatible with hybrid thick-film processing;<br>✓ Much better electrical performance than wire-bonding due to short interconnect path;<br>✓ 3D, multilayer integration applicable. | × High parasitic capacitance;<br>× Lack of stress reliever between silicon and copper interconnect (high demand for structure cohesion);<br>× Processing complexity;<br>× High cost due to laser drilling, sputtering. |
| ThinPack<br>(MCT) | | ✓ Good heat dissipation due to large-area soldering on both sides and the use of ceramic lid;<br>✓ Much better electrical performance than wire-bonding due to short interconnect path;<br>✓ 3D, multilayer integration applicable. | × Reliability concern for large-area soldering. |
| Area array solder Bumping<br>(IGBT, MOSFET) | | ✓ High packaging density;<br>✓ Much better electrical performance than wire-bonding due to short interconnect path;<br>✓ 3D, multilayer integration applicable;<br>✓ Lower cost than deposit metallization;<br>✓ ThinPack, or press-pack;<br>✓ Good reliability. | × Requires additional wafer processing;<br>× High cost for low-volume package;<br>× Fatigue of solder alloys. |

**Table 2.1. Pros and cons summary of various power packaging technologies [16].**

value for typical Si power devices. If a similar transistor, made for example on SiC, can operate at higher temperatures, a smaller heat-sink with, let's say 20 K/W of thermal

resistance, brings the semiconductor temperature up to 225 ºC. This trade-off between maximum device temperature and cooling system complexity has been considered a practical and simple way to increase the integration level in power converters.

As stated before, the implantation of this kind of solutions is slow due mainly to packaging limitations. Nowadays, some high temperature power packaging solutions are available, although they are usually expensive and are used in high added value applications such as space or military systems. Let's mention for example the metallic TO-257 package used for blocking-diodes in the solar panels of the Bepi-Colombo and Solar Orbiter ESA (European Space Agency) missions to Mercury and the Sun, respectively [29]. This package has been proved between -150 ºC and 300 ºC, but its fabrication involves expensive materials, such as Au, Ag, BeO ceramics, AuGe alloy, or ceramic feed-through, and relatively complex assembling processes, such as hermetic sealing. Research efforts in many R+D labs are now ongoing, aiming at low cost and reliable technologies. For example, [30, 31] describes a recent power module based on power SiC devices, able to operate with semiconductor temperatures up to 250 ºC. The proposed solution follows a quite classical structure (similar to the one shown in Figure 2.8) and the main effort has been carried out on new materials and fabrication processes.

## 2.4. Conclusions

Power electronics is a field of paramount economic and social importance, since it possibilities a high number of crucial applications. Power electronics systems are present in all the chains of generation, distribution and application of the electric energy. To provide a wide view on the framework of this work, this chapter presents the main power electronics applications and the used semiconductor devices.

The interface between the power devices and the application circuit is given by their package. Power electronics packaging must provide electrical interconnection to the device, heat extraction capability and mechanical and environmental protection. Thus, power packaging is one of the key elements in power electronics development, and it requires, at least, the same research efforts than semiconductor power devices and power converters. A detailed analysis of the main power packaging elements and materials has been also addressed in this chapter. Current available packaging

technologies and recent advanced packaging solutions have been presented for the two main scenarios of this field: discrete power devices and multi-chip power modules.

It has been discussed that power packaging involves many engineering fields due to the different physical phenomena present in such heterogeneous systems. In this sense, the thermal and thermo-mechanical issues in power electronics packages are becoming an ever more important concern. Today, the thermal and thermo-mechanical performances are being pushed from the device to the package limit by increasing heat fluxes, continued miniaturization and higher switching speeds.

Finally, it has also been explained that the performances of power electronic systems (mainly their integration level) become improved if high temperature semiconductor devices are used. Such high temperature devices also allow the development of new and crucial applications related with high environment temperatures (aerospace, automotive, etc.). Currently, the silicon technology reached its physical limits and a great effort in R+D is being done to develop devices based on wide bandgap semiconductors, such as SiC, GaN or Diamond. SiC and GaN devices with maximum operation temperatures up to 300 ºC are starting to be available, and one of the limiting elements for their implantation is the package.

All technological elements required for a high temperature (300 ºC) package showing high voltage and current capabilities must provide the same final reliability already reached for standard packaging solutions. Thus, the key points to reach this target not only involve an optimal thermal design of the package, but also an accurate thermo-mechanical study on die-attach, chip-to-package interconnections (wire- or bump-bonding) and encapsulants. This high temperature power packaging scenario will constitute the framework of the present research work, where the focus will be addressed to the thermo-mechanical reliability analysis of the die-attach layers, in particular for high temperature operation with special focus on Ag nano-particles sintering.

## 2.5. References

[1] S. Wen. "Thermal and Thermo-Mechanical Analyses of Wire Bond vs Three-dimensionally Packaged Power Electronics Modules," Thesis, Virginia Polytechnic Institute, December 1999.

[2] X. Perpinyà. "Mesura de la Temperatura interna en Dispositius de potencia," Màster Thesis, Universitat Autònoma de Barcelona, Setembre 2002.

[3] N. Mohan, T. Undeland, W. Robbins. "Power Electronics: converters, applications and design," New York. Wiley, 1994.

[4] P. L. Hower, S. Pendharkar, and T. Efland, "Current Status and Future Trends in Silicon Power Devices," *in Proc. IEEE Int. Electron Devices Meeting Conference*, pp. 13.1.1–13.1.4, 2010.

[5] J.A. Lainert, C. Knight, V. McKinney, and Ehrhardt-Martinez, K.ACEEE Report E094, May 2009.

[6] B. J. Baliga, "The Future of Power Semiconductor Device Technology,'' *IEEE*, vol. 89, issue: 6, pp. 822-832, June 2001.

[7] B. J. Baliga. "Evolution and Status of Smart Power Technology," *in Proc. Applied Power Electronics Conference and Exposition* (APEC), pp. 18-21, 1993.

[8] A. Pérez-Tomás , X. Jordá, P. Godignon. "Optimization of a very cost-effective high voltage p-channel transistor implemented in a standard twin-tub CMOS technology," *Microelectronic Engineering*, vol. 77, issue 2, pp. 158-167, 2005.

[9] A. Pérez-Tomás , X. Jordá, P. Godignon, J.L. Gálvez, M. Vellvehí and J. Millán. "IGBT gate driver IC with full-bridge output stage using a modified standard CMOS process," *Microelectronics Journal*, vol. 35, issue 8, pp. 659-666, 2004.

[10] B. J. Baliga, Adler, M.S. Gray, P.V. Love, R. P. Zommer N. "The insulated gate rectifier," *in Proc. Electron Devices Meeting* (IEDM), vol. 28, pp. 264-267, 1982.

[11] A. Nakagawa, Y. Kawaguchi, K. Nakamura, "Achieving Material Limit Characteristics in Silicon Power Devices,'' *in Proc. International Workshop on Physics of Semiconductor Devices* (IWSPD), pp. 762-767, 2007.

[12] M. T. Rahimo. "Ultra High Voltage Semiconductor Power Devices for Grid Applications," *in Proc. IEEE Electron Devices Meeting* (IEDM), pp. 13.4.1-13.4.4, 6-8 December 2010.

[13] W.W.Sheng, R.P. Colino, “Power Electronic Modules, Design and Manufacture,” CRC press, 2005.

[14] M. Pecht, “Handbook of electronic package design,” Marcel Dekker, New York, 1991.

[15] C. Wang, “High Temperature High Power SiC Devices Packaging Processes and Materials Development,” Thesis. Auburn University, August 2006.

[16] S. Wen, “Design and Analyses of a Dimple Array Interconnect Technique for Power Electronics Packaging,” Thesis, Virginia Polytechnic Institute, August 2002.

[17] Eupec, a power semiconductor producer, www.eupec.com.

[18] H. Matsuda, ; M. Hiyoshi, and N. Kawamura, “Pressure Contact Assembly Technology of High Power Devices,” *in Proc. IEEE International Symposium on Power Semiconductor Devices and IC's*, pp. 17-24, May 1997.

[19] V. Banu, P. Godignon, X. Perpiñà, X. Jordà, J. Millán, “Enhanced power cycling capability of SiC Schottky diodes using press pack contacts,” *Microelectronics Reliability*, vol. 52, no. 9-10, , pp. 2250-2255, 2012.

[20] X. He, X. Zeng, X. Yang, and Z. Wang. “A Hybrid Integrated Power Electronic Module Based On Pressure Contact Technology,” *in Proc. IEEE Power Electronics Specialists Conference* (PESC ’06), pp. 1-5, 18-22 June 2006.

[21] B. Ozmat, C. S. Korman, P. McConnelee, M. Kheraluwala, E. Delgado and R. Fillion. “New Power Module Packaging for Enhanced Thermal Management,” *in Proc. 7th Intersociety Conference on Thermal and Thermomechanical Phenomena in Electronic Systems* (ITHERM), Las Vegas, Nevada, vol. 2, pp. 287-296, 2000.

[22] Z. Liang, F.C. Lee. “Embedded Power Technology for IPEMs Packaging Applications,” *in Proc. Applied Power Electronics Conference and Exposition* (APEC), vol. 2, pp. 1057-1061, 4-8 March 2001.

[23] V. Temple, “ThinPak Technology Shrinks Power Modules, Power Hybrids and Ultra-High Speed Switching Devices,” pp. 32-38, May 2000.

[24] C.C. Meng, S. Stoeckl, H. Pape, F. M. Yee, and T.A Min. “Thermo-Mechanical Modeling of a 3D Flip Chip Fully Populated BGA Package,” *in Proc. Electronics Packaging Technology Conference* (EPTC), pp. 637-640, 8-10 December 2010.

[25] F.P. McCluskey, R. Grzybowski, and T. Podlesak. “High Temperature Electronics,” CRC press 1997.

[26] M. Östling. "Silicon Carbide Based Power Devices," *in Proc. IEEE Electron Devices Meeting* (IEDM), pp. 13.1.1-13.1.4, 2010.

[27] Z. Lin, and J. Yoon. "An AlN-based High Temperature Package for SiC Devices: Materials and Processing," *in Proc. International Symposium* on *Advanced Packaging Materials: Processes, Properties and Interfaces*, pp. 156-159, 16-18, March 2005.

[28] R. W. Johnson, C. Wang, Y. Liu, J. D. Scofield. "Power Device Packaging Technologies for Extreme Environments," *IEEE transactions on electronics packaging manufacturing*, vol. 30, pp. 182-193, July 2007.

[29] P. Godignon, X. Jordà, M. Vellvehi, X. Perpinyà, V. Banu, D. López, J. Barbero, P. Brosselard, and S. Massetti. "SiC Schottky Diodes for Harsh Environment Space Applications," *IEEE Transactions on Industrial Electronics*, vol.58, issue 7, pp. 2582-2590, July 2011.

[30] J. Hornberger, A. B. Lostetter, K. I. Olejniczak, T. McNutt, S. Magan Lal and A. Mantooth. "Silicon-Carbide (SiC) Semiconductor Power Electronics for Extreme High-Temperature Environments," *in Proc. IEEE Aerospace Conference*, vol. 4, pp. 2538-2555, 2004.

[31] J. M. Hornberger, S.D. Mounce, R.M. Schupbach, A.B. Lostetter and H. A. Mantooth. "High-Temperature Silicon Carbide (SiC) Power Switches in Multichip Power Module (MCPM) Applications," *in Proc. IEEE Industry Applications Conference*, vol. 1, pp. 393-398, 2005.

# CHAPTER 3 Ag Nano-Particles Sintering as Die-Attach Solution

## 3.1. Introduction

As described in the previous chapter, a typical power electronics package is made of diverse materials, each one having different mechanical properties. From the long-term reliability viewpoint, the difference in the coefficient of thermal expansion (CTE) between adjacent materials (e.g., die, die-attach and substrate) is the most limiting factor, since it induces thermo-mechanical strains during power packaging manufacturing or under operation conditions, which compromises and fixes the package wear-out. The thermo-mechanical strain may be associated with deformations and with resulting mechanical stresses during local or global temperature changes. In fact, temperature changes are commonly encountered during the device manufacturing or packaging, such as vapour depositions and soldering operations, and under actual working conditions, for instance switching operation and global environmental temperature changes.

The description and basic analysis of the die-attach technology based on sintering of Ag particles is the main objective of the present chapter. For this reason, first, the framework will be introduced by describing the main categories of die-attach materials and their thermo-mechanical properties, which determine the behaviour under working conditions. Then a brief review of most used methods for failure analysis (FA) will be provided, as well as the description of the methods used in this study to analyse the quality and the degradation of the die-attach layer. The chapter ends with the description of the sintering theory, and its adaptation to allow sintering as a die-attach technique.

## 3.2. The Die-Attach Layer in Power Electronics Assemblies

The die-attach constitutes one of the most critical part of power devices assemblies. In order to ensure that the package is a mechanically reliable and thermally/electrically efficient system, is very important satisfy certain requirements. These requirements

include sufficient adhesion between die and substrate, so that the die does not detach from the substrate, resilience to provide stress relaxation on the die (for suitable reliability), high thermal conductivity to dissipate heat, low electrical resistivity to minimize conduction losses, CTE matching between both substrate and die, ability to process at appropriate temperature (not too high) and good stability at operating temperature.

There are many categories of die-attach, including both high and low temperature use. The main categories are: solder alloys (eutectic and soft soldering), electrically conductive adhesives (ECA) based on polymers, and silver based die-attaches (such as silver glass die-attach, silver indium based and silver based on sintering of particles) [1]. The most relevant materials are summarized in Table 3.1. Among them, die-attach solder alloys are the most used and become a standard solution. Pure silver has been also included in Table 3.1 in order to compare its properties with those of the sintered nano-Ag. It is interesting to highlight that Ag has the highest electrical conductivity and the second best thermal conductivity among all materials, showing also good mechanical properties. Its high melting temperature enables it to work at higher temperatures than usual solders. For this reason, this material is used as a basis for different solder technologies.

Solder alloys are usually tin-, lead-, gold- or indium-based. Rich lead alloys (for example Pb95.5Ag2.5Sn2) have been used as the reference die-attach material for decades as they present a low cost and good ductility (which leads to lower stresses). As a result they exhibit robustness against failure [2, 3], but they have a lower melting point in comparison to hard or stiffer solders. For this reason, they are not suitable for very high temperature applications. Furthermore, lead-based alloys are not environmentally friendly and therefore several legislations around the world are gradually limiting the use of lead in electronics [4, 5]. To address this concern several Pb-free alternatives have emerged in response to these requirements. Among them, the most representative are Pb-free alloys, ECAs, and die-attach based on sintering of particles.

In the case of pb-free alloys, SnAg-based alloys are nowadays used in many applications, but are limited for standard operation temperatures. Gold-based eutectics

like AuSi, AuSn, and AuGe show higher ultimate tensile strength, and consequently offer excellent fatigue and creep resistance for high temperature applications (owing to the maximum working temperature of the device is limited by the eutectic temperature of the solder alloy). The disadvantage is primarily due to their stiffness which leads to high stresses (which arise due to thermal expansion mismatch among the die, die-attach, and the substrate) in the semiconductor. Besides, the high cost is another inconvenient.

| Material | Melting / Processing Temperature (ºC) | Density (Kg/m$^3$) | Thermal Conductivity (W/m ºC ) | CTE (ppm/ºC) | Young Modulus (GPa) | Poisson ratio |
|---|---|---|---|---|---|---|
| **Ag** | 961 [6] | 10500 [6] | 430 [6] | 19 [6] | 76 [6] | 0.37 [7] |
| **Au80 Sn20** | 280 [6] | 14700 [6] | 58 [6] | 16 [6, 8] | 68 [6] | - |
| **Au88 Ge12** | 356 [9, 10] | 14670 [11] | 44 [9, 10] | 13 [9, 10] | 63 [9 ]- 72.74 [11 ] | 0.32 [12] |
| **Au97 Si3** | 363 [9] | 1568 [9] | 293 [9] | 11 [9] | 69.5 [9] | - |
| **Pb95.5 Ag2.5 Sn2** | 300 [6] | 11200 [6] | 23 [6] | 30 [6] | 13.8 [6] | - |
| **Sn60 Pb40** | | 9000 [13] | 50 [13] | 21 [13] | 10 [13] | 0.4 [13] |
| **Sn37 Pb37** | 183 [6] | 8500 [6] | 51 [6] | 25 [6] | 16 [6] | - |
| **Sn93.6 Ag4.7 Cu1.7** | 218 [14] | 7400 [14] | 55 [14 ] | 21 [14] | 31 [14] | 0.4 [14] |
| **Sn96.5 Ag3.5** | 221 [9] | 7360 [11] | 33[11] | 26.5[15] | 38.5 [15] | 0.29 [15] |
| **Sintered nano Ag** | 280 [6] | 8600 [6] | 240 [6] | 19 [6] | 9 [6] | - |

**Table 3.1. Properties of die-attach materials.**

ECAs involve of a polymeric resin, which provides physical and mechanical properties such as adhesion, mechanical strength, impact strength, and metal filler that conducts electricity. Usually, the polymeric resin is an epoxy, a silicone, or a polyimide and metal filler can be silver, gold, nickel or copper [5]. ECAs are widely used as attachment materials due to their low cost and easy manufacture. These adhesives are not used for ceramic or hermetic metallic packages because the temperatures required to finish the encapsulation process after the die-attach, may degrade the properties of the adhesive. The polymer-based adhesives offer many advantages such as lower stresses due to low Young´s modulus and curing (processing) temperature, ease of use in a manufacturing environment, and low cost compared to conventional solder technology. Nevertheless, they show worst thermal and electrical properties than metals and their use is restricted to low- and medium-power applications. Another disadvantage is

conductivity fatigue owing to high temperatures and humidity aging decreases the conductivity [1, 5].

Among silver-based technologies, the silver glass die-attach, is an adhesive paste formed by silver (micro-flakes) and glass particles in an organic solvent medium [16]. This technology needs high temperature firing above 600 ºC during processing to create an appropriate die-attach. In fact, pressure can be used in order to reduce the firing temperature [17]. In the same sense, some researchers have been reported that this technology have been showed satisfactory adhesion and have been provided high thermal and electrical conductivity. Moreover, it has been demonstrated extremely resistant to degradation during temperature cycling from -65 ºC to 150 ºC. Nevertheless, the main disadvantage is its lengthy processing techniques, which are unsuitable for mass manufacturing purposes [6, 17].

Another silver based technology is a silver indium based. A film with 20 wt% of Indium ($Ag\text{-}In_{20}$) and therefore with a melting temperature beyond 700 ºC was created via thermal evaporation [1]. Besides, a silver-indium die-attach for high temperature at low process temperature of 206 ºC was obtained with practically void-free and uniform thickness around of 7.2 to 7.8μm. In fact, the process of the Ag-In die-attach requires two steps. The aim at first step is to produce the joint and the second step is for increase the melting temperature of the die-attach by an annealing process. Several Ag-In intermetallic layers are formed during process, but in particular, the intermetallic compound $Ag\text{-}In_2$ avoids the indium layer oxidation. Apparently this technology is very promising, but its disadvantage is its very long process.

Due to good physical properties of the Ag is widely used as basic material on sintering of particles. In the case of nano-scale particles is interesting because the bonding process can be performed at a temperature lower than that of the die-attach melting point. Therefore, is possible avoid the use of the high pressures, which is common in micro-scale particles [17, 18]. Moreover, they present the advantage of a low residual stress (owing to low-temperature process) and a better suitability for high-temperature operation (owing to high melting temperature). Besides, this property will avoid the remelting problem in the assembly processes of packaging. In fact, this property will be further discussed in section 3.4.

In the case of Ag nano-particle sintering, the porous microstructure of nano - scale sintered Ag can relieve the thermo-mechanical stresses generated from mismatched CTEs in the joined structure. Nano-particles Ag sintering seems to be a very promising die-attach solution also for high temperature applications, though it is still undergoing reliability studies,[3, 19, 20].

### 3.3. Methods for the Assessment of Die-Attach Layers

The die-attach layer is the joint between die and substrate in a package. In order to assess this layer, in this study we have used the following systems and methods: Optical Microscope, Optical Imaging Profiler, SAM (Scanning Acoustic Microscope), SEM-EDX, FIB-SEM and a specific tool for obtaining the adherence force between die and substrate (die-shear tester). The description of each technique, the associated equipment, its characteristics and some specifications are described below:

*Optical Microscope* is a non-destructive system for failure analysis. It uses the visible light and a system of lenses with the aim at magnifying the sample image to detect physical defects. In this study optical microscopy was used for obtaining optical micrographs of the tests vehicles at different phases of the experimental research. In fact it was the most used technique in this study.

*Optical Imaging Profiler (Sensofar PLu 2300)* is a non-destructive system that is constituted by an independent sensor head, which combines interferometry and white light confocal imaging techniques (see Figure 3.1(a)). The system acquires three-dimensional images of surface profiles, therefore, it can obtain measures of surface roughness and thickness of samples. In this study, the imaging profiler was mainly used to obtain surface roughness and the thicknesses of Cu substrates and semiconductor dice (Si and SiC) [21]. Figure 3.1(b) shows an image of the surface roughness of the Cu polished substrate in a small area of 138 x 102$\mu m^2$. In this case the Ra is approximately 35 nm. Figure 3.1(c) shows the roughness profile of the same polished substrate along X axis.

**(a)**

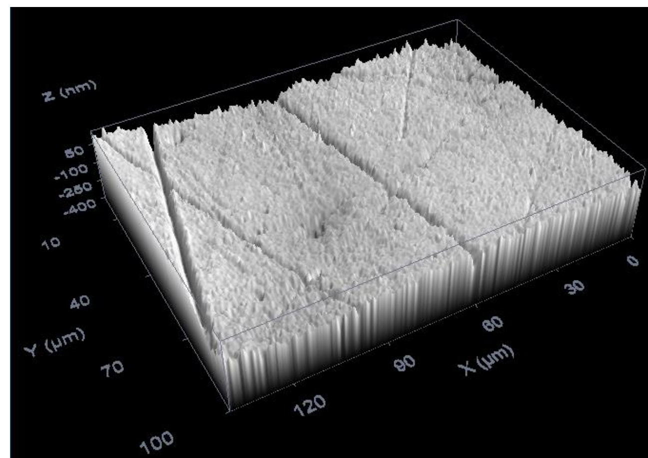


**(b)**

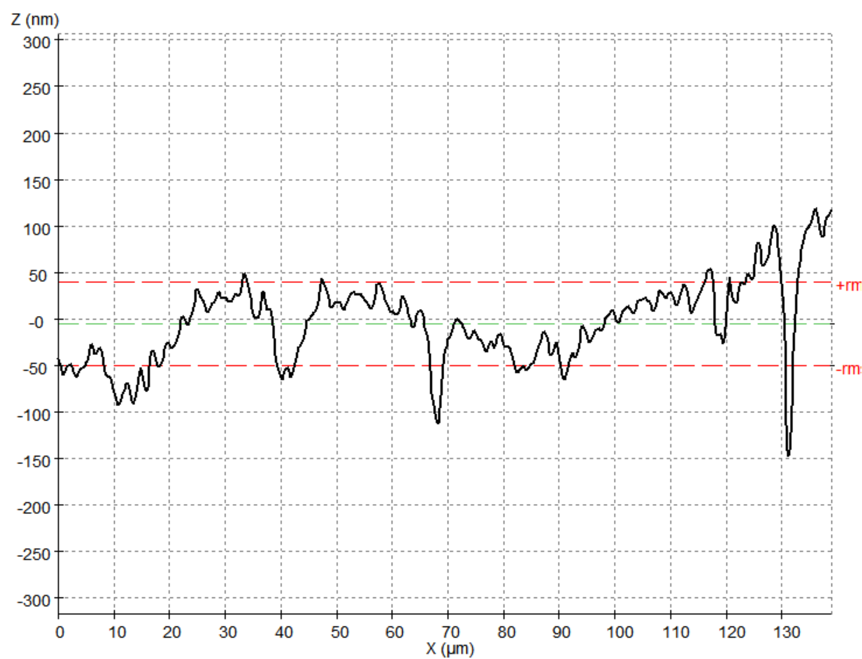


**(c)**

**Figure 3.1. (a) Sensofar PLu 2300 optical imaging profiler used to obtain roughness measurements. (b) Confocal image of a polished substrate (Ra= 35 nm). (c) Surface profile of the roughness in the X axis.**

*Scanning Acoustic Microscope (SAM) Sonoscan GEN-5* (see Figure 3.2) [22], is a non-destructive system that uses sound waves between 10 MHz and 240 MHz to acquire images, which can be useful to detect defects (failures) inside a package structure, originated during manufacturing or during accelerated testing. The failures (delamination, voids, cracks, etc.) appear mainly between interfaces of the package structure, i.e., failures in bonds, lead frames or die-attach materials. There are two basic SAM approaches, based on processing the echoes returned by the package (reflected echo) or processing the waveform of the sound transmitted at the opposite extreme of the package (transmission inspection). In the present study, only reflected echoes have been considered.

**Figure 3.2. Sonoscan GEN-5 SAM system used for die-attach analysis.**

There are three types of working modes for the GEN-5 SAM:

1) *A-scan mode.* It provides an oscilloscope like view of the echo signal at a given single position. Each pulse displayed in the screen provides information about its polarity (positive or negative), amplitude and position in time (which is correlated with the depth in the multilayer sample). All this information is related with the physical properties of the analysed materials and interfaces and, when properly processed, provides the two other working modes.
2) *B-scan mode*. This mode provides an image of non-destructive cross-sectional view of a sample in two dimensions (X-Z plane at depth Y).

3) *C-scan mode*. Provides an image of non-destructive description of the cross-sectional view of a multilayer sample (X-Y plane at depth Z). It is an extension of the A-SAM mode.

For our particular case the best option is the C-SAM mode for obtaining images of die-attach layers during different phases of the experimental research (after soldering or sintering process and during thermal cycling). For instance, Figure 3.3(a) displays a C-SAM image of die-attach layer after soldering with good quality. In contrast, a die-attach layer with poor quality is showed in Figure 3.3(b).

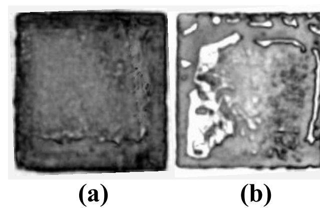


**Figure 3.3. C-SAM images after soldering process. (a) Poor quality. (b) Bad quality.**

*Universal Bond Tester (Royce 650)* is a system with several functions (mechanical testing) of micro-electronic samples (see Figure 3.4(a)) [23]. Basically, this equipment allows a controlled shear or pull force acquisition versus displacement. The main characteristics and functions of this system are:

1) Motorized height controlled microscope that stays in focus as it moves
2) Ultra-Fine Pitch (UFP) capable
3) Image Capture Option, Field Upgradable
4) Ribbon Bond testing for standard to high-power devices
5) Die-shear up to 200 kgf
6) Robust test modules with range switching, on board calibration memory, and tool protection.

In this study, it has been used the die-shear destructive function for evaluating the adherence force of die-attach layers. The die-shear test provides a quantified measure of the force necessary to detach the die from the substrate. In fact, the test method standard for microcircuits (MIL-STD-883H-2010 [24]) defined that the system must fulfil the next capabilities:

a) A die-shear tool which applies a uniform distribution of the force to an edge of the die. A compliant (conforming) material (e.g., nail polish, tape, etc.) may be applied to the face of the contact tool to ensure uniform force distribution on the edge of the die.
b) Provisions to assure that the die-shear tool are perpendicular to the die mounting plane of the header or substrate.
c) A rotational capability, relative to the header/substrate holding fixture and the die contact tool, to facilitate line contact on the edge of the die; i.e., the tool applying the force to the die shall contact the die edge from end-to-end.
d) A binocular microscope with magnification capabilities of 10X minimum and lighting which facilitates visual observation of the die and die-shear tool interface during testing.

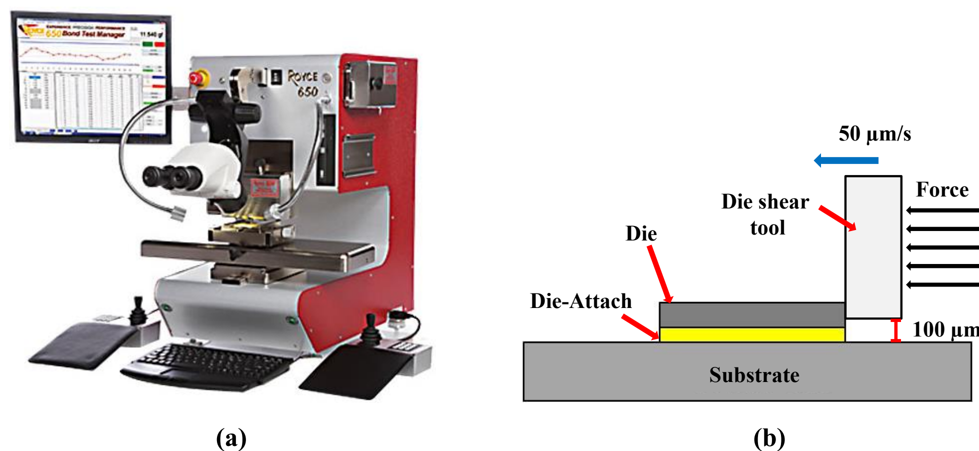


**Figure 3.4. (a) Universal bond tester used to measure the die-shear force between die and substrate. (b) Schematic view of the die-shear tests, showing the main involved elements and parameters during tests.**

In this sense, Universal Bond Tester (Royce 650) complies with these requirements. Besides, the parameters and settings of the equipment are critical for obtaining useful information. Figure 3.4(b) shows how the test is carried out: the die-shear tool is set at a 100 µm height over the substrate and pushes the die with a feed rate of 50 µm/s. In fact, these values were selected for various reasons. For instance, the height was chosen to avoid that the die-shear tool touches the die-attach, which has an approximately thickness of 30 µm. In the case of the feed rate, it has been selected this value because is necessary slow values to ensure adequately measure of die-shear force [25, 26].

In order to understand the cause of the physical failure more in depth analysis is necessary. In this sense, the test method standard for microcircuits (MIL-STD-883H-2010) and test method standard for semiconductor devices (MIL-STD-750D-1995 [27]) define 3 separation categories (failure modes) concerning the die-attach material condition after the die-shear test:

a) Shearing of the die with residual semiconductor remaining.
b) Separation of die from die-attach material.
c) Separation of die and die-attach material from package.

These MIL-STD criteria are suitable for most of the solder alloys where a failure across the die-attach layer bulk is very unprovable. Nevertheless, in the die-attach layer obtained by sintering processes the bulk adhesion among particles has also to be assessed. This was the motivation for redefining the criteria of separation categories in the next failure modes:

1) *Failure mode 1*. Failure in the interface between Ag sintered layer and substrate. The Ag sintered layer is detached from the substrate and, therefore, the Ag sintered layer is adhered onto the die. This behaviour indicates that the force of the joined interface between Ag sintered layer and substrate is smaller than the force between the other joined interface (die/Ag sintered layer) and smaller than the force among particles (see Figure 3.5(a)).
2) *Failure mode 2*. Failure in the bulk of Ag sintered layer. The fracture is in the die-attach, consequently, there are rests of Ag-sintered layer in both surfaces. In this case, the force of both interfaces is higher than the force among particles in the sintered layer (see Figure 3.5(b)).
3) *Failure mode 3*. Failure in the interface between Ag sintered layer and die. As a result, the Ag sintered layer is detached from the die and remains adhered onto the substrate. This failure mode indicates that the force of the joined interface between Ag sintered layer and die is smaller than force of the other interface (Ag sintered layer/substrate) and force among particles (see Figure 3.5(c)).
4) *Failure mode 4*. Failure in the die, i.e., the die is destroyed with residual semiconductor remaining. This behaviour indicates that force of both interfaces

and force among particles is higher than the strength of the die material (see Figure 3.5(d)).

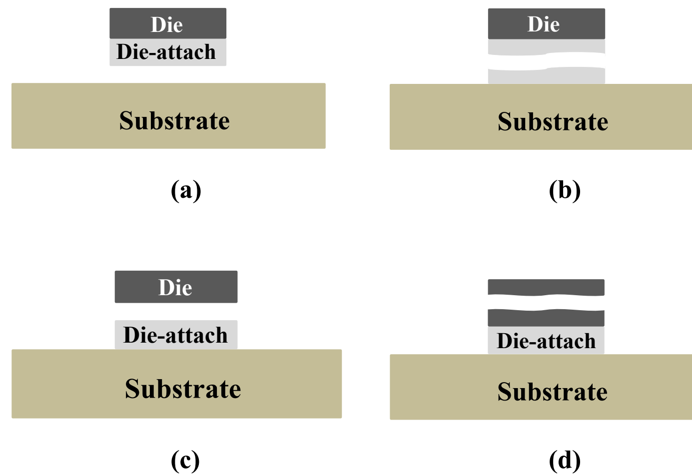


**Figure 3.5. Failure modes defined in our study for Ag sintered die-attach layers.**

**Figure 3.6. Carl Zeiss Auriga 40 SEM-EDX workstation used for die-attach layer analysis.**

*SEM-EDX* incorporates both functions in the same system. On the one hand, SEM (Scanning Electron Microscope) provides scanning high magnification images using a focused beam of electrons. The electrons interact with atoms in the sample, producing various signals that can be detected. These signals contain data about the surface topography and composition of the sample. On the other hand, EDX (Energy-dispersive X-ray spectroscopy), is an analytical technique, which is used for chemical characterization (elemental analysis) of a sample. The SEM-EDX system has been used in several steps in the experimental work, for instance microstructural and compositional analysis of sintered layer after sintering process. Also it has been used in

the analysis of die-attach materials during thermal cycling. In this study, we used the Auriga 40 (Carl Zeiss) Workstation (see Figure 3.6).

The SEM has various types of detectors, but in this study it has been used the In-lens and SE2 detectors. The typical application of the In-lens detector is the study of surface structure of the sample. In the case of the SE2 detector, is useful for study the topography of the sample. For instance, Figure 3.7(a) illustrates a FIB-SEM image of one layer sintered with paste type X (which will be described in chapter 4) used to In-lens detector. In this case, the image has been useful for observe the different orientation of each particle. An example of SE2 detector is displayed in Figure 3.7(b), wherein it can be observed a SEM image of the topography of the layer sintered with paste type X.

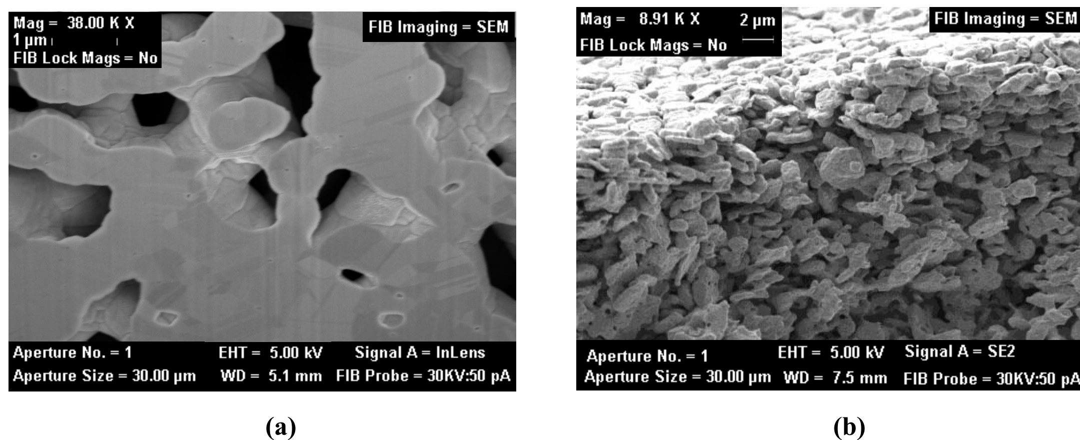


**Figure 3.7. Images of layer sintered with paste type X. (a) FIB-SEM image of sintered layer acquired with In-lens detector. (b) SEM image of sintered layer acquired with SE2 detector.**

*FIB-SEM* also incorporates both functions in the same system. Whereas the SEM uses a focused beam of electrons to image the sample in the chamber, FIB uses a focused beam of gallium ions. FIB (Focused Ion Beam) is a failure analysis technique used to carry out high magnification images, die-surface milling or cross sectioning, and even material deposition (sputtering). The FIB-SEM has been used in several steps in the experimental work, for instance for the microstructural and compositional analysis of layers after sintering process and during thermal cycling of the die attach materials for analysing the composition of degraded parts. In this study, we used the Carl Zeiss workstation model G34-1560 XB (see Figure 3.8). The 1560 XB CrossBeam combines in the same system the applications of a focused ion beam with the high imaging magnification of the SEM due to the GEMINI field emission column.

**Figure 3.8. Carl Zeiss G34-1560 XB FIB - SEM workstation.**

This system has been very useful in this study to analyse the porosity of the die-attach layer based on sintering of particles. In fact, for obtain a suitable image of porosity two steps are necessary. The first step consists in realized a one trench (see Figure 3.9(a)) of the sintered layer [28]. The second step consists of slightly polishing of the trench for obtain a suitable image of the porosity (see Figure 3.9(b)). It is important highlight that two aforementioned steps are necessary for ensure a real study of porosity.

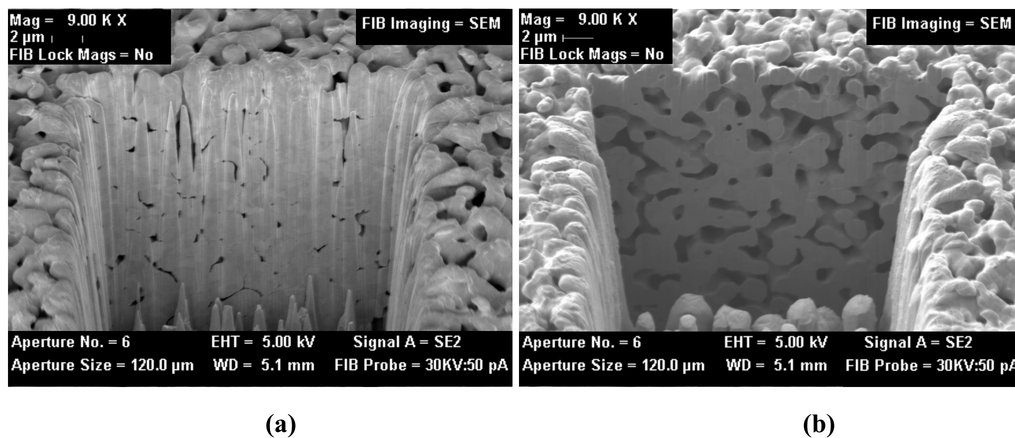


**(a)** **(b)**

**Figure 3.9. (a) FIB image of the trench in the sintered layer. (b) FIB image of the trench on the sintered layer after polishing.**

*Cross-sectioning (also called micro-sectioning).* This technique prepares one plane of the sample (for instance a complete package structure) for inspection, mainly in the framework of failure analysis. This technique is obviously destructive but it complements other non-destructive approaches such as C-SAM inspection. The cross-section allows direct inspection of internal defects (cracks, delaminations, etc.),

confirming the signals acquired during SAM. The procedure for preparing the sample is:

1) *Cleaning*. The sample is cleaned and prepared for the next step.
2) *Encapsulation.* In this step, the sample is mounted and encapsulated in polyester or epoxy resin.
3) *Sawing.* After encapsulated, the sample is sawed, with a diamond wheel cutter, along a plane parallel to the plane of interest.
4) *Grinding*. In this step the sample is grinded, usually grinding is carried out in several steps with an order descendent of the grinding material roughness (SiC paper, polishing cloth or diamond paste). Between each step is necessary rinsing the sample for avoiding scratches. In our particular case, it has been used carborundum powder with grain size of 320, 600, 800, 1000 and 1200.
5) *Polishing*. After grinding the sample is polished. This step is very similar to grinding, except that others materials, such as nylon or silk cloth with diamond or alumina paste or powder on the surface, is used instead of SiC paper. Also, all remaining scratches on the cross-section surface should be removed by this step. In this work it has been used nylon with diamond. The sizes in order descendent were 15 µm, 9 µm, 6 µm, 3 µm, 1 µm and 0.5 µm.
6) *Sample for analysis*. In this step the sample is prepared for analysis, i.e., the sample is cleaned and remaining scratches are removed.

The system used in our framework was the Precision Diamond Saw LECO VC50 (see figure 3.10), able to sectioning various materials, for instance, ceramics, minerals, metals, and electronic components. The maximum diameter for cut sections samples is 1.5 inches (38 mm) with insignificant material loss or deformation. The blade speed is kept constant (up to 500 RPM) under different load conditions in order to obtain a uniform cut surface. In this study it was mainly used to obtain micro-sections of diverse test vehicles including substrate, die-attach and die after the soldering process. In the future work can be useful during thermal cycling. As an example, Figure 3.11(a) displays a SEM image and of a test vehicle after cross-sectioning. Figure 3.11(b) shows another example, but in this case the image was acquired with optical microscope.

**Figure 3.10. Precision Diamond Saw LECO VC-50 used in this study.**

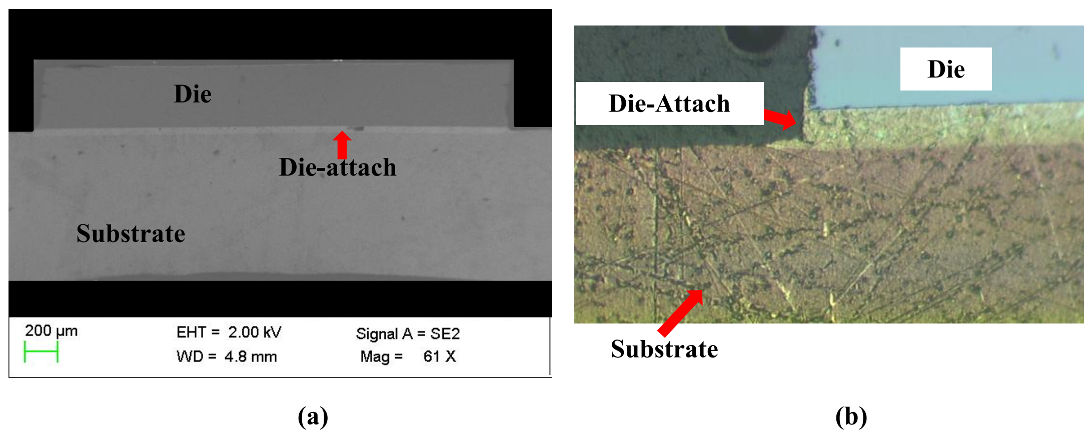


**(a)** **(b)**

**Figure 3.11. Cross-section of a test vehicle: (a) Acquire with SEM system. (b) Acquired with optical microscope.**

Two thermo-analytical techniques based on the NETZSCH STA 449 F1 Jupiter instrument (see Figure 3.12) have also been used, in particular for the characterization of Ag nano-particle pastes: *Thermal Gravimetric Analysis (TGA)* and *Differential Thermal Analysis (DTA)*.

*TGA* is a thermo-analytical technique, in which the mass of a sample is constantly measured, while the sample is subjected to a particular temperature profile. The reactions that arise during temperature profiles can be identified inside the interval wherein they occur. Some examples of reactions (related to a change in weight) are: loss of absorbed water, loss of chemically bound water, oxidations and reductions, evaporation of organics, etc.

**Figure 3.12. NETZSCH STA 449 F1 Jupiter TGA/DTA system used to characterize Ag pastes.**

*DTA* is a technique of thermal analysis that employs two thermocouples connected to a voltmeter. Whereas one of the thermocouples is positioned in an inert material, which is used as reference standard, the other thermocouple is positioned in the sample under study. In the analysis, the sample under test and the reference sample (typically alumina, $Al_20_3$) are submitted to the same heating profile, while any temperature difference between them is recorded. During heating, reactions occurring in the sample, either exothermic (peaks) or endothermic (valleys), are detected relative to the inert reference. The reactions, which result in a weight loss can be also detected in TGA analysis, although there are solid state reactions such as crystallization or melting, where weight is unchanged and they can be only detected by DTA.

The NETZSCH STA 449 F1 Jupiter instrument allows the measurement of weight and DTA signals as a function of temperature and time. The sensitivity of the balance is 0.07 micrograms while its internal furnace can operate from room temperature to 1400 ºC. The analyser may work in several atmospheres such as oxygen, air, nitrogen, argon and hydrogen (diluted at 5% in Ar), at ambient pressure and with using typical flow rates of 70 $cm^3$/min [29].

### 3.4. Ag Nano-Particles Sintering for Die-Attach Applications

The sintering has been used since thousands of years, for instance, one of the earliest applications of the sintering was the formation of bricks by heating clay bodies in an open pit fire. This was carried out in ancient civilizations of Mesopotamia, approximately 6000 B.C. As early as 3000 B.C., the Egyptians sintered metals and

ceramics and in the South America the Incas used sintering to make gold-platinum jewellery [30, 31]. Sintering as a solid-state science started during the period 1920-1950. The main contribution for understanding the sintering phenomena related to mass transport mechanisms were made by Frenkel, Kuczynski, Lenel, Coble, Kingery, German, and others. Nowadays, some products include: portable mobile terminals, ultrasonic transducers, arresters, automobile engines, electronics packages, rocket nozzles, dental implants, and artificial bones [32, 33]. The use of such a well-established technology for die-attach joints in the microelectronics industry, was also studied since the 90s of the past century. In these first works, a mixed of silver-glass were used for manufactured die-attach involving high temperatures around of 400 ºC [16, 34]. In the same sense, silver micro-flakes were used in process (for manufactured die-attach) involving relatively high temperatures (between 200 and 250 ºC) and pressures (between 10 and 100 MPa) [35]. Silver was the preferred material due to its superior electrical and thermal properties. More recently, the development of nano-technology made available silver particles in the nanometre scale (nano-particles), suitable for sintering processes involving lower temperatures and pressures. Therefore, in this section, the physical basis around the sintering phenomenon, the components of pastes used to implement this technology (in order to manufacture the die-attach) and, the advantages and disadvantages of used Ag nanoparticles, will be presented.

### 3.4.1. Sintering Physical Basis

In practical terms sintering is the joint of particles (usually quasi-spherical powders) for creating bulk material (implying particles densification) without reaching its melting point. This phenomenon is the result of atomic motion excited by energy (generally high temperature), wherein commonly diffusive mechanisms are the most determinant. Sintering is associated also with volume shrinkage (due to porosity decrease among the initial particles), combined with neck growth, grain growth and strong joining among neighbouring particles. The final properties of final sintered bulk depend of the initial powder properties (size, size distribution, distribution, shape of the particles, aggregates, and agglomerates) and the parameters of the process (cleaning of elements used in process, sintering time, sintering temperature, sintering pressure). In fact, it could be even possible to modify the material properties (changing the process parameters) according to needs of each specific application [36, 37].

### 3.4.1.1 Geometric Stages of Sintering

For major comprehension of the sintering phenomenon it is necessary to define its geometric progression [36, 37]. Generally, the geometric progression (which is due to joined particles and the decrease of porosity) is classified in three stages and each stage describes the main physical changes. The three stages that describe the geometric progression are mentioned below.

Regarding to the initial (also called first) stage, particles (powders) reorganize and the conformation of the initial necks at the contact point between each particle starts. The reorganization refers to contact points increase due to little motion or rotation of adjoining particles. Precisely in these contact points (wherein material transport can occur and surface energy is highest) is where the bonding phenomena arise (see Figure 3.13(a)).

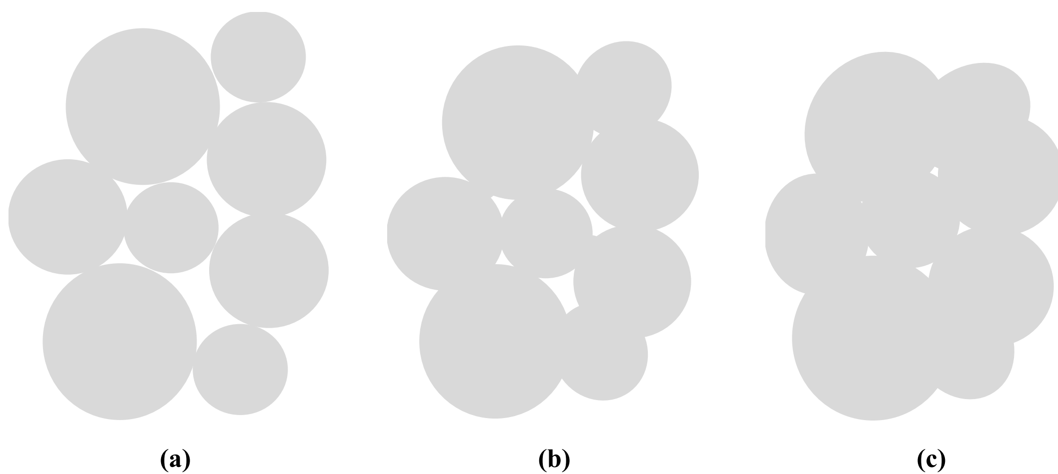


**Figure 3.13. Sintering process. (a) Shows the initial stage of sintering. (b) Shows the intermediate stage of sintering. (c) Shows the final stage of sintering.**

In the intermediate (also called second) stage the neck growth begins due to increment of the necks size among particles. At the same time, the porosity decreases due to movement of the particles centres. Therefore, the volume shrinkage is proportional to the decrement in porosity. Whereas one grain (formed by particles) begins to grow, other adjoining grains are consumed. This results in the grain boundaries lengthening so that allows geometry progression. The geometric changes are required to assist further neck growth and elimination or reduction of porosity. Whereas the pore channels are interconnected the second stage continues and ends when pores

become isolated. During the intermediate stage, most of the shrinkage occurs (see Figure 3.13(b)).

| Initial (first) Stage | Intermediate (second) Stage | Final (third) Stage |
|---|---|---|
| Particles reorganization | Neck growth | Significant grain growth |
| Neck formation | Grain growth (Grain boundaries lengthening) | Discontinuous pore phase |
| | High shrinkage | Elimination of grain boundary pores |
| | Pore phase continuous (porosity decreases) | Final reduction of porosity |

**Table 3.2. Main physical changes of geometric stages of sintering.**

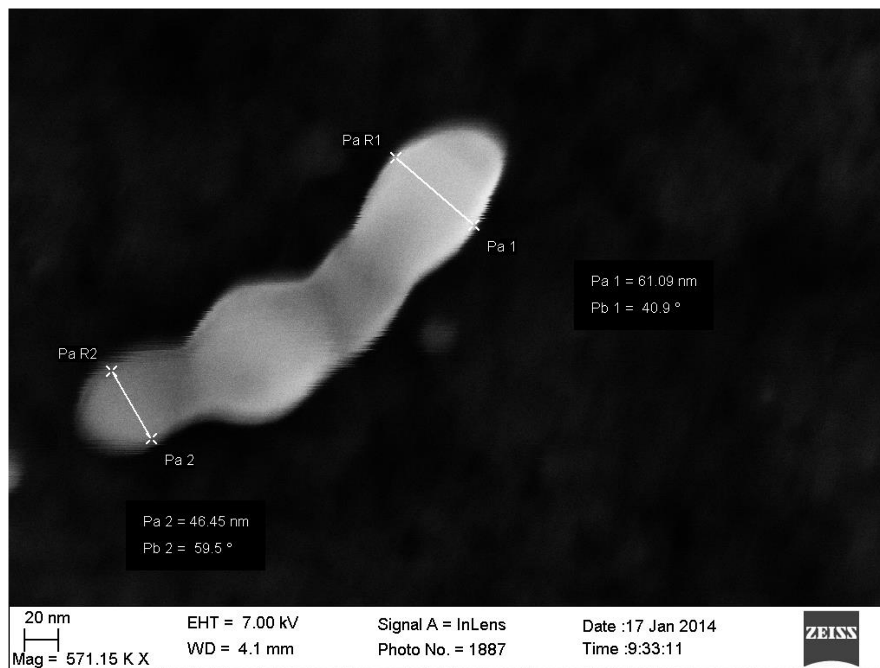


**Figure 3.14. SEM image of particles joined of the paste type X.**

In the case of the final (also called third) stage, the decrement of porosity continues by vacancy diffusion alongside the grain boundaries. Consequently, pores and grain boundaries remain close. The decrement of porosity and vacancy diffusion are assisted by motion of grain boundaries and regulated grain growth. On the other hand, monitoring the grain growth is very important because if grain growth is too fast, the grain boundaries can move faster than the pores and leave them isolated in the interior of a grain. Consequently, as the grain growth continues, the pore is increasingly separate from the grain boundary and decreases the possibility to be removed. Thus, to

reach the maximum porosity removal, grain growth must be controlled. In short, the last stage is related to the final decrease of porosity (see Figure 3.13(c)). Table 3.2 summarizes the main physical changes that arise in each sintering stage. Figure 3.14 shows SEM image of several silver particles, where it can observed that the four particles with different sizes are joined (the paste used in this case is type X of NBTECH). Besides, it can be observed that the diameter of particle is around 50 nm.

#### 3.4.1.2. Sintering Mechanisms

Section 3.4.1.1 reviewed the three geometric progression stages of typical sintering processes. The present section will review the mechanisms, driving forces and paths of material transport that promote sintering during its geometric progression.

The geometric progression in a sintering process is based in two processes. The first one is a mechanism for material transport, and the second a source of energy (driving force) to start and to maintain this material transport. The driving forces are defined as the trend of the material to reduce its chemical potential or energy. Generally, the heat is the principal energy source, in combination with energy gradients caused by the contact among particles and the surface tension. In fact, the electrical current and pressure are also other sources of energy that improve the densification of the final bulk material. Concerning the transport mechanisms they are divided in two main groups, surface transport and bulk transport:

1) *Surface transport*. This type of mechanism involves neck growth without bulk densification because the distance among particles remains unchanged. This is because the material transport is originated and ended at the particle surface. The prevailing mechanisms during surface transport are:

    a) *Surface diffusion*. Generally, is the main diffusion on the sintering of several covalent solids (for instance, boron and silicon carbide).
    b) *Evaporation-Condensation*. This mechanism has little influence, however is observed to influences the sintering of low-stability ceramics (for instance, sodium chloride).

2) *Bulk transport*. This type of transport mechanism controls the shrinkage during sintering. In this case the most important mechanisms (volume diffusion, grain boundary diffusion, plastic flow, and viscous flow) are described below.

   a) *Volume diffusion*. This sort of diffusion arises due to motion of atoms or vacancies throughout a surface or grain boundary or through bulk material. Besides, either grain boundaries or in case of through lattice dislocations, volume diffusion always results in shrinkage. In the case of ceramics, this mechanism is often limited by defects on the structure.
   b) *Grain boundary diffusion.* Generally, is the main diffusion on the sintering of most crystalline materials, and is very important for the densification of several ceramics (including alumina ($Al_20_3$)).
   c) *Plastic flow.* This kind of diffusion is usually irrelevant in the case of crystalline ceramics. This behaviour is because any dislocation motion would produce identical ionic neighbours (condition that is adverse). Besides, the stresses produced by surface tension found during sintering, are insufficient to create dislocations. Nevertheless, some interpretations with TEM (Transmission electron microscopy) show dislocation motion in the neck region owing to the thermal stresses related to rapid heating.
   d) *Viscous flow.* This effect appears in the sintering of amorphous materials (for instance plastics and glasses). Besides, it can also appear in the case of crystalline ceramics that contain glass phases on the grain boundaries. In this mechanism the particles coalesce at a rate, which is determined by the particle size and the material viscosity.

These sintering mechanisms are closely linked to the material transport paths (also called diffusion paths). Figure 3.15 shows the material transport paths described with respect to the neck region between two sintered particles, which can participate in the sintering. The main distinctive feature between surface and bulk transports is the densification. Whereas the bulk transport contributes to the densification, the surface transport only participates in the join between particles.

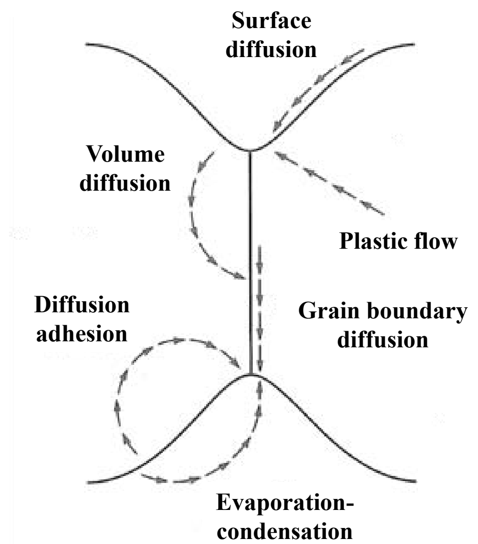


**Figure 3.15. Illustration of material transport paths respect to the neck region between two sintering particles [36].**

### 3.4.1.3. Sintering Types

This section will describe the sintering types that depend on the mechanisms responsible of the densification. In fact, the densification can be possible with one mechanism or in combination with other mechanisms. These sintering types are classified in solid state sintering, viscous sintering, liquid phase sintering, pressure assisted sintering and current assisted sintering [37, 38].

1) *Solid State Sintering*. This type of sintering involves material transport by volume diffusion and is typical in polycrystalline materials. [36, 37]
2) *Viscous Sintering*. This type of sintering is typical in amorphous materials, for instance in glasses. When the glass transition temperature is exceeded, the material behaves as a highly viscous medium and the viscous flow is frequently the primary material transport mechanism through which the surface area is minimized [39, 40].
3) *Liquid Phase Sintering*. This type of sintering requires the existence of a viscous liquid during sintering. For the most silicate systems this is the main mechanism for densification. The rate of sintering is determined by particle size, viscosity and surface tension. Adequately selected conditions for the liquid phase, can supply a better path for rapid material transport and, consequently, more rapid sintering [37, 38].

4) *Reactive Liquid Sintering.* This type (also called transient liquid sintering) contributes with the same types of paths for material transport of the liquid-phase sintering, because the liquid phase exists during sintering. The difference between both is that, in this type of sintering, the liquid has changes of composition or disappears. These changes can occur during or after sintering. Due to the liquid phase is consumed in the reaction; the final bulk material can have good high-temperature properties. In some cases the final material can be used at temperatures superior to the sintering temperature [37].
5) *Vapour phase sintering*. The material transport mechanism for this type is the evaporation-condensation. The driving energy is the differences in vapour pressure.
6) *Pressure assisted sintering*. Besides of volume diffusion, this type of sintering process uses an externally applied pressure to improve densification.
7) *Electrical current assisted sintering*. This type of sintering uses the electrical current for activate the sintering process or sinter-joining between metals. Various methods that combine current and pressure for sintering powders are available, but the most common one is the spark plasma sintering (SPS) [30].

| Type of sintering | Material transport mechanism | Driving energy |
|---|---|---|
| Solid state | Volume diffusion | Differences in free energy or chemical potential |
| Viscous | Viscous flow | Surface tension [39] |
| Liquid phase | Viscous flow and diffusion | Capillary pressure and surface tension |
| Vapour phase | Evaporation-condensation | Differences in vapour pressure |
| Reactive liquid | Viscous flow, solution precipitation | Capillary pressure, surface tension |
| Pressure assisted | Volume diffusion | Differences in free energy or chemical potential, externally pressure [41] |
| Electrical current assisted | Volume diffusion | Differences in free energy or chemical potential, externally pressure, electrical current |

**Table 3.3. Sintering types, material transport mechanism and its respective driving energy.**

Sintering types, material transport mechanisms and their respective driving energy are summarized in table 3.3.

#### 3.4.1.4. Particle Influence on Sintering for Die-Attach Applications

In the previous section it has been described the main basis of sintering theory, in the same sense, in this section it will describe the particle influence in the sintering for creates a die-attach material. The influence of particle size is well-known in the sintering theory, wherein small particles improve densification rate [33, 36, 37]. The parameters that characterize the particle are: shape, size, size distribution, particle distribution, aggregates, and agglomerates. In fact, these parameters play an important role in sintering phenomenon. In the particular case of die-attach applications, also the particle influence is determinant in the properties of the sintered layer and the adherence with surfaces (die and substrate).

In fact, in the first works it has been used pressures from 10 to 100 MPa and temperatures around 250 ºC for Ag micro-flakes [35]. Recently, a reliable die-attach based on sintering is possible using low temperatures (around 300 ºC) and pressures around 40 MPa [42, 55]. Nonetheless, high pressure can lead to die fracture and increases the residual stresses during sintering. For this reason, several efforts have been carried out in the research of the suitable particles in order to avoid the applied pressure. Such is the case of nano-particles (where the nano-scale is defined by particle size from 1 nm to 100 nm [38, 43]), which can obtain suitable results even at zero sintering pressure. Besides, another advantage is that sintering can be carried out at lower temperatures using nano-particles. This behaviour is due to the fact that the number of atoms in smaller particles is less, and therefore, the surface area is greater [44]. Consequently, the driving forces (provided for the surface) are more significant for nano-particles than micro-particles [18, 33]. In point of fact, the melting point of a particle reduces almost linearly with the inverse of the particle radius (due to surface energy contribution) [44, 45, 46]. In some studies, molecular dynamics simulation reveals that 2.4 nm nano-particles of Ag melt at about 350 ºC [47, 48]. Thus, this behaviour indicates that smaller particles sintered at lower temperatures than bigger particles. In fact, these arguments has been experimentally supported by investigations, which has been shown the densification is faster for Ag nano-particles (with size of 30 nm) than for nano-particles with size of 100 nm [49]. Besides, the Ag nano-particles around 11 nm show better adherence (between Ag sintered layer and, Cu substrate) than bigger particles around of 100 nm [44]. For all these reasons, the low temperature and

(and even zero) sintering pressure requirements, make this technology very attractive for improving the integration capability in power packaging processes. Consequently, several researches have been focused on Ag nano-particles in order to reduce the applied pressure and temperature to elaborated a die-attach based on sintering process [38, 42, 50, 51, 52, 53, 54, 55, 56, 57].

Nevertheless, some disadvantages are also associated to Ag nano-particles: these are agglomerates, aggregates and the surface diffusions (which are called non-densification diffusions because not contribute with densification) at low temperatures (see section 3.4.1.2). Agglomerate, is defined as a cluster of particles bonded together by weak forces such as van der Waals and/or electrostatic attraction. Generally, agglomerates can easily lead to aggregates. Aggregates are clusters of interconnected particles strongly bonded together by solid necks such as chemical bonds. It is possible undo the agglomerates by mechanical re-dispersion processes such as ultrasonic or mechanical agitation. But, in the case of aggregates is not possible re-dispersed by mechanical processes. In a powder with agglomerates or aggregates, the particle distribution loses its homogeneity and the effective particle size is higher than that of the individual particles. As a result, larger voids can be formed due to inhomogeneous distribution of particles and the benefits of using smaller particles (due to effective radius) are reduced (see Figure 3.16)[58].

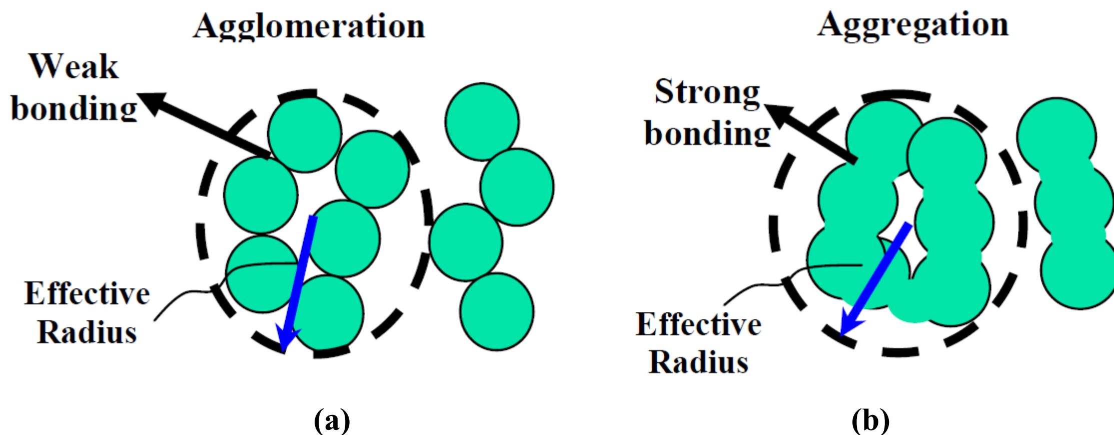


**Figure 3.16. Schematic of effective particle radius, which is due to: (a) Agglomeration. (b) Aggregation [38, 51].**

In the case of non-densification diffusions it refers to mechanisms that consume the driving force at low temperature, and thus a poor densification is obtained. According to

the theory, the non-densification mechanisms (surface diffusions) are activating at low temperatures and the densification mechanisms (bulk diffusions) appears at high temperatures [38, 51]. For this reason, in the case of nano-particles a real challenge is avoid that appears the non-densification mechanisms at low temperatures. Usually, the use of rapid heating rate is one option in order to avoid this problem [38, 51]. However, one disadvantage is that the rapid heating rates can cause fractures in the sintered layer [46]. Moreover, in the die-attach formation, can cause fractures on the device as a consequence of thermal shock. Another disadvantage of rapid heating rate is that is more complex and expensive than baking oven (used commonly in conductive adhesives) and reflow furnace (used commonly in solders). In order to avoid rapid heating rate, an alternative solution is to cover the particles with organic compounds with high evaporation temperature. Using organics with suitable evaporation temperature, the non-densifying surface diffusion can be retarded at a relatively low temperature. Consequently, after organic evaporation, the bulk diffusions are activated and densification can be carried out. For further explanation, a brief description of the main organic compounds using in a typical silver paste for die-attach applications will describe in the next section.

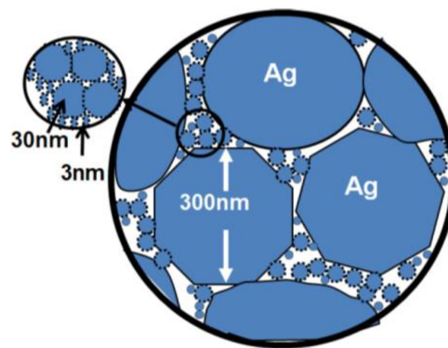


**Figure 3.17 Illustration of typical mix of nano-particles with larger particles [59].**

It is worth to point out that the mixture of Ag micron- and nano-particles produces also good densification on the sintered layer [46, 47, 59]. In fact, it have been demonstrated that the joint among particles is originated by nano-particles, which weld around of micron-particles. Also, this mixture enlarged the size distribution of particles and consequently an appropriate densification of the sintered layer is achieved. These observations has been carried out (see Figure 3.17) with nano-particles (particle size around 3-100 nm) and Ag micron-particles (particle size of 0.3 μm) [47]. Regarding to

die-attach, some researchers have obtained better results of die-shear force by mixing micron-flakes with spherical particles (size distribution of particles around 0.6 - 6.5 μm) than only when using micro-flakes (size distribution of particles around 0.5 - 6 μm) [60]. Finally, it is important highlight, that another advantage of using mixture of particles with different sizes is related to the cost.

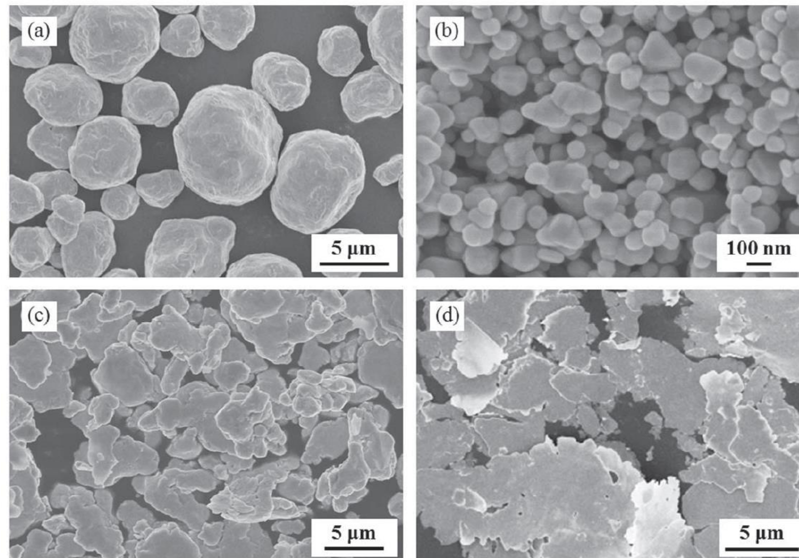


**Figure 3.18 SEM images of the four shapes of particles. (a) Ag micron-particles. (b) Ag nano-particles. (c) Ag micron-flakes. (d) Ag nano-thick-flakes [55].**

In the context of particle shape, recently works has been reported the behaviour of micron-flakes, nano-thick-flakes, micron-particles and nano-particles in the same processing conditions [55]. Figure 3.18(a) displays the Ag micron-particles, which has a diameter average of 5 μm and Figure 3.18(b) shows the Ag nano-particles, which has a diameter average of 100 nm. The micron-flakes have a diameter average of 5 μm and thickness of 260 nm (see Figure 3.18(c)). The nano-thick-flakes have a diameter average of 8 μm and thickness of 80 nm (see Figure 3.18(d)). Though the Ag micron-flake and Ag nano-thick-flakes have a smaller specific surface area than Ag nano-particles, the die-shear force of the samples manufactured with the Ag micron-flake and Ag nano-thick-flake pastes is higher than samples manufactured with the others pastes. In fact, in reference [60] it mentioned that flake shaped silver particles accelerated the diffusion process owing to this irregular shape and the high dislocation density. In other studie, it has been demonstrated that Ag nano-rods produce joints with lower die-shear

force than Ag nano-particles [61]. These observations indicate that further research is required in order to understand the particle shape influence.

Regarding to particle material, Ag is the most used because it offers very good properties for die-attach. Among these properties one can highlight its high melting temperature (961 ºC), high thermal conductivity (430 W/m.K) and high electrical conductivity (0.63 x $10^6$ $\Omega^{-1}cm^{-1}$). Nevertheless, one disadvantage related to the Ag nano-particles is the cost (see Table 3.4). Another disadvantage is the migration across dielectric materials, which can cause short circuit failure in electronics packages. For silver migration may occur need to pass a current through the dielectric from the cathode to the anode. For instance, in reference [ 62 ], the researchers have been demonstrated that the silver dendrites formed a bridge between the electrodes (gap of the 50mm) through of the alumina with a current of 1mA. Besides, have been founded that the oxygen plays a critical role in the silver migration, therefore, possible solutions for reduces this problem could be reached by encapsulation or hermetical packaging. In fact there are several efforts for avoiding silver migration, for instance, the use of alloys (silver with palladium) and reducing the partial pressure of oxygen inside of package [62].

| Property | Ag | Au | Al | Cu |
|---|---|---|---|---|
| **Electrical Conductivity (x $10^6$ ($\Omega^{-1}cm^{-1}$))** | 0.63 | 0.45 | 0.37 | 0.59 |
| **Thermal Conductivity (W/m ºC )** | 430 | 315 | 237 | 401 |
| **CTE (ppm/ºC)** | 19 | 14.2 | 23.0 | 16.5 |
| **Tensile Strength (MPa)** | 170 | 130 | 90 | 200 |
| **Young Modulus (GPa)** | 76 | 77 | 69 | 110 |
| **Ductility (% elongacion)** | 44 | 45 | 40 | 45 |
| **Melting point (ºC)** | 961 | 1064 | 660 | 1085 |
| **Price on March 2013 ($ US/kg)** | 1012.36 | 56717.06 | 1.89 | 7.61 |
| **Standard electrode potential (V)** | +0.800 | +1.420 | -1.662 | +0.340 |

**Table 3.4 Physical properties of bulk Ag, Cu, Au, and Al [6, 66].**

In order to improve the sintered layer (densification, the sinter-metal joint, mechanical properties and costs reduction) recently some researchers used other materials such as copper [63], silver mixed with several materials as aluminium [64, 65], copper [66], diamond and SiC [67, 68]. With the aim at compared the benefits of each metal (Ag, Au, Al and Cu), Table 3.4 shows the main properties of these metals.

In the case of silver mixed with aluminium, the researches has been used Ag particles (80 %) with mean sizes of 60 ± 20 nm mixed with Al particles (20 %) of 40 ± 10nm. The main reason for used Al is because is the second in electrical conductivity among metals, furthermore its thermal conductivity is appropriate, and is cheaper than Au and Ag. In consequence, the advantages of this mixture is the reduction in cost, and regarding to mechanical properties reduces the CTE, and young modulus, which are desirable for origin less stresses in the package. The low CTE and young modulus is believed that is owing to the porous structure. On the other hand, their adverse effects are the reduction in thermal and electrical conductivity [64, 65].

Although Cu is more expensive than Al, is cheaper than Ag and Au. For this reason, Cu is an interesting metal for mixed with Ag. Besides, Cu the second best electrical and thermal conductivities among other metals and its coefficient of thermal expansion is similar to Ag (see Table 3.4), therefore, it is appropriate to be mixed with Ag in a paste formulation. Cu and Al are malleable and ductile materials, but Cu and Ag have closer values of tensile strength and Young's modulus (see Table 3.4). Finally, the standard electrode potential is closer for Cu and Ag than Al and Ag, for that reason, the galvanic corrosion is minor.

In the case of silver mixed with diamond is an interesting solution due to the properties of diamond, i.e., has a low CTE and has a high thermal conductivity (see Table 4.1), therefore, a sintered layer with low CTE is carried out (8 ppm/°C, approximately). The case of the SiC is similar to the diamond, because is used to improve the thermal conductivity and diminishes the CTE of the final sintered layer. Nevertheless, diamond and SiC have high cost and both are hardness materials. In fact, diamond is the hardest known natural material on the Mohs scale of mineral hardness, therefore, is necessary more in deep research, especially in bonding and reliability test.

### 3.4.2. Ag Nano-Particles Sintering Pastes for Die-Attach Applications

Generally, the use of Ag nano-particles sintering in the electronics field is mainly based on pastes. In fact, the results of sintering are also dependent of the formulation and chemistry of the paste [69]. Generally, these pastes are a mixture of solid particles

(powders) and organic solvents and they differ by the size, size distribution, shape and material of the particles, as well as by their organic components (dispersant, binder, and thinner). In this section, the characteristics and components of pastes selected for this study and used to manufacture the die-attach, will be described.

Nevertheless, some disadvantages are also associated to Ag nano-particles processes, the main one being related to agglomerates formation on the green paste and during the temperature profile before densification. Another disadvantage is the non-densifying diffusions at low-temperatures, which has been described in the previous section. In fact, the selection of organic components on the green paste and uniform dispersion of particles is determinant for avoiding agglomerates.

Concerning the organic components, dispersant, binder and thinner are added to the solid powder to produce a paste with good particle distribution, flowability and adequate viscosity to ease the dispensing (for example, screen printing in our case) [38, 50, 58].

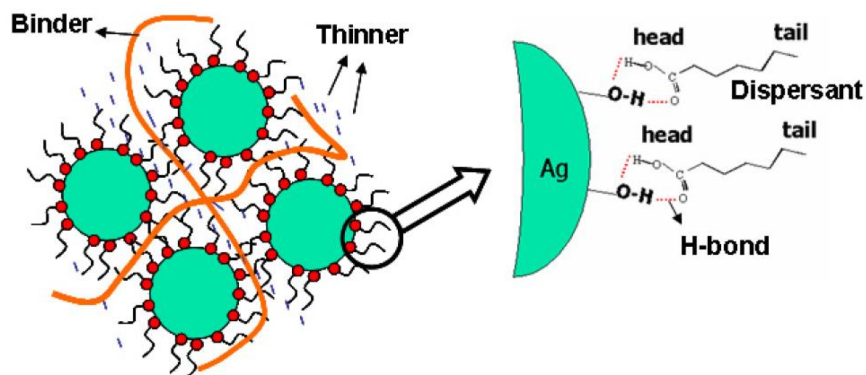


**Figure 3.19. Functions of the dispersant, binder and thinner, which are used to formulated the silver pastes based on nano-particles [38].**

The main function of dispersant in ensure uniform distribution of all particles in the paste. The dispersant typically is formed by a polar acid function in one end and a chain of hydrocarbon in the other end. In the case of binder, commonly are composites of polymer with long hydrocarbon chains in order that it can hold up the uniform distribution of silver particles to avoid cracks during sintering process. For illustrate this, in Figure 3.19 can be observed that the dispersant can adhere to silver nano-

particles through hydrogen bonds. The aim at thinner is regulate the viscosity of the paste. Typically are composites of polymer with short hydrocarbon chains.

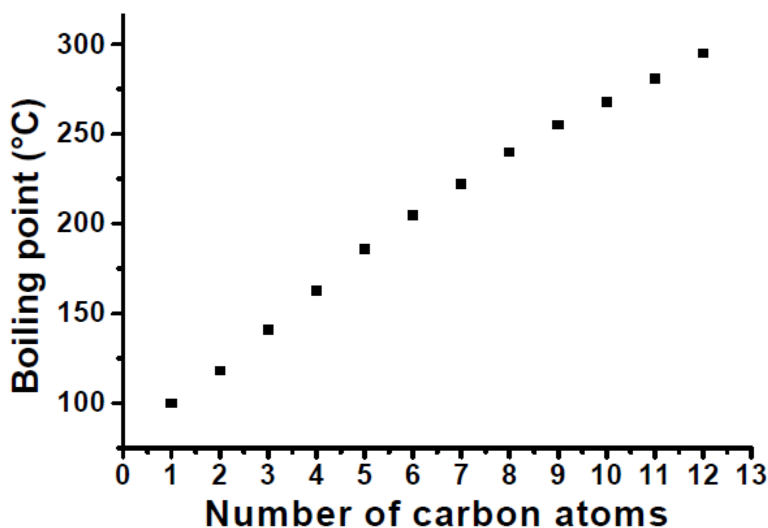


**Figure 3.20. Boiling point of fatty acid versus their number of carbon atoms (Adapted from the Sigma-Aldrich websites) [38].**

Besides, the organics determine the required temperature profile for sintering, because the thermal behaviour of these components is important for their correct elimination. In fact, suitable selection of organic components in combination with temperature profile can reduce the sintering temperature, and therefore obtain an optimum densification [18, 38, 51, 70]. As an example, Figure 3.20 represents like the boiling points of the fatty acids (dispersant) increase with the number of carbon atoms in the molecular of the dispersant. Therefore, if a paste which can be sintered at about 250 ºC is required, the fatty acids with carbon atoms around 9 should be selected, if not the fatty acids cannot be burned out, and the particles cannot be sintered appropriately at the selected temperature. Another consideration about of the selection of the organics is the functionalities in the formation of the paste. For instance, the fatty acids with relatively longer hydrocarbon chain can disperse the nanoscale silver particles better than those with relatively shorter hydrocarbon chain, and therefore avoid better the aggregates and agglomerates creation.

For all of these reasons, a correct selection of organic coating (also called shell or layer) in each particle is necessary, in order to avoid the formation of aggregates and agglomerates on the green paste and during temperature profile [44, 49, 51].

Also, the powder (nano-particles) production process is very important because it determines the size, distribution and shape of the particles. In fact, it has been demonstrated that different Ag particle sizes, distribution and shapes show different sintering properties which result in different bulk density and surface adherence [60, 61].

### 3.5. Conclusions

The die-attach layer is one of the most critical element of package structure. For this reason, special attention it has put in die-attach layer for high temperature applications, in particular the die-attach based on sintering phenomenon.

In this study, it has been realized a brief review about of the main failure analysis methods for power electronics. More in depth review, it has been carried out in the techniques and system used in this study for analysed the quality and degradation of die-attach layer. Besides, sintering physical basis, its mechanisms and the main types, also, has been described. Then, it has been analysed the particle influence in the sintering phenomenon. Finally, a brief description of the main components of pastes manufactured for die-attach application has been carried out.

### 3.6. References

[1] V. R. Manikam and K. Y. Cheong, "Die-attach materials for high temperature applications: A review," *IEEE Transactions on Components, Packaging and Manufacturing Technology,* vol. 1, no. 4, pp. 457 - 478, April 2011.

[2] J. Felix, "Impact of material and process parameters in soft solder die bonding," in *Proc. Semicon,* 2006, pp. 1 – 3.

[3] R. Khazaka, L. Mendizabal, D. Henry, R. Hanna, "Survey of High Temperature Reliability of Power Electronics Packaging Components," *IEEE Transactions on Power Electronics,* vol. 30 , no. 5, pp. 2456 - 2464, September 2014.

[4] F. P. McCluskey, M. Dash, Z. Wang, and D. Huff, "Reliability of High Temperature solder Alternatives," *Microelectronics Reliability*, vol. 46, no. 9 - 11, pp. 1910 - 1914. September - November 2006.

[5] Y. Li and C. P. Wong, "Recent advances of conductive adhesives as a lead-free alternative in electronic packaging: Materials, processing, reliability and applications," *A Review Journal* of *Materials Science and Engineering,* vol. 51, no. 1 - 3, pp. 1 - 35, January 2006.

[6] L. Coppola, D. Huff, F. Wang, R. Burgos, and D. Boroyevich, "Survey on High-Temperature Packaging Materials for SiC-Based Power Electronics Modules," in *Proc. IEEE Power Electronics Specialist Conference*, PESC 2007, pp. 2234 - 2240.

[7] http://www.wolframalpha.com/input/?i=poisson+ratio+silver

[8] http://www.indium.com

[9] F.P. McCluskey, R. Grzybowski, and T. Podlesak, "High Temperature Electronics," Florida: CRC press, 1997, Chap. 1 - 5.

[10] B. Grummel, R. McClure, L. Zhou, A. P. Gordon, L. Chow, and Z. J. Shen, "Design Consideration of High Temperature SiC Power Modules," in *Proc. IEEE Industrial Electronics Conference*, 2008, pp. 2861 - 2866.

[11] http://www.MatWeb.com

[12] S. Msolli, O. Dalverny, J. Alexis, M. Karama, "Mechanical Characterization of an Au-Ge Solder Alloy for High Temperature Electronic Devices," in *Proc. IEEE International Integrated Power Electronics Systems Conference*, CIPS 2010, pp. 1 - 5.

[13] COMSOL Multiphysics library of materials properties.

[14] T. Yamamoto, K. Tsubone. "Assembly technology using lead-free solder". *Fujitsu Scientific Technical Journal*, vol. 43, no. 1, pp. 50 - 58, 2007.

[15] M. Roellig, R. Metasch, K. Meier and F. Alt. "Characterization Methods for Determination of Temperature Depended Electrical, Thermal, Mechanical and Fatigue Properties of SnAg3.5 Solder," in *Proc. IEEE Electronic System Integration Technology Conference*, ESTC 2010, pp. 1-11.

[16] G. C. Bell, C. M. Rosell, and S. T. Joslin, "Rheology of Silver-Filled Glass Die Attach Adhesive for High-Speed Automatic Processing," *IEEE Transactions Components, Hybrids and Manufacturing Technology*, vol. 12, no. 4, pp. 507 - 510, December 1987.

[17] Ryszard Kisiel, Zbigniew Szczepański, Piotr Firek, Jakub Grochowski, Marcin Myśliwiec, Marek Guziewicz, "Silver Micropowders as SiC Die Attach Material for High Temperature Applications, " in *Proc. 35th International Spring Seminar on Electronics Technology (ISSE)*, May 2012, pp. 144 - 148.

[18] K. S. Siow, “Mechanical properties of nano-silver joints as die attach materials,” *Journal of Alloys and Compounds*, vol. 514, pp. 6 - 19, 2012.

[19] T. G. Lei, J. N. Calata, G. Lu, X. Chen and S. Luo, “Low-Temperature Sintering of Nanoscale Silver Paste for Attaching Large-Area (>100mm2) Chips,” *IEEE Transactions on Components and Packaging Technology*, vol. 33, no. 1, pp. 98 - 104, March 2010.

[20] J. G. Bai and G.-Q. Lu, “Thermomechanical reliability of low temperature sintered silver die attached SiC power device assembly,” *IEEE Transaction on Device and Materials Reliability*, vol. 6, no. 3, pp. 436 - 443, September 2006.

[21] L. A. Navarro, X. Perpiñà, M. Vellvehi, X. Jordà, “Silver Nano-Particles Sintering Process for the Die-Attach of Power Devices for High Temperature Applications,” *Sociedad Mexicana de Ingeniería Mecánica*, vol. 4, no. 3, pp. 97 - 102, September 2012.

[22] (2014). [Online]. Available: http://www.sonoscan.com/instruments/gen5.html

[23] (2014). [Online]. Available: http://www.royceinstruments.com/bond-testers/royce650.html

[24] Test Method Standard Microcircuits, MIL-STD-883H -2010.

[25] R. Dudek, R. Doering, K. Kreyssig, and B. Michel, “Theoretical Analyses on the Shear Test,” in *Proc. 11th International Conference on Thermal, Mechanical & Multi-Physics Simulation, and Experiments in Microelectronics and Microsystems (EuroSimE)*, pp. 1 -7. April 2010

[26] P. Hagler, P. Henson and R. W. Johnson, “Packaging Technology for Electronic Applications in Harsh High-Temperature Environments,” *IEEE Transactions on Industrial Electronics*, vol. 58, no. 7, pp. 2673 - 2682, July 2011.

[27] Test Method Standard Semiconductor Devices, MIL-STD-750D -1995.

[28] (2014). [Online]. Available: http://www.nbetech.com/products.shtml

[29] (2014). [Online]. Available: http://icmab.es/thermal-analysis-lab#about

[30] Z. A. Munir, U. Anselmi-Tamburini and M. Ohyanagi, “The effect of electric field and pressure on the synthesis and consolidation of materials: A review of the spark plasma sintering method,” *Journal of Materials Science*, vol. 41, no. 3, pp. 763 - 777, February 2006.

[31] E. Cooper, *Historia de la Cerámica*. Barcelona: Ceac, 1999.

[32] L.A. Navarro, “Caracterización Eléctrica de Varistores de ZnO Dopados,” Tesis, Universidad de Guanajuato, Salamanca, Guanajuato, México, Diciembre 2006.

[33] K. Inamori, Advanced Ceramic Technologies & Products, Springer, 2012.

[34] M. Y. N. Nguyen, "Low Stress Silver-Glass Die Attach Material," *IEEE Transactions on Components Hybrids and Manufacturing Technology*, vol. 13, no. 3, pp. 478 - 483, September 1990.

[35] H. Schwarzbauer and R. Kuhnert, "Novel Large Area Joining Technique for Improved Power Device Performance," *IEEE Transactions on Industry Applications,* vol. 27, no. 1, pp. 93 - 95, 1991.

[36] R. M. German, Fundamentals of Sintering in Engineered Materials Handbook, vol. 4 ASM International, 1991.

[37] D. W. Richerson, Modern Ceramic Engineering: Properties, Processing and Use in Design, 2nd edition, Marcel Dekker (New York), 1992.

[38] G. Bai, "Low-Temperature Sintering of Nanoscale Silver Paste for Semiconductor Device Interconnection". PhD thesis, Virginia Polytechnic Institute and State University. Blacksburg, Virginia, October 2005.

[39] W. D. Kingery and M. Berg, "Study of the Initial Stages of Sintering Solids by Viscous Flow,Evaporation-Condensation, and Self-Diffusion," *Journal of Applied Physics*, vol. 26, no. 10, pp. 1205 - 1212, October 1955.

[40] F. Varnik, A. Rios, M. Gross and I. Steinbach, "Simulation of Viscous Sintering Using the Lattice Boltzmann Method," *Modelling and Simulation in Materials Science and Engineering*, pp. 1 - 17, January 2013.

[41] G. E. Gazza, Fundamentals of Sintering in Engineered Materials Handbook, vol. 4 ASM International, 1991, pp. 296 - 303.

[42] C. Göbl, and J. Faltenbacher, "Low Temperature Sinter Technology Die Attachment for Power Electronics Applications," in *Proc. International Conference on Integrated Power Electronics Systems (CIPS),* pp. 1 - 5, March 2010.

[43] Y. J. Nam and J. R. Lead, "Manufactured nanoparticles: An overview of their chemistry, interactions and potential environmental implications," *Science of the Total Environment*, vol. 400, no. 1 - 3, pp. 396 - 414, August 2008.

[44] E. Ide , S. Angata, A. Hirose, K.F. Kobayashi, "Metal-metal bonding process using Ag metallo-organic nanoparticles," *Acta Materialia Journal* vol. 53, no. 8, pp. 2385 - 2393, April 2005.

[45] H. Jiang, K. S. Moon, H. Dong, F. Hua, and C. P. Wong, "Size-dependent melting properties of tin nano-particles," *Chemical Physics Letters*, vol. 429, nos. 4 - 6, pp. 492 - 496, October 2006.

[46] N. B. Bell, C. B. DiAntonio, and D. B. Dimos, “Development of conductivity in low conversion temperature silver pastes via addition of nanoparticles,” *Journal of Materials Research,* vol. 17, no. 9. pp. 2423 - 2432, 2011.

[47] H. Ogura, M. Maruyama, R. Matsubayashi, T. Ogawa, S. Nakamura, T. Komatsu, H. Nagasawa, A. Ichimura, and S. Isoda, “Carboxylate-Passivated Silver Nanoparticles and Their Application to Sintered Interconnection: A Replacement for High Temperature Lead-Rich Solders” *Journal of Electronic Materials*, vol. 39, no. 8, pp. 1233 - 1240, May 2010.

[48] S. J. Zhao, S. Q. Wang, D. Y. Cheng, and H. Q. Ye, “Three Distinctive Melting Mechanisms in Isolated Nanoparticles,” *Journal of Physical Chemistry,* vol. 105, pp. 12857–12860, November 2001.

[49] J. G. Bai, T. G. Lei, J. N. Calata, G.Q. Lu, “Control of Nanosilver Sintering Attained Through Organic Binder Burnout,” *Journal of Materials Research,* vol. 22, no. 12, pp. 3494 - 3500, December 2007.

[50] J. G. Bai, Z. Z. Zhang, J. N. Calata and G-Q. Lu, “Low-Temperature Sintered Nanoscale Silver as a Novel Semiconductor Device-Metallized Substrate Interconnect Material,” *IEEE Transactions on Components and Packaging Technologies*, vol. 29, no. 3, pp. 589 - 593, 2006.

[51] Z. Zhang, “Processing and Characterization of Micro-scale and Nanoscale Silver Paste for Power Semiconductor Devices Attachment,” PhD Thesis, Virginia Polytechnic Institute and State University, Blacksburg, Virginia, September 2005.

[52] C. Buttay, A. Masson, J. Li, M. Johnson, M. Lazar, C. Raynaud, H. Morel. “Die Attach of Power Devices Using Silver Sintering Bonding Process Optimisation and Characterization,” in *Proc. High Temperature Electronics Network (HiTEN)*, pp. 1 - 7, 2011.

[53] A. Masson, C. Buttay, H. Morel, C. Raynaud, S. Hascoet and L. Gremillard.“High-Temperature Die-Attaches for SiC Power Devices,” in *Proc. 14th European Conference on Power Electronics and Applications (EPE)*, 2011.

[54] W.Sabbah, R. Riva, S. Hascoët, C. Buttay, S. Azzopardi, E. Woirgard, D. Planson, B. Allard and R. Meuret, “Evaluation of silver-sintering die attach,” in *Proc. International Conference on Integrated Power Electronics Systems (CIPS)*, March 2012, pp. 1 - 7.

[55] S. Soichi, and K. Suganuma, “Low-Temperature and Low-Pressure Die Bonding Using Thin Ag-Flake and Ag-Particle Pastes for Power Devices,” *IEEE*

*Transactions on Components, Packaging and Manufacturing Technology*, vol. 3, no. 6, pp. 923 - 929, June 2013.

[56] L. A. Navarro, Xavier Perpiñà, P. Godignon, J. Montserrat, V. Banu, M. Vellvehi, and Xavier Jordà, "Thermomechanical Assessment of Die-Attach Materials for Wide Bandgap Semiconductor Devices and Harsh Environment Applications," *IEEE Transactions on Power Electronics*, vol. 29, no. 5, pp. 2261 - 2271, May 2014.

[57] L. A. Navarro, X. Perpiñà, M. Vellvehi, D. Sánchez and X. Jordà, "Sintering Process Analysis for Die-Attach of Power Packages for High Temperature Applications based on Silver Nano-Particles," in *Proc. XX Congreso Internacional Anual de la SOMIM*, September 2014, pp. 1-10.

[58] G-Q. Lu, J. N. Calata, and T. G. Lei, "Low-Temperature Sintering of Nanoscale Silver Paste for Power Chip Attachment," in *Proc. International Conference on Integrated Power Systems*, pp. 1 - 5, 2008.

[59] K. Sweatman, T. Nishimura, and T. Komatsu, "A NANO SILVER REPLACEMENT FOR HIGH LEAD SOLDERS IN SEMICONDUCTOR JUNCTIONS," in *Proc. SMTA Pan Pacific Symposium Conference*, January 2013.

[60] C. Fruh, M. Gunther, M. Rittner, A. Fix and M. Nowottnick, "Characterisation of silver particles used for the Low Temperature Joining Technology," *Electronic System-Integration Technology Conference (ESTC)*, September 2010, pp. 1 - 5.

[61] J. Jiu, K. Murai, K. Kim and K. Suganuma, "Synthesis of Ag nanorods and application to soft die attaching" in *Proc. 2nd IEEE International Interdisciplinary Conference on Portable Information Devices and the 7th IEEE Conference on Polymers and Adhesives in Microelectronics and Photonics*, 2008, pp. 1 - 5.

[62] G.-Q. Lu, W. Yang, Y.-H. Mei, X. Li, G. Chen and X. Chen, "Mechanism of Migration of Sintered Nanosilver at High Temperature in Dry Air for Electronic Packaging," *IEEE Transactions on Device and Materials Reliability*, vol. 14, no. 1, pp. 311 - 317, March 2014.

[63] S. Krishnan, A. Haseeb, and M. R. Johan, "Preparation and Low-Temperature Sintering of Cu Nanoparticles for High-Power Devices" *IEEE Transactions on Components, Packaging and Manufacturing Technology*, vol. 2, no. 4, pp. 587 - 592, April 2012.

[64] V. R. Manikam, K. A. Razak, and K. Y. Cheong, "Sintering of Silver-Aluminum Nanopaste With Varying Aluminum Weight Percent for Use as a High-

Temperature Die-Attach Material," *IEEE Transactions on Components, Packaging and Manufacturing Technology*, vol. 2, no. 12, pp. 1940 - 1948, December 2012.

[65] V. R. Manikam, K. A. Razak, and K. Y. Cheong, "Reliability of sintered $Ag_{80}$-$Al_{20}$ die attach nanopaste for high temperature applications on SiC power devices," *Microelectronics Reliability,* vol. 53, no. 3, pp. 473 - 480, March 2013.

[66] K. S. Tan and K. Y. Cheong, "Physical and Electrical Characteristics of Silver-Copper Nanopaste as Alternative Die-Attach," *IEEE Transactions on Components, Packaging and Manufacturing Technology*, vol. 4 , no. 1, pp.8 - 15, January 2014.

[67] J. H. Nadler, K. A. Ledford, H. M. Harris and B. K. Wagner, "Ag/Diamond Composite Shims for HPA Thermal Management," in *Proc. CS MANTECH Conference,* May 2013.

[68] H. Schwarzbauer, "Heat-Conducting Adhesive Joint with an Adhesive-filled, Porous Heat Conductor," United States Patent US6823915B2, Siemens AG, November 2004.

[69] V. R. Manikam and E. N. Tolentino, "Sintering of Ag paste for power devices die attach on Cu surfaces," in *Proc. IEEE Electronics Packaging Technology Conference* (EPTC), 2014, pp. 94 – 98.

[70] I. J. Rasiah, "Electrically Conductive Thermal Interface," United States Patent, US 7,083,850 B2, August 2006.

# CHAPTER 4 Ag Nano-particles Sintering Process

## 4.1. Introduction

This chapter explains the sintering process and the experimental set-up developed for manufacturing sintered Ag die-attach layers, as well as the required assessment methodology developed in the framework of the present research work in order to characterize different Ag pastes. This previous characterization gives useful indications for modifying the thermal profiles provided by the paste manufacturer and is based on physical analysis of the particles and the organic solvents (Scanning Electronic Microscopy SEM, Thermal Gravimetric Analysis TGA and Differential Thermal Analysis DTA). On the other hand, the results presented in the next chapters about Ag sintering will be based on the experimental studies obtained on test vehicles. The main characteristics and elements of such test vehicles will also be explained in this chapter, with special focus on the main thermo-mechanical properties of the different elements (dice, die-attach and substrates). Finally, an in depth explanation of the experimental set-ups and processing steps developed for implementing the different test vehicles (screen printing, drying and sintering under pressure) will also be described.

## 4.2. Ag Nano-Particles Paste Characterization

In this work, the K-series commercially available Ag paste from the NBE Tech company [1] has been extensively used, although some results are also presented for the Nanotach-X paste from the same company [2]. Each kind of paste requires different temperature processing profiles depending on its constitutive elements (organic solvents and particles) and the manufacturer recommends suitable temperature profiles, including the drying, sintering and cooling phases. Nevertheless, the details about the paste composition are usually confidential and little information is available for the end user to introduce modifications in the suggested process. For this reason, we made a physical analysis of the pastes, providing useful data in order to optimize the different processing steps for a given final application. The methodology developed for this kind of analysis would be applied to other pastes in future researches.

Let's first study the temperature profiles suggested by the manufacturer. These profiles are proposed for die-attach applications with the fresh paste layer applied between chip and substrate. This drying configuration is mainly suitable for relatively low area dice (up to 3 x 3 mm$^2$), as it will be discussed more in detail further on. Figure 4.1 shows the temperature profile proposed for the K-type paste that starts at room temperature with the drying phase (where the organic solvents vaporize) made of three successive steps at 50 ºC, 100 ºC and 150 ºC with heating rates of 3 ºC/min in the first and second step and 5 ºC/min for the third step. Then, the sintering phase starts with a faster temperature increase up to the sintering temperature (around 280ºC), which is kept constant for about 10 minutes (sintering time). In this phase, pressure can be applied in order to improve the densification and the adherence between surfaces (die and substrates). Finally, the sample is cooled down to room temperature. All this process is performed in air ambient.

B

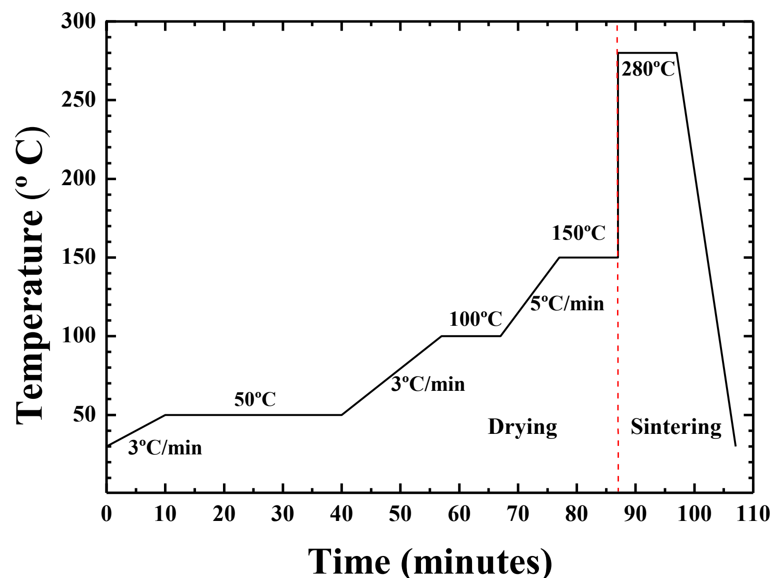


**Figure 4.1. Temperature profile for the K-series Ag nano-particles sintering paste.**

Figure 4.2 shows the temperature profile recommended for the Nanotach-X paste. In this case the drying phase begins from room temperature up to reaching 260 ºC with a heating rate between 5 to 7 ºC/min. The sintering phase is set at 260 ºC with a sintering time between 10 to 30 minutes and in principle any pressure is required for this paste. Finally, the sample is cooled down to room temperature. The two profiles show significant differences in both, drying and sintering phases. The Nanotach-X

drying is included in a single heating-up phase, obtaining the same effects than the 3 steps of the K-series paste. The Nanotach-X requires also 20ºC less than the K-series during the sintering phase but longer sintering times. These differences depend on the components of the two pastes.

C

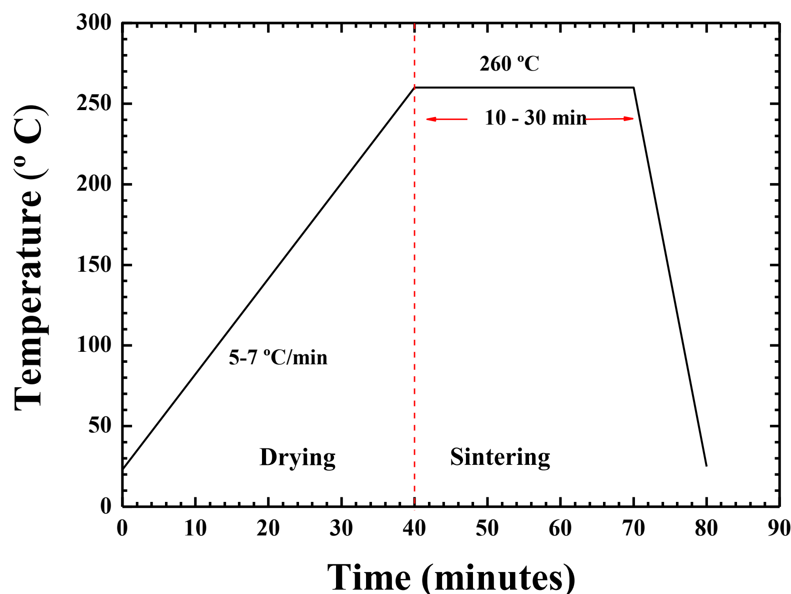


**Figure 4.2. Temperature profile for the Nanotach-X Ag nano-particles sintering paste.**

In order to study the particles structure and to measure the particle size of each paste, a drop of paste was applied and spread onto Ni plated and Si substrates (Ag nano-particles don't attach to Ni and Si surfaces). After that, the samples were dried at lower temperatures than specified in the datasheets and then, they were observed with a SEM system. Figure 4.3(a) shows a general view obtained for the K-series paste and Figure 4.3(b) a more detailed image of the individual particles. The mean particle diameter found for that paste is around 80 nm, with a size distribution between 30 nm and 140 nm. Figure 4.4(a) shows a SEM image of the Nanotach-X paste with the same magnification used in Figure 4.3(a) for the previous paste, wherein the mean particle size is between 800 nm and 2 μm. When looking more in detail at one of the particles (Figure 4.4(b)), it can be observed that they consist of agglomerates of smaller particles (in the 100 nm range). Extremely small particles have been also observed (in the range of the 20 nm and below) and it seems that their function is to favour the development of "necks" between the bigger particles during sintering.

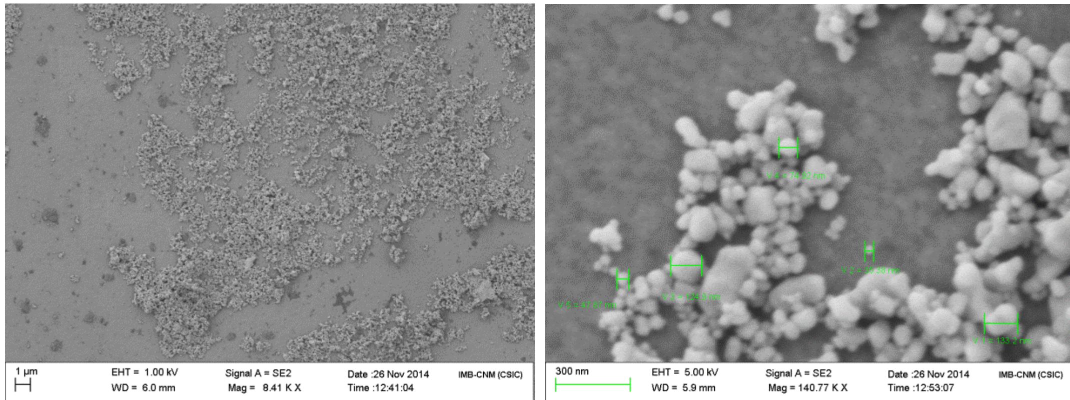


**Figure 4.3. SEM image showing mean size Ag particles of the K-series paste.**

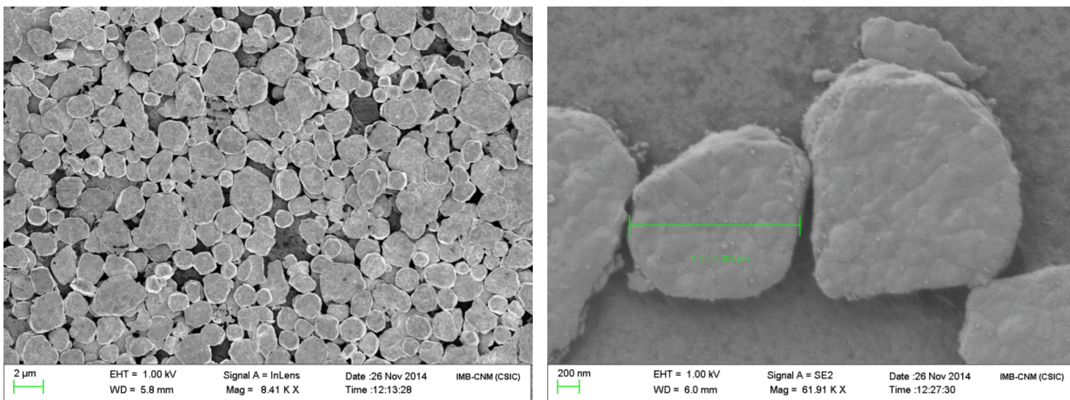


**Figure 4.4. SEM image showing mean size Ag particles of the Nanotach-X paste.**

After the SEM-based inspection of the solid particles, TGA and TDA analysis of the pastes used in this study have been realized in air and Nitrogen atmosphere. Figure 4.5 shows TGA and TDA results in air for the K type paste from 25 ºC to almost 1000ºC, at a heating rate of 10 K/min. This temperature variation slope is in the range of the ramps used during die-attach processing and is also used in many references. The TGA plot (green line) shows a mass loss of 17.4 % that occurs gradually from 25 ºC to 300 ºC. This effect corresponds with the evaporation of all the organic solvents. It can also be observed several effects and reactions in the DSC plot (blue line); in particular the energy variation observed from 200 ºC to 300 ºC (exothermal) is mainly associated with the evaporation of the solvents. Other exothermal reactions in air can be also considered such as oxidation processes causing the decomposition of organic components [11, 4, 5, 3]. At higher temperatures, the DSC peak associated with the Ag particles melting process (endothermal) is clearly visible around 960ºC.

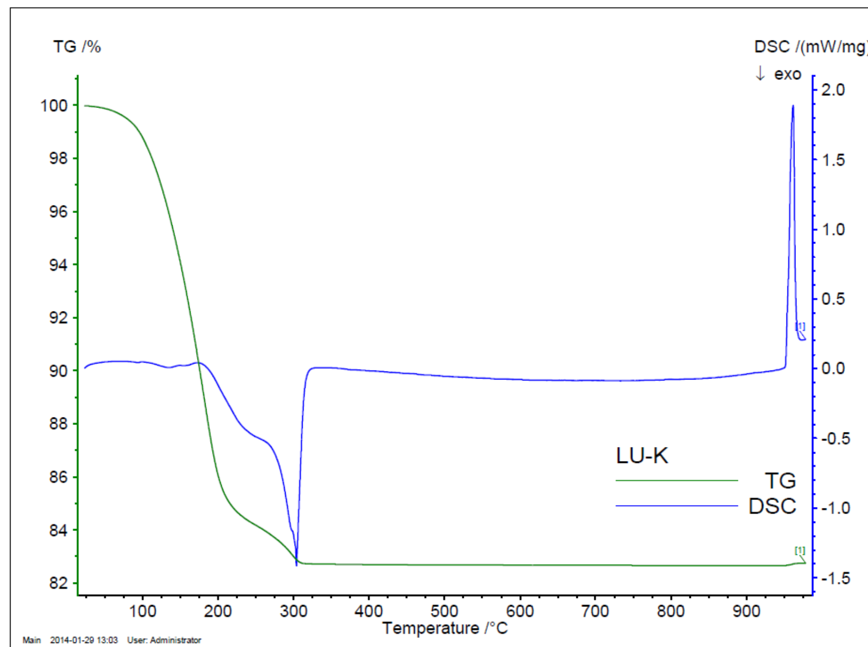


**Figure 4.5. TGA and DSC analysis for paste type K at 10 K/minute in air.**

The atmosphere used in the sintering process is determinant for the densification of the sintered layer and for the adherence between sintered layer and substrate. In fact, in the literature there are some results about the influence of the atmosphere. For instance, reference [4] concludes that sintering of Ag nano-particles in air produced lower shear strength than in nitrogen atmosphere for Cu substrates and Cu dummies. Also, thermo-mechanical (-55°C to 150°C) and thermo-electrical assessment was carried out (with Au-plated dice), wherein the best results was again for $N_2$ atmosphere. It is well-know that the volatilization of the organic components in nitrogen is lower and slower than in air atmosphere [4, 5,]. Nevertheless, the formation of oxide layers is a disadvantage of sintering in air due to the different thermo-mechanical properties of this oxidized layer. On the other hand, on [12, 6] it is described that this oxide layer doesn't interfere in the creation of inter-diffusion layers (between Cu and Ag nano-particles), which is crucial to suitable adherence. Besides, it has also shown the influence of Nitrogen and air atmosphere on adhesion of nano-Ag particles on Cu substrates, wherein the results indicate that in both atmospheres the adhesion presents similar values. Besides, they have demonstrated that some oxidized surfaces ($Cu_2O$, $Al_2O_3$, $SiO_2$) not adhere with nano-Ag particles with sintering temperatures of 230° C and sintering times of 60 minutes. In the same sense, the influence of oxygen pressure on copper substrates has been investigated. In fact, it has been considered that oxygen pressure of 0.08 atm is optimum to oxidize the dispersant. Also, this oxygen pressure is desirable for

preventing excessive oxidation of the copper substrates [6]. The influence of sintering atmosphere (in air and nitrogen), also has been demonstrated for Ag nano-particles (smaller than 50 nm), Cu substrates (38 mm x 27 mm x 1 mm) and Cu dummy chips (7.5 mm x 7.5 mm x 1 mm) both plated with Ag, wherein the results demonstrated that samples sintered with air show better densification than samples sintered in nitrogen atmosphere [8]. For the case of argon atmosphere, this solution presents a less dense sintered layer compared with air or Nitrogen [11], because it doesn't exist a complete volatilization of the organic components.

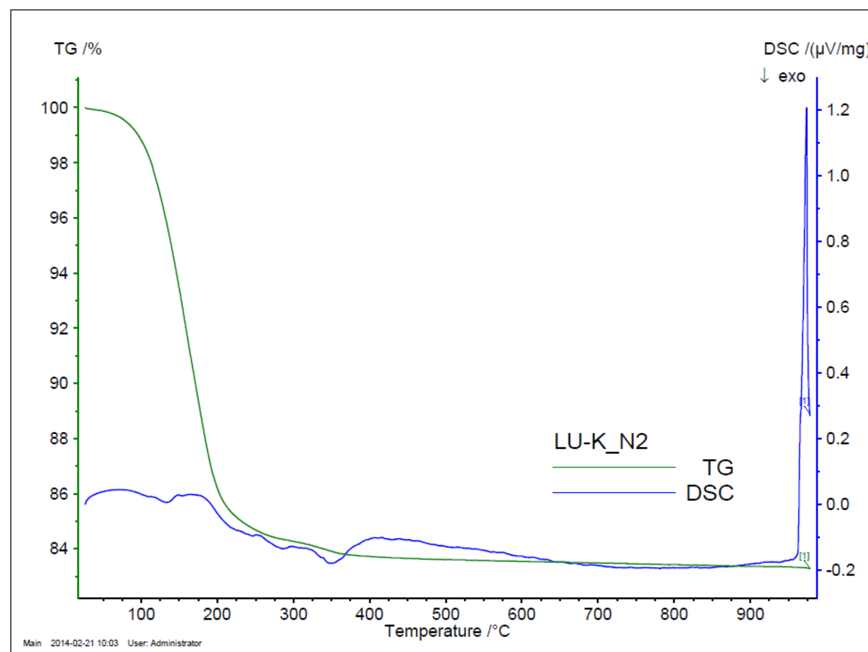


**Figure 4.8. TGA and DSC analysis for paste type K at 10K/minute in $N_2$.**

Concerning the K-series paste used in the present work, Figure 4.8 shows its TGA (green line) and DSC (blue line) analysis from 25 ºC to 1000 ºC with a heating rate of 10 K/min in nitrogen atmosphere. As it was expected from the information available in the literature, there are some differences with the curves in Figure 4.7 performed in air atmosphere. The TGA plot indicates a mass loss of 16.5 % that occurs from 25 ºC to 400 ºC approximately corresponding with the elimination of organics. The complete elimination of organic solvents was achieved at 300 ºC for the test in air. In addition, the DSC curves don't show the prominent exothermic peak at 300 ºC visible in Figure 4.7 in air, associated with a decomposition of the solvents assisted by oxygen. Therefore, it can be concluded that the decomposition of organic components is better in air than in nitrogen for the K-series paste. Figure 4.9 shows the direct TGA comparison between

air and nitrogen atmosphere, where it can be observed that mass loss is approximately 1% major for air atmosphere.

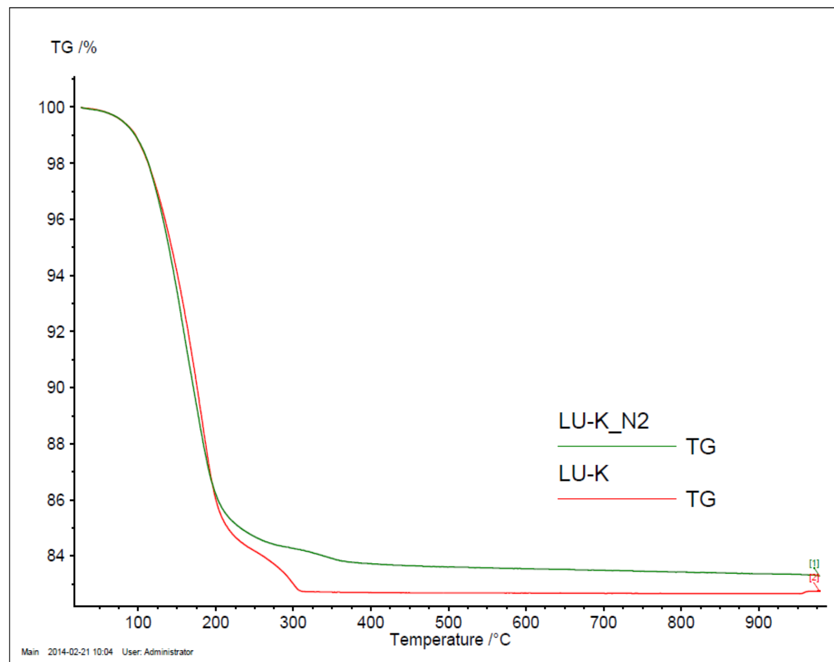


**Figure 4.9. TGA comparison of paste type K at 10K/minute in $N_2$(green) and Air(red) atmosphere.**

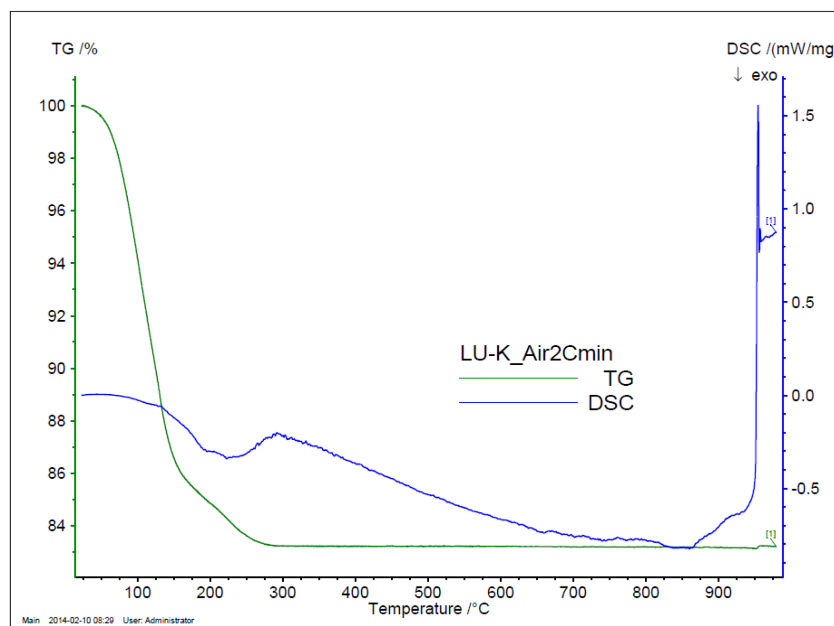


**Figure 4.10. TGA and DSC for paste type K at 2 K/minute in air.**

Figure 4.10 shows TGA and DSC analysis for the paste type K from 25 ºC to 1000 ºC with faster heating rate of 2 K/min in air atmosphere. The TG plot displays a mass

loss of 16.8 % that occurs from 25 ºC to 300 ºC as it was the case for the slower heating rate of 10 K/min. In the case of DSC plot, one can observe a quite different behaviour, indicating that the speed of the thermal profile will have an influence on the densification of the Ag paste.

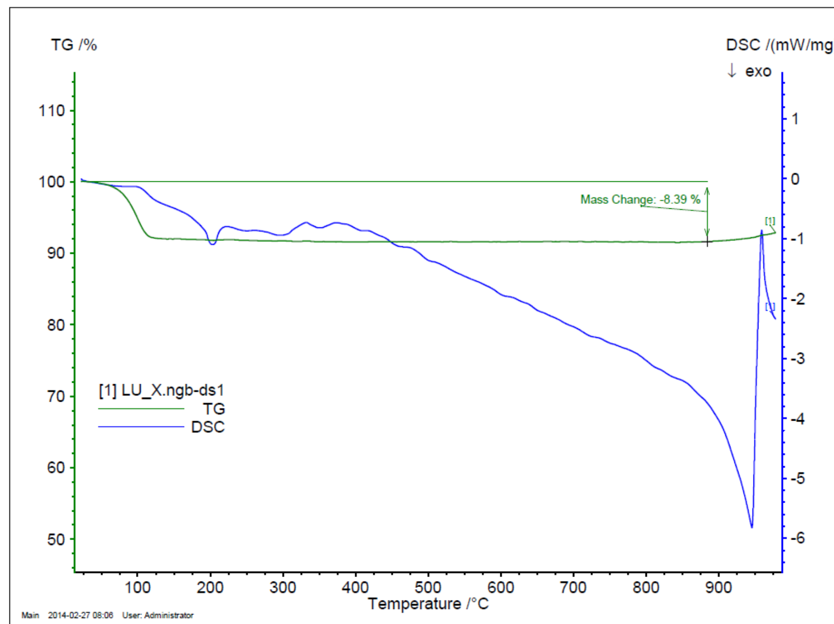


**Figure 4.11. TGA and DSC for paste typeX at 10K/minute in Air.**

Figure 4.11 shows TGA (green line) and DSC (blue line) analysis for paste type X from 25 ºC to 1000 ºC with a heating rate 10 K/min in air atmosphere. The TGA plot displays a mass loss of 8.39 % that occurs from 25 ºC to 125 ºC. This fact clearly indicates a very different composition of the organic solvents from comparing with the K-series paste. Multiple low peaks in the DSC curve indicate small endothermal and exothermal reactions in the solid fraction mainly in the 25 ºC to 450 ºC range with the more significant exothermal reaction observed at 200 ºC. Therefore, the reactions after maximum mass loss (125 ºC), can be associated with the chemical driving force reported in [7], which indicates that there are reactions after the elimination of organic components helping to improve the densification

The aim at drying is vaporize the organic components, and the main involved parameters are the heating rate and the dwell time. In the sintering phase (when the maximum densification is reached) the main involved parameters are the sintering temperature and the sintering time. In fact some researches have studied the influence of

the temperature and time [8] and reported that major sintering temperature showed major densification [9, 10, 11, 12]. Nevertheless, for manufacturing the die-attach temperature lower than 300ºC is desirable in order to avoid residual stresses during die-attach formation. The parameters of the cooling are the heating rate and the dwell time, in fact, in [13] the researches propose a cooling profile for stress relief annealing.

### 4.3. Test Vehicle Development for Die-Attach Assessment

In order to assess the adherence and thermo-mechanical behavior of die-attach materials, a test vehicle representative of a typical power electronic package has been designed. It is based on four semiconductor chips joined to a metal substrate, as highlighted in Figure 4.12.

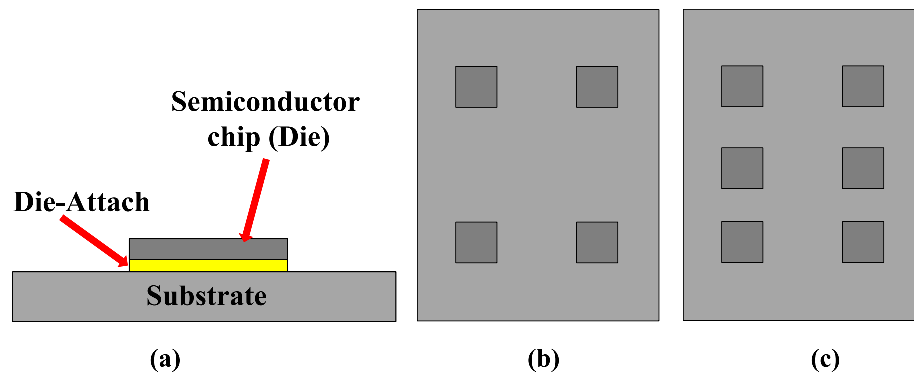


**Figure 4.12. (a) Parts of the test vehicle (schematic cross section). (b) Test vehicle with four dice (top view). (b) Test vehicle with six dice (top view)**

Figure 4.12(a) shows the schematic cross section and its main parts: die, die-attach layer, and substrate. Figure 4.12(b) provides a top view showing the distribution of four dice assembled on the center of each quarter of the substrate for thermo-mechanical assessment. In this configuration, the stress distribution is similar to that obtained in a centered single die assembly, where maximum normal stresses are the same in the four corners [14, 15]. In fact, this test vehicle aims at reproducing the CTE mismatch encountered in usual power electronic packages and evaluating the impact that this parameter should have when working at high temperature. In order to assess other parameters involved in the sintering process for manufacturing the die-attach layer and for increasing the statistical data, a test vehicle with six dice (Figure 4.12(c)) has also been used [16]. The next subsections will discuss more in detail the materials selection

for each test vehicle element. Basically, we have used two semiconductor materials for the dice and a single material as metallic substrate.

### 4.3.1. Devices used for Die-Attach Assessment

The semiconductor material is an essential element in a test vehicle for assessing the behaviour of die-attach materials. For example, different semiconductors will produce different stresses under thermal cycling and will degrade in a different way. Table 4.1 shows the thermo-mechanical properties of the main semiconductors used in different power electronics applications (including RF amplifiers, switching mode power converters, etc.). The maximum demonstrated operation temperatures are depicted in the table, although these values are higher than true maximum working temperatures in practical and commercial systems. Based on this table, it can be observed that diamond has the maximum operating temperature and thermal conductivity to support high power devices in high temperature applications. However, this technology is still very expensive, under development and is not mature for manufacturing functional devices. Consequently, diamond will not be considered in our study.

On the other hand, GaAs and Si are not the best option for high temperature applications due to their relatively low thermal conductivity and low band gap energy. Nevertheless, some Si-based technologies can also be used at high temperature, such as for example the SOI (Silicon On Insulator) devices, suitable for applications up to 250 ºC [17]. GaN devices are now produced on relatively thin layers growth on other semiconductor substrates, typically Si wafers and in a lower proportion, SiC and Sapphire. In this sense, from the die-attach evaluation point of view, the mechanical behaviour of a typical GaN-based device will be very similar to the one of its substrate material.

In the case of SiC, a very high number of crystal polytypes exist, and approximately 200 of them have already been described. The physical properties, e.g., the maximum electronic operating temperature, vary from polytype to polytype. The most common polytypes are 6H–SiC, 4H–SiC, and 3C–SiC. Thermo-mechanically 6H–SiC and 4H–SiC have larger CTE values than 3C–SiC. In addition, the availability of 6H–SiC and

4H–SiC polytypes in bulk wafer form has helped SiC to emerge as a relatively mature wide-bandgap semiconductor technology, and nowadays a number of commercially available RF and power devices are commercially available. In general, 4H–SiC is more used than 6H–SiC because it shows better electrical properties [18, 19].

| Material | Density (Kg/m)$^3$ | Thermal Conductivity (W/m-k) | CTE (ppm/°C) | Maximum demonstrated temperature (°C) | Young Modulus (GPa) | Poisson ratio |
|---|---|---|---|---|---|---|
| **Si** | 2329 [20] | 130 [20] | 2.6 [20]-4.1[21] | 150 [19] | 156 [21]-170 [20] | 0.28 [20] |
| **GaAs** | 5300 [21] | 55 [21] | 5.73 [21] | 350 [19] | 70 [21] | 0.31[22] |
| **3C-SiC** | 3170 [23] | 700 [23] | 2.77 [23] | 600 [19] | - | - |
| **6H-SiC** | 3216[20] | 490 [20]-700 [23] | 4.3[20]-5.12[23] | 700 [19] | 400 [21]-748 [20] | 0.45 [20] |
| **4H-SiC** | 3200 [21] | 370 [21]-700 [23] | 5.1 [21] | 750 [19] | 400 [21] | - |
| **GaN** | 6100 [**¡Error! Marcador no definido.**] | 110 [23]-130 [21] | 4[21]-7.2[23] | > 700 [19] | 181 [21] | - |
| **Diamond** | 3520 [**¡Error! Marcador no definido.**] | 600-2000 [**¡Error! Marcador no definido.** | 0.8 [**¡Error! Marcador no definido.**] | 1100 [19] | - | - |

**Table 4.1. Semiconductor properties.**

In conclusion, for the development of the test vehicles used in this work we focused on Si and SiC dice for the following reasons:

1) The first reason is practical, as the processing technologies of these semiconductors are available at IMB-CNM.
2) The second reason is because both have high temperature power electronics applications already reported in the literature. In addition, Si dice represent a well-established reference technology for comparing to any other option.
3) The third reason is because the aiming of this work is to study mainly thermo-mechanical effects at the die-attach level, although each semiconductor shows

different behaviour, any material gives us information about the mechanical stresses generated by thermal loads. Therefore, can be used for the result's comparison sake.

SiC Schottky diodes (high temperature device) and Si dummy chips (reference case, standard technology) with the same dimensions (300 µm thick and 2.8 × 2.8 mm$^2$ total area) have been used in the test vehicles. Si dummies backside metallization is based on four metal layers of different thicknesses: Al (0.5 µm)/Ti (100 nm)/Ni (500 nm)/Au (200 nm). This structure aims at allowing a good ohmic contact with the semiconductor (Al), ensuring a good adherence (Ti), establishing a diffusion barrier (Ni), and avoiding excessive surface oxidation (Au). On the other hand, SiC diodes have a similar backside multilayer metallization structure, but the first Al layer is replaced by Ni, which offers a much better ohmic contact with SiC. In addition, with the aim at analyzing the influence of die size in the die-attach processes, larger Si dummies (6 × 6 mm$^2$) have also been used.

### 4.3.2. Substrates used for Die-Attach Assessment

In the case of the substrate, the main used materials in practical assemblies are ceramics ($Al_2O_3$, AlN, $Si_3N_4$, BeO) with Cu layers on top and backside. These substrates, are basically used on power modules, they are relatively expensive and show a laborious processing. Other solutions are based on metallic substrates (mainly Kovar, Cu and Cu alloys and Cu metal matrix composites like Cu-Mo and Cu-W), mainly used, for example, for discrete packages such as TO-247, TO-220, etc., where the power semiconductor devices are soldered to a copper flange (acting as substrate, collector terminal and baseplate).

In the case of ceramics, the advantage of alumina ($Al_2O_3$) is its availability at relatively low cost. Beryllia (BeO) is chosen for applications requiring very high thermal conductivity but it is more expensive, potentially toxic and produces greater thermal stresses in the die and the die-attach at elevated temperatures, because of its higher CTE. Aluminium nitride (AlN) is a material that combines a relatively high thermal conductivity with better matched CTE with silicon than either alumina or beryllia.

Cu is often used as heat spreader for high power applications because it provides high thermal conductivity and can be easily machined although its high CTE value is an inconvenient because creates more thermal stresses than, for example, Kovar. Table 3.3 shows the main thermo-mechanical properties of the main substrate materials.

| Material | Density Kg/m$^3$ | Thermal Conductivity W/m-k | CTE ppm/°C | Young Modulus (GPa) | Electrical resistivity Ω-m | Poisson ratio |
|---|---|---|---|---|---|---|
| **Cu [20]** | 8700 | 400 | 17 | 110 | 1.72e-8 | 0.35 |
| **$Al_2O_3$ [24]** | 3970 | 24 | 6 | 310.3 | >1e12 | - |
| **AlN [24]** | 3260 | 150-180 | 4.6 | 310 | >1e12 | - |
| **BeO [24]** | 3000 | 270 | 7.0 | 345 | >1e12 | - |
| **$Si_3N_4$ [24]** | 2400 | 70 | 3.0 | 314 | >1e8 | - |

**Table 3.3. Properties of typical Substrates.**

Among all possible candidates as a metallic substrate, Cu has been selected in this study for developing the test vehicles because it represents the practical case of discrete components, it is easier to process than ceramic substrates and its simulation parameters are relatively well known from the literature. The Cu substrates provide high thermal conductivity (300 W/m·K), easy machinability, and lower cost than ceramic substrates used in packaging technology (such as DBC or direct bonded copper). Besides, the Cu coefficient of linear thermal expansion (17 ppm/◦C) is higher than that of other typical metal baseplates (Kovar: 6 ppm/◦C) or ceramics (Al2O3: 6.8 ppm/◦C; AlN: 4.7 ppm/◦C). Therefore, our test vehicle represents a worst-case scenario from the thermo-mechanical point of view. The dimensions of the Cu substrate are 15 mm × 20 mm × 0.8 mm, which are similar than those of the TO-247 package. Besides, it has been used a TO-257 substrate for some experiments.

Besides, in the last years, it has been observed an increased interest of working with nano-Ag sintering on bare copper substrates in order to avoid their plating with Au or Ag, which add additional manufacturing steps and increase the final costs [11, 12, 4, 25, 26,]. In the same sense, further research for creating sintered die-attach layers with Ag micro- and nano-particles onto Bare Cu substrates have been carried out [5, 27, 28, 29, 30, 31, 32, 33, 34]. In addition, there are some studies wherein Ag nano-particles have

been used to bond Cu wires to Cu pads at low temperatures [35, 36]. Nevertheless, one disadvantage of Cu is the oxidation, because CuO layers grow naturally on the Cu at moderately high temperatures. The thickness of this Cu layers are estimated to range from 23 to 147 nm [37]. Therefore, the surface treatment of the Cu surfaces in order to avoid the oxidation is the main challenge.

In the framework of sintering die-attach process, the substrate surface treatment is a primordial step in order to assure a suitable adherence with the die-attach layer. In fact, it is possible to improve the adherence between Ag layers and bare Cu substrates using diverse methods that remove the CuO layers. Commonly, diluted nitric acid [38] or hydrochloric acid [3, 25, 39, 42] have been used, before dispensing the Ag paste containing the particles onto the substrate. In the same sense, plasma treatment has been used for Ag micro- nano-particles paste on $Al_2O_3$ substrates, plated with Au. In fact, there is a close relationship between surface energy and die-shear force. Therefore, it is recommendable storing the substrate during 1 hour after plasma to achieve die-attach force above 20 $N/mm^2$ [40]. Besides, formic acid treatment has been used for bonding process at low temperature [41]. In the same sense, during sintering process the atmosphere and decomposition of the dispersant [3, 25, 42] are determinant for avoiding CuO layers and, therefore obtaining a suitable adherence.

Although exist an increment in the cost, another solution for avoiding the CuO layers during bonding process is plating the Cu substrate with other metals. For this reason, usually Cu substrates are Au or Ag plated (with and without nickel diffusion barrier plating). Besides, there is an additional reason for using Ag plated substrates, as the Ag nano-particles paste and Ag plated substrates have the same material across the interface and therefore the similar lattice constant. Therefore, it is expected that this configuration bonds easily. In the case of Cu, the lattice constant is 0.3615 nm, for the Au is 0.4079 nm and for the Ag is 0.4086nm [11]. Nevertheless, some researches have demonstrated that Ag nano-particles (around 11 nm), are adhered to Au surfaces better than to Ag surfaces at 5 MPa and sintering temperature of 300 ºC during 5 minutes in air atmosphere. In fact, several materials have also been investigated and the order of the adherence was: Au, Ag, Cu, Ni, Ti and Al, which is matching with the standard free energy value of the oxide formation for each metal. [25].

The results in the literature regarding to CuO layers, have been obtained with some differences on the geometry of test vehicles and different process parameters. For this reason, we have evaluated these approaches with our test vehicle and process. In the case of the surface treatment, it has developed a standard cleaning method for the substrates with the aim at ensure a suitable adherence. The Cu substrate cleaning, starts with acetone (10 minutes in ultrasonic bath) to remove the organic contaminants. Then, surface deoxidization using an etching agent is carried out and a final isopropanol cleaning to remove any remaining impurity (10 minutes in ultrasonic bath). Besides, Cu surface treatment with Ag plasma and formic acid vapour has also been investigated (see chapter 5).

In order to observe the influence of different substrate surface materials on the die-attach process, different plating metals (Ag, Au, Cu, Ni) have been used. In the case of Ag and Ni, substrates have been plated by electro-less chemical bath deposition, whereas the Au plating was performed by sputtering, achieving the deposition of a multiple layer: Ti (100 nm)/Ni(500 nm)/Au(200 nm) [43].

## 4.4. Sintering Process and Experimental set-up for Manufacturing Sintered Die-Attach Layers based on Ag Particles

This section will describe the sintering process and the experimental setup used to manufacture the die-attach layers based on Ag nano-particles.

The first step is cleaning the die and the substrate. The cleaning of the semiconductor dice starts with acetone (10 minutes in ultrasonic bath) to remove the organic contaminants and a final isopropanol cleaning (10 minutes in ultrasonic bath) to remove the traces of the organics solved by the acetone. The substrates follow the same cleaning scheme, but sometimes an intermediate step for surface deoxidization using an etching agent is also included as it was explained in the previous section.

Then, the Ag paste is mixed with the aim at homogenize its content before the application. After that, the Ag paste is deposited on the Cu substrate by screen printing. The corresponding mask is 100 μm thick (see Figure 4.13(a)) and it allows placing a controlled volume of paste for each chip by adjusting the size of the mask hole (see

Figure 4.13(b)). Then, the dies are placed on the fresh paste and at this point the thickness of the paste layer is set to, typically, 60 µm (see Figure 4.13(c). Finally, a thermal treatment is made in two steps: the drying (also called debinding phase) and the sintering.

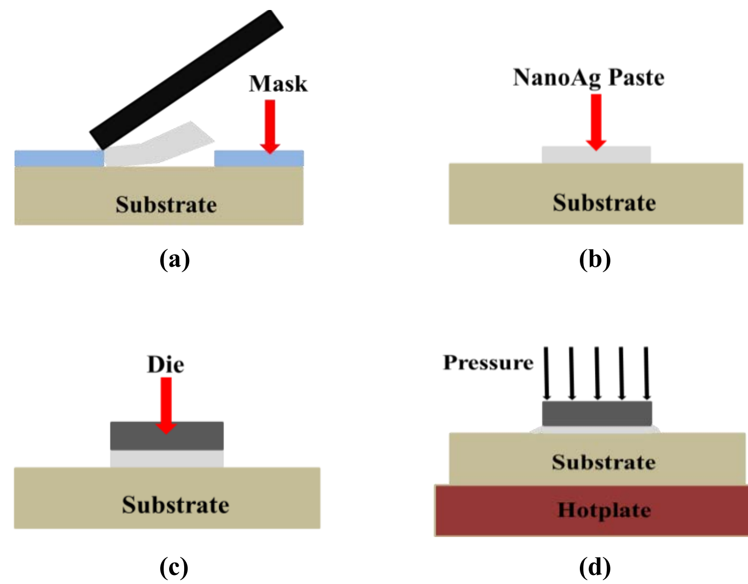


**Figure 4.13. Nano-Ag sintering die-attach process.**

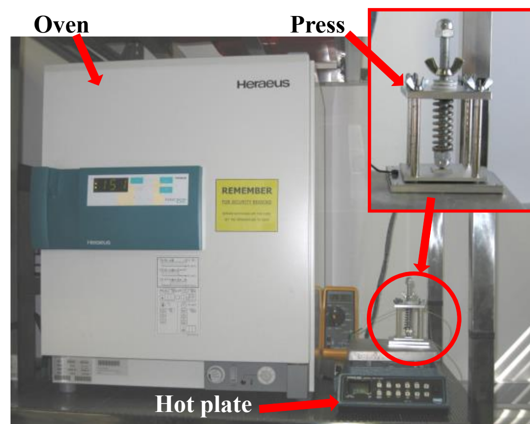


**Figure 4.14. Experimental set-up for nano-Ag sintering die-attach process.**

The drying step consists in the volatilization of the organic components (which coat the particles to be sintered) and the sintering is the step wherein the particles reached the maximum densification. The drying step is formed by several successive steps at different temperatures and depends directly of the component properties (such as organics and particles (size and shape)). After that, the temperature is quickly increased

up to sintering temperature (around 300 ºC). At the same time, a pressure can be applied on the dies, and the sintering process takes place (see Figure 4.13(d)).

In this study, the drying has been realized in an oven under air ambient, while the sintering step is performed on a hot plate with the test vehicle placed on a specifically designed press. Figure 4.14 shows the experimental set-up used to manufacture the die-attach with the K-type paste. The elements are an oven (Heraeus) with maximum temperature of 250 ºC, a hot plate (BT Electronics) with maximum temperature of 400 ºC that is controlled by a compact controller with program function JUMO Dtron 316. The temperature is measure with a K-type thermocouple connected to a four channels thermometer (Data Loger). Finally, also is showed the designed press (which will be described more in depth in the next sections).

### 4.4.1. Screen Printing Methodology

For the screen printing step it is necessary first to mix the Ag paste very well with a metal rod, in order to assure a correct particle distribution, mainly if the paste is stored in a jar. If the paste is stored in syringes a vortex mixer is necessary to homogenize the content [2]. The screen printing is de carried out with a mask that is put onto the substrate, and then the paste is deposited onto the mask and is spread with a squeegee. Finally, the mask is retired and the paste onto the substrate shows the shape of the hole of the mask. This method allows to control the volume of the paste deposited as well as its distribution (shape), allowing also to control the thickness of the final sintered die-attach layer. Figure 4.15 shows the mask used for the screen printing of the Ag pastes used in this work. Whereas Figure 4.15(a) and 4.15(b) show the masks used for test vehicle (used in the analysis of chapter 5), Figure 4.15(c) and 4.15 (d) show the masks used for a TO-257 substrate. The white holes (3.1 mm diameter) are used to hold the mask in a special designed holder with pins. The white squares in Figure 4.15(a) and (b) correspond to the holes allowing dispensing a given volume of paste on the substrate, and in the framework of this work we have used different sizes, although the standard one was squares of 2.5 mm x 2.5 mm. The white square of Figure 4.15(c) used for a TO-257 package is of 2.3 x 2.3 $mm^2$ in order to fix a predefined die-attach thickness. In the case of figure 4.15(d), the white pattern was not used for dispensing the paste but centering the TO-257 case in the press, which will be described in the next section.

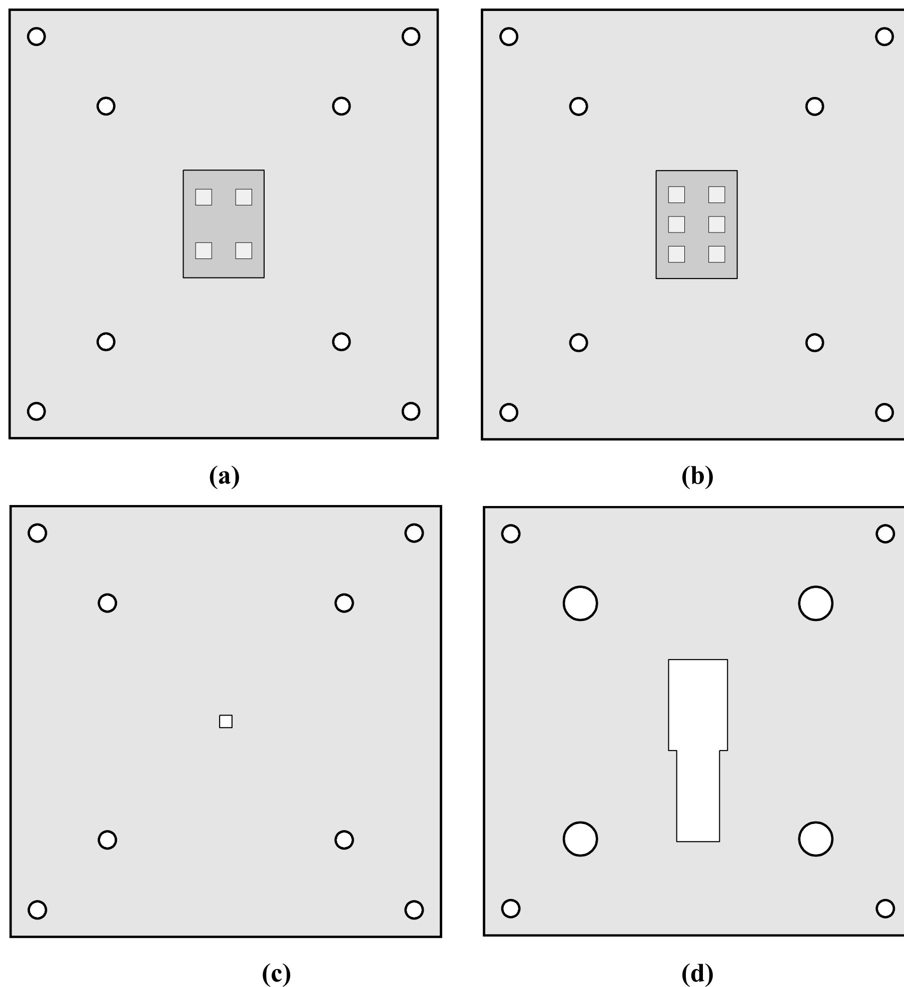


**Figure 4.15. Masks used to screen printing.**

### 4.4.2. Drying Process

In the literature there is a lot of information about the parameters that influence the densification of the sintered bodies. The most common are temperature, time, atmosphere, pressure and, of course, the characteristics of the elements of the pastes (particles and organic components). In fact, the drying step is dependent of the heating rate, dwell time, type of organic components and sintering atmosphere. Besides, the drying step can be carried out with dice or without dice on top of the green paste. In fact, some researchers have demonstrated that the Ag nano-particles paste has better densification without die than with die [8]. In order to evaluate the drying influence, it has been carried out some samples with Cu substrates, Au plated substrates and Au plated Si dice of 6 mm x 6 mm. Figure 4.16 shows C-SAM images, which demonstrated the influence of drying step in the sintering process. Figure 4.16 (a) shows the C-SAM

image of sample with Cu substrate and drying with dice. Figure 4.16 (b) shows the C-SAM image of sample with Au plated substrate and drying with dice. Figure 4.16 (c) shows the C-SAM image of sample with Au plated substrate and drying without dice. This sample showed the most uniform layer, which indicates better densification of die-attach layer. It is important to highlight that the die-shear force reaches values around of 140 kgf. Nevertheless, the evaluation with die-shear test is useless for lager dice because the die-fracture occurs before that the fracture of the sintered layer.

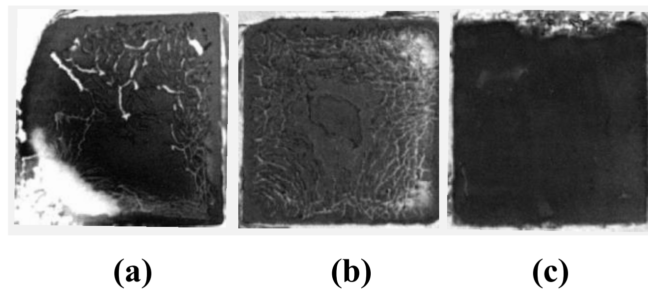

**(a) (b) (c)**

**Figure 4.16. C-SAM images of the sintered nano-Ag layer at 7MPa, 285 ºC, 10 minutes for different substrates. (a) Bare Cu substrate and drying with die. (b) Au plated substrate and drying with die. (c) Au plated substrate and drying without die. Au plated Si die of 6x6 mm$^2$.**

### 4.4.3. Sintering Press Development

Although more details about the effects of sintering pressure on the characteristics of the final Ag layers will be provided in chapter 5, Figure 4.17 shows the die-shear strength mean values for different test vehicles with Ag, Au, Cu and Ni plated substrates sintered at 0 MPa, 285 ºC, 10 minutes and the Ag paste dried with die. As expected, for the case of Ni plated substrates the die-shear force is 0 kgf [6] but the following best results are obtained with Au plated substrates (2.67 kgf) and Ag plated substrates (3.84 kgf). These values are extremely low for dice of 2.8 mm x 2.8 mm (the minimum acceptable value for such die area from MIL STD-750 standard is 5 kgf). Consequently, the sintering process must be enhanced with an additional applied pressure.

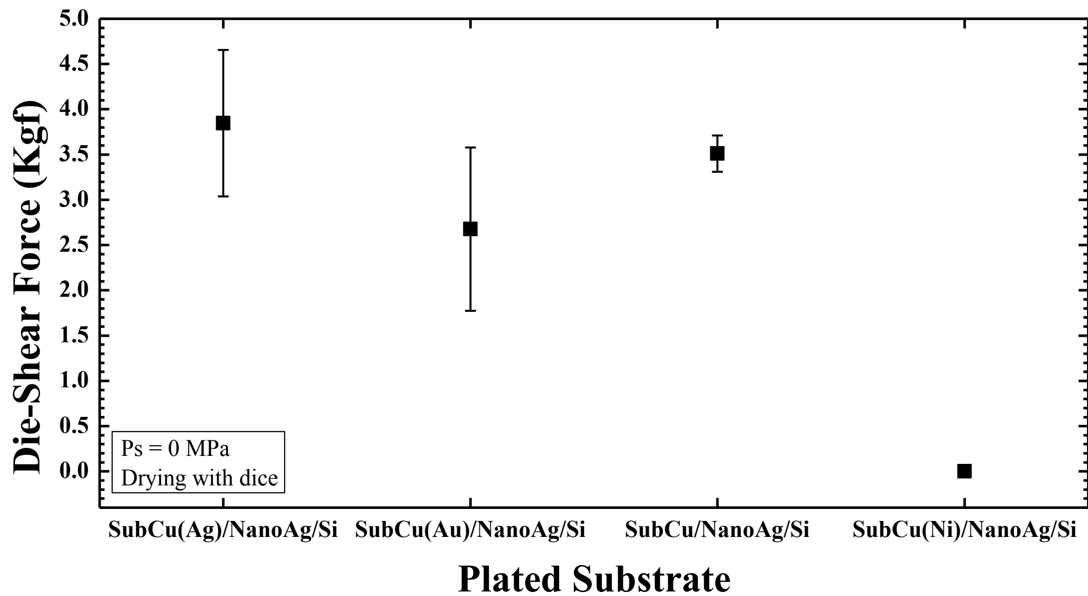

**Figure 4.17. Die-shear force values for different plated substrates at 0 MPa 285 ºC and the drying step with dice. Mean values for samples with two dice. Au plated Si dice have been used.**

Generally, there are three methods for applying pressure to a piece: the quasi hydrostatic pressing, the hot isostatic pressing and the uniaxial pressing [44]. In our case a press was designed for applying a constant uniaxial pressure controlled by a spring. Figure 4.18 schematically shows the press parts, consisting of four main elements. The first one is the base plate wherein the substrate is placed. The plate contains two thermocouples for accurate temperature monitoring. The second press element is an intermediate or mobile plate, which is the responsible for applying the pressure directly on top of the chips. A 75 µm Kapton layer is placed between the plate and the chips in order to avoid semiconductor damage and to assure an even pressure distribution among the dies on the substrate. Besides, the Kapton material was selected due to its low adhesion [12]. Aluminium spacers of different heights can also be placed on top of this plate to adjust the desired pressure. The third part is a stainless steel spring suitable for 300ºC operation [45], compressed against a top plate. This top plate and 4 assembly columns constitute the fourth structural element of the press. Initially, the substrate with the fresh paste and the dies are placed on the base plate, while the spring is compressed against the top plate thanks to a wing-nut and a threaded-rod. When the sintering process begins the spring is released and uniaxial pressure is applied directly to the intermediate plate and to the dice. The pressure can be adjusted to the targeted value through the spring elastic constant, the thickness of the spacers placed over the mobile plate and the length of the assembly columns. After sintering, the system cools down

naturally, so the overall cycle time takes around 2 hours. The final thickness of the sintered Ag layer at this point ranges between 20 μm and 35 μm depending on the applied sintering pressure.

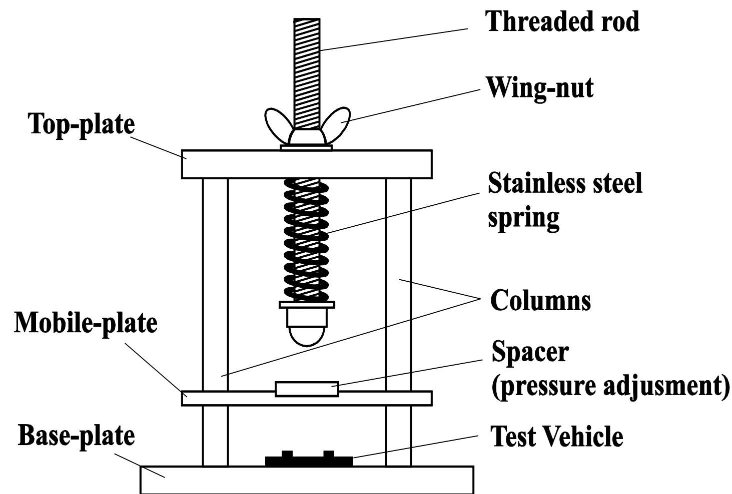


**Figure 4.18. Scheme of the developed press.**

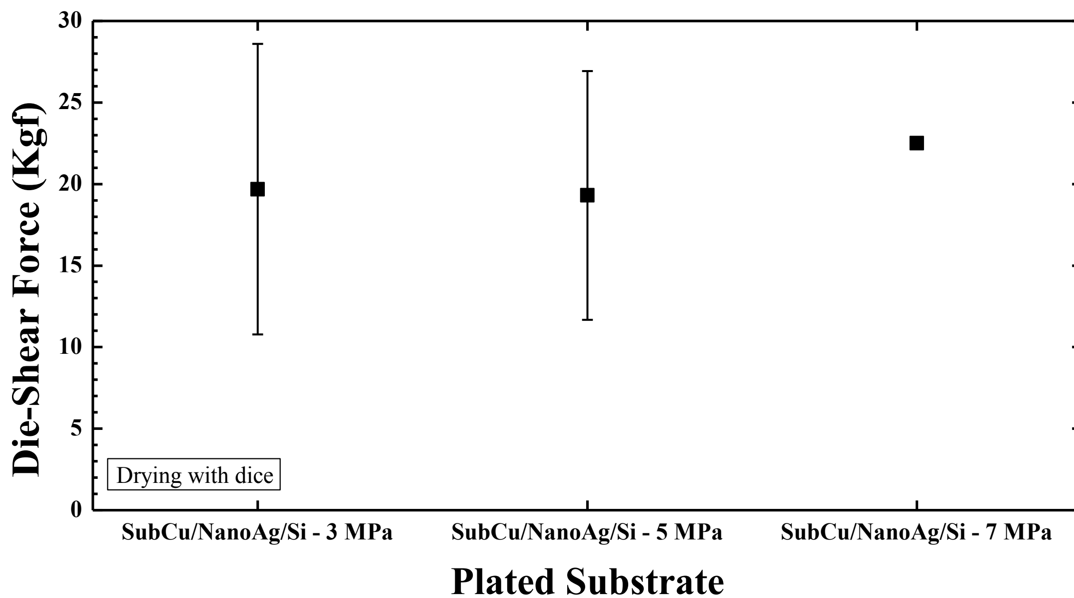


**Figure 4.19. Die-shear force values for different sintering pressures, 285 ºC and the drying step with dice. Au plated Si dice have been used.**

Figure 4.19 shows the die-shear force values of the first experiments for different sintering pressures, 285 ºC, 10 minutes and the drying step with die. Bare Cu substrates and Au plated Si dice (2.8 x 2.8 $mm^2$) have been used. The sintering pressures were 3 MPa, 5 MPa and 7 MPa and, as it can be observed, the die-shear strengths are an order

of magnitude higher than in the same process at 0 MPa. More details about this kind of results are provided in chapter 5.

### 4.5. Conclusions

This chapter presents the sintering process methodology and the experimental set-up for manufacturing sintered die-attach layers. Besides, the Ag pastes used in this study have been characterized. From the TGA and DSC analysis it can be concluded that elimination of organic components in air is better than in nitrogen atmosphere, although this approach can lead to oxidation of critical parts (Cu substrates, for example). The test vehicle used in this work has been designed and described. I includes a substrate, the die-attach layer and four or six dice onto the substrate depending on the kind of tests to be performed (thermal cycling or sintering process set-up). Moreover, the main properties of devices and substrates commonly used to manufacture the test vehicles have been described. The materials selected for this work are: Cu substrate, two types of semiconductors (Si and SiC) and two types of Ag sintering pastes (X and K series from NBE Tech). Other die-attach solder alloys will be also introduced in the thermal cycling tests presented in chapter 6. On the other hand, the brief description of the screen printing step, which is very important for quantifying the amount (volume) of paste used in the process, has been introduced. Then, it has been demonstrated that the drying process is one of the most important steps of the sintering process for assuring suitable densification and adherence of the sintered die-attach layer. Also, it is important to highlight that the assessment (die-shear tests) has been useless for lager dice (6 mm x 6 mm), because the die-fracture occurs before the fracture of the sintered layer. For this reason, further experimental research will be made with smaller dice of about 2.8 mm x 2.8 mm. Finally, the main elements of the press designed specifically for applying pressure during sintering process, has been described.

### 4.6. References

[1] (2012). [Online]. Available: http://www.nbetech.com/products.shtml]
[2] (2014). [Online]. Available: http://www.nbetech.com/products.shtml

[3] E. Ide , S. Angata, A. Hirose, K.F. Kobayashi, “Metal–metal bonding process using Ag metallo-organic nanoparticles,” *Acta Materialia Journal* vol. 53, no. 8, pp. 2385–2393, April 2005.

[4] H. Ogura, M. Maruyama, R. Matsubayashi, T. Ogawa, S. Nakamura, T. Komatsu, H. Nagasawa, A. Ichimura, and S. Isoda, “Carboxylate-Passivated Silver Nanoparticles and Their Application to Sintered Interconnection: A Replacement for High Temperature Lead-Rich Solders” Journal of Electronic Materials, vol. 39, no. 8, pp. 1233- 1240, May 2010.

[5] C. Fruh, M. Gunther, M. Rittner, A. Fix and M. Nowottnick, “Characterisation of silver particles used for the Low Temperature Joining Technology,” *Electronic System-Integration Technology Conference (ESTC)*, 2010, pp. 1 – 5, September 2010.

[6] K. S. Siow, “Mechanical properties of nano-silver joints as die attach materials,” *Journal of Alloys and Compounds,* vol. 514, pp. 6– 19, 2012.

[7] G.-Q. Lu, W. Yang, Y.-H. Mei, X. Li, G. Chen and X. Chen, “Mechanism of Migration of Sintered Nanosilver at High Temperatures in Dry Air for Electronic Packaging,” *IEEE Transactions on Device and Materials Reliability*, vol. 14, no. 1, pp. 311-317, March 2014.

[8] M. Knoerr, A. Schletz, “Power Semiconductor Joining through Sintering of Silver Nanoparticles: Evaluation of Influence of Parameters Time, Temperature and Pressure on Density, Strength and Reliability,” in *Proc. International Conference on Integrated Power electronics Systems,* pp. 1-6, March 2010.

[9] J. G. Bai, T. G. Lei, J. N. Calata, G.Q. Lu, “Control of Nanosilver Sintering Attained Through Organic Binder Burnout,” *Journal of Materials Research* vol. 22, issue 12, pp. 3494–3500, December 2007.

[10] N. B. Bell, C. B. DiAntonio, and D. B. Dimos, “Development of conductivity in low conversion temperature silver pastes via addition of nanoparticles,” *Journal of Materials Research,* vol. 17, issue. 9. pp. 2423-2432, 2011.

[11] Y. Akada, H. Tatsumi, T. Yamaguchi, A. Hirose, T. Morita and E. Ide “Interfacial Bonding Mechanism Using Silver Metallo-Organic Nanoparticles to Bulk Metals and Observation of Sintering Behavior,” *Materials Transactions,* vol. 49, no. 7, pp. 1537-1545, 2008.

[12] S. Joo, and D. F Baldwin, “Adhesion Mechanisms of Nanoparticle Silver to Substrate Materials: Identification,” *Nanotechnology,* vol. 21, no. 5, pp. 1-12, 2010.

[13] L. Jiang, "Thermo-Mechanical Reliability of Sintered-Silver Joint versus Lead-Free Solder for Attaching Large-Area Devices," Master Thesis, Virginia Polytechnic Institute and State University, Blacksburg, Virginia, December 2010.

[14] L. A. Navarro, "Study of Thermomechanical Stress on Die-Attach for High Temperature Power Packaging," Master Thesis, Universidad Autónoma de Barcelona, Barcelona, España, Septiembre 2011.

[15] L. A. Navarro, X. Perpiña, M. Vellvehi, V. Banu, and X. Jordà, "Thermal cycling analysis of high temperature die-attach materials," *Microelectronics Reliability*, vol. 52, no. 9 – 10, pp. 2314–2320, September - October 2012.

[16] L. A. Navarro, X. Perpiñà, M. Vellvehi, X. Jordà, "Silver Nano-Particles Sintering Pro-cess for the Die-Attach of Power Devices for High Temperature Applications," *Sociedad Mexicana de Ingeniería Mecánica*, vol. 4, no. 3, pp. 97-102, September 2012..

[17] P. Hagler, P. Henson and R. W. Johnson, "Packaging Technology for Electronic Applications in Harsh High-Temperature Environments," *IEEE Transactions on Industrial Electronics*, vol. 58, no. 7, pp. 2673 – 2682, July 2011.

[18] B. Ozpineci L. M. Tolbert Oak Ridge National Laboratory "Comparison of Wide-Bandgap Semiconductors for Power Electronics Applications," Oak Ridge National Laboratory, Oak Ridge, Tennessee, pp. 1-26. 2003.

[19] M. R. Werner*,* and W. R. Fahrner*. "*Review on Materials, Microsensors, Systems, and Devices for High-Temperature and Harsh-Environment Applications,*" IEEE Transactions on Industrial Electronics*, vol. 48, no. 2, pp. 249-257. 2001.

[20] COMSOL Multiphysics library of materials properties.

[21] J. Hornberger, A. B. Lostetter, K. I. Olejniczak, T. McNutt, S. M. Lal, and A. Mantooth "Silicon-Carbide (SiC) Semiconductor Power Electronics for Extreme High-Temperature Environments," in *Proc. IEEE Aerospace Conference*, vol. 4, pp. 2538-2555. 2004.

[22] M.G. Pecht. "Handbook of electronic package design". Marcel Dekker, New York, 1991.

[23] J. L. Hudgins, G. S. Simin, E. Santi and M. A. Khan, "An Assessment of Wide Bandgap Semiconductors for Power Devices," in *Proc. IEEE Transactions on Power Electronics*, vol. 18, no. 3, pp. 907-914. 2003.

[24] W.W. Sheng, R.P. Colino, "Power electronic Modules, design and manufacture". CRC press 2005.

[25] M.. Yeadon, J.C. Yang, R.S. Averback, J.W. Bullard and J.M. Gibson, "Sintering of Silver and Copper Nanoparticles on (001) Copper Observed by in-situ Ultrahigh Vacuum Transmission Electron Microscopy," Nanostructured Materials. vol. 10. no. 5, pp. 731-739.1998.

[26] E. Ide, S. Angata, A. Hirose, K. F. Kobayashi, "Bonding of Various Metals Using Ag Metallo-organic Nanoparticles - A Novel Bonding Process Using Ag Metallo-organic Nanoparticles-," *Materials Science Forum*, vol. 512, pp. 383-388, April 2006.

[27] T. G. Lei, J. N. Calata, G. Lu, X. Chen and S. Luo, "Low-Temperature Sintering of Nanoscale Silver Paste for Attaching Large-Area (>100mm2) Chips," *IEEE Transactions on Components and Packaging Technology*, vol. 33, issue 1, pp. 98-104, March 2010.

[28] T. Sünner, T. Behrens and T. Kaden, "Reliability Investigation of Drain Contact Metallizations for SiC-MOSFETs," *Materials Science Forum*, vol. 740-742, pp. 665-668, 2013.

[29] S. Hascoët, C. Buttay, D. Planson, R. Chiriac, d, A. Masson, "Pressureless Silver Sintering Die-Attach for SiC Power Devices," *Materials Science Forum*, vol. 740-742, pp. 851-854, 2013.

[30] A. Masson, C. Buttay, H. Morel, C. Raynaud, S. Hascoet and L. Gremillard,"High-Temperature Die-Attaches for SiC Power Devices," in *Proc. European Power Electronics and Applications Conference*, pp. 1-10, 2011.

[31] C. Buttay, A.Masson, J. Li,M. Johnson, M. Lazar, and C. Raynaud, "Die-attach of Power Devices Using Silver Sintering Bonding Process Optimisation and Characterization," presented at the High Temperature Electronics Network, Oxford, U.K., pp.1-6, 2011.

[32] H. Zheng, D. Berry, J. N. Calata, K. D. T. Ngo, S. Luo, and G. Lu, "Low-Pressure Joining of Large-Area Devices on Copper Using Nanosilver Paste," *IEEE Transactions on Components, Packaging and Manufacturing Technology*, vol. 3, no. 6, pp. 915-922, June 2013

[33] H. Zheng, J. Calata, K. Ngoa, S. Luo, and G. Lu, "Low-pressure (< 5 MPa) Low-temperature Joining of Large-area Chips on Copper Using Nanosilver Paste," in *Proc. International Conference on Integrated Power Electronics Systems (CIPS),* pp. 1-6, March 2012.

[34] W. Schmitt, Tanja Dickel, K. Stenger, "Process and Paste for Contacting Metal Surfaces," United States Patent, US 2009/0134206 A1, May 2009.

[35] H. A. Alarifi, "Ag Nanoparticles and their Application in Low-Temperature Bonding of Cu," PhD Thesis, University of Waterloo, Waterloo, Ontario, Canada, 2013.

[36] A. Hu, J. Y. Guo, H. Alarifi, G. Patane, Y. Zhou, G. Compagnini, and C. X. Xu, "Low temperature sintering of Ag nanoparticles for flexible electronics packaging," *Applied Physics Letters*, vol. 97, no.15 , pp.1-3, 2010.

[37] J. Zhang, S. Xie, X. Wei, Y.J. Xiang and C.H. Chen, "Lithium insertion in naturally surface-oxidized copper," *Journal of Power Sources*, vol.137, no. 1, pp. 88–92, 2004.

[38] D. Wakuda, K.-S. Kim, and K. Suganuma, "Ag Nanoparticle Paste Synthesis for Room Temperature Bonding," *IEEE Transactions on Components and Packaging Technologies*, vol. 33, no. 2, June 2010.

[39] H. Nagasawa, M. Maruyama, T. Komatsu, S. Isoda, and T. Kobayashi, "Physical Characteristics of Stabilized Silver Nanoparticles Formed Using a New Thermal-Decomposition Method," *Physics. State. Solid,* vol.191, no. 1, pp.67–76, May 2002.

[40] J. Kähler, N. Heuck, A. Stranz, A. Waag, and E. Peiner, "Pick-and-Place Silver Sintering Die-attach of Small-Area Chips," *IEEE Transactions on Components, Packaging and Manufacturing Technology*, vol.2, no. 2, pp. 199-207, February 2012.

[41] W. Yang, H. Shintani, M. Akaike, T. Suga "Formic Acid Vapor Treated Cu-Cu Direct Bonding at Low Temperature," in *Proc. International Conference on Electronic Packaging Technology and High Density Packaging*, pp. 1-4, August 2011.

[42] Y. Morisada, T. Nagaoka, M. Fukusumi, Y. Kashiwagi, M. Yamamoto, and M. Nakamoto, "A Low-Temperature Bonding Process Using Mixed Cu–Ag Nanoparticles," *Journal of Electronic Materials*, vol. 39, no. 8, 2010.

[43] L. A. Navarro, X. Perpiñà, M. Vellvehi, D. Sánchez and X. Jordà, "Sintering Process Analysis for Die-Attach of Power Packages for High Temperature Applications based on Silver Nano-Particles," in *Proc. XX Congreso Internacional Anual de la SOMIM*, , pp. 1-10, September 2014.

[44] C. Früh, M. Günther, M. Rittner, A. Fix, and M. Nowottnick, "Characterisation of silver particles used for the Low Temperature Joining Technology," in *Proc. Electronic System-Integration Technology Conference (ESTC)*, pp. 1-5, September 2010.

[45] (2012). [Online]. Available: http://www.muellesbosch.com

# CHAPTER 5 Analysis of the Ag Sintering Process Parameters

## 5.1. Introduction

In chapter 4, in particular in section 4.2 it was described the complete sintering process used to manufacture die-attach layers based on Ag particles. In the present chapter we will describe and analyse the effects of the main sintering process parameters on the properties of the final sintered layer. The parameters that will be analysed are pressure, temperature and sintering time. Additionally, the drying step, which is associated to the manufacture process, will be also evaluated. Besides, the parameters correlated to the substrate condition (surface material, roughness and treatment), will be finally considered.

## 5.2. Influence of the Sintering Pressure

In the present section the influence of the applied sintering pressure on the characteristics of the final Ag sintered die-attach layer will be analysed. In the direction of achieving this goal, FIB-SEM equipment has been used for characterizing the sintered Ag layer (microstructural analysis). From the macroscopic point of view, Ag layer thickness, C-SAM inspection and adherence (die-shear force) tests have also been performed including the failure modes analysis of the test vehicles.

### *5.2.1. Microstructure of the Die-Attach Layer*

In order to analyse the influence of the sintering pressure on the microstructure of the bulk die-attach material, a specific procedure was designed for obtaining individual sintered Ag layers (not attached to any substrate) from the K-type Ag paste. To do that, glass substrates and dice have been used instead of their metallic and semiconductor counterparts. As Ag doesn't attach to the glass, the final result was the mentioned individual Ag layer. With aiming at observe the microstructural changes under pressure on the Ag sintered layer this parameter has been modified from 0 MPa to 11 MPa.

Drying step with die has been used and the rest of the sintering process ($T_s$ = 285 ºC and $t_s$ = 10 min) was the same one described in section 4.2.

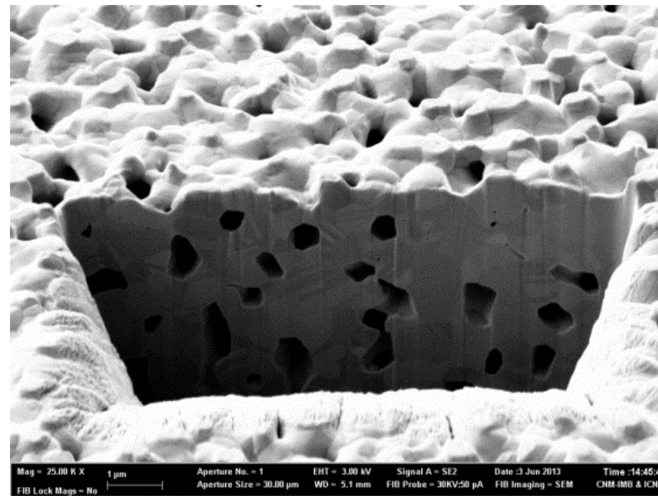


**Figure 5.1. (a) SEM image of a FIB microsection performed on an Ag layer sintered at 0 MPa.**

The microstructural analysis is based on Focused Ion Beam (FIB) microsections performed with a Carl Zeiss G34-1560 XB FIB-SEM workstation, which has been described in section 3.3. Figure 5.1 shows the SEM image of the FIB microsection of the Ag layer sintered at 0 MPa. Voids in the range of 0.5 - 1 μm of diameter can be observed, revealing a relatively poor densification of the material without sintering pressure applied during the process. In fact the porosity is approximately constant in all the Ag volume and can be quantified around 19 %.

For evaluating the impact of higher sintering pressures on the Ag layer microstructure, FIB microsections have been carried out in the edge and in the centre region of the sintered layer, with the aim at study the densification across all the area. Figure 5.2 illustrates a schematic of the sintered layer, indicating with the red rectangles the location of the edge and centre analysed regions. Figure 5.3 illustrates these FIB microsections in the central area for Ag layers sintered at 3 MPa, 7 MPa and 11 MPa. The layers sintered at 7 MPa and 11 MPa (see Figure 5.3(b) and (c)) present higher densification than the layer sintered at 3 MPa (see Figure 5.3(a)) clearly indicating that the evolution of the densification on the centre of the Ag layer depends directly of the sintering pressure. Nevertheless, for the 7 MPa and 11 MPa cases, the densification is very similar. Probably this behaviour is due to fact that the densification is very close to its limit (saturation).

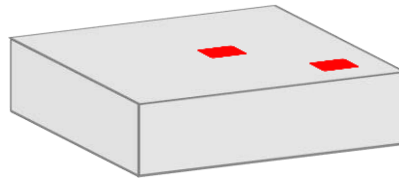

**Figure 5.2. Schematic of an Ag sintered layer indicating the location of the performed FIB microsections in the centre and in the edge regions.**

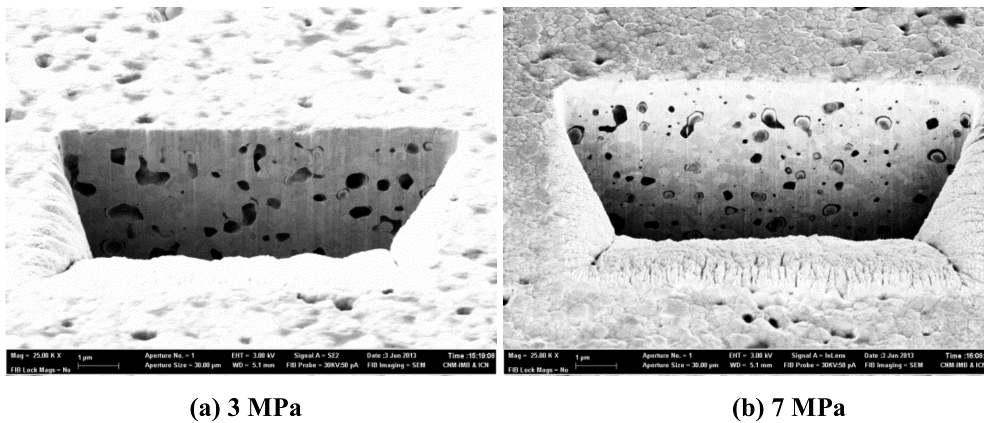

**(a) 3 MPa** **(b) 7 MPa**

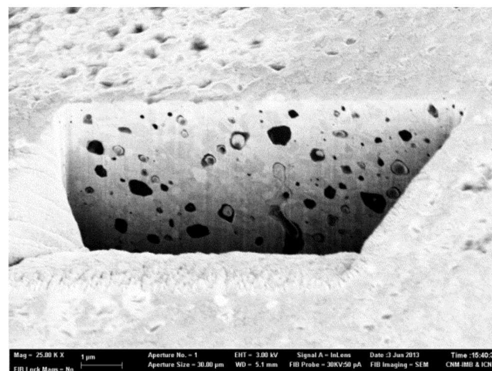

**(c) 11 MPa**

**Figure 5.3. FIB images of Ag sintered die-attach layers in the centre region. (a) Sintered at 3 MPa. (b) Sintered at 7 MPa. (c) Sintered at 11 MPa.**

The images of FIB microsections performed on the edge region of the sintered Ag layer are shown in Figure 5.4. As it was the case for the central zone, the densification is higher with increasing sintering pressure. In particular, the densification shown in Figure 5.4(c) for 11 MPa is clearly higher that those corresponding to 3 MPa (Figure 5.4(a)) and 7 MPa (Figure 5.4(b)). In addition, when comparing these results with those shown in Figure 5.3 for the central zone of the die-attach, it can be concluded that the sintered layers present higher densification in the edge than in the centre. This behaviour is due to the fact that the edge has better contact with the atmosphere during sintering (in this case the air) than the centre, and consequently, the edge has better

elimination (volatilization) of the organic components than the centre [1, 2]. This elimination of organic components of the fresh Ag paste helps joining the particles and the result is an adequate densification of the sintered layer.

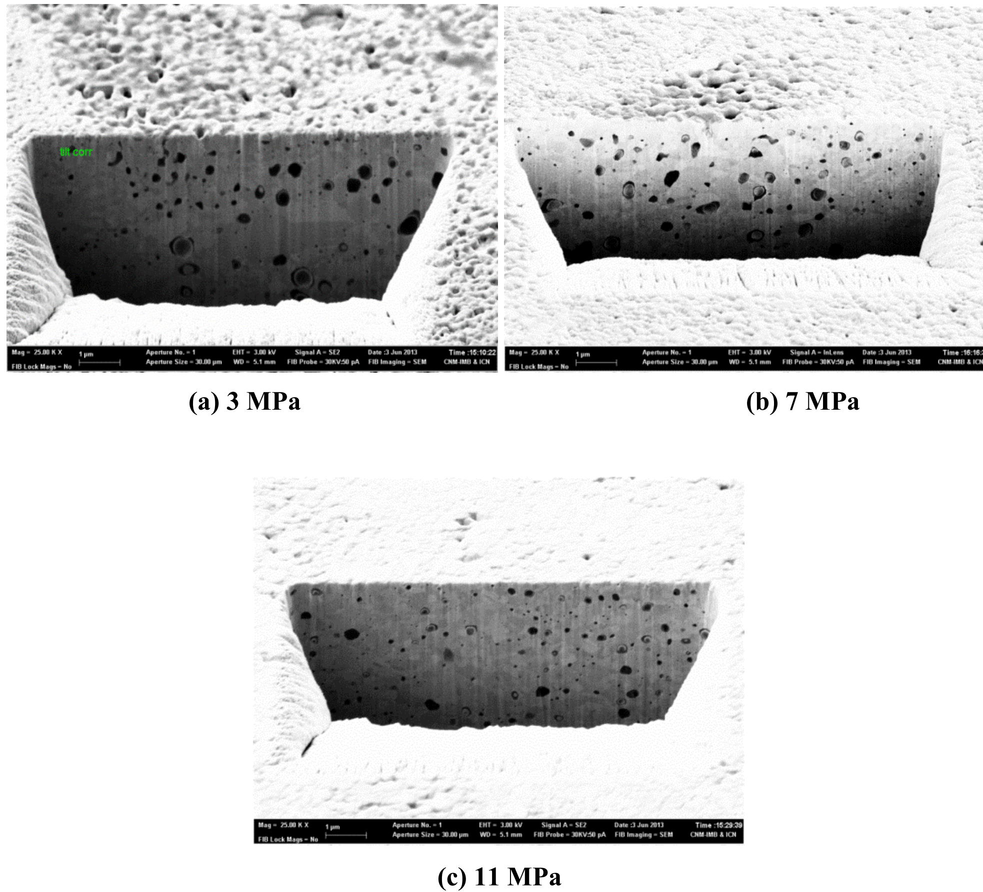

**(a) 3 MPa** **(b) 7 MPa**

**(c) 11 MPa**

**Figure 5.4. FIB images of Ag sintered die-attach layers in the edge region. (a) Sintered at 3 MPa. (b) Sintered at 7 MPa. (c) Sintered at 11 MPa.**

All previous results dealt with the influence of sintering pressure on densification of the Ag layer bulk. Now, we will describe and discuss the pressure influence on the interface between the sintered Ag layer and the Cu substrate. For this purpose, special test vehicles where developed with Cu substrates and glass dummy chips (instead of the Au plated dice of standard test vehicles). Then, FIB microsections were carried out in the centre and in the edge region of the Ag layer joined to the substrate. The images of the microsections are shown in Figure 5.5 for Ag sintered at 3 MPa and in Figure 5.6 for layers sintered at 7 MPa.

The SEM image of the FIB microsection in the centre region for the 3 MPa case is illustrated in Figure 5.5(a) while Figure 5.5(b) corresponds to the microsection in the

edge region. Whereas in Figure 5.5(a) there are many small voids, in Figure 5.5(b) there are less voids but bigger. It can also be observed that the edge region of the die-attach layer has major densification than the centre region as expected from the previous results. Besides, in the edge region there are more adherence zones between the sintered Ag layer and the Cu substrate than in the central region. This behaviour has been also associated with the fact that in the drying step the edge region has more contact with the environment improving the decomposition and elimination of organic components and, consequently, improving the adherence between Ag particles and the Cu substrate. Another relevant aspect that can be observed in Figure 5.5(b) is a thin (around 400 nm) dark layer between the Cu substrate and the sintered Ag. This layer can be in principle associated to Cu - Ag alloys or to oxides. As the dark layer is clearly observed at the edge of the layer but it is practically not present in the centre, the oxide hypothesis seems to be more consistent. This layer will be studied more in detail in section 5.3.1 using EDX analysis.

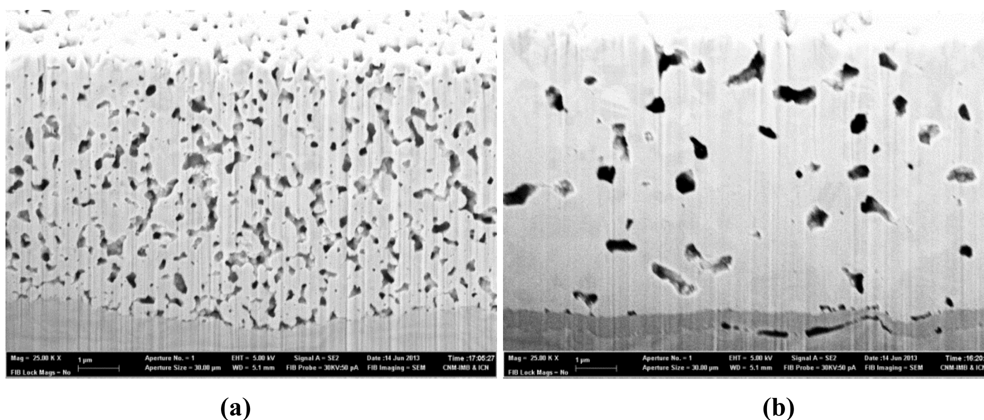

**(a)** **(b)**

**Figure 5.5. FIB images of Ag die-attach layers sintered at 3 MPa. (a) Interface between sintered layer and Cu substrate at the centre region. (b) Interface between sintered layer and Cu substrate at the edge region.**

The SEM images of the FIB sections at the interface between Cu substrate and Ag sintered at 7 MPa are displayed in Figure 5.6. Figure 5.6(a) corresponds to the centre region and Figure 5.6(b) shows the edge region. The behaviour is very similar than for the sample sintered at 3MPa (see Figure 5.5) with any significant difference to be mentioned when increasing the pressure (similar voids, similar detached areas in the Ag/Cu interface, the same intermediate thin layer between Ag and Cu, etc.).

The previous microstructural analysis revealed higher densification with increasing sintering pressure. As the initial amount of fresh paste was kept constant for all the experiments, a final Ag layer thickness diminution is also expected with increasing pressures.

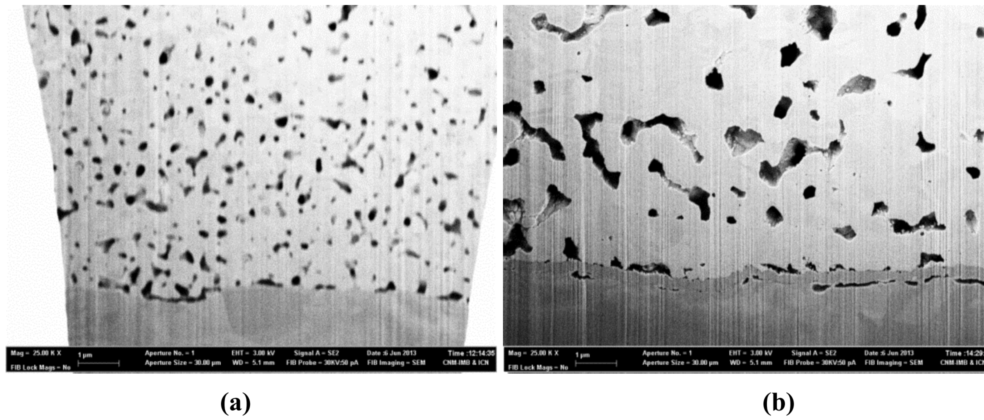

**(a) (b)**

**Figure 5.6. FIB images of Ag die-attach layers sintered at 7 MPa. (a) Interface between sintered layer and Cu substrate at the centre region. (b) Interface between sintered layer and Cu substrate at the edge region**

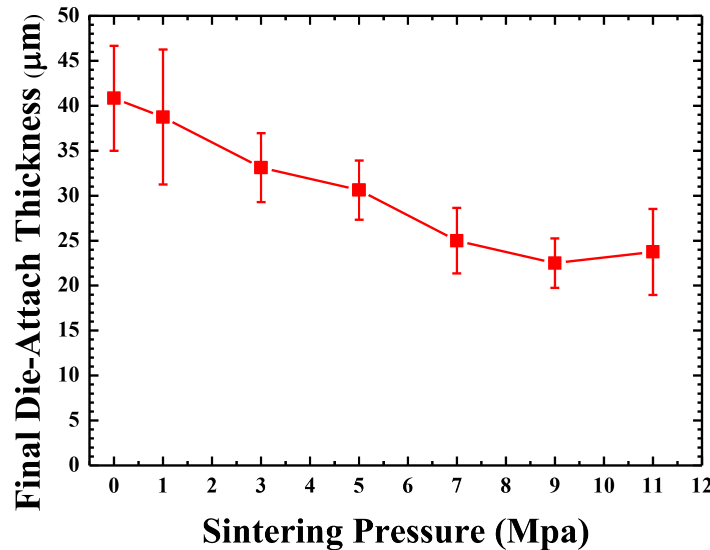


**Figure 5.7. Mean values of final die-attach thickness for different plated substrates sintered at different pressures. Bare Cu substrates and Au plated Si dice have been used.**

Figure 5.7 depicts the mean values of the final die-attach thickness as a function of the sintering pressure from 0 MPa to 11 MPa. It can be observed that from 0 MPa to 7 MPa the die-attach thickness decreases significantly (from 40 µm to 25 µm approximately) when the sintering pressures increases. Nevertheless, one can also observe that the final die-attach thickness has negligible variation after 7 MPa of

applied pressure. This behaviour suggests that after 7 MPa of applied pressure the densification reaches a saturation point with a constant thickness around 25 μm. Regarding to the dispersion values, it can observe that are biggest for 0 and 1 MPa. This comportment suggests that exist less control in the final die-attach thickness, which is related to low pressures with poor densification. Besides, this effect is undesirable in a package due to die-attach degradation during the operation, also is dependent of thickness.

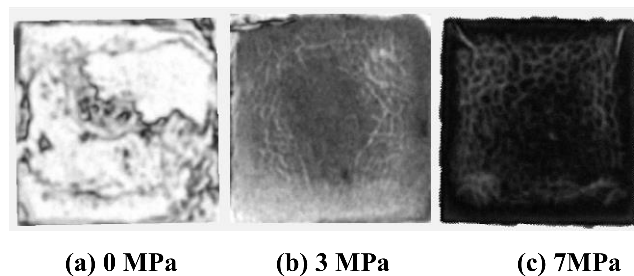

**(a) 0 MPa (b) 3 MPa (c) 7MPa**

**Figure 5.8. C-SAM images of the sintered Ag layer. (a) Sintered at 0 MPa. (b) Sintered at 3 MPa and (c) Sintered at 7 MPa. Bare Cu substrates and Au plated Si dice have been used.**

This final layer thickness analysis was complemented with the C-SAM inspections shown in Figure 5.8. Differences between C-SAM images at different sintering pressures are clear. For instance, at 0 MPa (Figure 5.8(a)) the images reveal a significant degree of detached areas (white zones), in the case of 3 MPa, the detached areas have diminished by the effect of pressure (Figure 5.8(b)) and at 7 MPa the most homogenous layer is found (Figure 5.8(c)).

### *5.2.2. Die-Shear Results for Sintering Pressure Influence*

The microstructural analysis presented above, described the effects of sintering pressure on the densification and joining of the Ag particles and their adhesion with the substrate. In order to obtain a macroscopic and measurable evaluation of the sintering pressure influence on the Ag die-attach joining, the standard test vehicle and methodology described in section 4.2 was applied although the test vehicles sintered at 0 MPa were assembled with six dice instead of four in order to obtain additional statistical data. In all cases, bare Cu substrates with the same range of surface roughness (80 - 150 nm) and Au plated Si dummy dice have been joined with the K-type Ag nanoparticles paste. The applied sintering pressure was increased from 0 to 11 MPa, the

sintering temperature was 285 ºC, the sintering time 10 minutes and the initial drying step was with die.

Figure 5.9(a) shows the variation of die-shear force mean value with the sintering pressure (from 0 MPa to 11 MPa) and Figure 5.9(b) depicts the boxplot graph for the same data. In the presented box plots, apart from the mean values of a set of die-shear tests (little squares), the median value is represented by the horizontal line inside each box (50$^{th}$ percentile), the top and bottom sides of the box correspond to 75$^{th}$ and 25$^{th}$ percentile values respectively and the data outside this percentile values are represented by the whiskers. In both graphs, the mean value of the die-shear force rises almost four times when increasing the sintering pressure from 0 MPa up to 11 MPa. The die-shear increase with higher sintering pressures has been already reported in other works [3, 4, 5, 6 ,7, 8], but the results presented here cover a wider range of pressures and are of direct practical application when using the particular Ag paste involved in our study and processed in the conditions already explained in chapter 4.

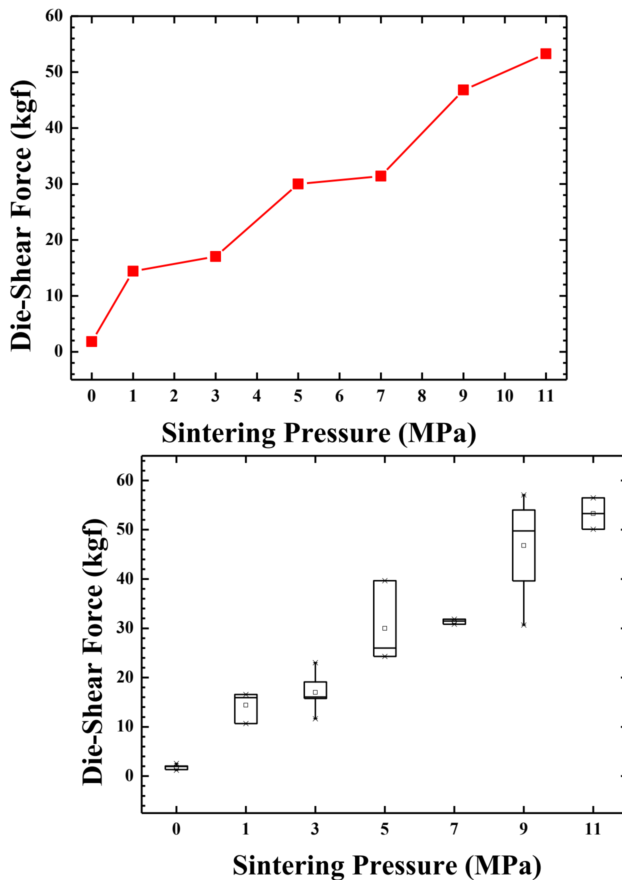


(a)

(b)

**Figure 5.9. Mean values of the die-shear force for different sintering pressures. (a) Mean values corresponding to the experimental data. (b) Box plot of the obtained experimental data.**

The curves in Figure 5.10(a) represent the relationship between the die-shear force and the horizontal displacement of the die during the die-shear tests (see chapter 3, section 3.3), for different die-attach layers sintered between 0 MPa and 11 MPa. As it can be observed, the slopes of the curves (defined as the “die-shear modulus”) are different, suggesting different mechanical properties for the analysed materials. Figure 5.10(b) shows the mean values of die-shear modulus derived from the die-shear tests. From this graph, it can be derived that the die-shear modulus increases almost three times when the sintering pressure increases from 0 MPa to 5 MPa, while from 7 MPa to 11 MPa there are insignificant variations in the die-shear modulus. This behaviour is in good agreement with the results presented for the final die-attach thickness in figure 5.7 and can be explained by the higher densification of the Ag layer at higher pressures, reaching a saturation value. The die-shear modulus and die-attach thickness saturations shown in Figures 5.10 and 5.7 respectively, contrast with the die-shear force increase in the 7 MPa to 11 MPa range observed in Figure 5.9. This fact can be explained because the adherence between the Cu substrate and sintered layer increases while the densification of the Ag bulk remains constant.

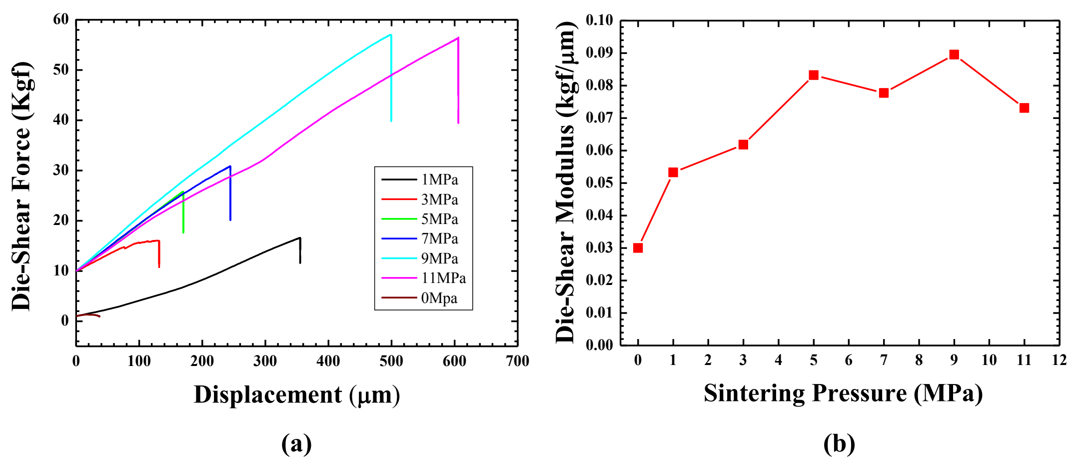


**Figure 5.10. (a) Die-shear curves sintered at different pressures. (b) Mean values of die-shear modulus sintered at different pressures.**

To conclude with the sintering pressure influence analysis, the failure modes of the test vehicles after die-shear test were performed. Figure 5.11(a) shows the pictures for the test vehicles sintered at 0 MPa. In this case, there are scraps (or fragments) of die-

attach in both surfaces (Cu substrate and Au plated die). This behaviour indicates that there is better adherence between die-attach and both surfaces than cohesion among sintered particles (failure mode 2). In the case of the test vehicle in Figure 5.11(b) sintered at 3 MPa, it can be observed that the major part of the sintered die-attach remains on the chip (failure mode 1). This indicates best adherence with the die surface (Au plating) than with the Cu substrate. Finally, the behaviour for the test vehicles sintered at 7 MPa is displayed in Figure 5.11(c), wherein the die is destroyed due to the high adherence to both interfaces and cohesive force among Ag particles in the die-attach layer (failure mode 4). It is important to emphasize that, in samples with lower sintering pressures (0 - 3 MPa), the die-attach mainly comes off during die-shear tests at its interface with the Cu substrate. This contrasts with samples carried out at higher sintering pressures (from 7 MPa to 11 MPa): the breaking mainly occurs in the chip (fracture) and in the die-attach layer. Probably, the explanation for this behaviour is that at low pressures the adhesion between the Ag particles and the Cu surface is obstructed by Cu oxidation, and at high sintering pressures this effect is minimized as Ag is forced to contact the Cu surface.

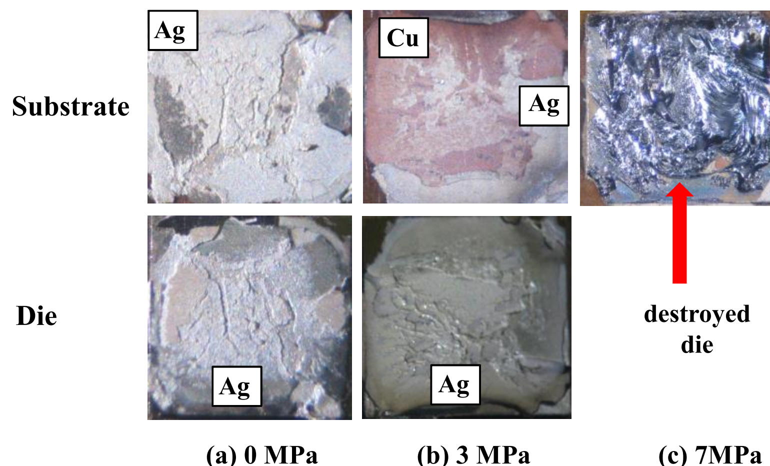


**Figure 5.11. Photographs corresponding to different failure modes of the test vehicles after die-shear test. (a) Sintered at 0 MPa. (b) Sintered at 3 MPa and (c) sintered at 7 MPa. Bare Cu substrates and Au plated Si dice have been used.**

### 5.3. Influence of the Sintering Temperature

In this section, it will be analysed and discussed the microstructure and macroscopic behaviour of different die-attach Ag layers by changing the sintering

temperature. The methodology is very similar than that used in the previous section for the sintering pressure influence analysis, but in this section, EDX measurements have also been performed in order to understand the composition of the thin layer appearing at the Ag/Cu interface (already mentioned in the previous section).

### *5.3.1. Microstructure of the Die-Attach Layer*

In section 5.2.1 the difference in densification between the edge and the centre of the Ag layer at different sintering pressures was clearly observed. A similar behaviour could be expected for processes at different sintering temperatures and, consequently, the microstructure analysis of the Ag layer was undertaken under the same conditions than in section 5.2.1. For this purpose we designed a specific sample providing a sintered Ag layer joined to a Cu substrate. The elements of these samples included a bare Cu substrate and a glass dummy chip, which doesn't join with the Ag. We used the sintering process described in section 4.2, modifying only the sintering temperature from 265 ºC to 325 ºC. The rest of the process parameters were fixed at a sintering pressure of 7 MPa, 10 minutes of sintering time and drying step with die. Figure 5.12 shows the pictures corresponding to two samples processed as it has been explained above for sintering temperatures at 265 ºC (Figure 5.12(a)) and 325ºC (Figure 5.12(b)). As the target was to perform FIB microsections in the sintered Ag, the thickness of the layer was kept relatively thin (below 20 µm) and this fact explains the low homogeneity of the Ag layer noticeable in Figure 5.12, even showing areas without Ag on the Cu substrate. In any case, the zones with the sintered Ag were suitable for the foreseen microstructural analysis of the Ag bulk and of the Ag/Cu interface.

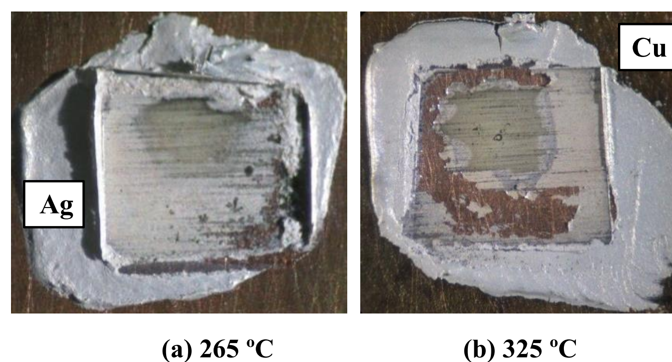


**(a) 265 ºC** **(b) 325 ºC**

**Figure 5.12. (a) Photographs of Ag layers on Cu substrates sintered at 7MPa, 10 minutes and drying step with die. (a) Sintering temperature 265 ºC. (b) Sintering temperature 325 ºC.**

The SEM images of the FIB microsections corresponding to the Ag layer sintered at 265ºC are shown in Figure 5.13(a) for the central region of the layer and in Figure 5.13(b) for the edge region. The sections include the Ag bulk as well as its interface with the Cu substrate. Both pictures present voids in the Ag bulk which result in detached zones at the interface with the Cu surface. Figure 5.13(a) shows the greatest amount of voids in the central area although smaller than those of the edge (Figure 5.13(b)), indicating less densification in the centre of the Ag layer. The better densification in the edge region can be explained in the same way than for the analysis performed in sections 5.2.1: the edge zone has better contact with the environment (air), which helps to complete decomposition and elimination of organic components of the fresh paste. This elimination of organic components improves joining among Ag particles and between Ag and Cu, improving also the densification of the sintered layer. Regarding to the interface between sintered Ag and Cu substrate, the same thin layer already described in section 5.2.1 can be observed, mainly at the edges of the Ag layer. The mean thickness of this layer can be estimated around 200 nm.

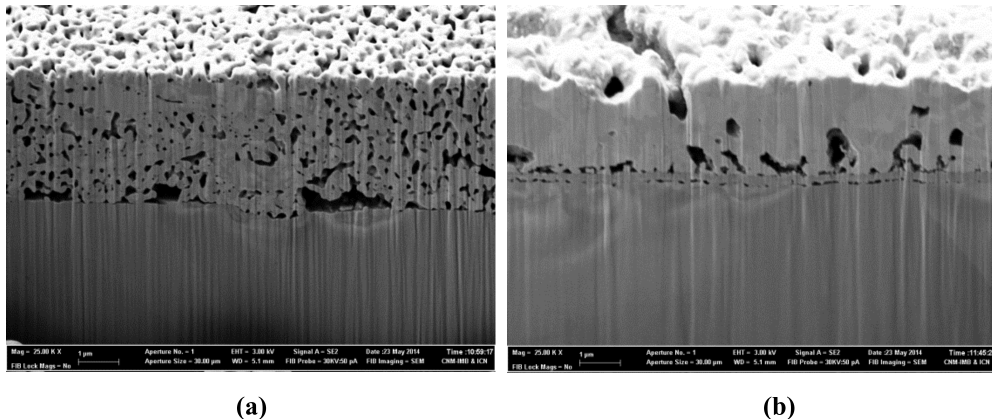

**(a)** **(b)**

**Figure 5.13. SEM images of the FIB microsections performed on Ag layers sintered at 7 MPa, 265 ºC and 10 minutes. (a) At the centre region of the layer. (b) At the edge region.**

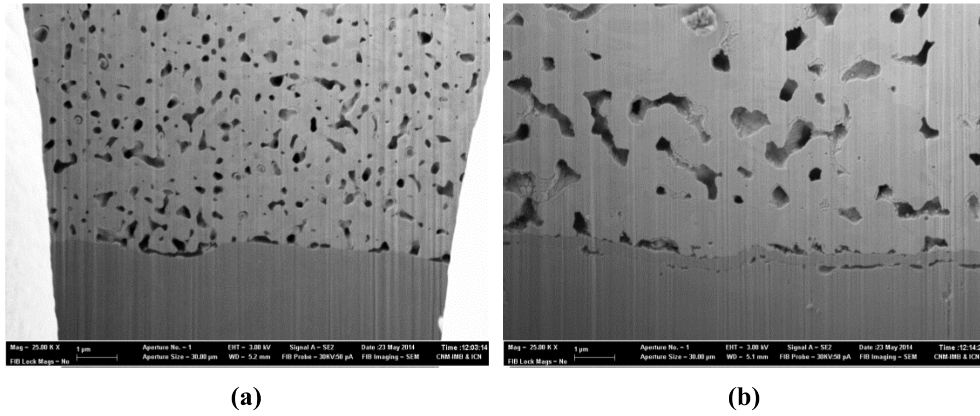

(a) (b)

**Figure 5.14 SEM images of the FIB microsections performed on Ag layers sintered at 7 MPa, 285 ºC and 10 minutes. (a) At the centre region of the layer. (b) At the edge region.**

Figure 5.14 shows the SEM images of the FIB microsections corresponding to the Ag layer sintered at 285ºC. In particular, Figure 5.14(a) shows the microsection performed in the centre region of the Ag layer and Figure 5.14(b) shows the FIB cut performed in the edge region. Qualitatively, the same comments already done for the 265ºC sintering time (Figure 5.13) can be also applied for the 285ºC case, but one can observe a better densification at 285ºC in both, the centre and the edge areas, with less although slightly bigger voids. Concerning the Ag/Cu interface, better adherence (higher contact areas between Ag and Cu) is obtained at 285ºC although the intermediate layer already described in the previous experiments (Figure 5.13 and Figure 5.6) is thicker (approximately around 400 nm). In addition, Figure 5.14(b) also shows that the intermediate layer is best adhered to the Ag side than to the Cu side, where it shows more detached zones.

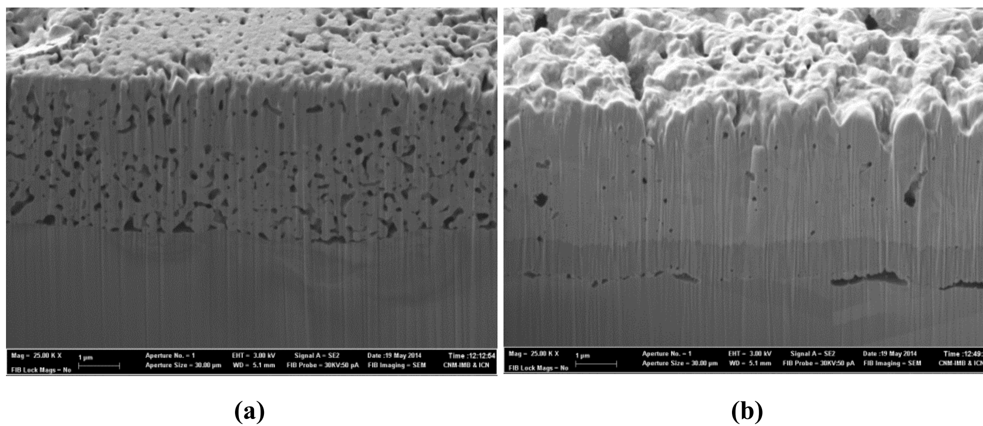

(a) (b)

**Figure 5.15. SEM images of the FIB microsections performed on Ag layers sintered at 7 MPa, 325 ºC and 10 minutes. (a) At the centre region of the layer. (b) At the edge region.**

Finally, the SEM images of the FIB microsections corresponding to the Ag layer sintered at 325ºC are shown in Figure 5.15(a) for the central region of the layer and in Figure 5.15(b) for the edge region. These results confirm the tendencies already observed at lower sintering temperatures: increasing the sintering temperature improves the densification of the Ag layer mainly in the periphery, improves also the adhesion between Ag and Cu and increases the thickness of the intermediate layer appearing in the Ag/Cu interface (around 1 μm in Figure 5.15(b)). In this figure, it is also clear that the intermediate layer is in perfect contact with the Ag while it shows more detached areas at the interface with the Cu.

In principle, looking at the microstructural evolution of the Ag layers with sintering temperature one could expect higher adherence during die-shear tests for higher temperatures. This point will be studied in the next subsection, but before, the composition of the Ag/Cu intermediate layer will be analysed. For this purpose, EDX analysis in the centre and the edge regions of the sintered Ag layer were carried out for each sintering temperature under study (265 ºC, 285 ºC and 325 ºC). A single point EDX measurement is not the best way for understanding the elements involved in the composition of each layer in a given structure, as the single measurement may be subject to local deviations from the main structure. Consequently, several EDX measurements have been performed along a vertical direction in the FIB microsections, providing a profile of the % in weight of each element. The main hypothesis concerning

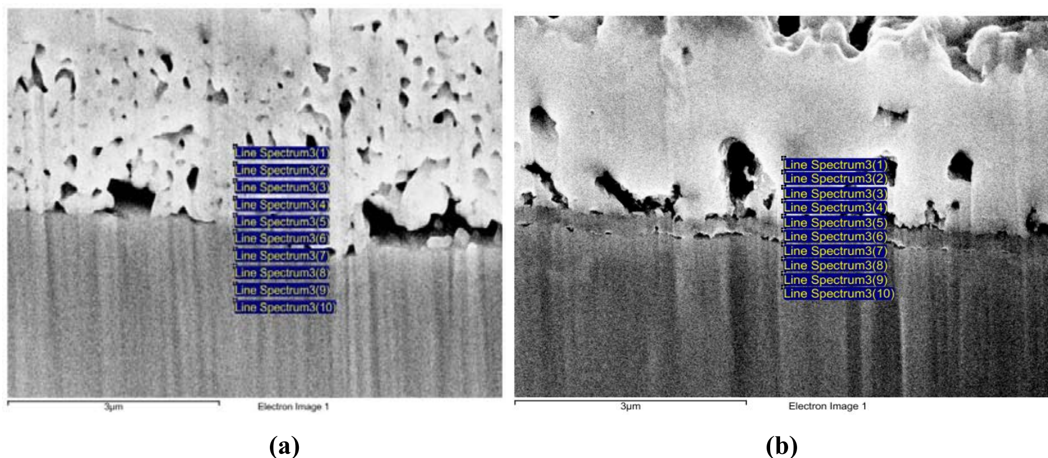


**(a)** **(b)**

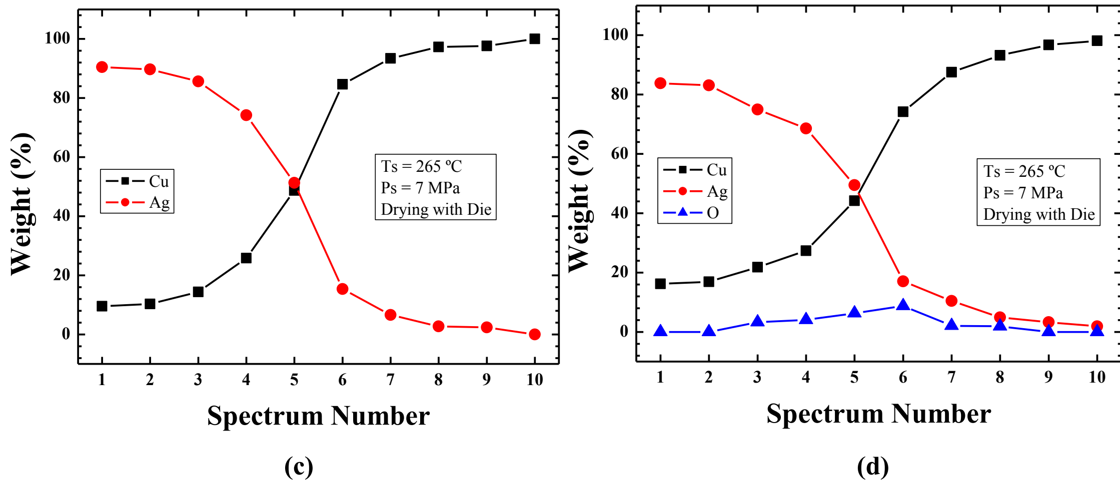


(c) (d)

**Figure 5.16. Spectrum points wherein the EDX analysis has been carried out. (a) In the centre region of the Ag sintered layer. (b) In the edge region of the Ag sintered layer. (c) Weight % for each material in the centre region of the Ag sintered layer. (d) Weight % for each material in the edge region of the Ag sintered layer.**

the composition of the intermediate layer observed in the Ag/Cu interface is that it corresponds with an oxide, as the layer is much more thicker in the periphery (in contact with the surrounding air ambient) than in the centre. Consequently, the selected elements to be monitored in the EDX measurements were Ag, Cu and O.

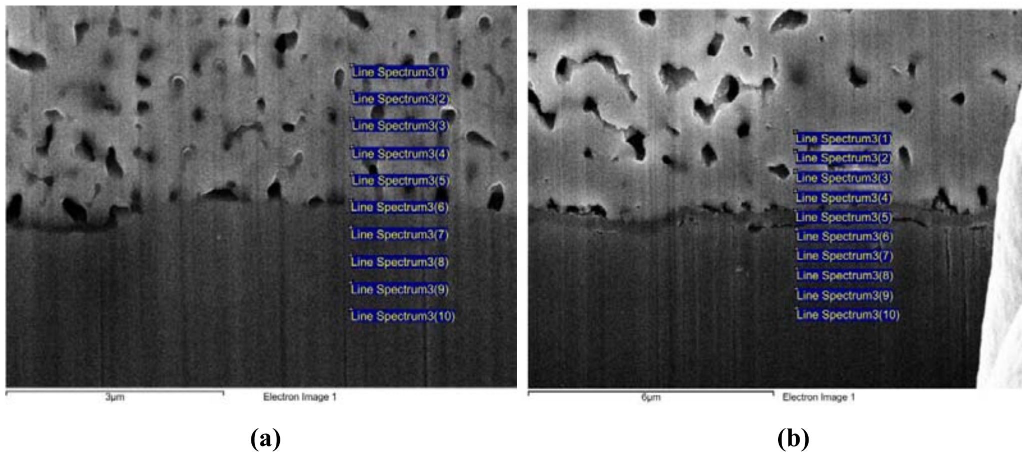


(a) (b)

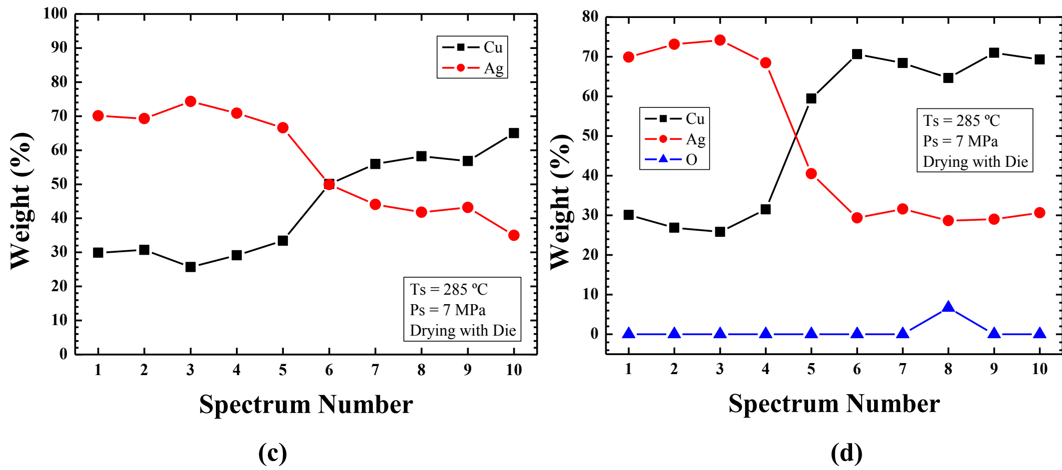


**Figure 5.17. Spectrum points wherein the EDX analysis has been carried out. (a) In the centre region of the Ag sintered layer. (b) In the edge region of the Ag sintered layer. (c) Weight % for each material in the centre region of the Ag sintered layer. (d) Weight % for each material in the edge region of the Ag layer.**

Figure 5.16 summarises the EDX analysis results corresponding to the Ag layer sintered at 265ºC. Figures 5.16(a) and 5.16(b) show the SEM images of the FIB microsections in the centre and periphery zones respectively, indicating the 10 points spaced approximately 200 nm in the vertical direction where EDX spectrum analysis were performed. Figure 5.16(c) represents the weight % curves only of Cu and Ag measured along the 10 inspection points, as O was not detected in the central zone of the sintered Ag layer. On the contrary, Figure 5.16(d) indicates the weight % curves for Cu, Ag and also O, as this element was clearly detected in the periphery zone of the Ag layer. In both Figures 5.16(c) and 5.16(d), inspection point number 5 is located approximately in the middle of the Ag/Cu interface, showing approximately 50 % content of Ag and Cu. Looking at the curves corresponding to the edge region in Figure 5.16(d), the O % in weight is very low well inside the Ag and Cu regions, but shows a peak at the interface, with a slightly higher content in the Cu region than in the Ag. This fact suggests that the layer created at the Ag/Cu interface corresponds basically with a copper oxide, although additional analysis would be required to precisely determine the composition of the intermediate layer. This study is out of the scope of this thesis, but the results presented here establish the basis for more in depth investigations to be performed in future works.

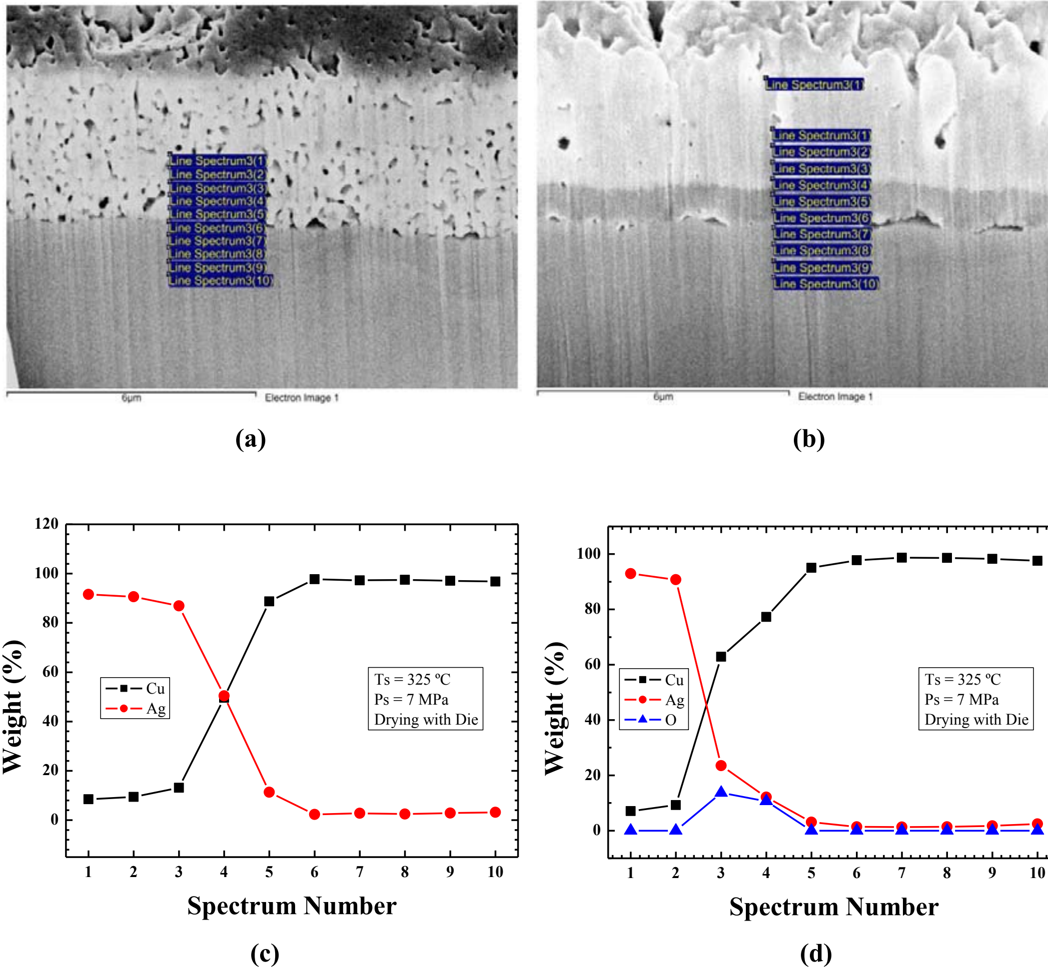


**Figure 5.18. Spectrum points wherein the EDX analysis has been carried out. (a) In the centre region of the Ag sintered layer. (b) In the edge region of the Ag sintered layer. (c) Weight % for each material in the centre region of the Ag sintered layer. (d) Weight % for each material in the edge region of the Ag layer.**

To conclude this subsection, Figures 5.17 and 5.18 show the EDX results obtained for the Ag layers sintered at 285 ºC and 325 ºC, respectively. The pictures corresponding to the FIB microsections and EDX spectrum curves are presented in a similar way than it has been done in Figure 5.16. The results obtained for 285 ºC and 325 ºC are in agreement with those obtained for the 265ºC case, although the O detection in Figure 5.17(d) seems to be shifted. In fact, all the EDX results in Figure 5.17 seem to be more disperse than the rest of performed measurements, and we have not focused on the 285 ºC case. On the other hand, the EDX curves in Figures 5.18(c) and 5.18(d) for 325 ºC sintering temperature show very clearly the O peak at the Ag/Cu interface, slightly shifted towards the Cu side. The peak is also higher than for the 265 ºC case in Figure 5.16(d), revealing that not only the oxide layer is thicker at higher

temperatures, but also that the O content is higher. After of review the main differences in both regions of die-attach, it can conclude that the, the densification also depends of the sintering temperature [9, 10, 11]. Moreover, the adherence zones depend of directly of sintering temperature owing to surface diffusion. However, although the sintering temperature has the advantages of improves the densification and the adherence of the Ag sintered with the Cu substrate, also has the disadvantage of create a considerable layer of CuO. This aforementioned layer can cause problems during thermal cycling. In fact, for future research it might be interesting the formation of intermetallic compounds and interaction with the CuO layer during thermal cycling test.

### *5.3.2. Influence of the Sintering Temperature on the Die-Shear Results*

In order to obtain a measurable evaluation (macroscopic analysis) of the sintering temperature influence on the Ag die-attach joining, the standard test vehicle and methodology described in section 4.2 was used to develop samples suitable for die-shear tests. In all cases, bare Cu substrates with the same range of surface roughness (80 - 150 nm) and Au plated Si dummy dice have been joined with the K-type Ag nanoparticles paste. The applied sintering pressures were 3 MPa and 7 MPa, the sintering time 10 minutes, the initial drying step was with die and the sintering temperatures were set at 265 ºC, 285 ºC and 325 ºC.

In a similar way than for the pressure influence study, before looking at the adherence of dice in test vehicles, we analysed first how the die-attach thickness depends on the sintering temperature, as this dependence is directly related with the microscopic structure of the sintered layer and, in particular, with the attained degree of densification described in the previous paragraphs. Figure 5.19 graphically shows the reduction of the Ag layer thickness before sintering (initial thickness of the fresh paste) and after sintering (final thickness of the die-attach) for samples processed at 3 MPa and at 7 MPa in the 265 ºC – 325 ºC range. In both cases, the thickness reduction (due to elimination of organic components and particle shrinkage [12]) is approximately 50 %, independently of the used sintering temperature. In addition, it can also be observed that the final die-attach thicknesses are similar for samples processed at 3 MPa and 7 MPa. In fact, the dependence of the die-attach thickness with sintering pressure was presented in Figure 5.7 and the difference between 3 MPa and 7 MPa was only 5 µm considering

the mean values and considering the respective error bars, it is reasonable to find the same final thickness for both pressures.

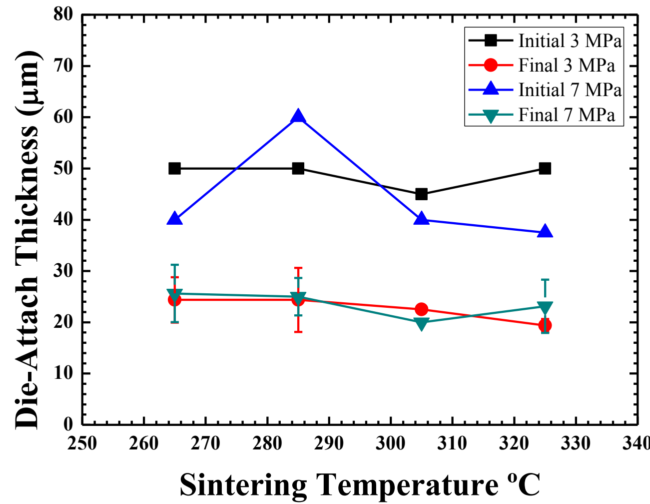


**Figure 5.19. Mean values of final die-attach thickness sintered at 3 MPa and 7MPa and different sintering temperatures. Bare Cu substrates and Au plated Si dice have been used.**

The die-attach layers of the studied tests vehicles have been inspected using C-SAM equipment. Figure 5.20 displays the C-SAM images corresponding to the die-attach layers sintered at 3 MPa and between 265 ºC and 325 ºC. First of all, it is worth pointing out that the white areas observed mainly in Figures 5.20(b) and 5.20(d) have been provoked by problems during the screen printing step (air bubbles in the paste, dirty areas on the substrate, etc.). Apart from this experimental problem, the more relevant aspect to stress in view of the C-SAM results in Figure 5.20 is that with increasing temperature the images are darker, indicating a better densification and a better interface between Ag and Cu. The samples sintered at 7 MPa show exactly the same tendency as it is depicted in the C-SAM images of Figure 5.21. As it was already found, the higher sintering pressure improves the die-attach layer homogeneity, densification and adherence with the substrate and, when adding also the positive effect of higher sintering temperatures, the consequence is the very high quality die-attach layers depicted in Figures 5.21(c) and 5.21(d) for 7 MPa and 305 ºC and 325 ºC respectively.

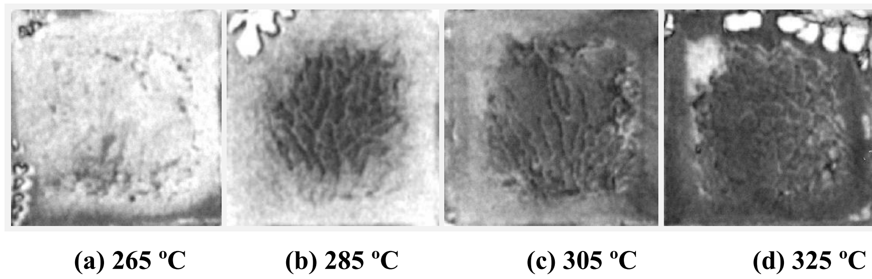

**(a) 265 ºC (b) 285 ºC (c) 305 ºC (d) 325 ºC**

**Figure 5.20. C-SAMs images of test vehicles sintered at 3 MPa with different sintering temperatures. (a) Sintering temperature of 265 ºC. (b) Sintering temperature of 285 ºC. (c) Sintering temperature of 305 ºC. (d) Sintering temperature of 325 ºC.**

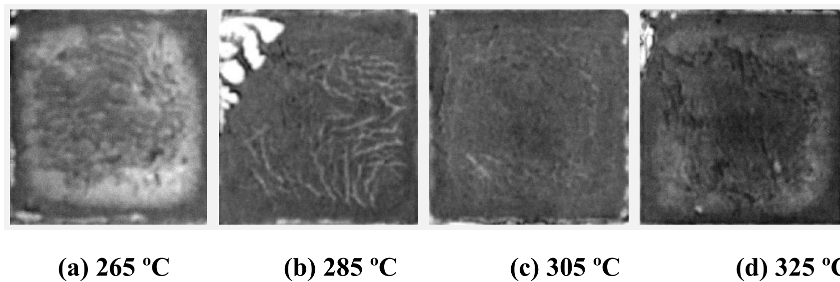

**(a) 265 ºC (b) 285 ºC (c) 305 ºC (d) 325 ºC**

**Figure 5.21. C-SAMs images of test vehicles sintered at 7 MPa with different sintering temperatures. (a) Sintering temperature of 265 ºC. (b) Sintering temperature of 285 ºC. (c) Sintering temperature of 305 ºC. (d) Sintering temperature of 325 ºC.**

Figure 5.22 presents the die-shear force dependence with different sintering temperatures for the test vehicles developed at 3 MPa (in black) and 7 MPa (in red). In the interest of clarity, Figure 5.22(a) shows only the mean values for the measured die-shear forces, while Figure 5.22(b) and Figure 5.22(c) represent the complete box-plots of all measured data for the 3 MPa and 7 MPa pressures respectively. The information provided in the box-plots follows the same definitions than for the pressure dependence analysis in section 5.2.2. The most relevant conclusion derived from the curves in Figure 5.22(a) is that die-shear force increases with the sintering temperature, and this increase appears more pronounced for the 7 MPa case than for the 3 MPa case, although this point requires additional analysis in view of the error bars of the box-plots. This result is in line with the conclusions from the microstructural analysis performed in section 5.3.1 and with the C-SAM images of the present section, as increasing sintering temperatures revealed better densification of the Ag particles, better adhesion with the Cu and more homogeneous interfaces in the C-SAM images.

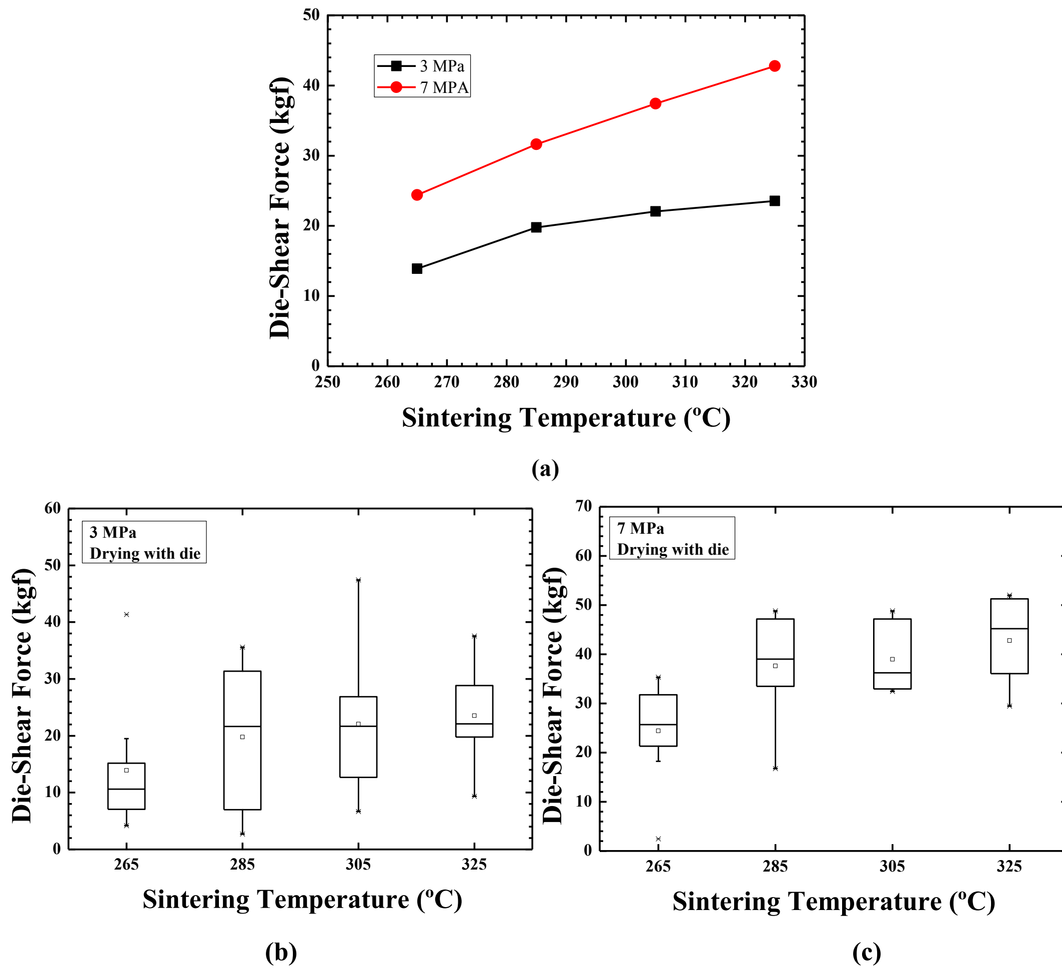


**Figure 5.22. Die-shear force values for different sintering temperatures. (a) Mean values for samples sintered at 3 and 7MPa. (b) Box plots for samples sintered at 3 MPa. (c) Box plots for samples sintered at 7 MPa.**

Apart from providing a measurable confirmation about the microscopic effects caused by the sintering temperature on the Ag layer, the curves in Figure 5.22(a) describe also the correlation between the two main sintering parameters. For instance, the sample sintered at 3 MPa and 325 ºC has a mean die-shear force of 23.5 kgf, which is similar to value of the sample sintered at 7MPa and 265 ºC (24.4 kgf). This fact can be useful for selecting the optimum sintering parameters in accordance to the requirements of given packaging materials. As an example, diminishing the sintering pressure can be useful in order to avoid die fracture during sintering [13], but the die shear force can be kept approximately constant with an increment of the sintering temperature. On the contrary, a limitation in process temperature could be compensated by increasing the sintering pressure. A further example is in a power electronics package technology, which is assembly with different materials. Commonly the process

package is carried out in several steps and each one has your own soldering process which is mandatory for the melting point of solder alloy [14, 15].

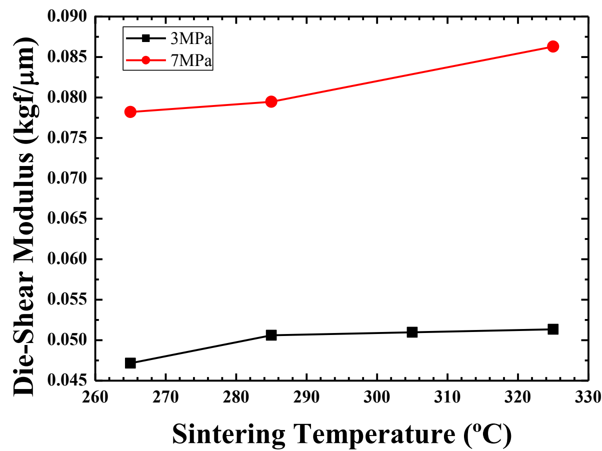


**Figure 5.23. Sintering temperature influence on the die-shear modulus for samples processed at 3 MPa and 7MPa. Bare Cu substrates and Au plated Si dice have been used.**

In a similar approach than for the pressure analysis (section 5.2.2) the behaviour of the die-shear modulus (the slope of the force versus distance curves during die-shear tests) as a function of the sintering temperature is represented in Figure 5.23. The red curve corresponds to the mean values for the samples sintered at 7 MPa and the black curve corresponds to the 3 MPa case. The curves in Figure 5.23 show that both shear modulus don't show a significant dependence with temperature although for the 7 MPa case the curve shows a slight increase (from 0.078 at 265 ºC up to 0.086 at 325 ºC). The die-shear modulus increase at higher sintering pressures demonstrated in section 5.2.2 is confirmed again in the curves of Figure 5.23 where the die-shear modulus evolves from values around 0.05 for the 3 MPa case up to values around 0.08 at 7 MPa.

The failure modes of the test vehicles after die-shear were determined by optical inspection of the substrates and dice after fracture. Figure 5.24 shows the pictures corresponding to the test vehicles sintered at 3 MPa and temperatures from 265 ºC up to 325 ºC. For practically all the sintering temperatures the main failure mode is the type 1 (Ag detached from the Cu substrate), although for higher temperatures some Si scraps remain attached to the substrate and for the 325 ºC case, some samples show a mode 4 failure (semiconductor fracture). Therefore, it can be inferred that from 265 ºC to 305 ºC the inter-particle force is higher than the force between the sintered layer and the surfaces (die and substrate). The die fracture is more evident at 325 ºC, indicating that

the force between the sintered layer and the surfaces (die and substrate) is higher than the inter-particle force of the Ag microstructure in that case.

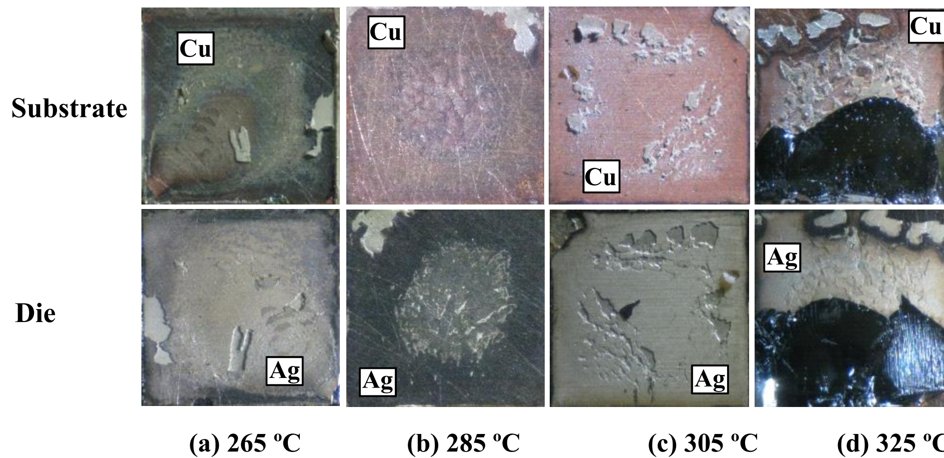


**Figure 5.24. Photographs of test-vehicles processed at 3 MPa and different sintering temperatures after die-shear tests. (a) Sintering temperature 265 ºC. (b) Sintering temperature 285 ºC. (c) Sintering temperature 305 ºC. (d) Sintering temperature 325 ºC. Bare Cu substrates and Au plated Si dice have been used.**

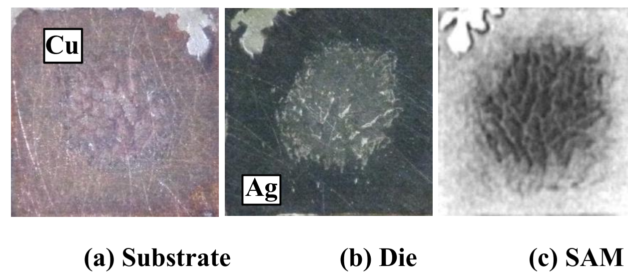


**Figure 5.25. Images of sample sintered at 7MPa and 285 ºC. (a) Bonded region of Cu substrate. (b) Ag sintered layer onto die. (c) C-SAM image of sample before of die-shear test. Bare Cu substrates and Au plated Si dice have been used.**

When looking at some of the pictures performed after die-shear tests, some colour patterns corresponding to the final Ag distribution on the die or substrate surface, or to oxidation marks, are similar with the patterns found in the C-SAM inspections. In this sense, Figure 5.25 shows a particular example for a sample developed at 285 ºC and 3 MPa. This observation seems very interesting as C-SAM images could provide valuable information about the shear failure mechanisms, but it has been concluded that additional inspection of the microstructure of the samples is required to fully understand the link between C-SAM images and failure modes.

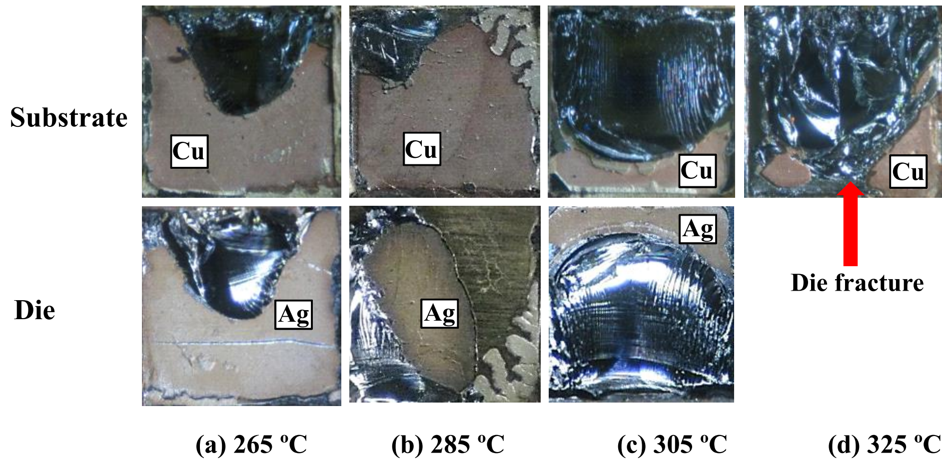


**Figure 5.26. Photographs of test-vehicles processed at 7 MPa and different sintering temperatures after die-shear tests. (a) Sintering temperature 265 ºC. (b) Sintering temperature 285 ºC. (c) Sintering temperature 305 ºC. (d) Sintering temperature 325 ºC. Bare Cu substrates and Au plated Si dice have been used.**

Figure 5.26 shows the pictures of the substrates and dice after die-shear tests corresponding to test vehicles processed at 7 MPa and sintering temperatures from 265 ºC to 325 ºC. It can be observed that in all cases the failure is related mainly with the die fracture (failure mode 4) in combination with failure mode 1 (Ag detached from the Cu substrate). When comparing these pictures with those in Figure 5.24, it is clear that the effect of the higher sintering pressure is improving the adherence of the Ag layer with the Cu substrate. In addition, it seems that in the case of samples sintered at 7 MPa there is less oxidation than for samples sintered at 3 MPa. Consequently, it is possible that higher sintering pressures help avoiding the oxidation of the Cu substrate. Nonetheless, more in deep analysis is necessary to support this hypothesis.

## 5.4. Influence of the Initial Ag Paste Thickness and Drying Method

Another manufacturing parameter than can be important for determining the final properties of the sintered Ag die-attach layer, is the initial thickness of the dispensed Ag paste. In order to analyse the influence of this initial paste thickness on the final die-attach properties, the standard test vehicle and methodology described in section 4.2 was used to develop samples suitable for die-shear tests. In all cases, bare Cu substrates with the same range of surface roughness (80 - 150 nm) and Au plated Si dummy dice have been joined with the K-type Ag nanoparticles paste. The applied sintering pressure was 7 MPa, the sintering temperature 285 ºC and the sintering time 10 minutes. In the

framework of these tests, it has been considered very relevant also to analyse the influence of the paste drying method (with and without die), because depending on the applied volumes of fresh paste the evacuation of solvents will show different behaviour. Consequently, test vehicles using drying steps with and without chip on top of the paste have been processed.

The need for using different initial fresh paste thicknesses before sintering can be explained by several reasons: the adjustment of the dispensing equipment, the availability of different screen printing masks, etc. In any case, a given initial paste thickness will provide a final die-attach thickness and knowing the relationship between both parameters for a given process flow is primordial. In the study presented in this section, different initial paste thicknesses from 50 µm to 350 µm were deposited by screen printing through apertures of the same size (2.5 mm x 2.5 mm) opened in different masks.

Figure 5.27 represents the reduction of the final die-attach thickness for three different initial paste thicknesses using the drying step with dice. The obtained curve is practically linear, showing an average thickness reduction of approximately 60 %. This behaviour will be extremely practical in future developments for predicting the final die-attach layer thickness from manufacturing parameters such as the screen-printing mask characteristics. Regarding to the error bars, they increase when the initial thickness increases, which indicate that exist less control of the die-attach thickness. In fact this effect is undesirable in the case a real manufactured package.

Figure 5.29 shows a similar curve but this time using a drying step without die. A practically linear response between initial paste thickness and final die-attach thickness is also obtained, but the reduction between both magnitudes is around 40 %. Thus, lower thickness reduction is obtained when using the drying step without die.

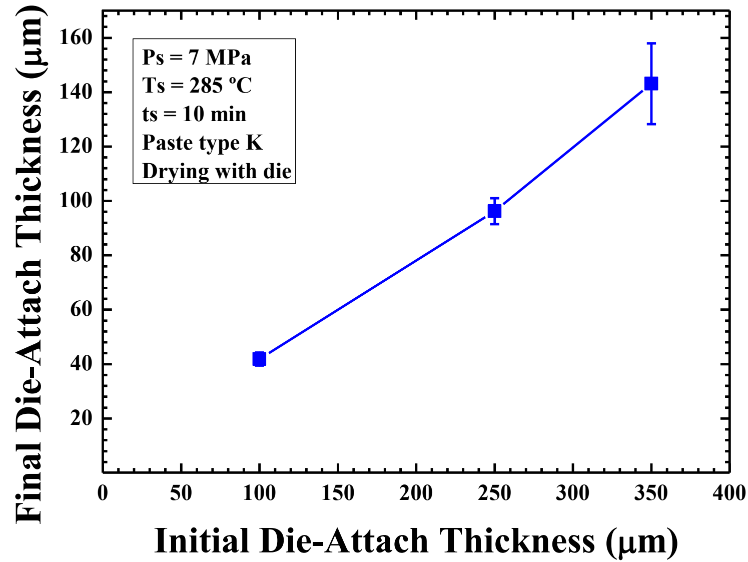


**Figure 5.27. Relationship between initial Ag paste thickness and final sintered die-attach thickness for test vehicles dried with die. Bare Cu substrates and Au plated Si dice have been used.**

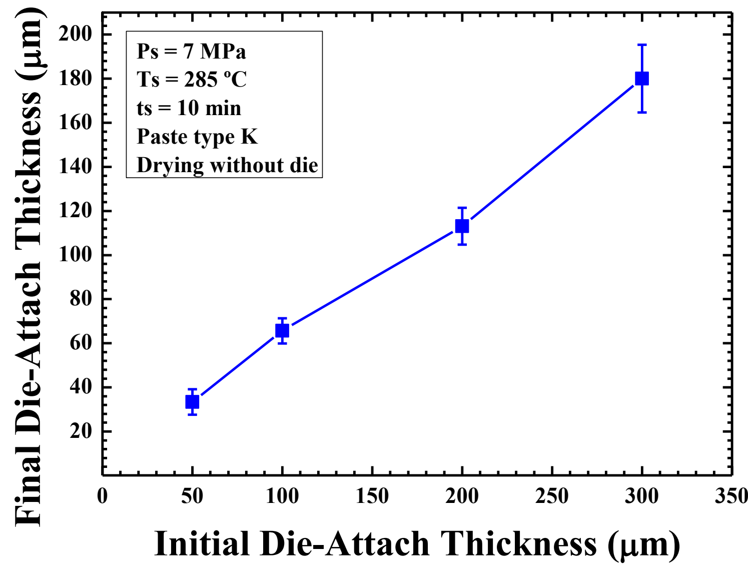


**Figure 5.28. Relationship between initial Ag paste thickness and final sintered die-attach thickness for tests vehicles dried without die. Bare Cu substrates and Au plated Si dice have been used.**

Figure 5.29 displays the C-SAM images for the test vehicles corresponding to the curve in Figure 5.27 (drying step with die). The final die-attach thicknesses are 40 μm, 95 μm and 140 μm, and all samples show fractures on the Ag layer. Besides, the internal area appears in clearer grey tones than the periphery, accounting for a less dense Ag layer due to the less efficient drying process with the die on top of the fresh paste.

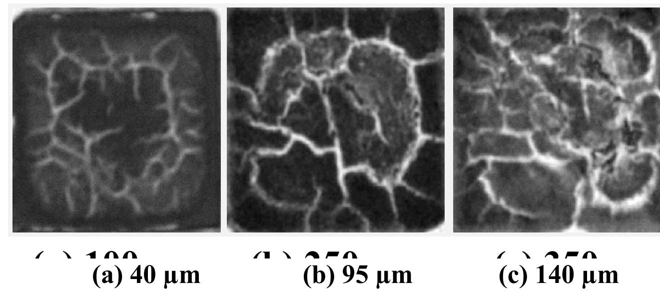

**(a) 40 µm (b) 95 µm (c) 140 µm**

**Figure 5.29. C-SAM images for different die-attach thickness sintered at 7MPa, 285 ºC, 10 minutes and drying step with die. Au plated Si dice and bare Cu substrate have been used. (a) Final thickness 40 µm. (b) Final thickness 95 µm. (c) Final thickness 140 µm.**

In the same sense, C-SAM images for test vehicles corresponding to the results of Figure 5.28 (drying step without die) are shown in Figure 5.30. In general, best densification and more regular die-attach layers are obtained when drying the paste without die. In particular samples with die-attach thickness of 30 µm and 65 µm (Figures 5.30(a) and 5.30(b) respectively) show very homogeneous C-SAM images, while samples with final thickness of 115 µm and 180 µm (See Figures 5.30(c) and 5.30(d) respectively), present some fractures (withe lines) and slight uniformities (light grey areas).

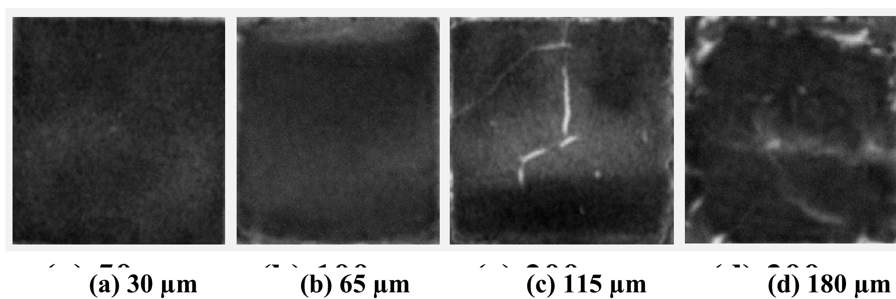

**(a) 30 µm (b) 65 µm (c) 115 µm (d) 180 µm**

**Figure 5.30. C-SAM images for different die-attach thickness sintered at 7MPa, 285 ºC, 10 minutes and drying step without die. Au plated Si dice and bare Cu substrate have been used. (a) Final thickness 30 µm. (b) Final thickness 65 µm. (c) Final thickness 115 µm. (d) Final thickness 180 µm.**

The effect of the different processing options presented above, was quantified by the die-shear tests summarized in the curves of Figure 5.31, showing the final thickness and drying step influence on the die-shear force. The first relevant result that can be observed is the higher die-shear force obtained in all cases when using the drying step without die (black curve). In addition, the die shear force is almost independent of the die-attach thickness in the analysed range (30 µm – 180 µm), with shear force values never below 40 kgf. This result is in good agreement with the homogeneous die-attach

layers observed for such kind of drying step. For the drying step with die (red curve), a significant die-shear force reduction is observed for die-attach thicknesses above 100 µm (from 36 kgf to 20 kgf). This result reveals that Ag sintering processes differing only on their initial pre-drying steps can provide die-attach layers of the same thickness but with very different mechanical properties.

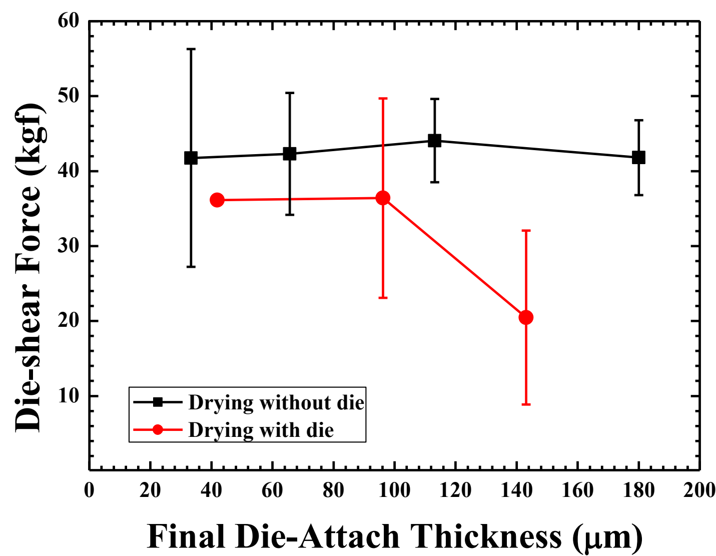


**Figure 5.31. Die shear force mean values for different die-attach thicknesses using a drying step with die (red circles) and without die (black squares). Sintering parameters are 7 MPa, 285ºC and 10 minutes. Au plated Si dice on bare Cu substrates.**

The previous assertion is also supported by the die-shear modulus dependence with die-attach thickness, represented in Figure 5.32 for the drying steps with die (black curve) and without die (red curve). When drying the paste without die, any clear dependency with the die-attach thickness can be concluded. On the other hand, the die-shear modulus when drying with die clearly decreases (from 0.08 to 0.035 kg/µm) when the final die-attach thickness increases. This behaviour indicates that apart from the adherence diminution already presented in Figure 5.31, the Ag layer presents different mechanical properties (such as the Young modulus) depending on its thickness when the pre-drying step is performed with the die on top of the paste. The observed diminution of the “stiffness” (somehow proportional to the shear modulus) in Figure 5.32 for the drying with die method, is a consequence of the poor elimination of organics in the Ag paste. As a conclusion, different thermo-mechanical responses will be expected between both drying methods.

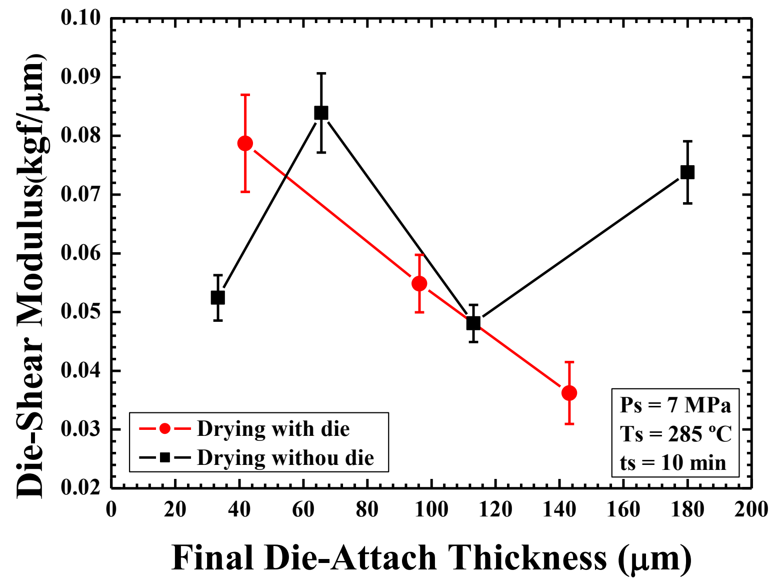


**Figure 5.32. Mean values of die-shear modulus for different final die-attach thicknesses using a drying step without die (red circles) and with die (black squares). Same sintering parameters than in the previous figure used.**

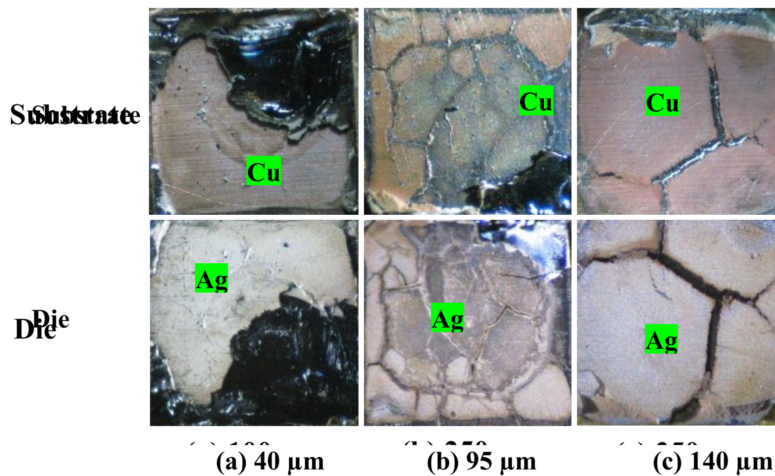


**Figure 5.33. Photographs of substrate and die after die-shear tests for determining the failure modes for several die-attach thicknesses obtained using a drying step with die. (a) Final thickness 40 µm. (b) Final thickness 95 µm. (c) Final thickness 140 µm.**

To conclude with our study, Figure 5.33 displays photographs of the substrate and chip after die-shear tests for determining the failure modes of the test vehicles dried with die. The final thickness for the analysed samples was from 40 µm to 140 µm. Although the predominant failure in samples with final thickness of 40 µm is the die fracture (failure mode 4) some samples show detached areas in the Cu substrate (see Figure 5.33(a)). In the case of samples with final thickness of 95 µm (Figure 5.33(b)) the failure mode 1 is the predominant, although with presence of die fracture (failure

mode 4). Finally, Figure 5.33(c) displays a photograph of a sample with final thickness of 140 µm, wherein all samples presented the Ag sintered layer detached from the Cu substrate (failure mode 1). In summary, the main conclusion that can be derived from this analysis is that for thick Ag layers dried with die, the failure mode after die shear tests indicates a weak adhesion of the Ag particles with the Cu substrate, mainly due to a bad evacuation of organics during the drying process.

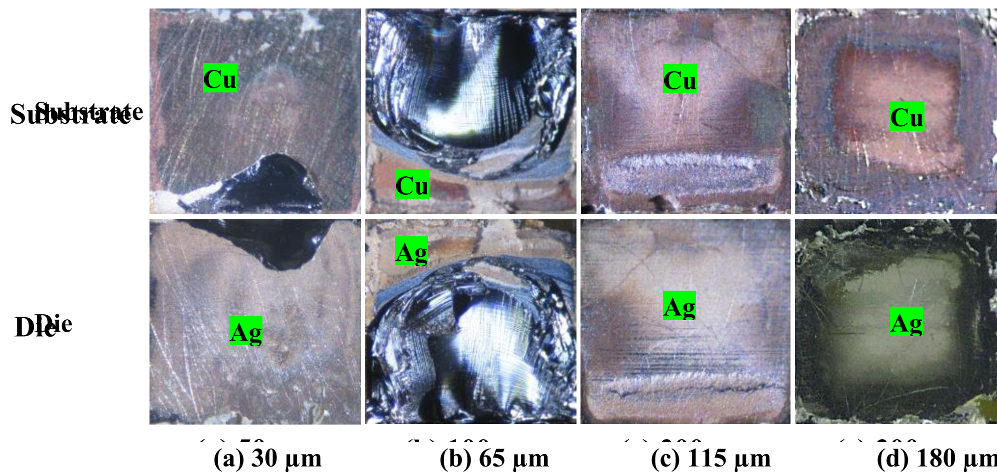


**Figure 5.34. Photographs of substrate and die after die-shear tests for determining the failure modes for several die-attach thicknesses obtained using a drying step without die. (a) Final thickness 30 µm. (b) Final thickness 65 µm. (c) Final thickness 115 µm. (d) Final thickness 180 µm.**

In the same way, Figure 5.34 displays the photographs corresponding to the samples dried without die with final die-attach thicknesses ranging from 30 µm to 180 µm. Although the predominant failure mode in samples with die-attach thicknesses between 30 µm and 65 µm is the die fracture (failure mode 4) some samples show detached areas in the Cu substrate (see Figure 5.34(a) and (b)). For samples with final thickness of 115 µm (Figure 5.34(c)) the failure mode 1 is the predominant one, although some samples present die fracture (failure mode 4). Finally, Figure 5.34(d) presents the pictures for the sample with final thickness of 180 µm, wherein the Ag sintered layer is detached from the substrate (failure mode 1). Nevertheless, for this die-attach thickness some samples have also presented the failure mode 4. In conclusion, for samples dried without die, the same failure modes found previously for drying step with die are observed, although in this case, more samples show failure mode 4 (partial die fracture) indicating a better adhesion between Cu and Ag.

## 5.5. Influence of the Sintering Time

Another relevant parameter that can be adjusted during the Ag sintering process proposed in chapter 4 after pressure and temperature is time. In this section, the influence of the applied sintering time on the characteristics of the final Ag die-attach layer will be analysed, although we have not performed an exhaustive analysis of the microstructural effects of different sintering times as it was the case for pressure and temperature. Basically, we have evaluated the macroscopic mechanical characteristics of the die-attach at different sintering times when fixing the rest of the process parameters. With the aim at achieving this goal, optical microscope, C-SAM and die-shear characterization tools have been used. Besides, the failure modes of the test vehicles will be discussed.

In order to obtain a measurable evaluation of the sintering time influence on the Ag die-attach joining, the standard test vehicle and methodology described in section 4.2 was used to develop samples suitable for acquiring experimental data. For this study, apart from bare Cu substrates we have also included some Au plated Cu substrates (in the 80 - 150 nm range of surface roughness), Au plated Si dummy dice and K-type Ag nanoparticles paste. The applied sintering pressure was 7 MPa, the sintering temperature 285 ºC, the initial drying step was without die and the sintering time was set at 5, 10 and 20 minutes.

Before performing the destructive die-shear tests, we measured the variation of the Ag layer thickness during sintering. Figure 5.35 shows the mean values of the final die-attach thickness for the different sintering times. In all cases the initial thickness of the green paste was 100µm. Au plated Si dice have been used for the case of bare Cu substrates (in black) and also for Au plated Cu substrates (in red). Nevertheless, with the Au plated substrates, the point corresponding to the 10 minutes of sintering time includes Au plated SiC dice instead of the habitual Si dummies. It can be observed that for all kind of Cu substrates (bare or Au plated surface) the variation of the die-attach thickness is not significant from 5 minutes to 20 minutes of sintering time, mainly taking also into account the experimental error involved in such measurements.

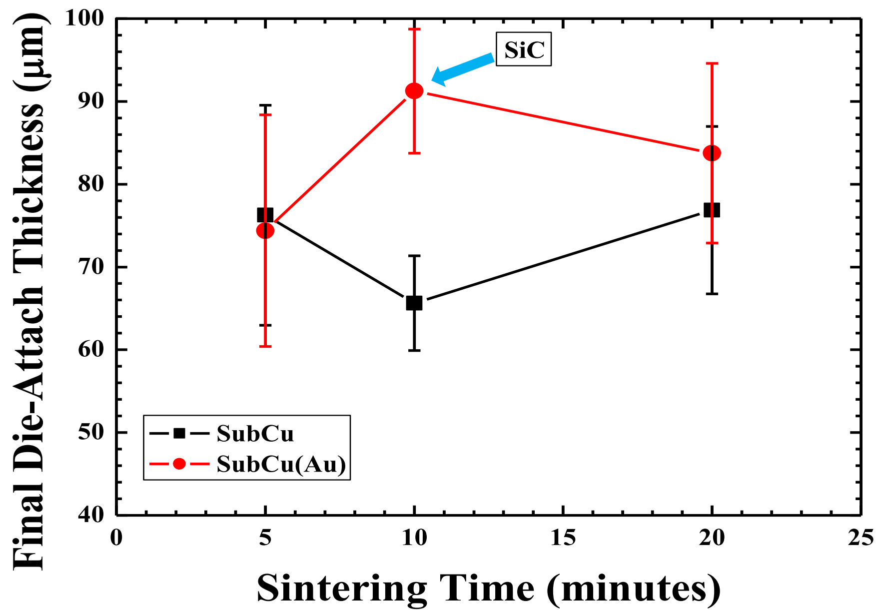


**Figure 5.35. Final die-attach thickness mean values for Au plated and Cu substrates sintered at different sintering times (5, 10 and 20 min). Bare Cu substrates, Au plated substrates and Au plated (Si and SiC) dice have been used.**

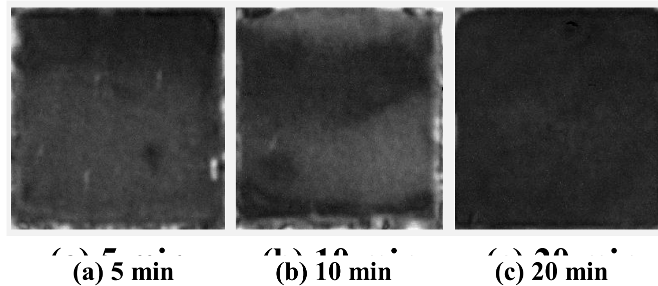


**Figure 5.36. C-SAM images of the sintering time influence onto bare Cu substrates. (a) Sintering time 5 minutes. (b) Sintering time 10 minutes. (c) Sintering time 20 minutes. Bare Cu substrates and Au plated Si dice have been used.**

Concerning the quality of the Ag layers after processing using different sintering times, Figures 5.36 and 5.37 provide C-SAM images corresponding to test vehicles developed with bare Cu and Au plated Cu substrates respectively. The final die-attaches appear very regular and homogeneous, as it is the usual case for the samples dried without die. In any case, the only comment that can be done is that the quality of the Ag layer (in terms of homogeneity and defects) seems to be improved when increasing the sintering time. This tendency is very logical as sintering time is one of the driving elements for ensuring elimination of organics and adhesion among particles. Unfortunately, the influence of the sintering time has not been analysed in samples dried with die, where elimination of organics is more critical and longer times could

help in allowing a complete volatilization. These tests have been identified as priority tasks to be developed in future research works related with the present one.

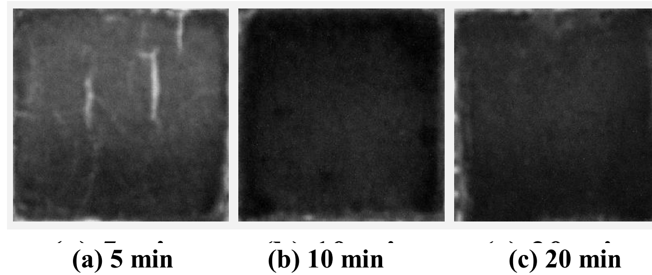


**Figure 5.37. C-SAM images of the sintering time influence onto Au plated substrates. (a) Sintering time 5 minutes. (b) Sintering time 10 minutes. (c) Sintering time 20 minutes. Au plated substrates and Au plated dice (Si and SiC) have been used**

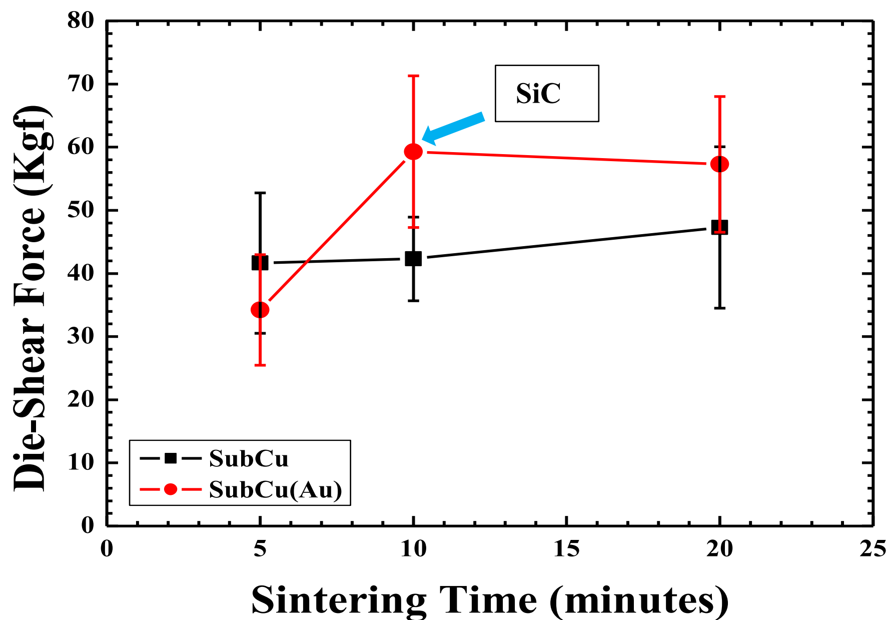


**Figure 5.38. Die-shear force mean values for test vehicles sintered at 7 MPa and different sintering times (from 5 minutes to 20 minutes). Bare Cu substrates, Au plated substrates and Au plated dice (Si and SiC) have been used.**

Figure 5.38 shows the measured mean values of the die-shear forces as a function of the sintering time for the test vehicles described at the beginning of this section. Taking into account the experimental error of such measurements (derived from the standard deviation associated with the dies tested for each point), it can be concluded that negligible influence of the sintering time can be associated with the die-shear force, at least in the considered range of 5 to 20 minutes. This result demonstrates that the most critical parameters for controlling the sintering process are pressure and

temperature, and they require more attention in setups and processes in order to obtain suitable die-attach layers.

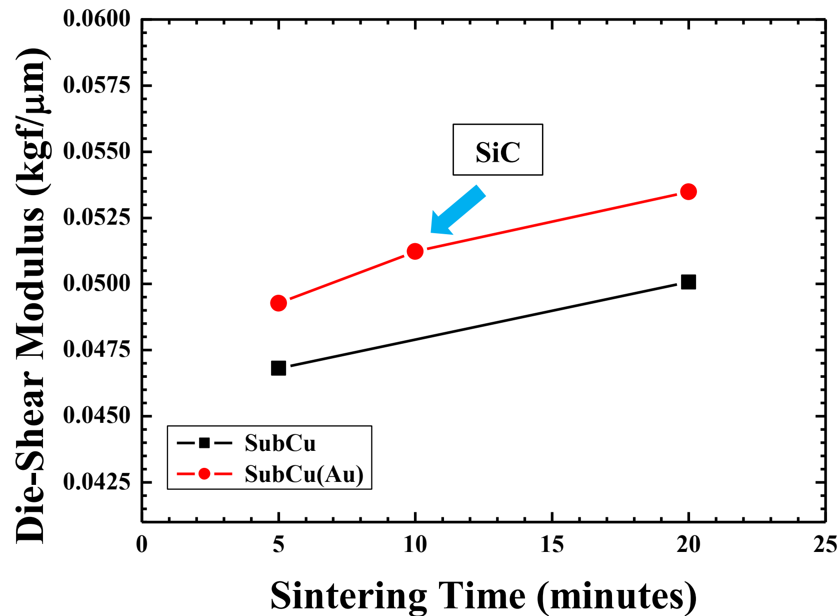


**Figure 5.39. Mean values of die-shear modulus for Au plated and Cu substrates sintered at 7 MPa and 285 ºC. Bare Cu substrates, Au plated substrates and Au plated dices (Si and SiC) have been used.**

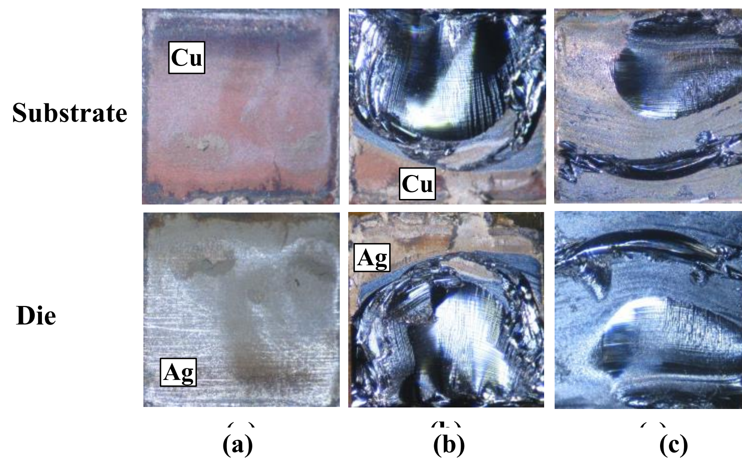


**Figure 5.40.Photographs of failure modes for sintering time influence onto Cu substrates. Au plated Si dice have been used.**

In a similar way, the die-shear modulus was also evaluated for the developed test vehicles at three sintering times. The results are plotted in the curves of Figure 5.39 were it can be clearly observed that the mechanical properties of the Ag layer represented by the die-shear modulus are almost independent of the sintering time.

Figure 5.40 shows the photographs of the substrates and dice allowing the analysis of the failure modes after die shear tests. Figures 5.40(a), (b) and (c) correspond to samples processed on bare Cu substrates using sintering times of 5 minutes, 10 minutes and 20 minutes respectively. Die fracture (failure mode 4) is the main failure mode (for instance, see Figure 5.40(c)). In some cases, although die fracture is the predominant failure mechanism, some areas show the Ag layer detached from the Cu substrate (mode 1), for example the case shown in Figure 5.40(b). The main exception concerns test vehicles sintered for 5 minutes (Figure 5.40(a)) where the main failure mechanism is Ag detachment from the Cu substrate (mode 1). This fact means that 5 minutes is too short for ensuring a good adhesion among the Ag and the Cu although the cohesion among the Ag particles seems to be completed. Similar results have been found for the Au plated Cu substrates.

## 5.6. Influence of the Substrate Condition

The substrate is one of the main elements of the package as it provides not only mechanical support to others elements [15] (including the semiconductor die), but also heat extraction capability, current conduction, etc. For these reasons, the aim of this section is to assess the influence of the substrate condition (roughness, surface treatment, plating material) in the Ag sintering process. To analyse this influence, we followed a similar approach than in previous sections, developing different test vehicles and testing the quality of the die-attach layers based on die-shear strengths, SAM inspection, etc. The section will describe first the influence of the substrate roughness on the characteristics of the Ag die-attach, at zero and higher sintering pressures. Then, the effect of two treatments (based on formic acid vapours and Ar plasma) for improving the Ag adherence to the Cu substrate will be described. After that, the influence of the plating material will be also characterized under different sintering conditions (pressure, drying method, etc.). All these tests will be performed with the K-type paste already used in previous sections of the chapter, but to finish this section, we will present the results obtained with the X-type paste from NBE Tech, suitable for zero pressure sintering [16, 17].

### *5.6.1. Influence of the Substrate Surface Roughness*

An important parameter influencing the adhesion properties on a given surface is its roughness (Ra). For analysing the substrate roughness influence on the Ag sintering process, it has been used the test vehicle described in chapter 4 with K-type Ag paste dried with die, Au plated Si dice and bare Cu substrates. The initial Cu substrates used in this work, show Ra values around 290 nm. This mean value was obtained using confocal microscope measurements on five small areas (138 x 102 $\mu m^2$) of the substrate surface. In order to analyse the effect of different Ra values, we polished different substrates using two types of polishing slurry. The polished substrates have shown mean Ra values around 100 nm and 30 nm respectively. The confocal images of Figure 5.41 evidence the difference between an unpolished and a polished substrate.

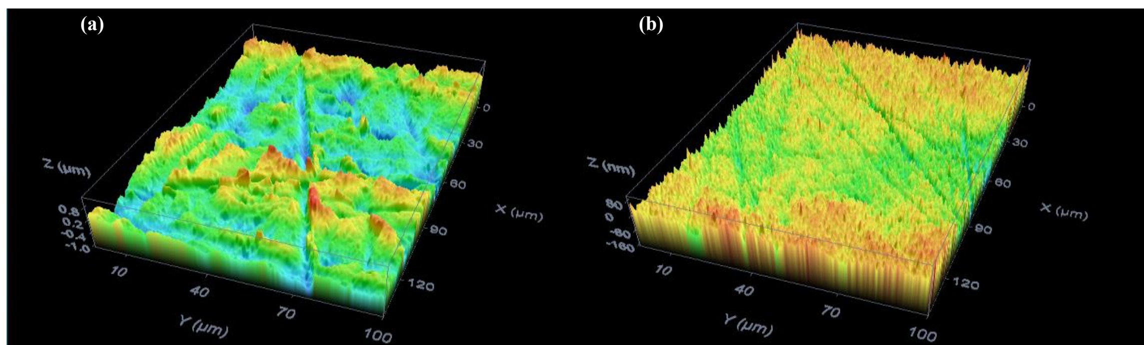


**Figure 5.41. (a) Confocal image of the initial unpolished substrate (Ra=290 nm). (b) Confocal image of a polished substrate (Ra= 100 nm).**

#### *5.6.1.1. Substrate Surface Roughness influence at 0 MPa Sintering Pressure*

The first tests about the substrate surface influence on the sintered Ag die-attach layers, was performed on test vehicles sintered without any pressure applied to the die. Figure 5.42 shows, in a box plot diagram, the die-shear strength results obtained for zero sintering pressure. In this case, we have analysed more than two test vehicles to discard problems related to the sintering process (e.g., substrate surface contamination or wrong temperature control). As it can be observed, the die-shear forces are very low (mean values between 2 kgf and 4.2 kgf), with a relatively high dispersion, and the values decrease for higher roughness values (in the 50 up to 300 nm range). Probably, the interaction between Ag particles and Cu surface is hindered by its higher roughness. These results also confirm the improvement of the Ag adherence with sintering pressure

for the lowest limit of the curve, where the pressure is zero. The failure modes observed after die-shear correspond predominantly with the mode 2 (failure in the bulk of the die-attach layer), revealing also a poor densification of the Ag, although in many samples, detachment from the substrate (mode 1) is also evident. Another significant point observed after die-shear is that the Cu surfaces show a relatively high level of oxidation. The poor quality of the die-attach layers sintered at zero pressure on substrates of different roughness was also evident on the SAM images that revealed many voids and delaminated areas.

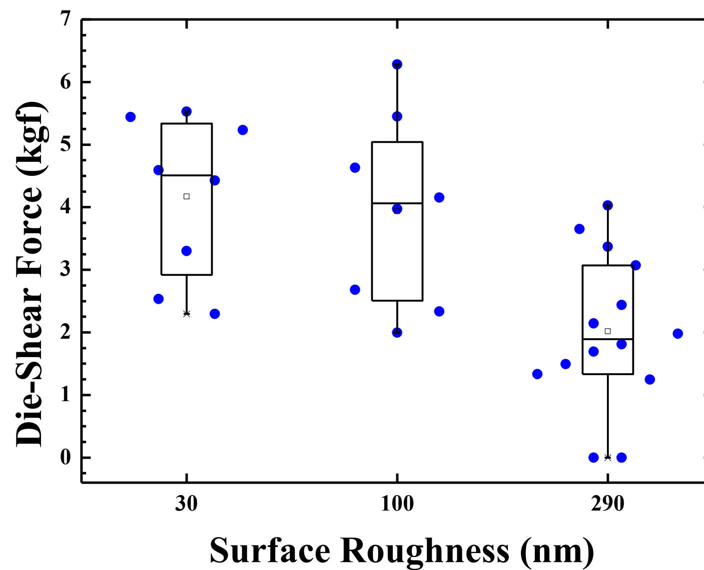


**Figure 5.42. Box-plots of die-shear force for bare Cu substrate with different surface roughness and Ag sintered at zero pressure and drying step with die.**

### *5.6.1.2. Substrate Surface Roughness influence at 7 MPa Sintering Pressure*

In the same sense than the previous tests, the die-shear force values obtained for different substrate surface roughness using Ag die-attach layers sintered at 7 MPa, are represented in Figure 5.43. This figure shows the box plots diagram for the measured samples but this time the obtained die-shear values are an order of magnitude higher than the values displayed in Figure 5.42, and the influence of the substrate roughness can be practically neglected in the analysed range. In this case, the point for substrate roughness of 800 nm was obtained using a commercial alumina DCB substrate instead of our standard bare Cu substrate, confirming that the Cu roughness has little influence on the Ag layer adhesion, provided that the sintering process is performed under

pressure. All these results can be explained by the fact that pressure improves significantly the contact between the substrate and the Ag particles. The SAM images of the die-attach layers has not shown any difference for samples on substrates with different surface roughness. The failure mode analysis performed after die-shear tests demonstrated both, better densification of the Ag (any sample shows mode 2 failure) and a much better adhesion to the substrate, as the predominant failure mode was type 4 (die fracture).

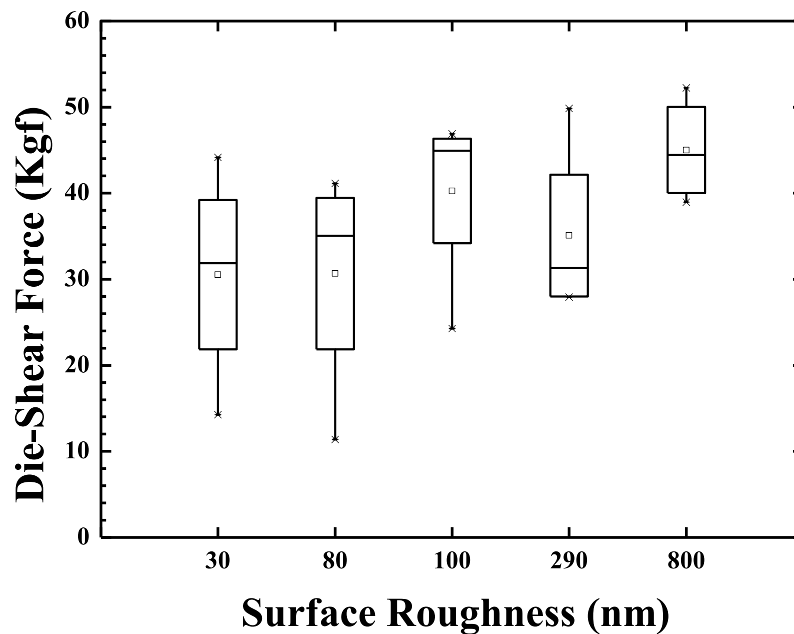


**Figure 5.43. Box plot of die-shear force values for bare Cu substrate with different surface roughness and Ag layers sintered at 7 MPa and drying step with die.**

### *5.6.2. Influence of the Substrate Surface Treatment*

In order to improve the adherence between the Ag layer and the Cu substrate, surface treatments with Ar plasma and formic acid vapour were also undertaken. The Ar plasma process is based on a low pressure "ATTO" plasma system from Diener, implementing and RF generator of 40 kHz – 200 W. The formic acid process consists basically on applying formic acid (HCOOH) vapours carried by $N_2$ to the sample in a closed chamber at 150 ºC. The sintering process adopted to analyse the effect of such treatments on bare Cu substrates with 290 nm roughness, was: 7 MPa, 285 ºC, 10 minutes, and drying step with die

Figure 5.44 shows the box plots of the die-shear force data obtained for several test vehicles including two types of semiconductor dice (Si and SiC) and two types of surface treatment (formic acid and Ar plasma). The first experiments aimed at comparing the adherence of SiC and Si dice attached to the same kind of substrate. As it can be observed, they show similar values (36 kgf for SiC and 31 kgf for Si), what is coherent with the fact that both kind of dice present similar backside roughness and plating scheme (final Au layer).

It can be observed that the samples processed with Ar plasma and formic acid show an improvement of the die-shear strength. Although the mean value is similar for both cases (41 kgf), the formic acid has lower dispersion than the Ar plasma, becoming an attractive method to be implemented in manufacturing processes. Nevertheless, as the die shear results with standard cleaning processes demonstrate good adherences (above the minimum values specified in standards) the substrate cleaning cannot be considered a critical aspect.

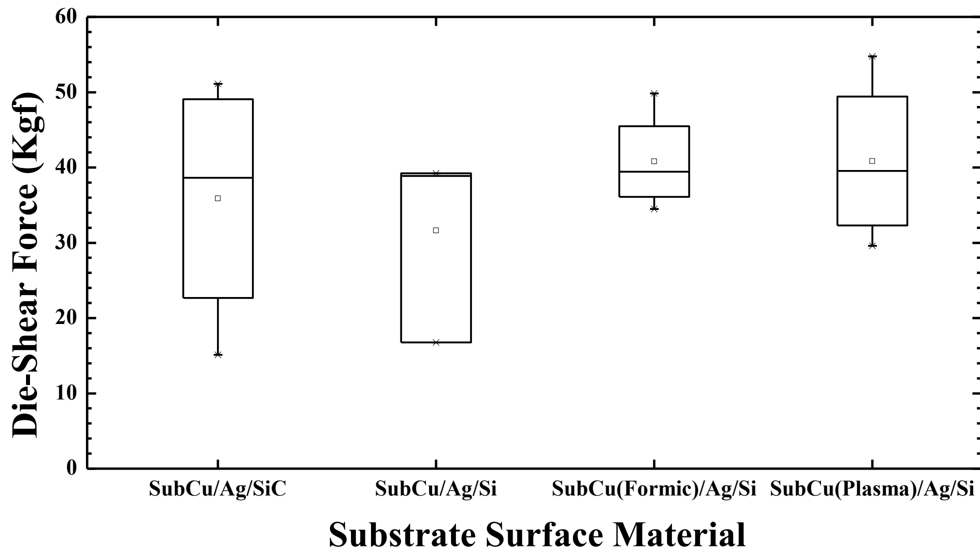


**Figure 5.44. Die-shear results for test vehicles based on bare Cu substrates and different surface treatments (formic acid and Ar plasma). Sintering parameters: 7 MPa, 285 ºC, 10 minutes, drying with die.**

Although the failure mode predominant at 7 MPa (see section 5.1.1.2) is die fracture, some differences can be observed when the substrate cleaning process is carried out with formic acid. Figure 5.45(a) displays the typical die fracture observed on all the test vehicles with the substrate cleaned with formic acid (in fact, only the broken

die is visible). On the other hand, Figure 5.45(b) shows an example of a sample cleaned using the standard method, where the Cu substrate can be partially oxidized. Therefore, it seems that an efficient de-oxidation of the Cu substrate clearly improves the adherence of the Ag layer, although further microstructural analysis is required for explaining the specific effects of such surface treatments.

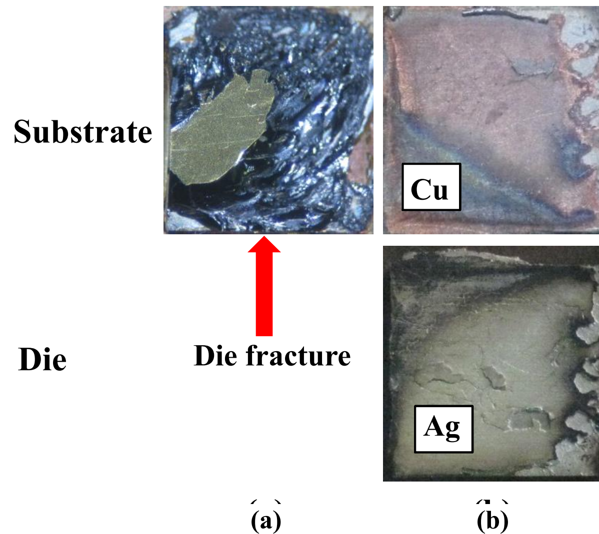


**Figure 5.45. Photographs of test vehicles after die-shear test sintered at 7MPa. (a) Substrate cleaned with formic acid. (b) Substrate cleaned with standard process. Oxidized Cu zones can be observed.**

### *5.6.3. Influence of the Substrate Surface Material*

Whit the aim at analyse the influence of the substrate surface material on the Ag die-attach quality, some experiments were also performed, using test vehicles with different materials on the Cu substrates surface: bare Cu, plated Ag, plated Au and plated Ni. For a better understanding about the influence of the different parameters introduced on each test, we divided this part of the study in the experiments at zero pressure and the experiments at 7 MPa of sintering pressure.

#### *5.6.3.1. Influence of the Substrate Surface Material at 0MPa*

The results corresponding to the first set of experiments are summarized in the die-shear strength values represented in Figure 5.46. The points in the plot correspond to the K-type paste sintered at 0 MPa, 285 ºC, 10 minutes and the two drying methods proposed in this work: with die (black squares) and without die (red circles).

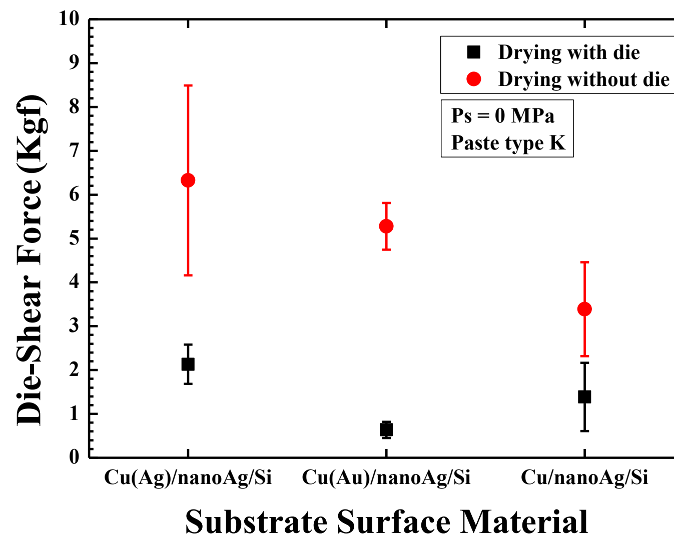


**Figure 5.46. Mean values of die-shear forces for test vehicles with different substrate surface materials: bare Cu, Ag and Au. Paste type K sintered at 0 MPa and drying step with die (black squares) and without die (red circles).**

The first relevant conclusion is that, again, improving the drying step using the method without die increases significantly the adherence of the Ag layer. For example, for Ag plated surfaces the shear strength goes from 2.13 kgf drying with die up to 6.4 kgf when drying without die. The second aspect to be mentioned is that when drying with die, there is not a clear dependence with the substrate surface material and all die-shear values are quite low. On the other hand, when drying without die, the best results are clearly obtained for Ag plating (6.32 kgf), then for Au plating (5.39 kgf) and finally, bare Cu substrate shows the lower die-shear strength (3.40 kgf). It seems coherent that the best adherence of the Ag particles is obtained with the same material on the substrate surface. The results for Au are slightly lower in mean value, although taking into account the experimental error they are not so far from the results for Ag plating. Finally, bare Cu substrate surface clearly shows a lower adhesion that can be explained by a higher tendency to oxidize than in the Ag and Au cases. This conclusion is supported by the mode of failure analysis after die shear. Figure 5.47 shows the pictures corresponding to the substrate and die surfaces after die-shear failure. It can be seen that for the Ag (Figure 5.47(a)) and Au (Figure 5.47(b)) plated substrates, the dominant failure mode is type 2 (bulk die-attach material fracture), although for Au plated substrates, the sintered Ag layer remaining on the substrate side is very thin. Concerning the bare Cu substrates, the failure mode is type 1 (die-attach detached from substrate)

and Figure 5.47(c) shows oxidation traces on the Cu side. It is worth to point out that, as expected, the adherence of the sintered Ag on Ni plated surfaces was zero [8] and it has not been represented in any plot.

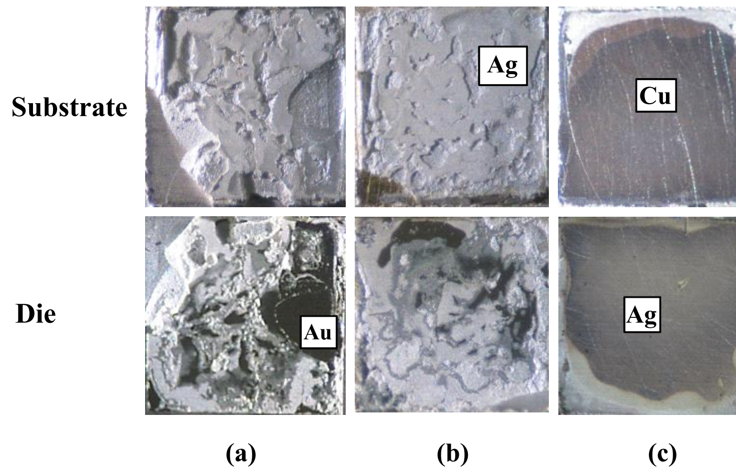


**Figure 5.47. Photographs of test vehicles after die-shear test with K-type Ag paste sintered at 0 MPa and drying step without die. (a) Ag plated substrate. (b) Au plated substrate and (c) Bare Cu substrate**

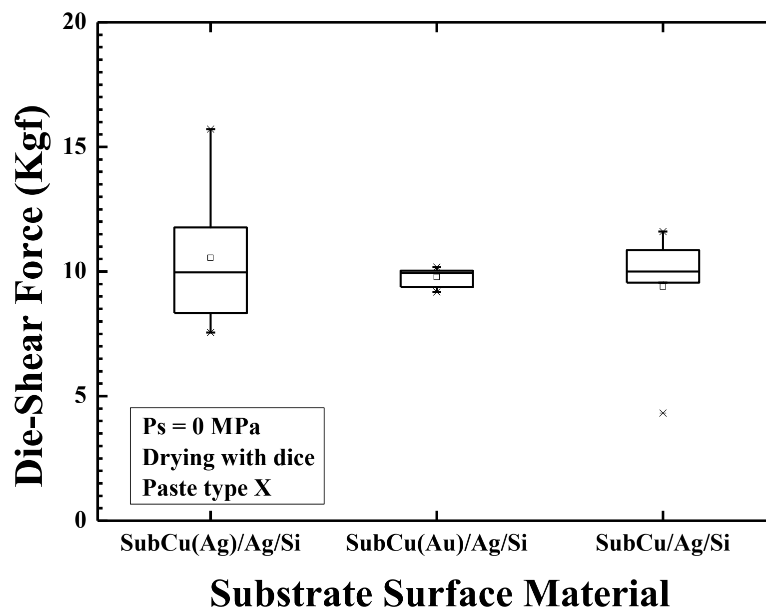


**Figure 5.48. Box plots of the die-shear force values obtained in test vehicles using the X-type Ag paste sintered at 0 MPa and dried with die, for different substrate surface materials.**

Independently from the material on the surface of the substrate it has been clearly demonstrated that the die-shear results for Ag die-attach layers sintered at 0 MPa are very poor. Even when drying the paste without die and the substrate is Ag plated, the mean die-shear results are above the minimum required by the standards (5 kgf for the

used dice from the MIL STD-750), but there is a big dispersion and some of the tests are below the stablished threshold. As die-attach sintering without pressure is a very interesting solution from the practical point of view (the manufacturing process is simplified), manufacturers of Ag pastes are investing big efforts on designing new formulations allowing this approach. In this sense, during the development of this work, NBE Tech commercialised the X-type NanoTach paste, evolved from the K-type, specifically for the zero pressure applications. In order to compare the results obtained with both pastes, we have developed several test vehicles using this X-type paste, following the guidelines and processing steps already mentioned in chapter 4.

Figure 5.48 shows the box plots of the die-shear strength values obtained for test vehicles developed with the X-type Ag paste and with three types of substrate surfaces (Ag and Au plated and bare Cu). The drying step of the X-paste was with die, i.e. the most unfavourable condition, and the sintering was performed without any applied pressure. As it can be derived from the plotted points, all the performed tests are above the threshold fixed by the MIL STD-750 standard (5 kgf) for all the substrate surface materials involved in the measurements, with mean die-shear force values between 9 kgf and 11 kgf. It seems that for this kind of paste the influence of the surface material is negligible, although for Au plated substrates the dispersion of the results is very low. This is probably due to the fact that Au is not affected by oxidation processes during sintering.

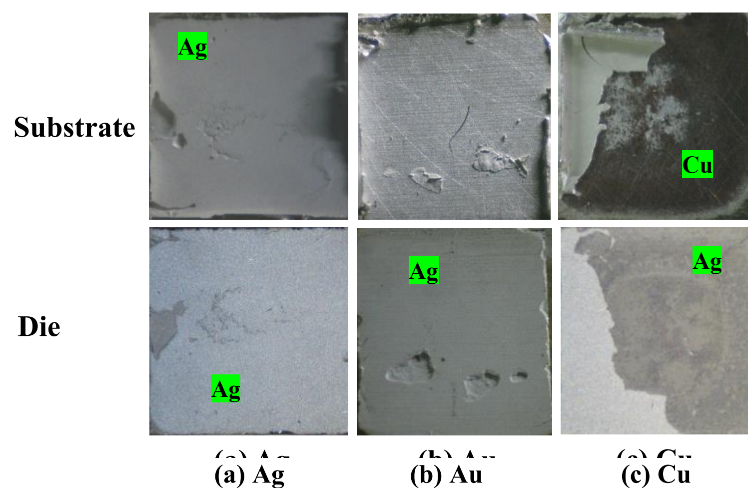


**Figure 5.49. Photographs of test vehicles after die-shear test with X-type Ag paste sintered at 0 MPa and drying step without die. (a) Ag plated substrate. (b) Au plated substrate and (c) Bare Cu substrate.**

Figure 5.49 shows some photographs of the substrates and dice after the die-shear tests summarized in Figure 5.48 for the X-type Ag paste. These pictures allow identifying the dominant failure mechanisms, which are similar but not exactly the same ones than for the K-type paste. In the case of Ag plated substrates (Figure 5.49(a)) the Ag sintered layer is broken (failure mode 2) but the main volume of the sintered layer is attached to the Ag plating on the substrate surface, while a very thin layer is observed on the backside of the die (attached to the Au plating of the die). The Au plated substrate (Figure 5.49(b)), also, shows the failure mode 2, but the major volume of the sintered layer is onto the die surface and only a thin layer onto the substrate. Figure 5.49(c) shows the situation for bare Cu substrates, wherein the Ag sintered layer is partially broken (failure mode 2) but a large area is detached from the Cu substrate. The detailed explanation about the different failure modes requires more in depth analysis, and the only conclusion that seems reasonable to be derived from the pictures in Figure 5.49 is that Cu surfaces experience again a significant oxidation that weakens the joint with the sintered Ag.

#### *5.6.3.2. Influence of the Substrate Surface Material at 7 MPa*

As it was already demonstrated in section 5.2, the sintering process assisted by a given sintering pressure, improves significantly the adherence of the Ag die-attach layer. This section is devoted to the study of this adherence improvement with increasing pressure for each kind of substrate surface material.

Figure 5.50 shows the die-shear strength values corresponding to the K-type paste sintered at 7 MPa, 285 ºC, 10 minutes and the two drying methods proposed in this work: with die (black squares) and without die (red circles). As expected, the values are an order of magnitude higher than those for the similar tests performed for Ag paste sintered at 0 MPa (for the Ag plating case, the die-shear strength goes from 2.13 kgf in Figure 5.46 up to 27.8 kgf in Figure 5.50). And once again, the die-shear strengths obtained for the paste drying step without die are higher than for test vehicles with Ag paste dried with die (for example, from 31.60 kgf up to 42.30 kgf mean values for bare Cu substrates). As it can be also observed from Figure 5.50, the highest die-shear strength values of all the present work have been found for the Au plated substrate with SiC dice and K-type Ag paste sintered at 7 MPa and drying step without die, with a

mean value of 52.30 kgf and a maximum sample reaching the 72 kgf. In any case the influence of the substrate surface material is residual, and the only surprising issue is the relatively low value obtained for the Ag plated substrates. In fact, looking at the pictures of Figure 5.51 corresponding to a test vehicle with Ag plated substrate after die-shear failure, it can be observed that the Ag plating layer has lifted-off from the Cu surface. This weak adhesion of the Ag plating explains the relatively low die-shear strength found and cannot be associated with any failure mode of interest for our study. For the rest of samples (Au plated and bare Cu substrates) the die-shear failure mode is type 4 (die fracture).

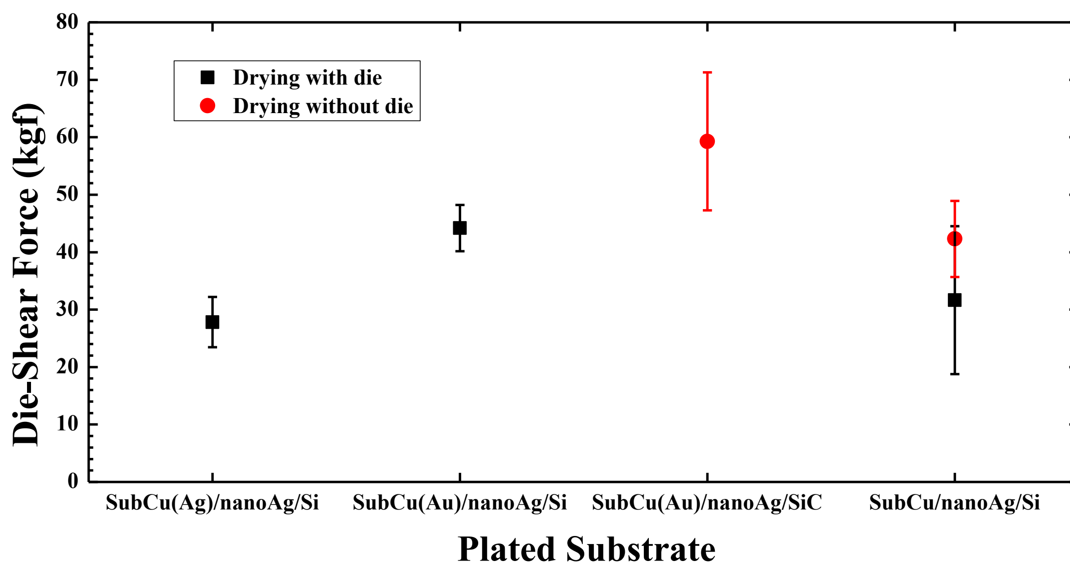


**Figure 5.50. Mean values of die-shear forces for test vehicles with different substrate surface materials: bare Cu, Ag and Au. K-type paste sintered at 7 MPa and drying step with die (black squares) and without die (red circles).**

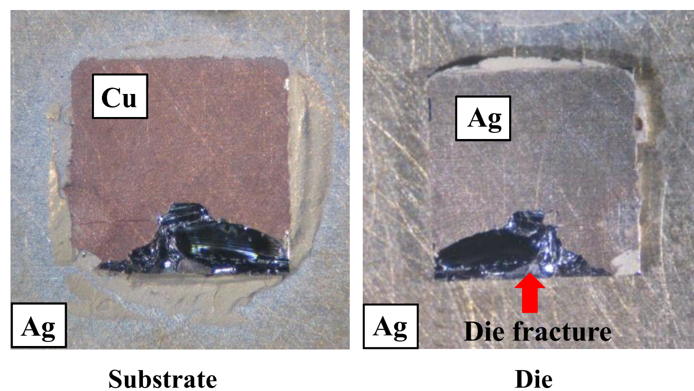


**Figure 5.51. Photographs of a test vehicle after die-shear with an Ag plated substrate, K-type Ag paste sintered at 7 MPa and drying step without die. The Ag plating layer has lifted-off from the Cu surface.**

## 5.7. Conclusions

In Chapter 5 we have analysed the effect of the main sintering process parameters on the final characteristics of the Ag die-attach layer. The aim of this study was twofold: first, to obtain useful information about the used Ag paste for its direct application in future power assemblies, and second to understand the main mechanisms governing the properties of the sintered Ag layers.

The first parameter analysed in the chapter was sintering pressure. Apart from several test vehicles manufactured as explained in chapter 4 at different pressures, specific samples of single Ag layers were also developed for microstructural inspection based on FIB microsections. The results revealed (as expected) that the densification of the Ag layer clearly improves with increasing sintering pressure, while the porosity diminishes. The adhesion of the Ag particles to the Cu substrate also improves at higher pressures, but a clear difference is observed between the sintered Ag in the central area and in the periphery of the layer. In the central part, the level of densification is lower than in the periphery, showing more but smaller voids. Nevertheless, at the edges of the Ag a thin layer appears at the Ag/Cu interface, showing a very good adhesion with the Ag and more detached zones with the Cu. The EDX analysis of this layer demonstrates that it corresponds to a Cu oxide, evidencing that the die-attach periphery is strongly influenced by the surrounding ambient (air in our case). This fact is also related with the difference of densification level achieved between the centre and the edge of the die-attach, as the periphery zone of the Ag layer, close to the ambient, can better decompose and eliminate the organic components of the original paste.

The higher densification level observed when increasing the sintering pressure is also in good agreement with the experimental reduction of the die-attach thickness (approximately 45 - 50 % in the range from 0 MPa to 11 MPa). It is interesting to stress that for sintering pressures higher than 5 MPa (approximately) the die-attach thickness "saturates" at a minimum value that doesn't decrease for higher applied pressures (up to 11 MPa). This effect is also reflected when looking at the "die-shear modulus" (the slope of the force versus displacement curves during die-shear tests). This parameter is related with the Young modulus of the Ag layer and our results evidenced that the shear-modulus increases with the sintering pressure (the Ag is "more stiff") but the

value saturates from approximately 5 MPa and above. In addition, as the die-shear force curve as a function of sintering pressure grows constantly in the 0 - 11 MPa range (from 2 kgf up to 55 kgf) and doesn't show any clear saturation around the 5 MPa it seems reasonable to derive that the Ag layer stops its densification at this point and the increase of the die-shear force is due to the adhesion improvement at the interfaces, mainly in the Cu substrate one. This effect is supported by the dominant failure modes after die shear, showing a transition from mode 1 (die / substrate detachment) to mode 4 (die fracture).

The second main process parameter analysed was sintering temperature. Temperature acts as a driving force for sintering processes as it is also the case of pressure and, in fact, the conclusions derived for both parameters have been similar. Higher temperatures improve densification of the Ag layer with better efficiency in the edges of the Ag layer than in the centre, but simultaneously, the Cu oxide layers at the Ag/Cu interface are thicker.

The die-shear forces recorded for sintering temperatures from 265 ºC up to 325 ºC show also a significant increase (around 40 % in the mentioned temperature range), although the mechanical properties of the Ag layer present almost no change, i.e. the die shear modulus doesn't change with increasing sintering temperature. This fact seems to indicate that the major improvements observed in the adherence curves come from best adhesion at the interfaces. This hypothesis is partially supported by the fact that the main failure mechanism after die-shear is die fracture for the higher temperatures.

A very interesting result obtained in this chapter is the experimental evidence that sintering pressure and temperature can be adjusted complementarily to obtain a given die-shear value (representing a particular die-attach quality). In this way, the sintering process can be adapted to different assembly conditions such as, for example, samples compatible with high pressures but not with high temperatures or vice versa.

All the results reported above were obtained when drying the Ag green paste with the die on top of the paste. The obtained results and, in particular, the microstructural differences between the Ag central zone and its periphery, suggested that the paste drying process was very critical. For this reason a specific study was performed in order

to evaluate the effect of the different drying methods already mentioned in chapter 4. In fact, the C-SAM images performed on different samples showed that a much more homogeneous and regular die-attach is obtained when drying without die, although from the practical point of view this process is more complex than simply proceed with the complete temperature profile with the die on place.

In addition, die-shear tests revealed higher fracture force values for the drying without die approach and, what it is perhaps more important, the die-shear force is independent of the final die-attach thickness. In contrast with this result, die-attach layers dried with die present a clear decrease of the die-shear force from a given Ag thickness (in the range of 100 µm in our case). This effect has been associated with unfavourable drying conditions when the die is on top of the fresh paste and its volume is significant. This hypothesis is reinforced by the fact that the die-shear modulus obtained for the samples dried with die are also significantly lower than those for the samples dried without die, meaning that the Ag layer is “softer” in the first case due to a higher content of voids (pores).

In parallel with the evaluation of the drying methods, a more practical assessment concerning the Ag thickness reduction during the sintering process was also performed. The main result is that the relationship between initial green paste and final die-attach thickness follows a linear function, allowing an easy prediction of this critical parameter from practical manufacturing data such as the screen-printing mask thickness. It has been determined that the Ag shrinkage effect is more important when using the drying method with die (60 %) than when using the drying step without die (40 %).

Another critical aspect to be considered in die-attach issues is the state of the surfaces and in particular, the substrate surface condition. The substrate surface roughness doesn’t show any significant effect on the die-attach adherence in the range from 80 nm to 800 nm when sintering with pressure (7 MPa). At zero pressure, it seems that die-shear strength decreases with surface roughness, but the adherence is very low. Improving the drying step (Ag paste dried without die) provides better results at zero sintering pressure and, for example, Ag plated substrates show quite acceptable adherence values for the K-type Ag paste. Nevertheless, the best results at zero pressure have been obtained with another paste, the X-type, which is able to provide good joints

(above the threshold given by standards) thanks to a specific formulation for this kind of processes.

In summary, this chapter provides practical information for processing die-attach layers using the Ag paste and process used and developed in this work, giving a relatively complete explanation about the effect of each process parameter on the characteristics of the final die-attach. Nevertheless, as many factors have been analysed, additional questions raised (such as the effect of sintering time when drying the paste with die, the link between Ag microstructure and SAM images, the role of periphery Cu oxide layers in die-shear tests, etc.). These subjects (among other) have been identified as interesting research topics in future works.

## 5.8. References

[1] H. Ogura, M. Maruyama, R. Matsubayashi, T. Ogawa, S. Nakamura, T. Komatsu, H. Nagasawa, A. Ichimura, and S. Isoda, "Carboxylate-Passivated Silver Nanoparticles and Their Application to Sintered Interconnection: A Replacement for High Temperature Lead-Rich Solders" Journal of Electronic Materials, vol. 39, no. 8, pp. 1233- 1240, May 2010.

[2] C. Fruh, M. Gunther, M. Rittner, A. Fix and M. Nowottnick, "Characterisation of silver particles used for the Low Temperature Joining Technology," *Electronic System-Integration Technology Conference (ESTC)*, 2010, pp. 1 – 5, September 2010.

[3] M. Knoerr, A. Schletz, "Power Semiconductor Joining through Sintering of Silver Nanoparticles: Evaluation of Influence of Parameters Time, Temperature and Pressure on Density, Strength and Reliability," in Proc. International Conference on Integrated Power electronics Systems, pp. 1-6, March 2010.

[4] A. Masson, C. Buttay, H. Morel, C. Raynaud, S. Hascoet and L. Gremillard."High-Temperature Die-Attaches for SiC Power Devices," in *Proc. 14th European Conference on Power Electronics and Applications (EPE)*, 2011.

[5] C. Buttay, A. Masson, J. Li, M. Johnson, M. Lazar, C. Raynaud, H. Morel. "Die Attach of Power Devices Using Silver Sintering Bonding Process Optimisation and

Characterization," in *Proc. High Temperature Electronics Network (HiTEN)*, pp. 1 - 7, 2011.

[6] W.Sabbah, R. Riva, S. Hascoët, C. Buttay, S. Azzopardi, E. Woirgard, D. Planson, B. Allard and R. Meuret, "Evaluation of silver-sintering die attach," in *Proc. International Conference on Integrated Power Electronics Systems (CIPS)*, March 2012, pp. 1 - 7.

[7] Y. Mei, G. Chen, Y. Cao, X. Li, D. Han, and X. Chen, "Simplification of Low-Temperature Sintering Nanosilver for Power Electronics Packaging," *Journal of Electronic Materials*, vol. 42, no. 6, pp. 1209-1218, 2013.

[8] K. S. Siow, "Mechanical properties of nano-silver joints as die attach materials," *Journal of Alloys and Compounds,* vol. 514, pp. 6– 19, 2012.

[9] R. M. German, Fundamentals of Sintering in Engineered Materials Handbook, vol. 4 ASM International, 1991

[10] G. E. Gazza, Fundamentals of Sintering in Engineered Materials Handbook, vol. 4 ASM International, 1991, pp. 296 - 303.

[11] L. A. Navarro, X. Perpiñà, M. Vellvehi, D. Sánchez and X. Jordà, "Sintering Process Analysis for Die-Attach of Power Packages for High Temperature Applications based on Silver Nano-Particles," in *Proc. XX Congreso Internacional Anual de la SOMIM*, , pp. 1-10, September 2014.

[12] K. Inamori, Advanced Ceramic Technologies & Products, Springer, 2012.

[13] L. A. Navarro, Xavier Perpiñà, P. Godignon, J. Montserrat, V. Banu, M. Vellvehi, and Xavier Jordà, "Thermomechanical Assessment of Die-Attach Materials for Wide Bandgap Semiconductor Devices and Harsh Environment Applications," *IEEE Transactions on Power Electronics*, vol. 29, no. 5, pp. 2261–2271, May 2014.

[14] S. Massetti , P. Godignon , E. Ciancetta , D. Lopez , R. Meurer, C. Baur and X. Jordà, "Development and Evaluation of a SiC Schottky Diode for Harsh Environment Space Applications," in *Proc. European Space Power Conference,* pp.1-9, 2011.

[15] W.W. Sheng, R.P. Colino, "Power electronic Modules, design and manufacture". CRC press 2005.

[16] (2012). [Online]. Available: http://www.nbetech.com/products.shtml

[17] (2014). [Online]. Available: http://www.nbetech.com/products.shtml

# CHAPTER 6 Analysis of High Temperature Die Attach Materials under Thermal Cycling

## 6.1. Introduction

Currently, the demand by new application scenarios of increasing operating device temperatures in power systems is requiring new die-attach materials with higher melting points and suitable thermo-mechanical properties. This makes the die-attach material selection, die-attaching process, and thermo-mechanical evaluation a real challenge in nowadays power packaging technology. Since this perspective, die-attach degradation is one of the main issues that limit the package reliability, and it is possible to minimize such effects by exploring new materials (e.g., Pb-free alloys), technological solutions (e.g., sintering of Ag particles, TLP (Transient Liquid Phase) or interconnection strategies (e.g., press-pack or bump bonding).

For this reason, this chapter presents a comparative analysis of the thermo-mechanical performances of established high-temperature die-attach materials as a solder alloys (AuGe and PbSnAg) and sintered layers (based on sintering of Ag particles) under harsh thermal cycling tests. This study is carried out using test vehicles formed by four dice (considering Si and SiC semiconductors) and Cu substrates (bare Cu and Au plated surfaces), which have been described in chapter 4. The thermally cycled test vehicles have been evaluated using the methods described in chapter 3 (die-shear tests, optical and acoustic microscopy inspections) and to support the interpretation of the results, additional thermo-mechanical simulations and warpage measurements have been also carried out.

The Ag paste used in this study was the NBE Tech Type K, which has been already introduced in detail in chapters 4 and 5, and is representative for this kind of solutions. It is worth mentioning that the tests corresponding to sintered Ag layers on bare Cu substrates have special interest as little information is still available for such assemblies. Many results are published about Ag sintering on plated Cu surfaces, but there is a

practical interest on avoiding Cu plating with Au or Ag, as this additional manufacturing step increases the final costs.

### 6.2. Initial Evaluation of High Temperature Die-Attach Materials

The die-attach materials considered in our study will be the Ag sintered layers processed as described in chapters 4 and 5, and two well established solder alloys: Au88Ge12 and Pb95.5Sn2Ag2.5. The former offers exploiting the sintering phenomenon benefits (moderate temperature processing, in this particular application < 300 ºC) as well as the outstanding physical properties of Silver: high melting point (961 ºC), thermal conductivity (430 W/m.K), and electrical conductivity (0.63 x $10^6$ $\Omega^{-1}$cm$^{-1}$). On the other hand, Au88Ge12 (hereafter termed as AuGe) is a solder alloy compatible with standard soft-soldering equipment that presents acceptable thermal (44 W/m.K) and electrical conductivities (0.2 x $10^4$ $\Omega^{-1}$cm$^{-1}$), a moderate coefficient of thermal expansion (13.4 ppm/ºC), and a relatively high Young modulus (between 63 and 72 GPa) [1, 2, 3, 4]. It has a melting point of 356 ºC and its suitability as a harsh environment die-attach material has been demonstrated, for instance, in [5]. Finally, Pb95.50Sn2Ag2.50 belongs to the family of PbSnAg alloys, which have been used from decades in the industry as a standard die-attach material and, currently, are being progressively removed due to its lead content. Its melting point (300 ºC) makes it a good candidate for high temperature applications, showing also acceptable physical parameters: thermal conductivity (23 W/m.K), CTE (30 ppm/ºC) and electrical conductivity (0.35 x $10^5$ $\Omega^{-1}$cm$^{-1}$). In comparison to AuGe, it presents a lower Young modulus (13.80 GPa [6]), which will cause lower thermo-mechanical stresses to the die-attach layer when integrated in the final package configuration and also during operation.

Therefore, the physical properties of the aforementioned materials make them suitable for high temperature applications, but they present different thermo-mechanical properties. It is expected then to observe different results when they are cycled and the objective of this study was to compare and analyse their response under the same conditions. The critical point is that die-attaches resulting from sintering of Ag particles may not present the same properties as the structure of the sintered Ag bulk material and

the Ag interfaces with substrate and die, depend on the processing conditions [7, 8] as it was already explained in chapter 5.

A first evaluation of the starting die-attach materials (before any ageing or cycling degradation process) was initially performed. Figure 6.1 shows the C-SAM images acquired for the three die-attach materials and Si dice (2.80 mm x 2.80 mm) with Ti/Ni/Au on their backside, before any applied stress. Figure 6.1(a) shows the image for AuGe and an Au plated Cu substrate, Figure 6.1(b) corresponds to PbSnAg onto bare Cu and Figure 6.1(c) shows the SAM for sintered Ag (7 Mpa, 285 ºC, 10 minutes and drying step with die) onto bare Cu substrate. The images show that the Ag sintered die-attach provides a very low level of voids, similar to the one provided by the solder alloys. Therefore, it can be expected that the sintered layer will show a good adhesion. With the aim at confirm this prediction, die-shear force tests were performed and the results are shown in the box plots of Figure 6.2. In the graph, “subCu” is the abbreviation for bare Cu substrate and “subCu(Au)” is the abbreviation for Au plated Cu substrate. In the case of the die-attach based on Ag nanoparticles, the abbreviation is “nanoAg”.

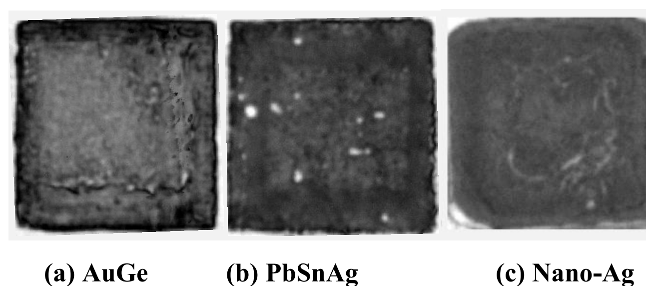

**(a) AuGe (b) PbSnAg (c) Nano-Ag**

**Figure 6.1. C-SAM images of different die-attach materials for 2.8 mm x 2.8 mm Si dummy chips.**

The first relevant consideration derived from Figure 6.2 is that all obtained values are in agreement with the MIL-STD-883H standard and, consequently, all die-attaches are suitable in principle for developing practical systems. In the particular case of AuGe, Au plated and bare Cu substrates were used. In the box plots, one can observe that although Au plated substrates show higher dispersion, they also show higher die-shear forces (35 kgf mean value) than for bare Cu surface substrates (18 kgf mean value). The possible reason is that the Au surface finishing (formed in fact by Ti (100 nm) / Ni (500 nm) / Au (200 nm) layers deposed by sputtering) prevents from intermetallic formation and oxidation of the Cu and Ge elements during processing. [9], [10]. Concerning the

Ag sintered layers on bare Cu substrates, they were obtained using a drying process with die and 3 MPa and 7 MPa / 285ºC / 10 minutes sintering parameters. The die-shear force for the 3 MPa case (17 kgf) is similar than the value obtained for PbSnAg (19.00 kgf), while the die-shear for sintered Ag at 7 MPa (43 kgf) is in the range of the AuGe solder (35 kgf). In conclusion, the die-shear mean values and dispersion of sintered Ag layers are comparable with those obtained for AuGe and PbSnAg solder alloys.

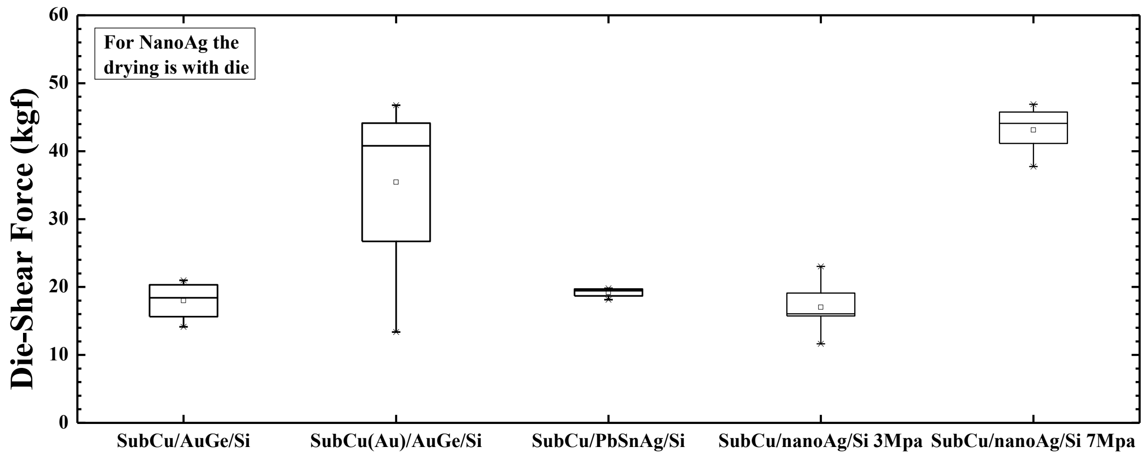


**Figure 6.2. Die-shear forces for Si dice and different die-attach materials. Sintering performed at 3 and 7 MPa / 285 ºC / 10 minutes, using K-type Ag paste dried with die.**

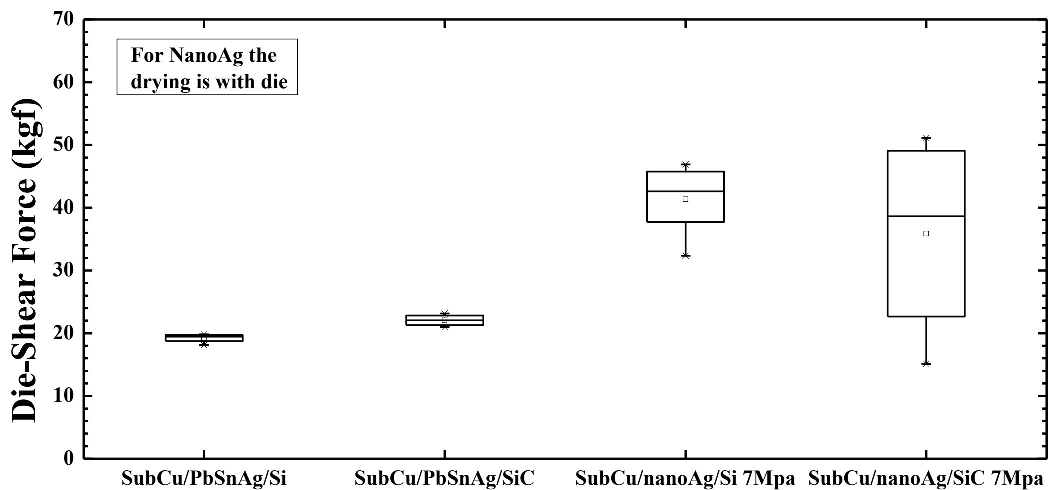


Box Chart o
Box Chart o
Box Chart o

**Figure 6.3. Die-shear results for test vehicles based on Si and SiC chips joined with different die-attach materials onto Cu substrate. Sintering performed at 7 MPa / 285 ºC / 10 minutes using K-type paste dried with die.**

Another element to take into account in our comparative study is the semiconductor die material used in the test vehicles. In this sense, Figure 6.3 shows the results aimed at comparing the adherence of Si and SiC dice attached to the Cu substrates. The used SiC

dice are Schottky barrier diodes with the same size and similar backside metallization than the Si dummies (see chapter 4) [11]. Similar die-shear force values are obtained for Si and SiC dice joined with PbSnAg onto Cu substrates (19 kgf and 22 kgf respectively). For the case of nano-Ag sintering the values are also similar (43 kgf for Si and 36 kgf for SiC, respectively) with an applied sintering pressure of 7 MPa. For the Si case and for both die-attach materials, the dispersion is lower than for SiC dice because the Si dummy surfaces are completely flat, whereas the SiC diodes show a certain relief in the top surface (several microns) due to the passivation and the thick anode metal pattern, introducing slight pressure differences among dice during sintering. In any case, the adherence properties are mainly governed by the device backside metallization structure and, as expected, similar die-shear values are found indistinctly for Si and SiC chips.

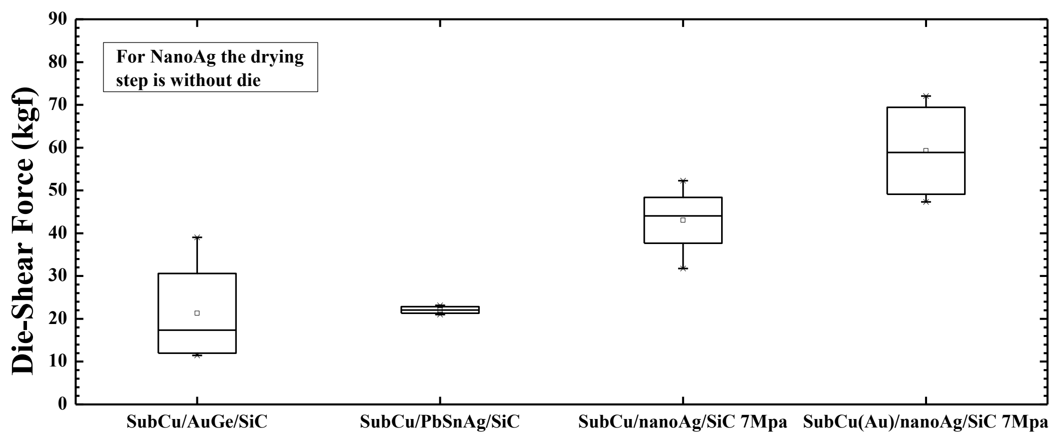


**Figure 6.4. Die-shear forces for different die-attach materials. Sintering performed at 7 MPa / 285 ºC / 10 minutes using K-type paste dried with die.**

Finally, another relevant aspect to be considered for the comparative analysis of the die-attach materials before thermal cycling tests is the difference between the two drying methods already described in chapter 5 for Ag sintered layers. Figure 6.4 shows the die-shear force values for Ag die-attach dried without die and sintered at 7 MPa / 285ºC / 10 minutes, compared with the values obtained for the solder alloys (AuGe and PbSnAg). In all cases, SiC dice and Cu substrates have been used except for Ag sintered layers where Au plated substrates have also been assessed. As it can be observed, the die-shear values for sintered Ag without die during the drying step are higher than those for AuGe and PbSnAg solder alloys. In addition, higher adhesion force is obtained for

Au plated Cu substrates (59 kgf) than for bare Cu substrates (43 kgf), although both values are very high, denoting in principle good quality joining layers.

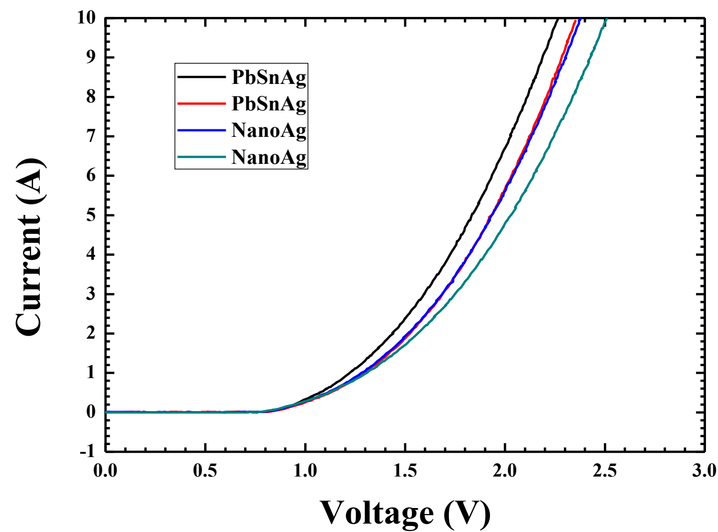


**Figure 6.5. I-V forward characteristics of SiC Schottky diodes attached to the Cu substrate with PbSnAg and sintered Ag layers. Sintering performed at 7 MPa / 285 ºC / 10 minutes using K-type paste dried with die.**

The initial validation of the analysed die-attach solutions included also electrical measurements. For this purpose we obtained I - V curves for several SiC Schottky diodes attached by sintering Ag particles and PbSnAg solder. Figure 6.5 shows the aforementioned curves and any practical difference between the sintered Ag and soldered PbSnAg die-attach layers has been appreciated in the typical measurement range of such devices. In fact, the differences between curves can be attributed to the dispersion of the device characteristics.

## 6.3. Thermal Cycling Tests

In the literature, different testing methods for evaluating die-attach degradation have been reported (ageing accelerated test at constant temperature, power cycling test, thermal cycling, thermal shock test, etc.) [12, 13, 14]. Among them, we have focused on thermal cycling for our investigations. There are several standards concerning the thermal cycling of electronic parts. In this study, it has been proposed a temperature cycling profile partly inspired in both MIL-STD-883H and MIL-STD-750E. The severity or destructive capability of the profile depends on: its ramp slope (heating and

cooling), dwell time, and swing of temperature, defined by maximum temperature ($T_{MAX}$) and minimum temperature ($T_{MIN}$). The die-attach degradation increases with increasing the temperature ramp slopes, because fast temperature changes do not allow the material relaxation. On the other hand, it has been reported in [15, 16] that the die-attach lifetime decreases when the dwell time increases. Typical values of the dwell time in thermal cycling experiments are between 7 - 15 minutes and, for example, the MIL-STD-883H standard suggests 10 min. Bearing in mind all this information, the selection criterion for the slopes was based on the limits of the used test equipment (described below) which, in our case, is 40 ºC/min for the positive or heating ramp, 10 ºC / min for the negative or cooling ramp and 15 minutes for the dwell time.

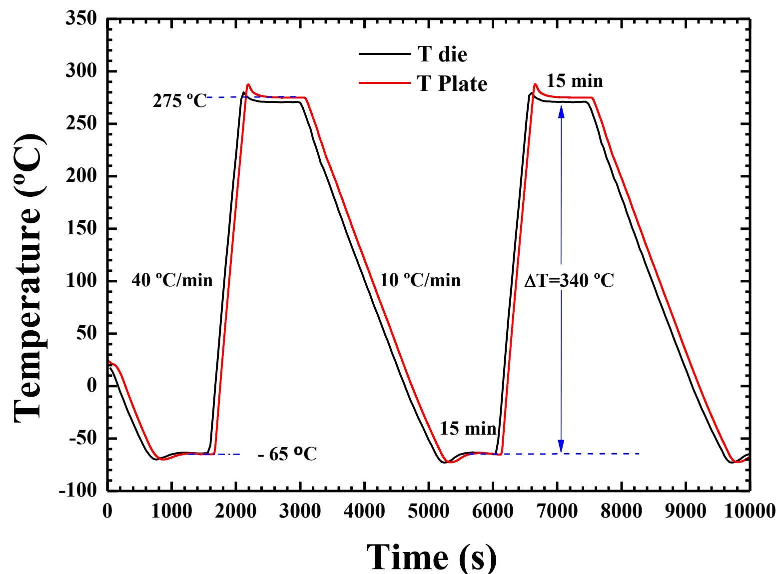


**Figure 6.6. The proposed thermal cycling profile implemented by the thermal cycling system used in this work (section 6.3.1). This figure also depicts the temperature profile experienced by one die in a test vehicle (in black, $T_{die}$) and the value fixed by the controller on the base plate (in red, $T_{Plate}$).**

Regarding to the temperature swing, the MIL-STD-883H standard defines several possibilities depending on the components and materials to be analysed. Two test conditions can be contemplated in our case. The former establishes $T_{MAX}$ = 200 ºC and $T_{MIN}$ = - 65°C and the latter fixes $T_{MAX}$ = 300 ºC and $T_{MIN}$ = - 65 ºC. This last extreme temperature condition is suitable for AuGe and sintered Ag nano-particles die-attaches (melting point 359 ºC and 961 ºC respectively), but it is excessive for PbSnAg alloys (in this particular case the melting point is around 300 ºC). For this reason, we have selected $T_{MAX}$ = 275 ºC and $T_{MIN}$ = -65 ºC (see Figure 6.6), because this value for $T_{MAX}$

allows us to study under the same conditions, die-attach materials with melting points between 280 ºC and 360 ºC (AuSn, PbSnAg, AuGe, AuSi, sintered Ag). It is also worth to point out that the designed temperature cycle is very similar to the one used for simulating real operation conditions in some space exploration missions [17] and that it produces severe overstress situations when compared with conventional lower temperature swing cycles [18].

### 6.3.1. Experimental Set-up and Evaluation Protocol

For implementing the thermal cycles shown in Figure 6.6, a relatively complex heating / cooling system is required. Few thermal cycling systems based on ovens are available for the extreme temperatures required in harsh environment electronics. In addition, systems with moving parts (such as transport belts) are relatively complex. For this reason, we oriented our investigations towards cycling systems based on cold and hot plates. For this purpose, Figure 6.7 shows a schematic diagram of the system and Figure 6.8 shows a picture of the main elements of the experimental set-up developed. This set-up is based on a system from the US based INSTEC company, which has been modified and adapted in the framework of the present study, to allow long term and safe thermal cycling tests. As it can be observed, an Al plate inside a closed chamber can be heated up to 400 ºC and cooled down to -100 ºC with a liquid Nitrogen circuit. The closed chamber can be filled with Nitrogen gas to avoid oxidation of the samples. Figure 6.7 represents also test vehicles on the hot / cold plate and the inset in Figure 6.8 shows a detail of one of the test vehicles used with 4 dice.

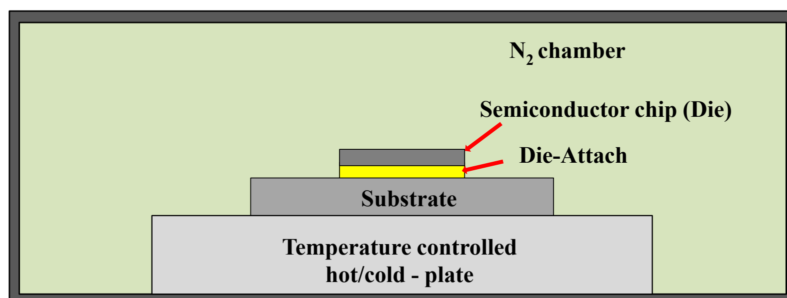


**Figure 6.7. Scheme of the main elements of the experimental set-up for thermal cycling experiments.**

With the aim of ensure a correct application of the targeted temperatures in the test vehicles during thermal cycling, a validation assessment was performed. Figure 6.6 shows the measured temperature variation at die level using a test vehicle with SiC Schottky diodes ($T_{die}$, in red) and the temperature monitored at the hot plate ($T_{Plate}$, in black) and demonstrates that the thermal cycling equipment correctly applies the targeted profile to the devices assembled in the test vehicles. For the $T_{die}$ temperature measurement, the voltage drop of SiC diodes at low current levels (10 mA) has been used as a thermo-sensitive parameter. The good agreement between the temperature profile monitored in the hot plate and the value imposed in the dice, means that the thermal response of the test vehicle is faster than the cycle change and, consequently, cycled samples are maintained at the same temperature during the tests.

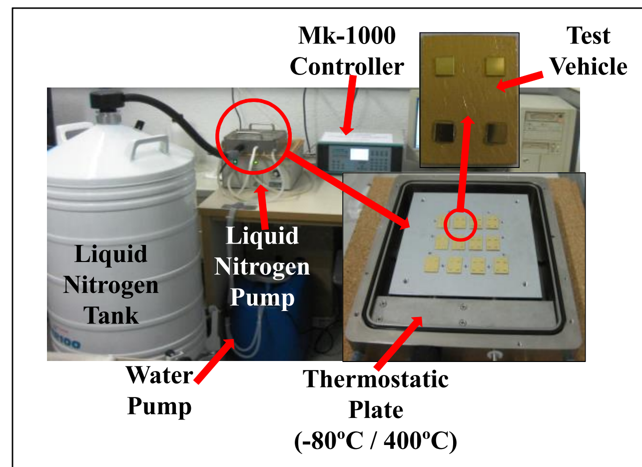


**Figure 6.8. Thermal cycling experimental set-up developed in this work.**

In order to analyse the evolution of die-attach layers before and during thermal cycling tests, a systematic experimental protocol has been defined (see Figure 6.9), based on the existing equipment available at IMB-CNM. Basically, this procedure analyses the evolution of the defects in the interfaces of the die-attach with a Scanning Acoustic Microscope (SAM, non-invasive inspection system based on ultrasonic waves), die-shear tester and visual inspections (see chapter 3 for additional information about these systems and techniques). The SAM (or C-SAM) inspections performed before die-shear tests, monitored the degradation of the die-attaches and provided information about the degradation pattern of the die-attach layer during cycling. In fact, the stresses induced during the thermal cycling will drive the defect propagation and

will degrade the die-attach, inducing a die-shear force reduction [19]. In detail, the established procedure is as follows:

1) Initially all samples are analysed using the SAM (Sonoscan GEN-5). This reveals the possible defects in the interfaces of the structure, such as scratches, voids or cracks.

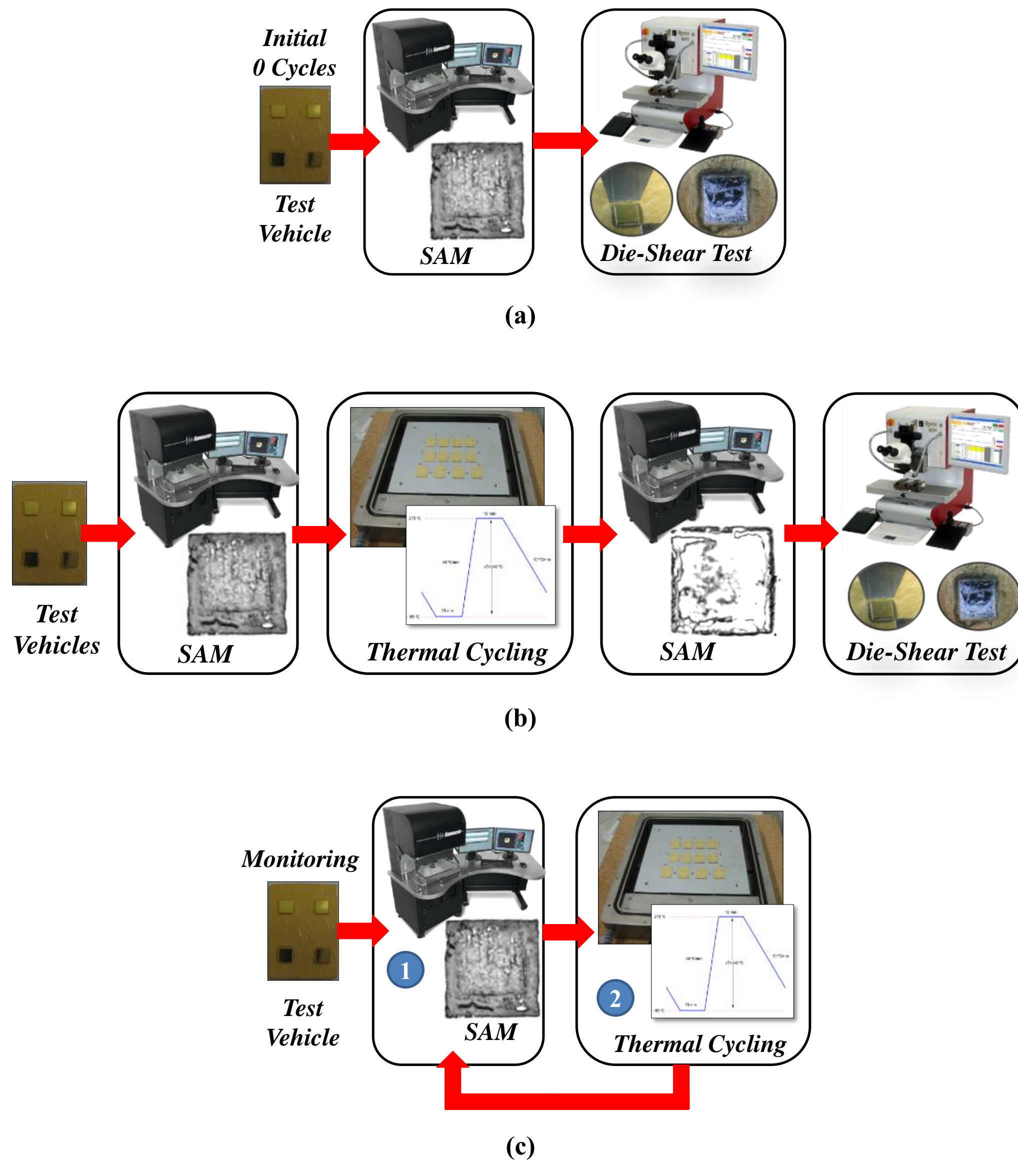


**Figure 6.9. Experimental protocol to analyse the evolution of die-attach layers before and during thermal cycling tests. (a) For initial sample at 0 cycles. (b) Test vehicles under thermal cycling. (c) Monitoring (control) sample.**

2) Before starting the thermal cycling (0 cycles), one sample is selected for obtaining initial values of the die-shear force using a Royce 650 die-shear tester system (Figure 6.9(a)).
3) The remaining samples are placed in the INSTEC hot / cold plate equipment to start the thermal cycling process (Figure 6.9(b)).
4) Approximately every 100 cycles (this value can vary depending on the observed evolution of the samples degradation) we take out a sample for obtaining SAM images, and the other samples continue the cycling process.
5) After the SAM inspection of each sample, we evaluate the die-shear force of the 4 dice (Figure 6.9(b)).

In the same sense, the data for each point comes, at least, from a test vehicle (i.e., 4 chips), but when high dispersion is observed, two test vehicles per point (8 chips) have been used to get enough statistical data for their interpretation. In this way, we can distinguish the effects coming from die-attaching process dispersion or thermal cycling tests. Finally, it is worth to point out that during thermal cycling experiments, one of the test vehicles under test is considered a control sample and SAM images are acquired regularly allowing monitoring the die-attach degradation evolution in the same sample (Figure 6.9(c)).

**6.4. Thermo-Mechanical Stress Analysis in the Test Vehicles**

One of the most important challenges in high temperature power electronics is to minimize the thermo-mechanical stresses, which appear in the packages under working conditions and in harsh environments, especially at the die-attach level. In this sense, we have used finite elements simulation tools for understanding the thermo-mechanical loads in the test vehicles used during our thermal-cycling experiments.

Thermal stresses are due to the physical properties mismatch among materials used in power electronic packages. In fact, the mismatch of thermal expansion coefficient (CTE) of the materials involved in the package structure is one of the most influential parameters in thermo-mechanical degradation processes, since it provokes the thermal stresses. The principle of the thermo-mechanical degradation can be briefly summarised as follows. First, the thermal strain arises by the deformation of expansion or

contraction due to the temperature changes in the absence of mechanical loads. In fact, the thermal strain is not exactly proportional with temperature change. Nevertheless, for relatively small temperature changes, this strain can be linearly related to the temperature change [20]. Finally, the result of the temperature change is a thermal stress, which is proportional to the thermal strain assuming an elastic behaviour, with its magnitude proportional to the Young modulus.

In this context, computer simulation is an important tool for studying this kind of phenomena. In fact, computer simulation has become an essential part of science and engineering. Numerical analysis of components, in particular, is important when developing new products or optimizing designs. Today a broad spectrum of options for simulation is available and researchers use everything from basic programming languages to various high-level packages implementing advanced methods. A computer simulation environment is simply a translation of real world physical laws into their virtual (mathematical) form. How much simplification takes place in the translation process helps to determine the accuracy of the resulting model.

In this framework, COMSOL Multiphysics is an interactive environment tool for modelling and solving scientific and engineering problems. When solving the models, COMSOL Multiphysics uses the proven finite element method (FEM). The software runs the finite element analysis together with adaptive meshing (if selected) and error control using a variety of numerical solvers. The studies can make use of multiprocessor systems and cluster computing, and one can run batch jobs and parametric sweeps. In the context of this study, it has been used basically steady-state thermo-mechanical simulations of COMSOL for analysing the stresses and strains induced in test samples including semiconductor chips, die-attach layers and substrates [21].

### 6.4.1. Thermal Stress Module in COMSOL Multiphysics

In the practical case of device operation, heat is generated in the semiconductor and dissipated into the package obeying the equation of heat diffusion. In this case the "heat equation" will determine the temperature field, which in turn allows us to study the thermo-mechanical effects. In the framework of the present study, the operation has been limited to the case where a controlled hot / cold plate imposes the entire sample

temperature because this configuration describes the experimental set-up that will be used for thermal cycling investigations (see Figure 6.7). For this particular target, COMSOL Multiphysics has a Thermal Stress Module with a predefined one-way coupling for thermal-structure interaction (thermal stress), which combines a Solid Mechanics Module with the Heat Transfer Module. By default, COMSOL Multiphysics takes advantage of the one-way coupling and solves the problem sequentially: first solves for temperature and then performs the stress-strain analysis using the computed temperature field from the heat transfer equation [20, 22, 23].

Heat is energy in transit that appears when two objects near one another are at different temperatures, and then heat flows from the hotter object to the colder object. There are three modes the heat can transfer: conduction, convection and radiation. As conduction is the main mode of heat transfer within die and package, which is our case of study, we only applied this transfer mode in the simulation. Conduction is defined as the transfer of thermal energy from a region of elevated temperature to a region of lower temperature through direct molecular contact within a medium or between media in physical contact. The basic set of equations used by the solver is described below [20, 22, 23].

On the basis of experimental observations, the three dimensional form of Fourier's law of heat conduction states that in a homogenous substance, the local heat flux $q$ is proportional to the local temperature gradient $\nabla T$ as:

$$q = -k \cdot \nabla T \qquad (1)$$

Furthermore, the fundamental law governing for heat transfer is the first law of thermodynamics, commonly referred to as the principle of conservation of energy. Based on this principle, the following equation governing pure conductive heat transfer for an isotropic medium is:

$$\rho C_p \frac{\partial T}{\partial t} + \nabla \cdot (-k \nabla T) = Q \qquad (2)$$

$Q$ generated heat per unit volume (W/m$^3$)

$\rho$ is the mass density of the medium (kg/m$^3$)

$C_p$ is the specific heat capacity at constant pressure of the medium (J/kg.K)

$T$ is the absolute temperature (K)

$t$ time (s)

$k$ is the thermal conductivity of the medium (W/m.K)

$q$ conductive heat flux (W/m$^2$)

On the other hand, for solid mechanics module the Cauchy's first law of motion in steady-state is applied where the basic equation is an equilibrium equation stating that the gradient of the Cauchy stress tensor is equal to the applied volume force $F_V$.

$$-\nabla \cdot S = F_V \tag{3}$$

$S$ cauchy stress tensor (N/m$^2$)

$F_V$ volume force (N/m$^3$)

And for linear elastic materials, the strain tensor is written in terms of the displacement gradient as:

$$\varepsilon = \frac{1}{2}(\nabla u + \nabla u^T) \tag{4}$$

$\varepsilon$ strain tensor

$u$ displacement

In the same sense, the Duhamel-Hooke’s law relates the stress tensor to the strain tensor and temperature:

$$S = S_0 + \mathrm{C} : (\varepsilon - \varepsilon_0 - \varepsilon_{th}) \tag{5}$$

$\mathrm{C}$ is the 4$^{th}$ order elasticity tensor

$:$ stands for the double-dot tensor product (or double contraction)

$S_0$ initial stresses

$\varepsilon_0$ initial strains

Wherein the thermal strain is:

$$\varepsilon_{th} = \alpha\,(T - T_{ref}) \tag{6}$$

$T$ current temperature

$T_{ref}$ reference temperature

### 6.4.2. Boundary Conditions and Mesh Definition for the Thermo-Mechanical Simulations

There are several boundary conditions, which should be chosen properly to obtain suitable results in the simulations. In the case of the COMSOL Thermal Stress Module, boundary conditions must be established first for the Heat Transfer Module and second for the Solid Mechanics one. Boundary conditions for heat transfer and solid mechanics are mentioned, and then brief descriptions of the main boundary conditions are reviewed below.

In general, boundary conditions for the Heat Transfer Module are: temperature, thermal insulation (the default boundary condition), outflow, symmetry, convective cooling, heat flux, inflow heat flux, open boundary, surface-to-ambient radiation, periodic heat condition and highly conductive layer features. In addition, it is possible to specify a boundary heat Source. In 3D and 2D it is also possible to add a point heat source. 3D furthermore supports a line heat source [22].

In the case of the boundary conditions for the Solid Mechanics the constraints are available on exterior boundaries, and in some cases on domains, edges or points. Boundary conditions for the Solid Mechanics Module are: free (default boundary condition, it means that there are no constraints and no loads acting on the boundary), fixed constraint (available on domains, boundaries, edges, and points), prescribed displacement (available on domains, boundaries, edges, and points), prescribed velocity (for time-dependent and frequency-domain studies; also available for domains), prescribed acceleration (for time-dependent and frequency-domain studies; also available for domains), symmetry, anti-symmetry, rigid connector and roller. If there are

subsequent boundary conditions specified on the same geometrical entity, the last one takes precedence [23].

To simulate our case of study (test vehicle diagram of Figure 6.7) in COMSOL Multiphysics, three blocks are essential for establishing their thermo-mechanical properties (die, die-attach and substrate), the other elements (hot/cold plate and $N_2$ chamber) are defined with boundary conditions.

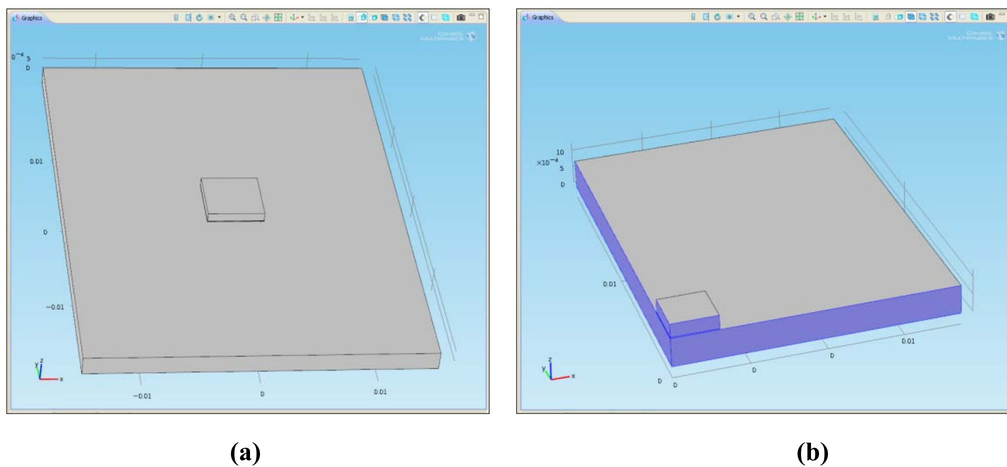

(a) (b)

**Figure 6.10. (a) Full geometry of a basic die/die-attach/substrate assembly. (b) A quarter of the full geometry with symmetry boundary conditions.**

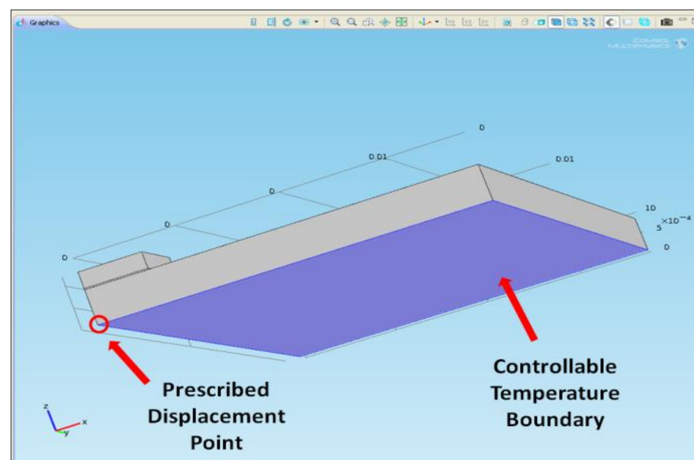


**Figure 6.11. Boundary conditions on the structure backside: Prescribed displacement in one point (centre) and fixed temperature surface.**

In the case of mechanical boundary conditions, symmetry boundary condition is essential in order to greatly reduce the size of a model and hence reduce the computing requirements and solution time. For instance, Figure 6.10(a) shows the full geometry for

a basic die / die-attach / substrate assembly where the dimensions are 15 mm x 20 mm x 0.8 mm for the Cu substrate; a 300 µm thick 2.7 mm x 2.7 mm centred SiC die; and a 30 µm thick AuGe die-attach layer. Figure 6.10(b) shows the quarter of the full structure using the symmetry boundary condition; in this figure one can observe the boundaries in blue colour for establishing the symmetry condition.

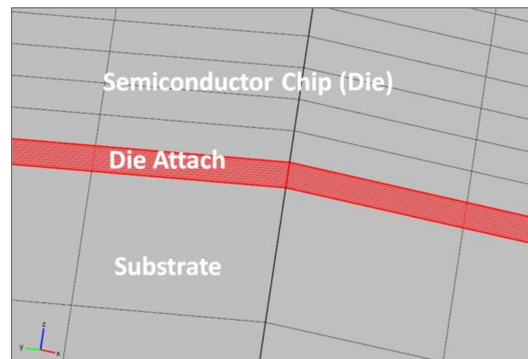


**Figure 6.12. Zoom in one corner of the die-attach layer showing the simulation mesh.**

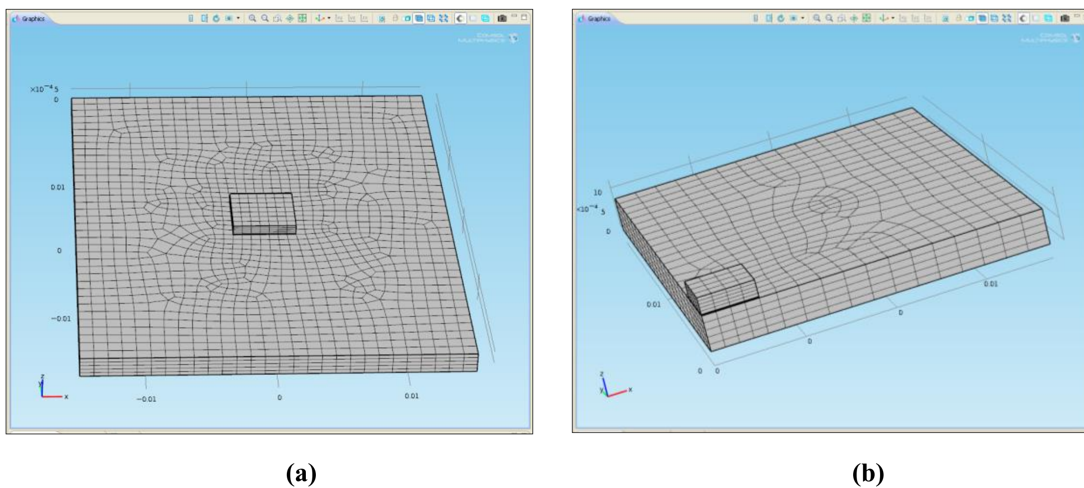

**(a)** **(b)**

**Figure 6.13. (a) Full Geometry mesh (6980 points). (b) Quarter of full geometry mesh (1910 points).**

Concerning the mechanical boundary conditions of the basic structure defined in Figure 6.10, we prescribed (fixed) displacement in one point in the centre of the back-side of the Cu substrate (Figure 6.11); together with the body load option to simulate sample weight (gravity effects). On the other hand, the thermal boundary conditions are adiabatic around all parts of the structure to simulate the Nitrogen chamber, except on the Cu backside where a fixed temperature is defined to simulate the hot plate effect

(see Figure 6.11). These conditions neglect convection effects inside the chamber, in front of the conduction mechanisms between test vehicle and hot-plate.

Besides the boundary conditions, meshing is another critical issue to be taken into account. The mesh features enable the discretization of the geometry model into small units of simple shapes, referred to as mesh elements. The mesh generator discretizes the domains of the structure to be simulated into tetrahedral, hexahedral, prism, or pyramid mesh elements whose faces, edges, and corners are called mesh faces, mesh edges, and mesh vertices, respectively [24]. Figure 6.13 shows the mesh used in this study, which is the most suitable due to the geometry of our model (Figure 6.10).

In order to perform simulations with the same predictive results in a reasonable time, the meshing process should be optimized reducing the final number of elements of the considered structure. Two approaches can be addressed: non-equal number of elements along the structure and use of symmetry boundary conditions. The first strategy consists in introducing a higher number of elements in material layers and interfaces where big changes of strain, stress or temperature are expected. In this way, the convergence of simulation results is ensured. For instance, this usually occurs in the interfaces between materials

In our case, important strains will be also concentrated at the die-attach, as it will be shown further on. For this reason, a higher number of nodes along the Z axis have been defined in the die-attach layer and interfaces in comparison to the rest of the simulated structure, as shown in Figure 6.12. On the other hand, symmetry boundary conditions have also been considered in our modelling. To illustrate this, the computation time required with a full structure of 6980 elements (see Figure 6.13(a)) has been compared to that of a quarter part of this structure with 1910 elements (see Figure 6.13(b)), in which the aforementioned boundary symmetry conditions have been applied. As a result, a drastic reduction of computation time has been observed: full and symmetric structures have required computational times of 2705 s and 60 s, respectively.

### 6.4.3. Analysis of Basic Thermo-Mechanical Phenomena on Single Die Structure

In order to analyse the main thermo-mechanical effects appearing in typical device / die-attach / substrate assemblies, the basic structure already introduced in Figures 6.10 to 6.13 was simulated with COMSOL Multiphysics, considering the size and materials of the analysed test vehicles. Figure 6.14(a) shows its top view and dimensions, and Figure 6.14(b) a detail of a die corner, indicating the involved materials. One of the most influential properties is the CTE, because it originates the bending (strain) of the different elements. On the other hand, the Young modulus and Poisson ratio are the responsible for the magnitude of stresses induced in the structure.

As it was already stated, the geometry of the test vehicle is formed by a 15mm x 20mm x 0.8mm Cu substrate; a 300 µm thick 2.5mm x 2.5mm SiC die on the centre; and a 30 µm thick AuGe die-attach layer (see Figure 6.14).

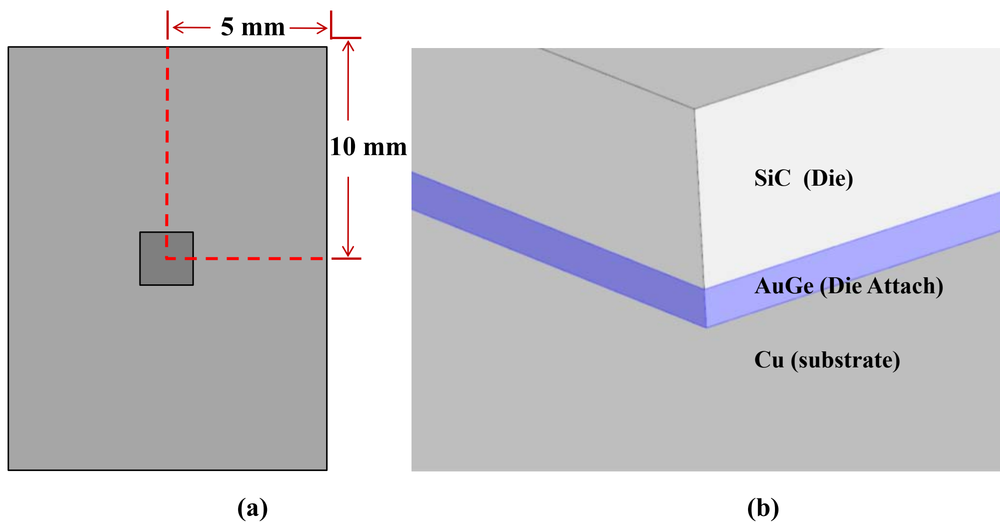


**(a)** **(b)**

**Figure 6.14. (a) Geometry of the basic single die test structure. (b) Detail of one of the corners of the SiC die, AuGe die-attach layer and Cu substrate.**

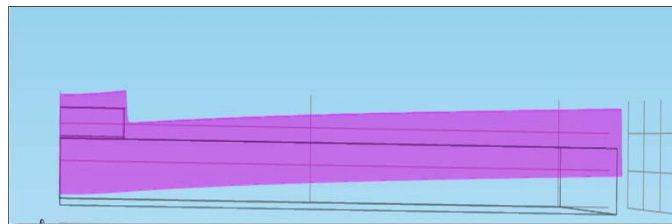

**(a)**

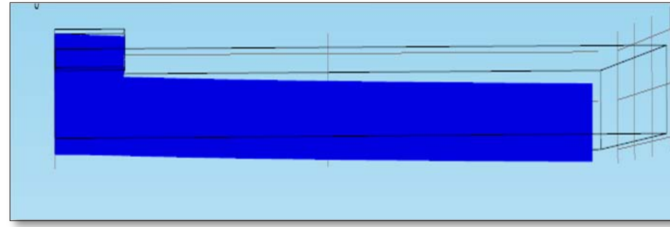

**(b)**

**Figure 6.15. Basic single die sample (a quarter of the structure) under thermal load of 200 ºC (a) and -65ºC (b). The vertical axis is magnified a scaled factor x 30.**

The simulation parameters for each material are those compiled in the Table 3.1 of chapter 3 and Tables 4.1 and 4.2 of chapter 4. The thermo-mechanical effects are simulated with the linear elastic model equations explained in section 6.4.1. The geometry of the structure is discretized using the mesh shown in Figure 6.13(b) with a total of 16180 points. The mechanical boundary conditions are established with a fixed point in the centre of the back-side of the Cu substrate, the activation of the "body load" option to account for the sample weight and the symmetry boundary conditions (Figure 6.13(b)).

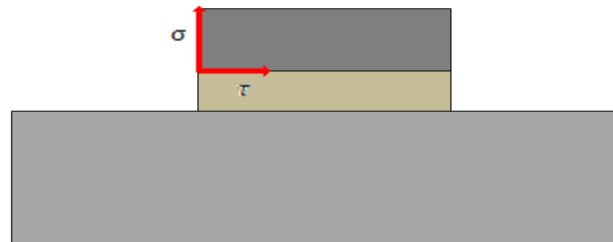


**Figure 6.16. Schematic cross section of the test structure showing the normal (σ) and shear (τ) components of the stress at the die/die-attach interface.**

The thermal boundary conditions are adiabatic around the different parts of the structure, except on the Cu backside where an isothermal surface is defined. This set of boundary conditions describe the behaviour of the sample lying over a temperature controlled plate.

Figure 6.15(a) shows the bending of the structure under a thermal load of 200 ºC. In order to appreciate this bending of $1.6396 \times 10^{-5}$ m at the edges of the Cu substrate, the vertical axis is magnified by a scaled factor of 30. On the other hand, Figure 6.15(b) shows the bending of $-5.352 \times 10^{-6}$ m under a thermal load of - 65 ºC. As it can be

observed, the sign of the flexions depends on the sign of the temperature. In general, the bodies expand under a positive temperature increase and contract under a negative temperature decrease. Each material alone has a tendency to expand or contract differently by their difference in CTE. Consequently, the bowing in Figure 6.15 is the consequence of the differential deformation of the bodies.

As a consequence, stresses arise in the structure, in particular between the interfaces of the bodies enabling the main degradation mechanisms under thermal cycles. Figure 6.16 shows a schematic cross section of the test structure representing the vertical or normal component of the stress (σ) and the horizontal or shear stress component (τ), evaluated at the edge of the die/die-attach interface.

Figures 6.17(a) and 6.17(b) show the normal component of the stress along the Y edge of the die from the chip centre to the corner, evaluated at the die/die-attach interface (magenta curve), in the middle of the die-attach layer (orange curve) and at the die-attach/substrate interface (blue curve). The results of Figure 6.17(a) correspond to the thermo-mechanical simulation of the single die test structure at 200 ºC and the curves of Figure 6.17(b) correspond to the simulation at -65 ºC. We can observe with respect to Figure 6.16 that, as expected with a pure elastic model, the stresses are directly proportional to the strain originated by the deformation [25, 26, 27]. Due to the symmetry of the structure, the same stress curves are found along the X axis and the points of maximum stress are located at the corners. As it can be observed, the stresses are higher in the die-attach/substrate interface. The maximum values attained in the 4 corners are $1.1070 \times 10^9$ Pa at 200 ºC and $-3.5669 \times 10^8$ Pa at -65 ºC (see Table 6.1).

| | Between Die-Attach and Copper substrate | | Between Die and Die-Attach | |
|---|---|---|---|---|
| | Stress (Pa) | Strain | Stress (Pa) | Strain |
| **Single Die 200°C** | $1.1070 \times 10^9$ | 0.0075 | $7.0414 \times 10^7$ | 0.0023 |
| **Single Die -65°C** | $-3.5669 \times 10^8$ | -0.0024 | $-1.2813 \times 10^7$ | $-7.2418 \times 10^4$ |

**Table 6.1. Normal stress and strain values at the corners of the die/die-attach and die-attach/substrate interfaces.**

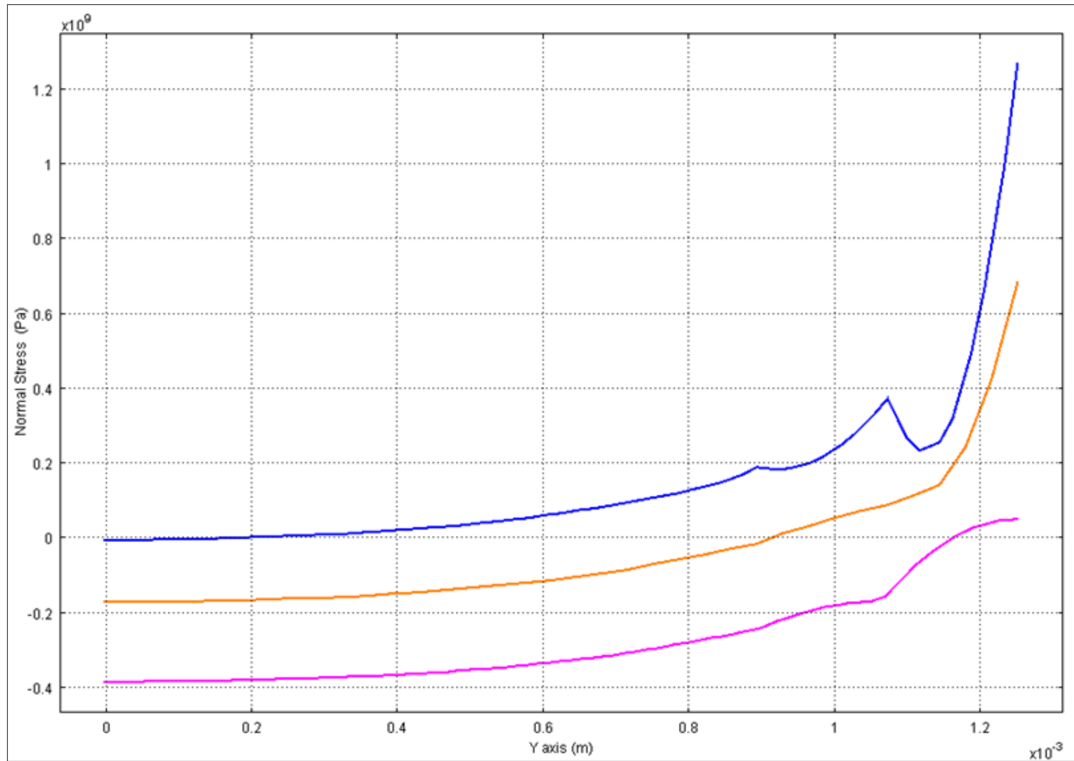


**(a)**

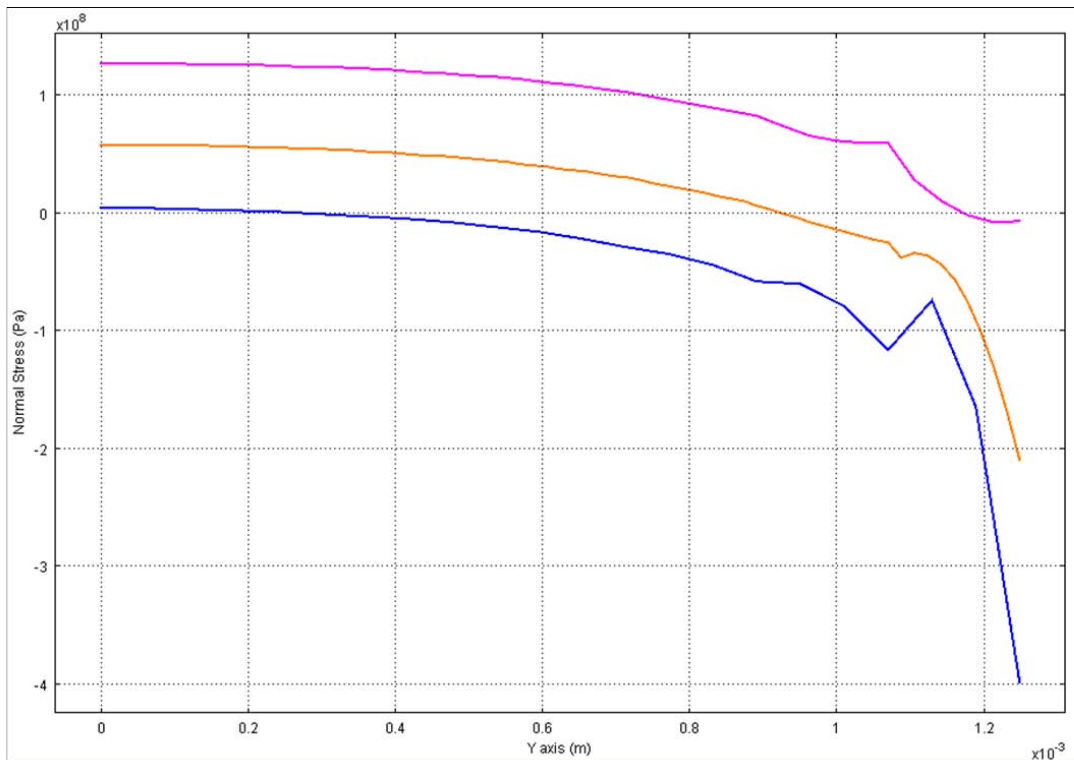


**(b)**

**Figure 6.17. Normal component of the stress along the Y direction evaluated at the die/die-attach interface (magenta), in the middle of the die-attach (orange) and at the die-attach/copper interface at 200 ºC, (a) and at -65ºC (b).**

### 6.4.4. Simulated Stress Distributions for AuGe and PbSnAg Die-Attaches

In order to determine and understand the stresses distribution in the test vehicle used for AuGe and PbSnAg die-attach materials, thermo-mechanical simulations have been performed with Cu substrate and Si dice as explained in the previous section. The sintered Ag layers have not been simulated as their physical parameters (Young and Poisson modulus, CTE, etc.) strongly depend on the processing details and they are not available in the literature. For the simulations, only the elastic behaviour has been accounted for. Besides, they have been carried out at 275 ºC and - 65 ºC, which are the maximum ($T_{MAX}$) and minimum ($T_{MIN}$) temperatures in the thermal cycle defined in section 6.3 (see Figure 6.6) respectively. Concretely, the stress distribution can be analysed by monitoring the normal stress distribution in the corner of the die / die-attach and within the die-attach. Figures 6.18 and 6.19 depict this stress distribution at the die-attach corner in an axisymmetric view and at three different depths for AuGe (Figure 6.18) and PbSnAg (Figure 6.19) when $T_{MAX}$ (275 ºC) is reached (expansion). The depths considered in Figures 6.18 and 6.19 correspond to the following interfaces: die-attach / substrate interface (Figures 6.18(b) and 6.19(b)) at the middle of die attach (Figures 6.18(c) and 6.19(c)), and die / die-attach interface (Figures 6.18(d) and 6.19(d)). It can be observed that the maximum normal stresses are achieved for both alloys, at the corner of the interface die-attach / substrate (see Figures 6.18(b) and 6.19(b)). In both materials, the stress distribution along the die-attach goes as follows: it decreases from its maximum at the die-attach / substrate interface corner up to die / die-attach interface, being always a tensile stress (positive stress). Along the die-attach lateral side edges it slightly decreases, being always tensile, but then, it rapidly diminishes as we get far from the edge. Depending on the interface, its behaviour can change: it becomes compressive (negative stress) at the die-attach / substrate, for being again tensile with lower values in the centre, and is maintained compressive (nearly zero values) as it approaches to the die / die-attach interface. As a main difference between both materials, AuGe die-attach presents higher values, especially at the die-attach / substrate interface corner (10.44 GPa for AuGe and 3.61GPa for PbSnAg) and along the edges of this interface (see Figures 6.18(c) and 6.19(c)). This stress distribution is maintained along the thermal cycling, reaching during contraction stage ($T_{MIN}$ = -65 ºC), a similar behaviour but changing the nature of the stress: tensile stresses become compressive and vice versa. All these results corresponding to stress distributions across

representative test vehicle structures, are in good agreement with the 1D stress profiles depicted in Figure 6.17 for a more basic assembly.

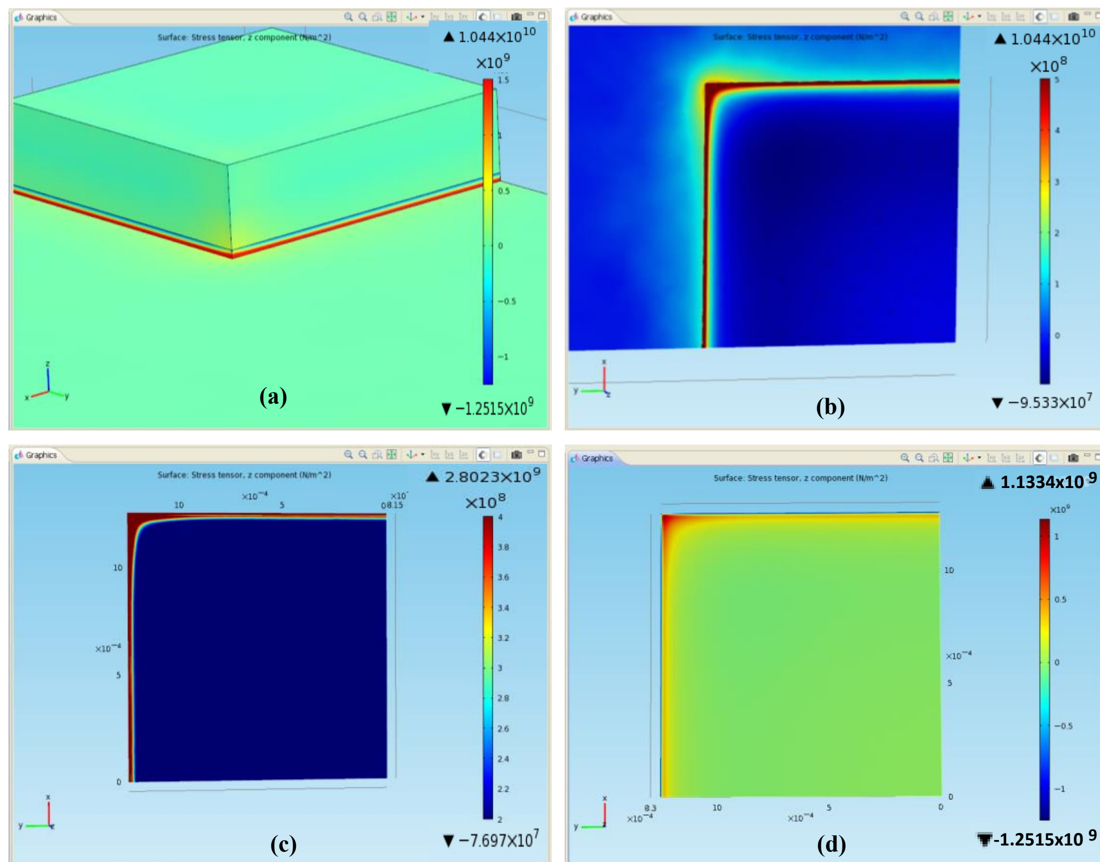


**Figure 6.18. Simulated normal stress distributions at 275 ºC for a test vehicle based on AuGe die-attach. (a) 3D view of a die corner. (b) Detail of the die-attach/copper interface. (c) Detail of the middle of the die-attach layer. (d) Detail of the die/die-attach interface.**

From these simulation results, one can conclude that the normal stress distribution depends on the geometry of the die itself and the most stressed interface corresponds to the die-attach / substrate one, with a maximum in the corner. This fact will enhance the detachment of the die-attach from the substrate in the corners during thermal cycling and, consequently, the corners will act as starting points for the delamination of the structure. This correlates with results obtained from SAM inspection performed on tests vehicles based on the same solder alloys. For instance, Figure 6.20 shows the die-attach SAM images for the first 6 inspection points of a test vehicle soldered with AuGe after 230 thermal cycles from Figure 6.6. The normal stress at the edges is responsible for increasing the clear areas observed at this location, especially at the corners (in agreement with simulation results). These clearer areas are associated to voids and

detached zones between interfaces of the die-attach. In the performed simulations, no voids have been considered but in a real situation, voids are detachment nucleation points, as Figure 6.20 depicts. It is clear that after 20 cycles, the degradation is more pronounced, especially in the corners of the die-attach. Additional results concerning die-attach degradation after thermal-cycling will be presented in section 6.5.

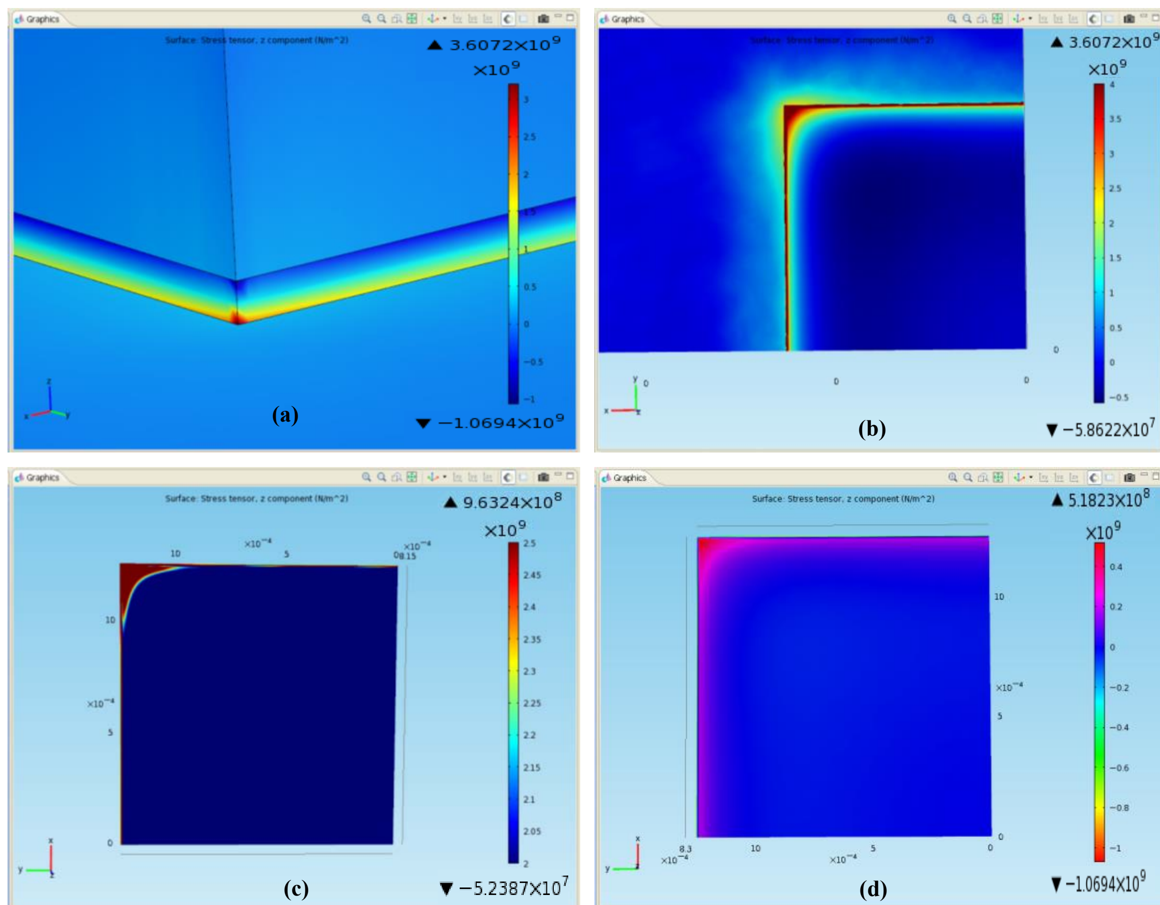


**Figure 6.19. Simulated normal stress distributions at 275ºC of a test vehicle based on PbSnAg die-attach. (a) 3D view of one die corner. (b) Detail of the die-attach/copper interface. (c) Detail of the middle of the die-attach layer. (d) Detail of the die/die-attach interface.**

Another interesting feature linking thermal cycling results with the performed thermo-mechanical simulations is that die cracking has only been observed in AuGe-based test vehicles. For instance, Figure 6.21 shows some fractured dies. This can be understood by the previous simulation results together with the stress distribution shown in Figure 6.22. This figure depicts the normal stress distributions in the middle of the die for AuGe- and PbSnAg-based structures respectively. In this figure, it can be observed that the negative stresses (compressive stresses) are distributed in the centre of

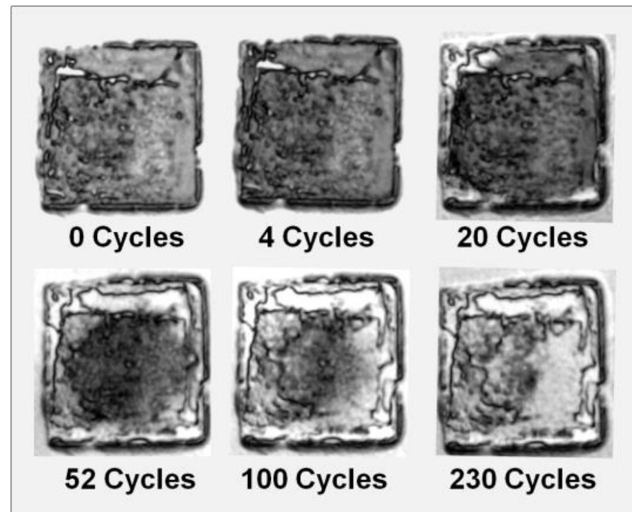


**Figure 6.20. Evolution of SAM images corresponding to the AuGe die-attach layer of a test vehicle during thermal cycling (see section 6.3).**

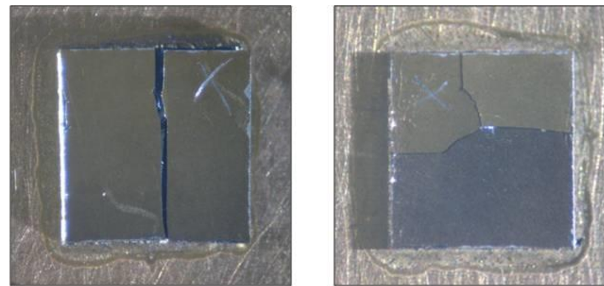

**Figure 6.21. Typical die cracks during thermal cycling for AuGe-based test vehicles. These fracture patterns are compatible with the simulated stress distributions at die level (Figure 6.22).**

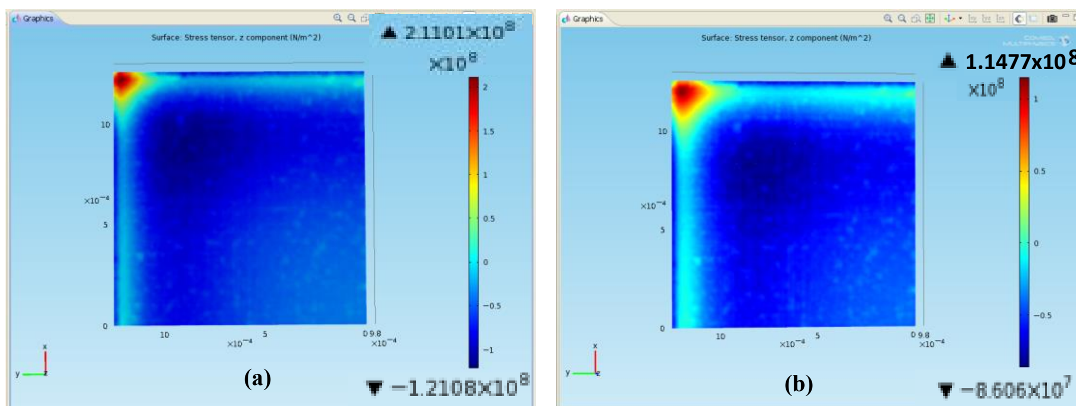


**Figure 6.22. (a) Simulated normal stress distributions in the middle of the die at 275 ºC for AuGe. (b) Simulated normal stress distributions in the die at 275 ºC for PbSnAg.**

the die, and the positive stresses (tensile stresses) are distributed in the corners of the die. This normal stress distribution is perfectly compatible with the die fracture pattern observed in Figure 6.21. Besides, we can observe that stresses are higher in AuGe than

in PbSnAg, due to their different mechanical properties (mainly in Young´s modulus and CTE), making AuGe "stiffer" than PbSnAg. This result is also consequent with the fact that only AuGe-based test vehicles have shown broken dice during the thermal-cycling test presented in section 6.5 [ 28, 29].

### 6.4.5 Warpage Measurements

Although the previous thermo-mechanical simulations provide a useful tool for understanding the effects of the induced stresses in the analysed structures under thermal-cycling, and simulation results are coherent with experimental results, we considered that a direct simulation validation could be of main interest. This direct validation was undertaken through experimental deformation measurements of test vehicles under thermal cycling conditions. With this purpose in mind, we acquired experimental warpage (volume deformation) measurements of several test vehicles based on bare Cu substrates, different die-attaches and dice. AuGe, PbSnAg and Ag sintered layer have been used as die-attaches, and Si and SiC as semiconductors.

The test vehicles have been assembled into a TDM® (Topography and Deformation Measurement) warpage measurement system from the French company Insidix (Figure 6.23). This system allows a strain measurement by image correlation based on optical non-homogeneities of a surface, i.e. variations of the reflection and absorption properties in the plane of the surface leading, for example, to variations of the grey levels of a recorded image.

The temperatures of the thermal cycle described in section 6.3 (see Figure 6.6) have been applied to the samples by the TDM system, which combines a heating and cooling mechanisms with a real time acquisition of the 3D topography. The experimental set-up includes a sample holder, bottom and top thermocouples / cooling / heating, light source and camera (Figure 6.23). The acquisition of deformation measurement is based on the projection Moiré principle: First, structured light is projected onto the sample by means of a programmable light projector. Usually the projection angle is 45º. Then, the image is captured by a CCD camera and finally, the images are processed [30, 31, 32].

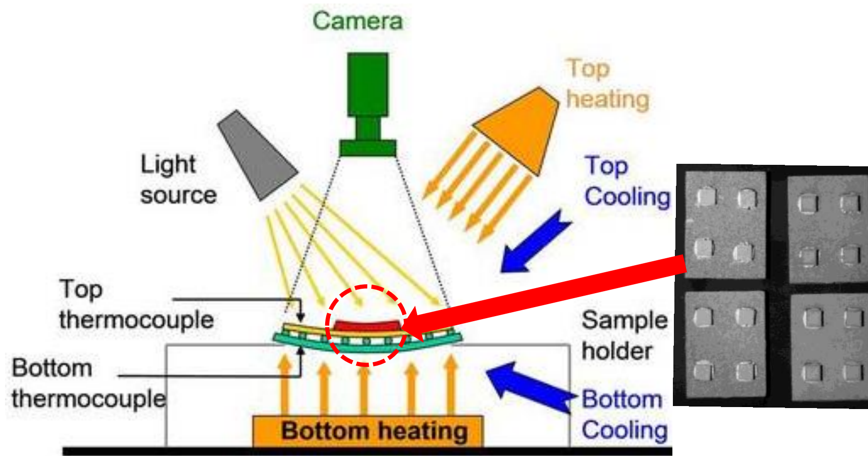


**Figure 6.23. Sketch of the TDM® set-up from Insidix used for measuring the warpage of different test vehicles [30, 31, 32].**

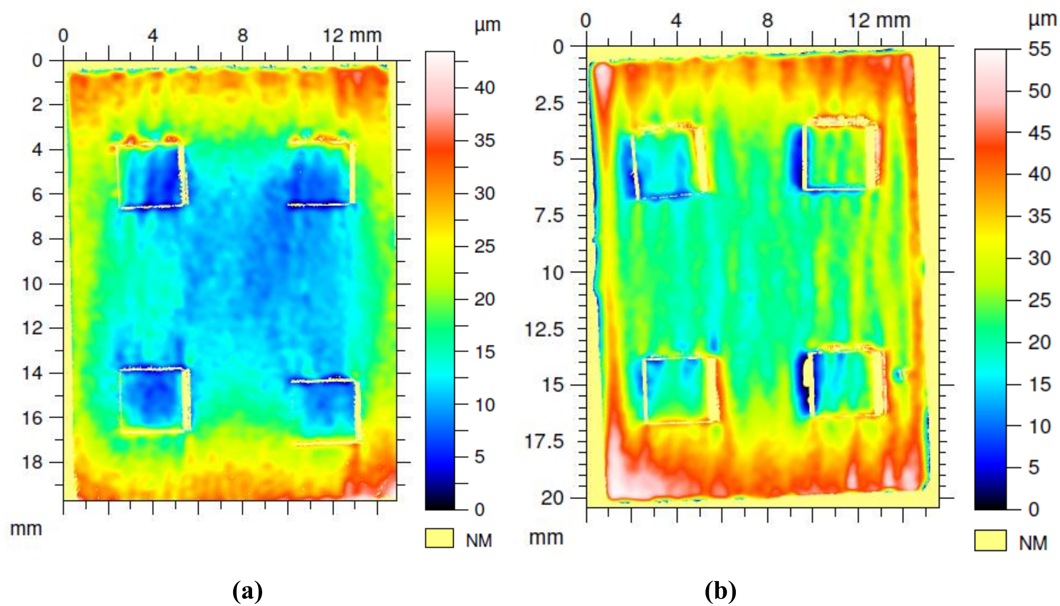


**Figure 6.24. Warpage measurement images for tests vehicles with Cu substrates and AuGe die-attach. (a) Au plated Si dice. (b) Au plated SiC dice. (NM stands for "not-measured").**

Figure 6.24 shows the total warpage distributions of two test vehicles for a complete section of the thermal cycle from -65 ºC to 275 ºC. Figure 6.24(a) corresponds to the test vehicle assembly with Si dice, AuGe die-attach and Cu substrate. The test vehicle of Figure 6.24(b) is similar, except because SiC dice have been used. Major deformation for the test vehicle with SiC dice can be observed in the periphery of the Cu substrates and around the SiC dice.

Figure 6.25(a) corresponds to the test vehicle assembly with Si dice, PbSnAg die-attach and Cu substrate. The image in Figure 6.25(b) is similar than the previous one, except because SiC dice have been used instead of the Si ones. For these test vehicles based on PbSnAg solder alloy, it can be observed again that the assemblies with SiC present major deformation than those with Si, but the magnitude of the deformation is lower than for the AuGe case.

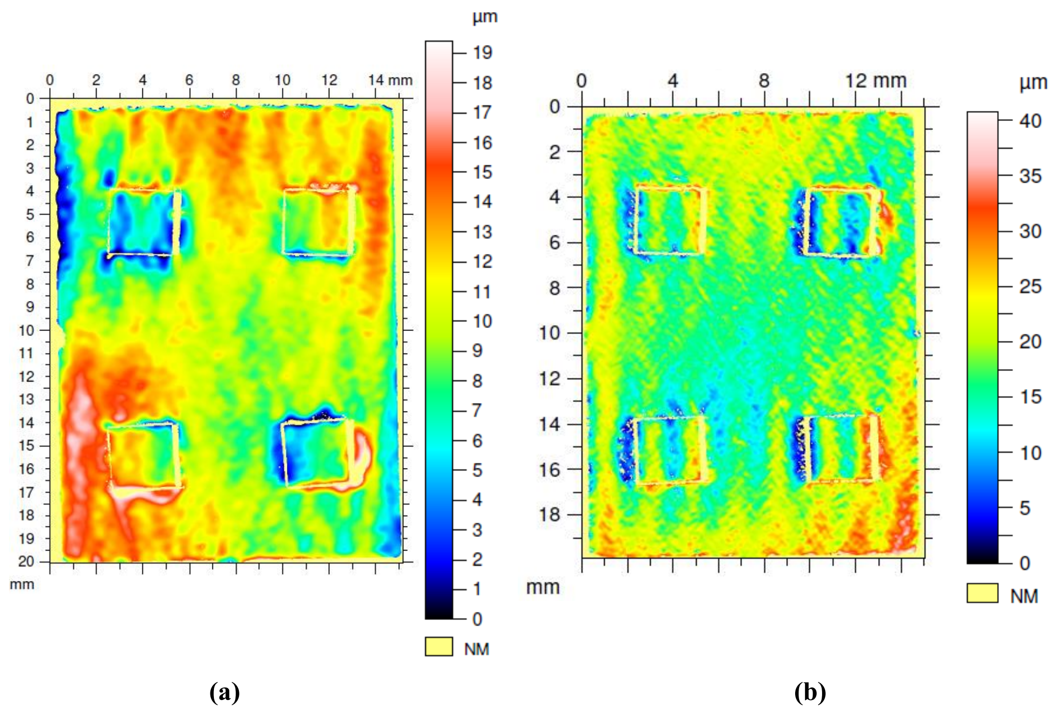


**Figure 6.25. Warpage measurement images for tests vehicles with Cu substrates and PbSnAg die-attach. (a) Au plated Si dice. (b) Au plated SiC dice.**

Figure 6.26 shows the deformation distribution acquired in the same conditions than previous images (Figures 6.24 and 6.25), but using sintered nano-Ag for the die-attach. Whereas in Figure 6.26(a) Si dice have been used, in Figure 6.26(b) the dice material is SiC. In this case, differences are negligible between test vehicles with SiC and Si dice. In fact, the deformation in the Cu substrate around the dice is similar in both cases, although the obtained distributions don't show very regular patterns.

With the aim at comparing the warpage measurements with the corresponding displacements obtained in thermo-mechanical simulations, two simulations at 275 ºC and -65 ºC were performed. Cu substrate, AuGe and Si die have been selected for simulating the test vehicles. The thermo-mechanical effects are modelled considering

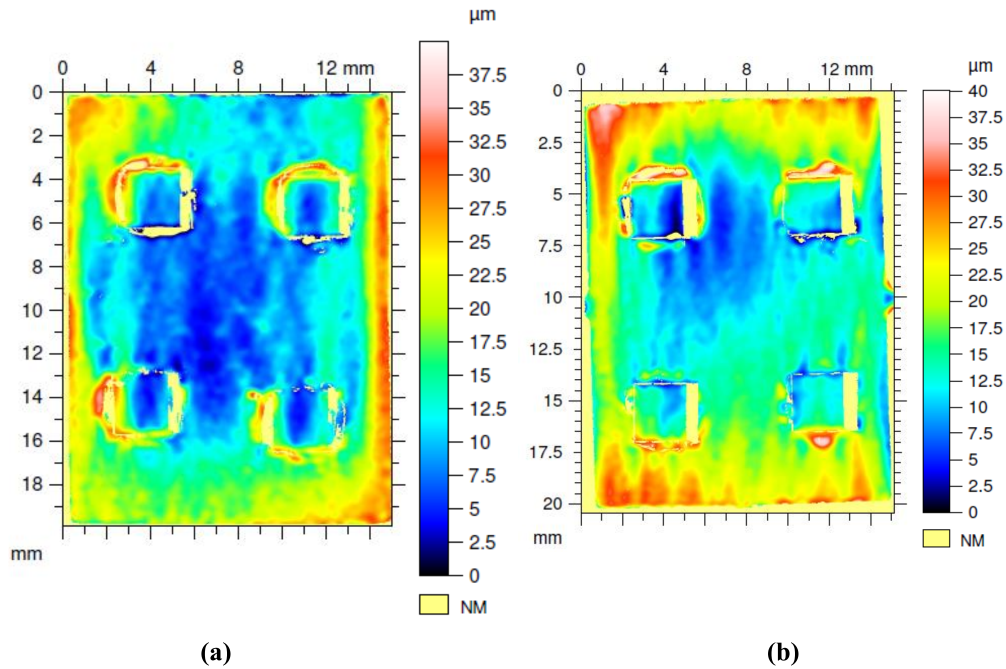


(a) (b)

**Figure 6.26. Warpage measurement images for tests vehicles with Cu substrates and Ag sintered nano-particles as die-attach. (a) Au plated Si dice. (b) Au plated SiC dice.**

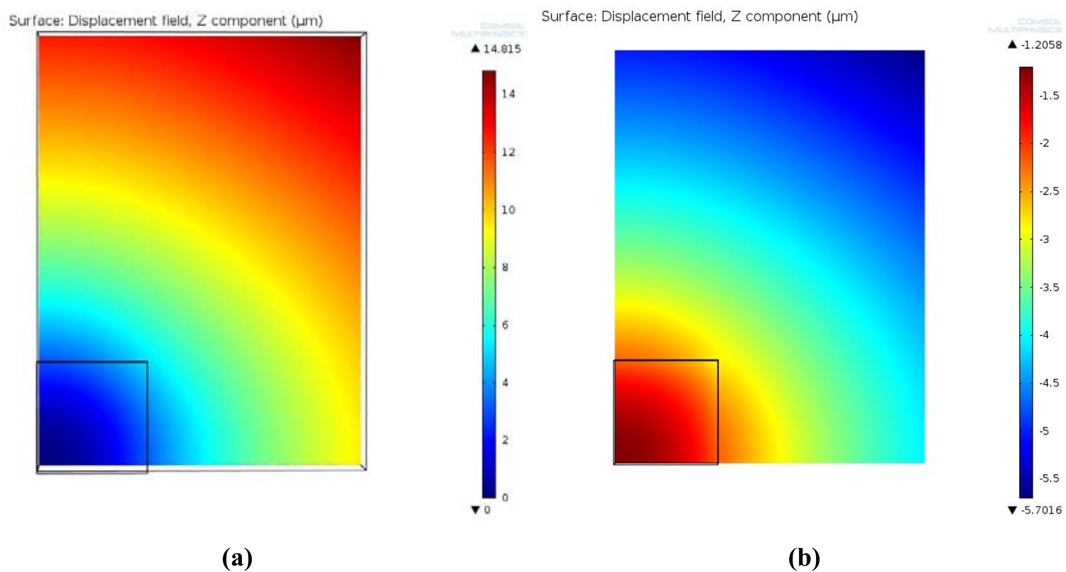


(a) (b)

**Figure 6.27. Simulated vertical displacement of an AuGe-based test vehicle at 275 ºC (a) and at -65 ºC (b).**

the linear elastic equations explained in section 6.4.1, the geometry of the structure is discretized using a mesh with a total of 97440 points and the boundary conditions are the same that in the simulations of section 6.4.3 and 6.4.4. Figure 6.27(a) displays the Cu surface displacement at 275 ºC for the AuGe-based test vehicle. It can be observed that the maximum displacement (14.8 µm) is in the Cu corner (opposite from the die).

On the contrary, the test vehicle simulated at -65 ºC and shown in Figure 6.27(b), presents a maximum total displacement of -4.5 μm of the same Cu substrate corner. Therefore, the total displacement of the Cu surface from - 65 ºC to 275 ºC (a complete temperature swing of the thermal cycle), is around 19 μm. This value don't match with those measured in the warpage tests, although the order of magnitude is correct.

Summarizing, the performed warpage measurements provided qualitative data about the deformations of the test vehicles that can be correlated with the obtained thermo-mechanical simulations, but they don't provide a precise framework for validating simulation models and this research line will require additional efforts in the future.

### 6.5. Experimental Thermal-Cycling Results

In the previous sections, we described the test vehicles and the combination of materials to be analysed, the thermal cycle to be applied in those test vehicles and the experimental set-up required to do that, the protocol for evaluating die-attach degradation and the thermo-mechanical simulations required to understand the deformations and stresses induced by temperature cycling. In this section we will compare the evolution of the mean value of die-shear force for different assembly materials during thermal cycling tests, considering the standard deviation among all dice for each point as the experimental error bar. In the presented plots, exponential interpolations have been performed in order to better appreciate the obtained tendencies. The materials used to this purpose are bare and Au plated Cu substrates, Si and SiC dice, AuGe and PbSnAg solder alloys and sintered Ag nano-particles. In the case of nano-Ag sintered layers, two different types of drying processes have been used (with die and without die), sintering pressures of 3 MPa and 7MPa, sintering temperature of 285 ºC and sintering time of 10 minutes.

First of all, we performed an evaluation concerning only AuGe-based assemblies. Figure 6.28 shows mean die-shear values of thermally cycled test vehicles with AuGe solder alloy, bare and Au plated Cu substrates and Si and SiC dice. It can be observed that Au plated substrates with Si dice present the highest adherence at 0 cycles. In fact these test vehicles based on Au plated substrates present the lowest degradation during

thermal cycling (i.e., from 29.50 kgf to 8.50 kgf in 200 cycles), as the assemblies with bare Cu substrates show a drastic shear force decrease during cycling (from 18 kgf to 3 kgf after 150 cycles for Si chips). The reason is that the Au plating in the surface of the Cu substrate limits intermetallic formation and surface oxidation responsible of weakening the joint [9, 10] which will suffer the most severe mechanical stresses with AuGe as it was demonstrated in previous simulations (section 6.4.4). For this reason, in subsequent experiments, only Au plated substrates have been considered in test vehicles involving AuGe die-attach. Concerning the die material influence, Si dice soldered onto bare Cu substrate, show a similar behaviour than samples with SiC dice for the number of cycles analysed in these tests (up to 300).

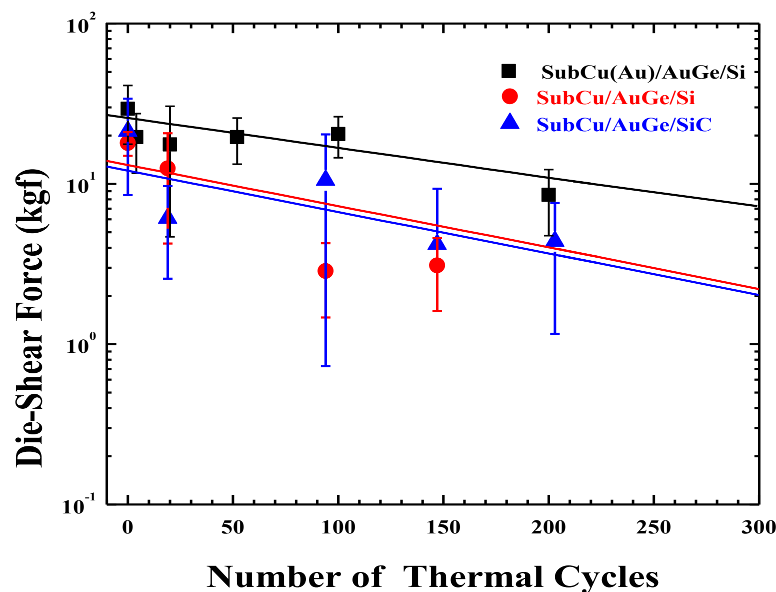


**Figure 6.28. Comparison of die-shear results for test vehicles based on AuGe die-attach, bare and Au plated Cu substrates and Si and SiC dice. The die-attach degradation is analysed during thermal cycling.**

The results plotted in Figure 6.29 correspond to the comparison among the three basic die-attach solutions analysed in this work (PbSnAg, AuGe and nano-Ag) using Si dice in the test vehicles. The sintered Ag layers were processed using a pre-drying step with die and two different sintering pressures (3 MPa and 7 MPa). Although at the beginning AuGe and nano-Ag sintering presented the highest adherence to the substrate (29.50 kgf and 37 kgf respectively), these materials degrade more rapidly than PbSnAg. This observation is in good agreement with the thermo-mechanical simulations performed in the previous section and is due to the fact that PbSnAg shows lower

Young modulus in comparison to the other die-attach materials as a consequence of the presence of Pb in the alloy. The resulting effect is lower normal stress in the material interfaces acting as a degradation driver. Figure 6.29 also depicts that although the nano-Ag sintered at 7 MPa presents higher shear force results at zero cycles (37 kgf), the degradation rate is slightly faster than for the 3 MPa case (initially showing 17.50 kgf), and both materials show similar shear values after 100 cycles (approximately 4 kgf). This fast degradation could not be explained only from the nominal thermo-mechanical parameters of pure Ag and the microscopic structure of the sintered Ag reveals that we are far from an ideal homogeneous Ag layer including pores and defects. In this case, the propagation of defects and cracks driven by the temperature cycles, the exposition of the interfaces to oxygen, the diffusion mechanisms through the adjacent metallization, etc., could be at the origin of the fast degradation shown by sintered Ag layers. Another relevant point to be considered is that the maximum cycling temperature (275 ºC) is close to the sintering one (285 ºC), and it cannot be ruled out that drying and sintering process slowly continue during the tests. This point was investigated more in detail by using an alternate drying process in a new batch of samples, and the obtained results are presented further on (Figure 6.31).

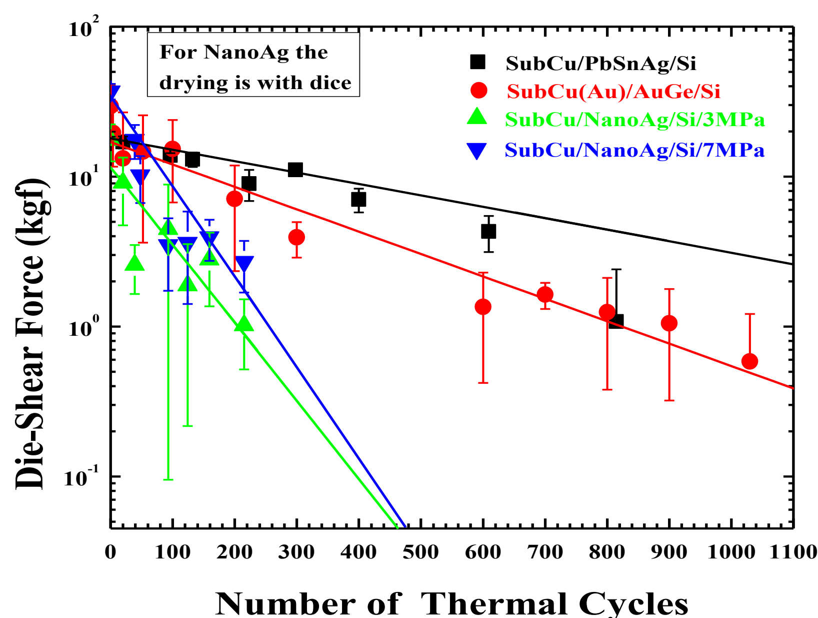


**Figure 6.29. Comparison of die-shear results for test vehicles based on Si dice and different die-attach materials: PbSnAg, AuGe and sintered nano-Ag (3 MPa and 7MPa and drying with die).**

Another interesting parameter affecting the thermo-mechanical behaviour of the test vehicles is the semiconductor die material. Figure 6.30 presents the shear force results concerning the evolution of PbSnAg and sintered Ag die-attaches with Si and SiC dice. SiC-based test vehicles show a faster degradation rate than the samples with Si dummies. This is in agreement with previous simulations and is justified by the higher Young modulus of SiC, which makes it a stiffer material than Si. As a result, higher stresses are induced in the case of SiC when considering the thermal profiles previously presented. Besides, this also indicates that for a better evaluation of package thermo-mechanical performances oriented to high temperature applications, these evaluations should be performed accounting for the semiconductor that will be finally used in order to have predictive results. However, the use of Si could be useful for developing the evaluation procedure and the die-attach processing techniques (such as Ag sintering), as it is cheaper than SiC.

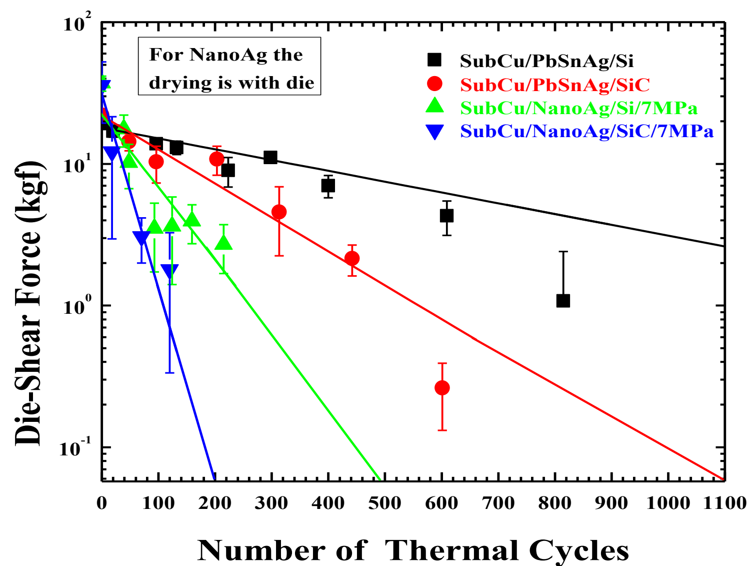


**Figure 6.30. Comparison of die-shear results for test vehicles with Si and SiC dice and PbSnAg and nano-Ag die-attach after thermal cycling.**

As stated before, Figure 6.31 shows the results for the sintered Ag die-attach solution using the drying step without die, and compares the observed shear-force decay with the two solder alloys, AuGe and PbSnAg, for bare and Au plated Cu substrates. As it can be observed, the best behaviour with SiC dice is found for the nano-Ag die-attach and Au plated substrates (approximately 5 kgf after 600 cycles). In fact, sintered Ag die-attach shows even better shear force decay rate than the solder alloys (approximately 1.00 kgf after 600 cycles). This behaviour indicates that the drying step without die

improves the elimination of organics and the subsequent densification, adherence and thermo-mechanical behaviour of the sintered Ag layer, as it was already stated in chapter 5. Another interesting result confirmed in the plots of Figure 6.31 is that the Au plating of the Cu substrates improves the thermal cycling response of the nano-Ag as assemblies with bare Cu substrate degrade with lower number of cycles.

All die-shear evolution curves presented above, can be supported by the corresponding C-SAM images revealing the degradation occurred in the die-attach layers. In this sense, Figure 6.32 shows the sequence of the acoustic images for Si-based test vehicles and all die-attaches (AuGe, PbSnAg and sintered Ag at 7 MPa), from zero up to a number of cycles revealing a significant degree of detached areas (see white zones). These SAM pictures can be associated with the die-shear evolution curves depicted in Figure 6.29. At 0 cycles, a uniform die-attach is observed in all the samples and this correlates with the high die-shear values obtained for 0 cycles in Figure 6.29 (and also in Figures 6.2, 6.3 and 6.4). During thermal cycling tests, nano-Ag rapidly degrades, followed by AuGe (assembly with Au plated substrate), and PbSnAg remaining almost unaltered. This result contrasts with the fact that nano-Ag presented the highest adhesion at 0 cycles (37 kgf) and PbSnAg the lowest one (19kgf).

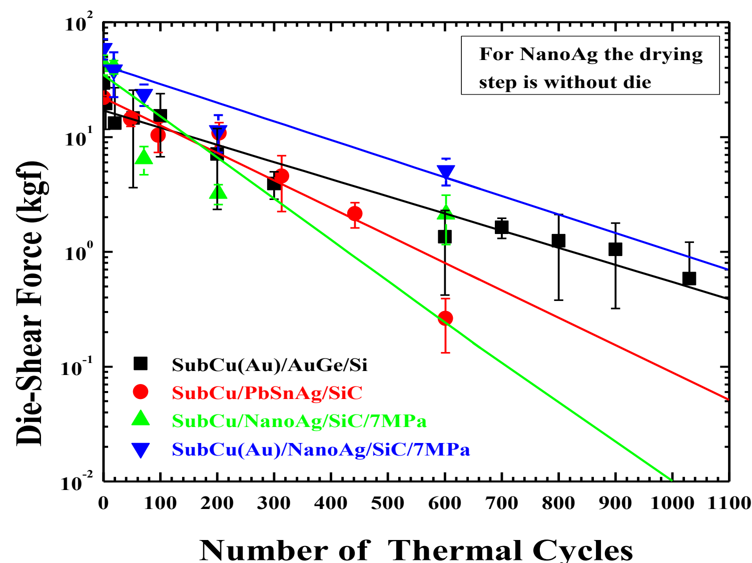


**Figure 6.31. Comparison of die-shear results for test vehicles involving die-attach solder alloys (AuGe and PbSnAg) and nano-Ag sintering layers obtained with a drying step without die. SiC and Si dice have also been used.**

Figure 6.33 shows what occurs with SiC dice attached with PbSnAg and sintered Ag (at 7 MPa) after several thermal cycles. It can be observed that for the same number of cycles shown in Figure 6.32 for Si-based assemblies, the degradation through the die-attach is higher for the SiC case (see also Figure 6.30). Moreover, for SiC dice, PbSnAg is less affected by thermal cycles than sintered Ag die-attach. In any case, Figures 6.32 and 6.33 present a similar degradation pattern in all the samples: white areas mainly concentrate around the periphery of the chip. The explanation was already done in section 6.4.4: during thermal cycling, the periphery of the die-attach / substrate interface experiences high normal stresses acting as failure nucleation points (mainly in the corners) predicting the concentric normal stress distributions which are directly correlated with the die-attach delamination pattern [28]. This behaviour is best appreciated for the AuGe case in Figure 6.32, probably because this solder alloy presents the higher value of Young modulus and, therefore, the higher normal stresses.

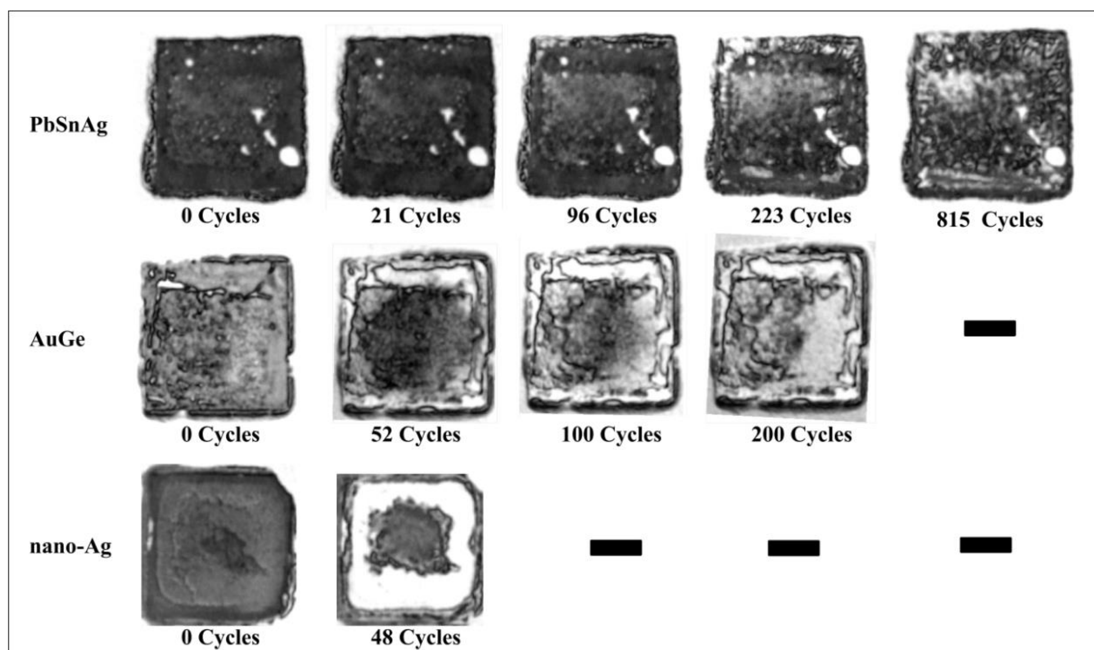


**Figure 6.32. C-SAM images evolution of considered die-attaches with Si chips from zero to a certain number of cycles when a high degradation is observed: PbSnAg (top row), AuGe (middle row), sintered Ag (bottom row).**

In the particular case of nano-Ag sintered layers, we have observed a specific pattern in the C-SAM images after thermal cycling: the centre and a piece of the periphery of the die-attach are joining the substrate and the die, while the rest of the Ag layer is detached. The SAM images do not reveal which interface delaminates, but

Figure 6.34 shows a photograph after die-shear of the substrate (a) and the die (b) degraded under thermal cycling (70 cycles). It depicts the nano-Ag layer (corresponding to the SAM images shown in Figure 6.33) that remained attached to the substrate and to the die backside, indicating the interface where degradation occurred (centre and periphery bonded to the substrate, whereas the rest of the Ag layer remains attached to the die). This has been also observed in other recent works, being also studied by simulation [33, 34]. They show that cracks propagate through the die-attach up to almost reaching the substrate interface, inducing a first relaxation of the assembly. After that, crack propagates near this interface, as the substrate presents a higher CTE value than the chip (see Figure 6.35) [34].

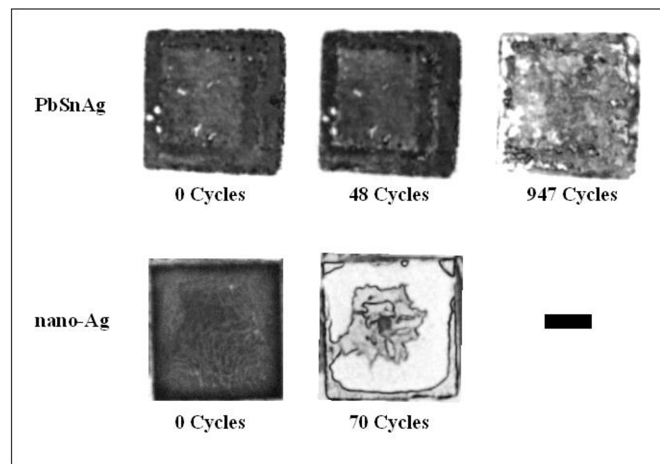


**Figure 6.33. C-SAM images evolution of test vehicles with SiC dice considering two die-attaches from zero to a certain number of cycles when a high degradation is observed: PbSnAg (top row), sintered Ag at 7MPa and drying step with die (bottom row).**

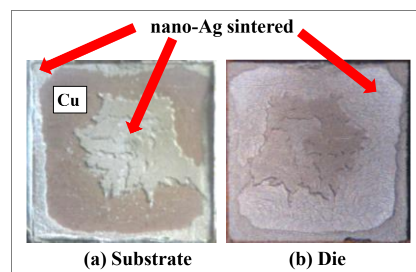


**Figure 6.34. Photographs after die-shear of the nano-Ag layer sintered at 7 MPa remaining attached to the substrate (a) and to the SiC die backside (b), after 70 cycles. Compare with SAM images of Figure 6.33.**

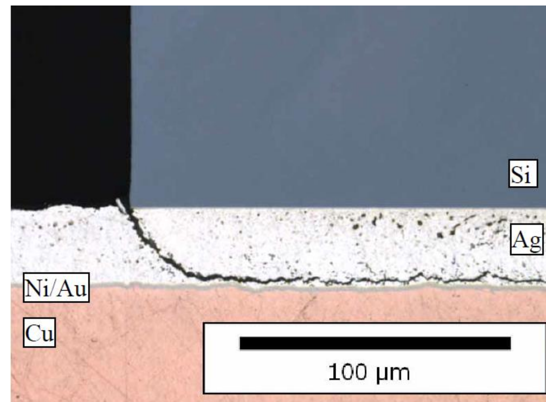


**Figure 6.35. Structure with a Si die attached to an Au plated substrate showing a crack propagation after 1250 cycles of thermal shock (from -28 ºC to -182ºC) [34].**

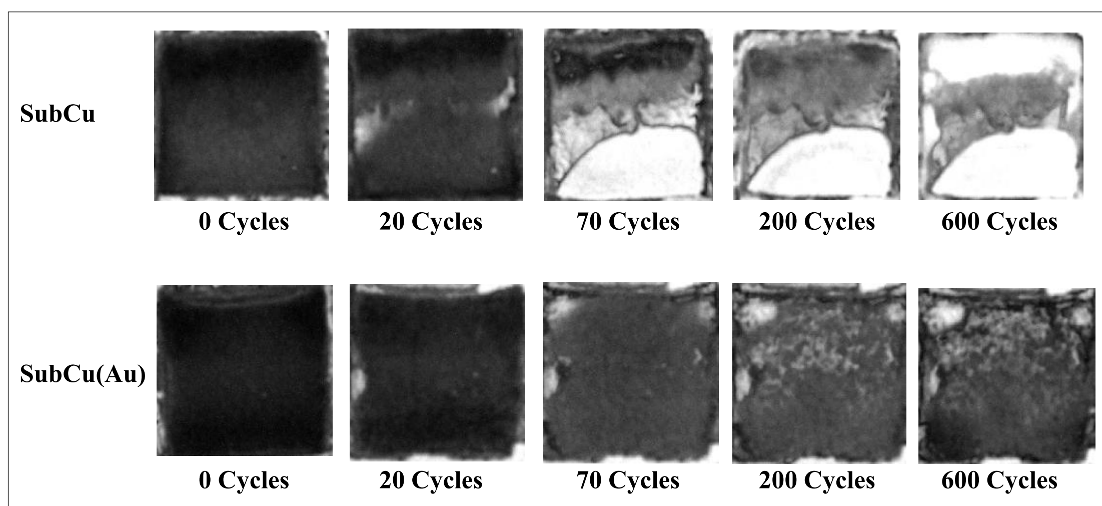


**Figure 6.36. C-SAM images evolution of the sintered Ag nano-particles layer when using a drying step without die (SiC dice), from zero to a certain number of cycles: Cu substrate (top row) and Au plated substrate (bottom row).**

Nevertheless, the origin of this SAM image pattern was suspected to come from a poor drying process, leaving organic residuals in the Ag layer (see chapter 5 for more details). This hypothesis was confirmed in Figure 6.36, which shows the thermal cycling evolution of test vehicles manufactured with sintered Ag particles at 7MPa, 285 ºC, 10 minutes and the drying step without die. The top row displays the test vehicles based on raw Cu substrates and the bottom row displays the test vehicles using Au plated Cu substrates. In both cases, SiC dice have been used. The SAM patterns are completely different of those in Figure 6.34 for nano-Ag layers sintered using a drying step with die. The higher homogeneity of the SAM images shown in Figure 6.36 reveal that the drying process was optimized and the densification and quality of the final Ag layer is much better when drying allows the complete evacuation of organics. Besides,

the test vehicles with Au plated Cu substrate experienced less degradation that samples with bare Cu substrate (as it was repeatedly observed in other test vehicles) because the Au plating avoids Cu oxidation. It is worth pointing out that although the tests have been performed in a chamber with $N_2$ ambient, residual $O_2$ traces are present and oxidize critical surfaces during the long-term cycling tests (in our case, 550 cycles correspond to one month).

**6.6. Conclusions**

This chapter presents a comparative analysis of different die-attach materials suitable for semiconductor devices in harsh environment applications, based on thermal cycling tests. The study focused on sintered Ag over bare Cu substrates, as there is a lack of information on this combination of materials with high commercial interest. Sintered Ag is an attractive die-attach solution, because it offers high performances (both, thermal and electrical, including also a high melting point at 961 ºC), involving low process temperatures (< 300 ºC). The Ag paste analysed was the commercially available K-type NanoTach from NBE Tech Company already mentioned in chapters 4 and 5. Au plated substrates and AuGe and PbSnAg solder alloys have also been considered in the study. PbSnAg was selected as a well-known reference die-attach material and AuGe is a suitable solution among all lead-free die-attach materials for high temperature applications.

The proposed experimental study is based on the test vehicles described in chapter 4 combining the different materials and required assembly techniques. These test vehicles represent the basic structure of the most common power device assemblies reproducing the CTE mismatches find in power electronics packages.

As it was mentioned, the study is based on thermal cycling of samples designed for operation at high temperature. Consequently, a suitable temperature profile was defined based on the information available in different standards. To implement these temperature cycles (between - 65 ºC and + 275 ºC) a specific harsh temperature cycling bench has been developed, based on a commercial hot / cold plate system and including a number of modifications allowing its safe continuous operation. In parallel, in order to evaluate the degradation of the die-attach layers under thermal cycling in a rigorous

way, an experimental protocol has been also designed, based on the characterization equipment available. In particular, the quality and degradation of die-attach layers over time has been basically monitored by C-SAM acoustic microscope and die-shear tests.

Before starting the degradation study under thermal cycling, it has been verified that all the test vehicles passed the quality criteria defined in well-established standards, mainly in terms of die-shear strength and SAM inspection (content of voids in the die-attach). In particular, we can roughly place the initial (zero cycles) shear strengths for each die-attach in the range of the 20 kgf for PbSnAg, 30 kgf for AuGe, 40 kgf for sintered Ag drying the paste with die and 50 kgf for sintered Ag drying the paste without die.

The degradation rate shown by sintered Ag nano-particle layers where the drying step was with die, was clearly higher than for AuGe and PbSnAg, although nano-Ag sintering presented the higher initial die-shear force values. In addition, although at zero cycles, the test vehicles sintered at 7 MPa showed higher die-shear forces than those sintered at 3 MPa (37 kgf and 17.50 kgf respectively), after 100 - 200 cycles both kind of samples presented similar degradation (approximately 4 kgf of die-shear strength). In general, the internal microstructure of the sintered Ag layer and its interfaces (with die and substrate) is far from being homogeneous and regular as it was demonstrated in chapter 5, and any of the initial defects present in the material could act as starting point for crack propagation. Nevertheless, we have demonstrated that in our particular case the main reason for the fast degradation of the Ag layers was a poor drying process, leaving some organic residuals in the structure. In this sense, the test vehicles developed with sintered Ag without die during the drying step (optimum drying process of the paste) presented the lowest degradation rate during thermal cycling, with results even better than for AuGe- and PbSnAg-based samples. Therefore, it can be concluded that despite the very bad cycling results obtained for sintered Ag dried with die, the optimization of the paste drying process can lead to a completely different behaviour, making nano-Ag the best choice.

Concerning the semiconductor material, the obtained thermal cycling results have demonstrated that the degradation rate is faster for SiC- than for Si-based test vehicles, while concerning strictly the solder alloys PbSnAg shows better results than AuGe. All

these results can be explained by the higher stresses induced by the stiffer materials (higher Young modulus), that is AuGe and SiC. In this sense, a thermo-mechanical simulation work was also performed in order to better understand the thermo-mechanical mechanisms behind the observed degradation patterns during thermal cycling. The simulations demonstrated that the higher normal stresses associated with temperature swings were located at the die-attach / substrate interface, with the maximum values in the corners of the die and its periphery. These results qualitatively explain the SAM images showing concentric die-attach delamination patterns and, even, die fractures in AuGe-based samples. An attempt was made for quantitatively validate the thermo-mechanical simulations comparing direct warpage measurements of tests vehicles with strain simulations. Although simulated and measured results were in the same order of magnitude (a factor 2 or 3 of difference), the warpage measurements were not enough accurate for such validation purposes, and additional research work will be required in the future on this topic.

### 6.7. References


[1] B. Grummel, R. McClure, L. Zhou, A. P. Gordon, L. Chow, and Z. J. Shen, "Design Consideration of High Temperature SiC Power Modules," in *Proc. IEEE Industrial Electronics Conference*, 2008, pp. 2861 - 2866.

[2] F.P. McCluskey, R. Grzybowski, and T. Podlesak, High Temperature Electronics. Florida: CRC press, Chapters 1 - 5, 1997.

[3] (2015). [Online]. Available: http://www.matweb.com/

[4] S. Msolli, O. Dalverny, J. Alexis, M. Karama, "Mechanical Characterization of an Au-Ge Solder Alloy for High Temperature Electronic Devices," in *Proc. IEEE International Integrated Power Electronics Systems Conference*, 2010, pp. 1 - 5.

[5] S. Massetti , P. Godignon , E. Ciancetta , D. Lopez , R. Meurer, C. Baur and X. Jordà, "Development and Evaluation of a SiC Schottky Diode for Harsh Environment Space Applications," in *Proc. European Space Power Conference*, 2011.

[6] L. Coppola, D. Huff, F. Wang, R. Burgos, and D. Boroyevich, "Survey on High-Temperature Packaging Materials for SiC-Based Power Electronics Modules," in *Proc. IEEE Power Electronics Specialist Conference*, 2007, pp. 2234 - 2240.

[7] L. A. Navarro, X. Perpiñà, M. Vellvehi, X. Jordà, “Silver Nano-Particles Sintering Process for the Die-Attach of Power Devices for High Temperature Applications,” *Sociedad Mexicana de Ingeniería Mecánica*, vol. 4, issue 3, pp. 97 - 102, September 2012.

[8] L. A. Navarro, X. Perpiñà, M. Vellvehi, D. Sánchez and X. Jordà, “Sintering Process Analysis for Die-Attach of Power Packages for High Temperature Applications based on Silver Nano-Particles,” in *Proc. XX Congreso Internacional Anual de la SOMIM*, September 2014, pp. 1 - 10.

[9] F. Lang, S. Tanimoto, H. Ohashi and H. Yamaguchi, “Long-Term Joint Reliability of SiC Power Devices at 330ºC,” in *Proc. IEEE European Microelectronics and Packaging Conference,* 2009, pp.1 - 5.

[10] V. Chidambaram, H. B. Yeung and G. Shan “Long-Term Joint Reliability of SiC Power Devices at 330ºC,” in *Proc. 19th IEEE International Symposium on the Physical and Failure Analysis of Integrated Circuits,* 2012, pp. 1 - 6.

[11] S. Massetti, P. Godignon, E. Ciancetta, D. Lopez, R. Meurer, C. Baur, and X. Jordà, “Development and evaluation of a SiC Schottky diode for harsh environment space applications,” *in Proc. European Space Power Conference*, 2011.

[12] J. Lutz, H. Schlangenotto, U. Scheuermann, and R. de Doncker, Semiconductor Power Devices. Germany: Springer, 2011, Chapter 11.

[13] J. M. Hu, D. Barker, A. Dasgupta, A. Arora, “Role of Failure-Mechanism Identification in Accelerated Testing,” in *Proc. IEEE Annual Reliability and Maintainability Symposium*, 1992, pp. 181 - 188.

[14] M.G. Pecht. “Handbook of electronic package design”. Marcel Dekker, New York, 1991.

[15] M. Bouarroudj, Z. Khatir, S. Lefebvre, “Temperature Levels Effects on the Thermo- Mechanical Behaviour of Solder Attach During Thermal Cycling of Power Electronic Modules,” in *Proc. IEEE Power Electronics Specialists Conference*, 2008, pp. 2435 - 2440.

[16] C. J. Zhai, Sidarth and R. Blish, "Board Level Solder Reliability Versus Ramp Rate and Dwell Time During Temperature Cycling", *IEEE Transactions device and materials reliability*, vol. 3, no. 4, pp. 207 - 212, December 2003.

[17] S. Massetti , P. Godignon , E. Ciancetta , D. Lopez , R. Meurer, C. Baur and X. Jordà, “Development and Evaluation of a SiC Schottky Diode for Harsh

Environment Space Applications," in *Proc. European Space Power Conference,* 2011, pp.1 - 9.

[18] L. A. Navarro, Xavier Perpiñà, P. Godignon, J. Montserrat, V. Banu, M. Vellvehi, and Xavier Jordà, "Thermomechanical Assessment of Die-Attach Materials for Wide Bandgap Semiconductor Devices and Harsh Environment Applications," *IEEE Transactions on Power Electronics*, vol. 29, no. 5, pp. 2261 - 2271, May 2014.

[19] P. Hagler, P. Henson, and R. Wayne Johnson. "Packaging Technology for Electronic Applications in Harsh High-Temperature Environments". *IEEE Transactions on Industrial Electronics*, vol. 58, issue 7, pp. 2673 - 2682, 2011.

[20] G.Q. Zhang, W.D. van Driel and X.J. Fan. "Mechanics of Microelectronics". Springer, 2006, Chapter 3.

[21] Introduction to COMSOL Multiphysics.

[22] Heat Transfer Module, User Guide, COMSOL Multiphysics.

[23] Structural Mechanics, User Guide, COMSOL Multiphysics.

[24] COMSOL Multiphysics, User Guide.

[25] I. B. Mirman, "Effects of peeling stresses in bimaterial assembly". in *Proc. ASME Journal Electronic Packaging*, vol. 113, 1991, pp. 431 - 433.

[26] M. Bouarroudj, Z. Khatir, J.P. Ousten, L. Dupont, S. Lefebvre, F. Badel. "Comparison of stress distributions and failure modes during thermal cycling and power cycling on high power IGBT modules," in *Proc. IEEE European Power Electronics and application Conference*, EPE, 2007, pp. 1 - 10.

[27] J. M. Gere, S. P. Timoshenko. "Mecánica de materiales". Cuarta edición, ITP, 1998.

[28] L. A. Navarro, X. Perpiñà, M. Vellvehi, V. Banu, X. Jordà, "Thermal cycling analysis of high temperature die-attach materials," *Microelectronics Reliability*, vol. 52, issues 9 - 10, pp. 2314 - 2320, September 2012.

[29] L. A. Navarro, "Study of Thermomechanical Stress on Die-Attach for High Temperature Power Packaging," Master Thesis, Universidad Autónoma de Barcelona, Barcelona, España, Septiembre 2011.

[30] (2015). [Online]. Available: http://www.insidix.com/Topography-and-Deformation-Measurement-TDM.26.0.html

[31] Jedec Standard. Package Warpage Measurement of Surface-Mount Integrated Circuits at Elevated Temperature. JESD22 - B112A. 2009.

[32] M. Hertl and D. Weidman, "Innovative Assessment of Thermomechanical Stress Effects in Electronics Components and Assemblies," *Electronic Device Failure Analysis*; vol. 13, no. 3, pp. 4 - 11. August 2011.

[33] T. Sünner, T. Behrens and T. Kaden, "Reliability Investigation of Drain Contact Metallizations for SiC-MOSFETs," *Materials Science Forum*, vol. 740 - 742, pp. 665 - 668, 2013.

[34] T. Herboth, C Früh, M. Günther, J. Wilde "Assessment of Thermo-Mechanical Stresses in Low Temperature Joining Technology," in *Proc. 13th International Conference on Thermal, Mechanical and Multi-Physics Simulation and Experiments in Microelectronics and Microsystems,* 2012, pp. 1 - 7.

# CHAPTER 7 General Conclusions and Discussion

To conclude the present work about die-attach solutions for high temperature power electronics applications, with special attention to Ag sintering, we will present the main conclusions derived from each one of the chapters of this report.

Chapter 1 provided the framework and the motivation of this research work. Besides, the main objectives and general description of the chapters that constitutes the study have been summarized.

Then in Chapter 2 the importance of power electronics, the technological domain in which this work is developed, has been described. Power electronics is a field of paramount economic and social importance, since it possibilities a high number of crucial applications. Power electronics systems are present in all the chains of generation, distribution and application of the electric energy. To provide a wide view on the framework of this work, this chapter presents the main power electronics applications and the used semiconductor devices.

The interface between the power devices and the application circuit is given by their package. Power electronics packaging must provide electrical interconnection to the device, heat extraction capability and mechanical and environmental protection. Thus, power packaging is one of the key elements in power electronics development, and it requires, at least, the same research efforts than semiconductor power devices and power converters. A detailed analysis of the main power packaging elements and materials has been also addressed in this chapter. Current available packaging technologies and recent advanced packaging solutions have been presented for the two main scenarios of this field: discrete power devices and multi-chip power modules.

It has been discussed that power packaging involves many engineering fields due to the different physical phenomena present in such heterogeneous systems. In this sense, the thermal and thermo-mechanical issues in power electronics packages are becoming an ever more important concern. Today, the thermal and thermo-mechanical

performances are being pushed from the device to the package limit by increasing heat fluxes, continued miniaturization and higher switching speeds.

Finally, it has also been explained that the performances of power electronic systems (mainly their integration level) become improved if high temperature semiconductor devices are used. Such high temperature devices also allow the development of new and crucial applications related with high environment temperatures (aerospace, automotive, etc.). Currently, the silicon technology reached its physical limits and a great effort in R+D is being done to develop devices based on wide bandgap semiconductors, such as SiC, GaN or Diamond. SiC and GaN devices with maximum operation temperatures up to 300 ºC are starting to be available, and one of the limiting elements for their implantation is the package.

All technological elements required for a high temperature (300 ºC) package showing high voltage and current capabilities must provide the same final reliability already reached for standard packaging solutions. Thus, the key points to reach this target not only involve an optimal thermal design of the package, but also an accurate thermo-mechanical study on die-attach, chip-to-package interconnections (wire- or bump-bonding) and encapsulants. This high temperature power packaging scenario will constitute the framework of the present research work, where the focus will be addressed to the thermo-mechanical reliability analysis of the die-attach layers, in particular for high temperature operation with special focus on Ag nano-particles sintering.

In chapter 3, the importance of the die-attach layer in power assemblies is introduced. The die-attach layer is one of the most critical element of the package structure. For this reason, special attention has put in die-attach layer for high temperature applications, in particular the die-attach based on sintering phenomenon.

In this study, it has been realized a brief review of the main failure analysis methods for power electronics assemblies. A more in depth review has been carried out about the techniques and system used in this work for analysing the quality and degradation of die-attach layers. Besides, sintering physical basis, its mechanisms and the main types, have also been described. Then, it has been analysed the particle

influence in the sintering phenomenon and, finally, a brief description of the main components of Ag pastes manufactured for die-attach application has been carried out.

Chapter 4 presents the sintering process methodology and the experimental set-up for manufacturing sintered die-attach layers. Besides, the Ag pastes used in this study have been characterized. From the TGA and DSC analysis it can be concluded that elimination of organic components in air is better than in nitrogen atmosphere, although this approach can lead to oxidation of critical parts (Cu substrates, for example). The test vehicle used in this work has been designed and described. I includes a substrate, the die-attach layer and four or six dice onto the substrate depending on the kind of tests to be performed (thermal cycling or sintering process set-up). Moreover, the main properties of devices and substrates commonly used to manufacture the test vehicles have been described. The materials selected for this work are: Cu substrate, two types of semiconductors (Si and SiC) and two types of Ag sintering pastes (X and K series from NBE Tech). Other die-attach solder alloys will be also introduced in the thermal cycling tests presented in chapter 6. On the other hand, the brief description of the screen printing step, which is very important for quantifying the amount (volume) of paste used in the process, has been introduced. Then, it has been demonstrated that the drying process is one of the most important steps of the sintering process for assuring suitable densification and adherence of the sintered die-attach layer. Also, it is important to highlight that the assessment (die-shear tests) has been useless for lager dice (6 mm x 6 mm), because the die-fracture occurs before the fracture of the sintered layer. For this reason, further experimental research will be made with smaller dice of about 2.8 mm x 2.8 mm. Finally, the main elements of the press designed specifically for applying pressure during sintering process, has been described.

In Chapter 5 we have analysed the effect of the main sintering process parameters on the final characteristics of the Ag die-attach layer. The aim of this study was twofold: first, to obtain useful information about the used Ag paste for its direct application in future power assemblies, and second to understand the main mechanisms governing the properties of the sintered Ag layers.

The first parameter analysed in the chapter was sintering pressure. Apart from several test vehicles manufactured as explained in chapter 4 at different pressures, specific samples of single Ag layers were also developed for microstructural inspection

based on FIB microsections. The results revealed (as expected) that the densification of the Ag layer clearly improves with increasing sintering pressure, while the porosity diminishes. The adhesion of the Ag particles to the Cu substrate also improves at higher pressures, but a clear difference is observed between the sintered Ag in the central area and in the periphery of the layer. In the central part, the level of densification is lower than in the periphery, showing more but smaller voids. Nevertheless, at the edges of the Ag a thin layer appears at the Ag/Cu interface, showing a very good adhesion with the Ag and more detached zones with the Cu. The EDX analysis of this layer demonstrates that it corresponds to a Cu oxide, evidencing that the die-attach periphery is strongly influenced by the surrounding ambient (air in our case). This fact is also related with the difference of densification level achieved between the centre and the edge of the die-attach, as the periphery zone of the Ag layer, close to the ambient, can better decompose and eliminate the organic components of the original paste.

The higher densification level observed when increasing the sintering pressure is also in good agreement with the experimental reduction of the die-attach thickness (approximately 45 - 50 % in the range from 0 MPa to 11 MPa). It is interesting to stress that for sintering pressures higher than 5 MPa (approximately) the die-attach thickness "saturates" at a minimum value that doesn't decrease for higher applied pressures (up to 11 MPa). This effect is also reflected when looking at the "die-shear modulus" (the slope of the force versus displacement curves during die-shear tests). This parameter is related with the Young modulus of the Ag layer and our results evidenced that the shear-modulus increases with the sintering pressure (the Ag is "more stiff") but the value saturates from approximately 5 MPa and above. In addition, as the die-shear force curve as a function of sintering pressure grows constantly in the 0 - 11 MPa range (from 2 kgf up to 55 kgf) and doesn't show any clear saturation around the 5 MPa it seems reasonable to derive that the Ag layer stops its densification at this point and the increase of the die-shear force is due to the adhesion improvement at the interfaces, mainly in the Cu substrate one. This effect is supported by the dominant failure modes after die shear, showing a transition from mode 1 (die / substrate detachment) to mode 4 (die fracture).

The second main process parameter analysed was sintering temperature. Temperature acts as a driving force for sintering processes as it is also the case of

pressure and, in fact, the conclusions derived for both parameters have been similar. Higher temperatures improve densification of the Ag layer with better efficiency in the edges of the Ag layer than in the centre, but simultaneously, the Cu oxide layers at the Ag/Cu interface are thicker.

The die-shear forces recorded for sintering temperatures from 265 ºC up to 325 ºC show also a significant increase (around 40 % in the mentioned temperature range), although the mechanical properties of the Ag layer present almost no change, i.e. the die shear modulus doesn't change with increasing sintering temperature. This fact seems to indicate that the major improvements observed in the adherence curves come from best adhesion at the interfaces. This hypothesis is partially supported by the fact that the main failure mechanism after die-shear is die fracture for the higher temperatures.

A very interesting result obtained in this chapter is the experimental evidence that sintering pressure and temperature can be adjusted complementarily to obtain a given die-shear value (representing a particular die-attach quality). In this way, the sintering process can be adapted to different assembly conditions such as, for example, samples compatible with high pressures but not with high temperatures or vice versa.

All the results reported above were obtained when drying the Ag green paste with the die on top of the paste. The obtained results and, in particular, the microstructural differences between the Ag central zone and its periphery, suggested that the paste drying process was very critical. For this reason a specific study was performed in order to evaluate the effect of the different drying methods already mentioned in chapter 4. In fact, the C-SAM images performed on different samples showed that a much more homogeneous and regular die-attach is obtained when drying without die, although from the practical point of view this process is more complex than simply proceed with the complete temperature profile with the die on place.

In addition, die-shear tests revealed higher fracture force values for the drying without die approach and, what it is perhaps more important, the die-shear force is independent of the final die-attach thickness. In contrast with this result, die-attach layers dried with die present a clear decrease of the die-shear force from a given Ag thickness (in the range of 100 µm in our case). This effect has been associated with

unfavourable drying conditions when the die is on top of the fresh paste and its volume is significant. This hypothesis is reinforced by the fact that the die-shear modulus obtained for the samples dried with die are also significantly lower than those for the samples dried without die, meaning that the Ag layer is "softer" in the first case due to a higher content of voids (pores).

In parallel with the evaluation of the drying methods, a more practical assessment concerning the Ag thickness reduction during the sintering process was also performed. The main result is that the relationship between initial green paste and final die-attach thickness follows a linear function, allowing an easy prediction of this critical parameter from practical manufacturing data such as the screen-printing mask thickness. It has been determined that the Ag shrinkage effect is more important when using the drying method with die (60 %) than when using the drying step without die (40 %).

Another critical aspect to be considered in die-attach issues is the state of the surfaces and in particular, the substrate surface condition. The substrate surface roughness doesn't show any significant effect on the die-attach adherence in the range from 80 nm to 800 nm when sintering with pressure (7 MPa). At zero pressure, it seems that die-shear strength decreases with surface roughness, but the adherence is very low. Improving the drying step (Ag paste dried without die) provides better results at zero sintering pressure and, for example, Ag plated substrates show quite acceptable adherence values for the K-type Ag paste. Nevertheless, the best results at zero pressure have been obtained with another paste, the X-type, which is able to provide good joints (above the threshold given by standards) thanks to a specific formulation for this kind of processes.

In summary, this chapter provides practical information for processing die-attach layers using the Ag paste and process used and developed in this work, giving a relatively complete explanation about the effect of each process parameter on the characteristics of the final die-attach. Nevertheless, as many factors have been analysed, additional questions raised (such as the effect of sintering time when drying the paste with die, the link between Ag microstructure and SAM images, the role of periphery Cu oxide layers in die-shear tests, etc.). These subjects (among other) have been identified as interesting research topics in future works.

Finally, chapter 6 presents a comparative analysis of different die-attach materials suitable for semiconductor devices in harsh environment applications, based on thermal cycling tests. The study focused on sintered Ag over bare Cu substrates, as there is a lack of information on this combination of materials with high commercial interest. Sintered Ag is an attractive die-attach solution, because it offers high performances (both, thermal and electrical, including also a high melting point at 961 ºC), involving low process temperatures (< 300 ºC). The Ag paste analysed was the commercially available K-type NanoTach from NBE Tech Company already mentioned in chapters 4 and 5. Au plated substrates and AuGe and PbSnAg solder alloys have also been considered in the study. PbSnAg was selected as a well-known reference die-attach material and AuGe is a suitable solution among all lead-free die-attach materials for high temperature applications.

The proposed experimental study is based on the test vehicles described in chapter 4 combining the different materials and required assembly techniques. These test vehicles represent the basic structure of the most common power device assemblies reproducing the CTE mismatches find in power electronics packages.

As it was mentioned, the study is based on thermal cycling of samples designed for operation at high temperature. Consequently, a suitable temperature profile was defined based on the information available in different standards. To implement these temperature cycles (between - 65 ºC and + 275 ºC) a specific harsh temperature cycling bench has been developed, based on a commercial hot / cold plate system and including a number of modifications allowing its safe continuous operation. In parallel, in order to evaluate the degradation of the die-attach layers under thermal cycling in a rigorous way, an experimental protocol has been also designed, based on the characterization equipment available. In particular, the quality and degradation of die-attach layers over time has been basically monitored by C-SAM acoustic microscope and die-shear tests.

Before starting the degradation study under thermal cycling, it has been verified that all the test vehicles passed the quality criteria defined in well-established standards, mainly in terms of die-shear strength and SAM inspection (content of voids in the die-attach). In particular, we can roughly place the initial (zero cycles) shear strengths for

each die-attach in the range of the 20 kgf for PbSnAg, 30 kgf for AuGe, 40 kgf for sintered Ag drying the paste with die and 50 kgf for sintered Ag drying the paste without die.

The degradation rate shown by sintered Ag nano-particle layers where the drying step was with die, was clearly higher than for AuGe and PbSnAg, although nano-Ag sintering presented the higher initial die-shear force values. In addition, although at zero cycles, the test vehicles sintered at 7 MPa showed higher die-shear forces than those sintered at 3 MPa (37 kgf and 17.50 kgf respectively), after 100 - 200 cycles both kind of samples presented similar degradation (approximately 4 kgf of die-shear strength). In general, the internal microstructure of the sintered Ag layer and its interfaces (with die and substrate) is far from being homogeneous and regular as it was demonstrated in chapter 5, and any of the initial defects present in the material could act as starting point for crack propagation. Nevertheless, we have demonstrated that in our particular case the main reason for the fast degradation of the Ag layers was a poor drying process, leaving some organic residuals in the structure. In this sense, the test vehicles developed with sintered Ag without die during the drying step (optimum drying process of the paste) presented the lowest degradation rate during thermal cycling, with results even better than for AuGe- and PbSnAg-based samples. Therefore, it can be concluded that despite the very bad cycling results obtained for sintered Ag dried with die, the optimization of the paste drying process can lead to a completely different behaviour, making nano-Ag the best choice.

Concerning the semiconductor material, the obtained thermal cycling results have demonstrated that the degradation rate is faster for SiC- than for Si-based test vehicles, while concerning strictly the solder alloys PbSnAg shows better results than AuGe. All these results can be explained by the higher stresses induced by the stiffer materials (higher Young modulus), that is AuGe and SiC. In this sense, a thermo-mechanical simulation work was also performed in order to better understand the thermo-mechanical mechanisms behind the observed degradation patterns during thermal cycling. The simulations demonstrated that the higher normal stresses associated with temperature swings were located at the die-attach / substrate interface, with the maximum values in the corners of the die and its periphery. These results qualitatively explain the SAM images showing concentric die-attach delamination patterns and, even,

die fractures in AuGe-based samples. An attempt was made for quantitatively validate the thermo-mechanical simulations comparing direct warpage measurements of tests vehicles with strain simulations. Although simulated and measured results were in the same order of magnitude (a factor 2 or 3 of difference), the warpage measurements were not enough accurate for such validation purposes, and additional research work will be required in the future on this topic.